The interaction of antimicrobial peptides with lipopolysaccharide aggregates and model membranes.

Bello, Gianluca

Awarding institution:
King's College London

Title: The interaction of antimicrobial peptides with lipopolysaccharide aggregates and model membranes.

Author: Gianluca Bello

KING'S COLLEGE LONDON

The interaction of antimicrobial peptides with lipopolysaccharide aggregates and model membranes.

Gianluca Bello

A thesis submitted for the degree of

Doctor of Philosophy

in the Institute of Pharmaceutical Science

of the School of Biomedical Sciences

March 2014

Abstract

Lipopolysaccharides (LPS) released from the outer membrane (OM) of Gram negative bacteria form aggregates which trigger an inflammatory response in humans and can result in severe septic shock. LPS molecules are heterogenic, macro-amphiphilic oligosaccharides with a pro-inflammatory activity strictly related to the colloidal structures formed in solution; the morphology of the colloids formed by LPS is dependent upon the molecular conformation of the LPS monomers. The intact LPS molecule (smooth chemotype) forms elongated micelles in solution whereas truncated LPS molecules (rough chemotypes) form lamellar aggregates. Biological toxicity tests revealed that the different chemotypes have different toxic activities on cultured macrophage cells. It is believed that the micellar aggregates are responsible for the toxic effect of LPS, while the lamellar phase should not trigger an inflammatory response. The data presented in this thesis revealed that there might be a more complex connection between the toxicity of LPS and the aggregate structures. The amphiphilic cationic antimicrobial peptides (CAPs) LL37 and LFb possess putative anti-endotoxic activities and were therefore studied using small-angle neutron scattering (SANS) and cryo transmission electron microscopy (cryo-TEM) to assess any modification induced to the colloidal structure of LPS, ideally from a high toxic state to a lower toxic morphology of the aggregates. The peptides LL37 and LFb are able to induce changes to the aggregates from different LPS chemotypes in relation to their conformation and the LPS molecular structure. Neutron reflectivity experiments on monolayer and bilayer membrane models containing different chemotypes of LPS were performed in the presence of the peptides; the data revealed that the two peptides have different mechanisms of interaction with membrane models containing LPS. These investigations provide new insight into the structure-activity of LPS in conditions which are more biologically-relevant than previously published data. Additionally the activity of CAPs on membrane models of the Gram negative bacteria OM was investigated to elucidate the different mechanisms of interaction and their possible anti-inflammatory role.

Acknowledgements

I would like to express my sincere gratitude to Dr. Richard Harvey and Dr. James Mason for their supervision, their knowledge and their invaluable support of my research. I could not have asked for better supervisors.
A special thanks goes to Richard for being the person he is, always available and patient. I appreciate his goodwill and encouragement to become an independent scientist. Thank you for what you taught me in the lab and outside University. I wish you the very best in every aspect of your life.
I would like to thank James for being kind and helpful during my PhD, always. I wish you and your family a brilliant future. A big thanks goes to Dr. David Barlow and Prof. Jayne Lawrence for their advice and inestimable help on everything that concerns neutrons.
I would like to thank all the people that helped me during my project. I am grateful to Dr. Thomas Vargues for all the good time we had during my first year and his guidance on peptide expression and purification. Thank you for making the approach to the PhD life more enjoyable. I would further like to thank Alice and Giacomo for their help during my project; I have learnt from you more than what I could teach you. A particular thanks goes to Ewelina and Dr. Lea Ann Dailey for their help with the cell culture studies. I acknowledge all the scientists that assisted me during the neutron time, Dr. Rob Barker (ILL), Dr. Luke Clifton (ISIS), Dr. Ann Terry and Dr. Stephen King (ISIS). I acknowledge Mr. Jonny Eriksson and Prof. Katarina Edwards at Uppsala University (Sweden) for the Cryo-TEM experiments. I acknowledge the EPSRC for funding the project. I thank all the nice people I had the fortune to meet at King's, who made my experience very enjoyable.
I am exceptionally grateful to my family for their everlasting support, encouragement and affection. Thank you. All this time would not have been the same without you Anna, grazie per esser parte di me.
These years in London would not have been as likable and fun without the good people I have spent most of my time with. Thank to 'la Marti', 'la Laurrrrrr' and 'la Cri' for sharing a spot on the deck of this boat. A kind thought goes to all the 'Fredians' and the 'Face', old and new... you know who you are out there. Thanks to Paolone, Bibi, Berti, Francesca, Viky and Nanda, Franzi, the 5^{th} floor people and all the Erasmus crew, Toooom!, from back in time when my adventure

actually started. A kind thought goes to my old chaps of 'the Good Parlour', the best ever: I salute you all.

Contents

List of Figures

List of Tables

Glossary

C_S surface compressive modulus for a monolayer at the air-water interface.

E_S compressibility modulus of a monolayer at the air-water interface.

Λ area per molecule.

Π surface pressure.

E. coli *Escherichia coli*.

S. friedenau *Salmonella enterica* serotype Friedenau.

S. minnesota *Salmonella enterica* serotype Minnesota.

D_{62}DPPC chain deuterated 1,2-dipalmitoyl-*sn*-glycero-3-phosphocholine.

DAN 2-3 diaminonaphthalene.

DPPG 1,2-dipalmitoyl-*sn*-glycero-3-phosphglycerol.

ESI-ms electrospray ionization mass spectrometry.

Gal galactose.

Glc D-glucose.

GlcN Glucosamine.

GlcNac N-acetyl-D-glucosamine.

hDPPC fully hydrogenated 1,2-dipalmitoyl-*sn*-glycero-3-phosphocholine.

Hep heptose.

Kdo 3-deoxy-D-mannooctulosonic acid or keto-deoxyoctulosonate.

L-Trp amino acid L-Tryptophan.

LFb bovine lactoferricin peptide.

LL37 human cathelicidin peptide.

LPS bacterial lipopolysaccharide or endotoxin.

mCD14 membrane protein cluster of differentiation 14.

MD-2 protein associated to TLR4.

MTT 3-(4-5-dimethylthiazol-2-yl)-2-5 diphenyltetrazolium bromide salt.

PEtn phosphoethanolamine.

POPG 1-palmitoyl-2-oleoyl-*sn*-glycero-3-phosphglycerol.

PPEtn phospho-phosphoethanolamine.

Rha L-rhamnose.

$\mathbf{S_{CD}}$ smoothed deuterium order parameter profile.

sCD14 soluble protein cluster of differentiation 14.

TLR4 toll-like receptor 4.

Acronyms

ACMW air contrast matched water.

BAM Brewster angle microscopy.

BCA bicinchoninic acid.

CAP cationic antimicrobial peptide.

CDC Centre for Disease Control and Prevention.

CMC critical micellar concentration.

CPP critical packing parameter.

cryo-TEM cryo-transmission electron microscopy.

DMEM Dulbecco modified eagle medium.

EARS-net European Antimicrobial Resistance Surveillance Network.

ECDC European Centre for Disease Prevention and Control.

FBS fetal bovine serum.

FEP fluorinated ethylene propylene.

ff-TEM freeze fracture transmission electron microscopy.

HAI healthcare associated infection.

ICU intensive care unit.

IFN-γ interferon gamma.

IL-1 interleukin 1.

LB Langmuir-Blodgett.

LBP lipopolysaccharide binding protein.

LC liquid condensed.

LE liquid expanded.

MBC minimal bactericidal concentration.

NO nitric oxide.

NR neutron reflectivity.

OM outer membrane.

PBS phosphate buffered saline.

PDB protein data bank.

PEG poly(ethylene glycol).

PHE Public Health England.

Phe phenylalanine.

POM polyoxymethylene.

PTFE polytetrafluoroethylene.

SANS small-angle neutron scattering.

SDS sodium dodecyl sulphate.

SLD scattering length density.

SMW silicon matched water.

SSI surgical site infection.

TEM transmission electron microscopy.

TNF-α tumor necrosis factor alpha.

Trp tryptophan.

Tyr tyrosine.

Symbols

L total length of a flexible cylinder (contour length).

M_L the mass of a certain molecule present in one unit of length in an elongated object (Da/Å).

$P(Q)$ form factor of a particle.

R radius of an elongated particle or sphere or ellipsoid.

$R_{g,xs}$ cross sectional radius of gyration.

R_g radius of gyration.

$S(Q)$ structure factor or inter-particle correlation distance.

T total thickness of a bilayer.

T_m main phase transition temperature of amphiphiles (from gel to liquid-crystalline phase).

δ density (g/cm^3) note: the original symbol for density ρ has been substituted with δ to avoid misunderstanding with the symbol of the scattering length density.

$\langle b \rangle$ average scattering length of an isotope (10^{-14} m).

ϕ volume fraction.

ρ scattering length density (10^{-12} cm).

σ scattering cross section of a scattering centre.

a_h hydrophobe cross-sectional area.

a_o hydrophile cross-sectional area.

b scattering length of an isotope (10^{-14} m).

d**-spacing** space in between bilayers or lamellae.

l length of each segment of a flexible cylinder (Khun length).

l_c extended chain length.

n number of segments of a flexible cylinder.

r_c radius of the core of an elongated particle.

t_c thickness of the core of a bilayer.

t_s thickness of the shell of a bilayer or other structures.

$\boldsymbol{F}$ Force.

Å Ångström (10^{-10} m).

$P - Area$ surface pressure-area isotherm.

Z atomic number.

Physical Constants

$\boldsymbol{N_A}$ Avogadro's Number 6.022×10^{23} mol^{-1}.

$\boldsymbol{k_B}$ Boltzmann's constant 1.381×10^{-23} J K^{-1}.

$\boldsymbol{m_n}$ mass of the neutron 1.675×10^{-24} kg.

$\boldsymbol{h}$ Planck's constant 6.626×10^{-34} J.

Chapter 1

Introduction.

1.1 Gram negative bacterial infections.

Amongst all the principal diagnosis which required the patient hospitalization registered in the US in the years 1997-2009, septicemia is the seventh most common diagnosis and grew by 78% over the decade, the second highest diagnosis increase after osteoarthritis ; septicemia represented an additional financial burden in the light of the fact that it was the most expensive condition in 2009 and it showed a striking increase by 11.3% average annual growth in aggregate costs of hospitalization from the year 1997 to 2009, the highest amongst all the diagnosis [1]. In the period from September 2006 to October 2007, 89% of the nosocomial infections registered in US hospitals where caused by strains of only ten common pathogens of which 10% were *Escherichia coli* (*E. coli*) [2]. According to the UK Public Health England (PHE), *E. coli* was the most frequent pathogen associated with healthcare associated infection (HAI) in the UK in 2011 [3] and the UK PHE periodic report on the surgical site infection (SSI) surveillance over the years 2004 and 2011 collected by NHS hospitals, established that Enterobacteriaceae (the family of *E. coli* and other Gram negative bacteria) were the predominant microorganisms causing almost 30% of the SSI cases [4]. In addition to that, between the years 2001 and 2006, one-fifth of all bacteriemias cases in the UK were provoked by *E. coli* strains with an increased drug resistance [5]. Surgery and other invasive techniques such as the application of catheters, mechanical ventilation, vascular access and physiological status monitoring, are the most common ways to contract nosocomial infections amongst intensive care unit (ICU) patients and have

been strictly surveilled [6, 7] in the light of the increasing bacterial drug resistance and its epidemiological and economic consequences. The most critical resistance trends are those observed for Enterobacteriaceae [8] and the latest survey of the European Centre for Disease Prevention and Control (ECDC) [9, 10], shows how bacterial resistance towards common antibiotics in Europe continues to increase amongst Gram negative bacteria. The data released by the European Antimicrobial Resistance Surveillance Network (EARS-net) [10] reported in Figure 1.1 shows the prevalence of resistant *E. coli* strains toward several antibiotics with different mechanism of action. It is clear from the maps how both cephalosphorin and fluorquinolone resistance have increased over the last few years in Europe. The data report a high percentage of resistance to aminopenicillins already at the beginning of this study starting in the late 1990's. In general the data show how the development of resistance has been a continuous process which does not seem to affect the carbapenem family yet. Recent evidence in the 2013 [11] from the US Centre for Disease Control and Prevention (CDC), and supported by the 2012 ECDC survey [9], report the discovery of carbapenem-resistant Enterobacteriaceae isolates with an astonishingly high mortality rate, resulting in the death of half of the patients whose bacteriemia was caused by these resistant strains.

The increase of antimicrobial resistance is sometimes described as 'catastrophic' because of the limited amount of new antimicrobial drugs introduced onto the market to counter this trend [12]. The paucity of new antimicrobial agents has an economical explanation since the investment and effort that the pharmaceutical industry has to input in order to get new drugs onto the market are unlikely to have a good return [13]. An antimicrobial drug is meant to treat mostly acute diseases but still requires the same regulatory approval of long-term drugs, therefore it is economically unfavorable when compared to the profit obtained from the commercialization of a long-term drug developed for the treatment of chronic diseases [13]. The antimicrobial drug market is of course dependent on large and small biotechnology companies which need to be encouraged to support R&D and probably the issues found during the development of new drugs are political rather then scientific [14, 15] suggesting that a different approval route or greater financial support may be needed. In the light of the obvious increased incidence of antibiotic resistance in Gram negative bacteria and the necessity for obtaining more active drugs, these efforts should be probably focused towards developing new classes of compounds from the improvement of the well known class of peptide antibiotics [16, 17].

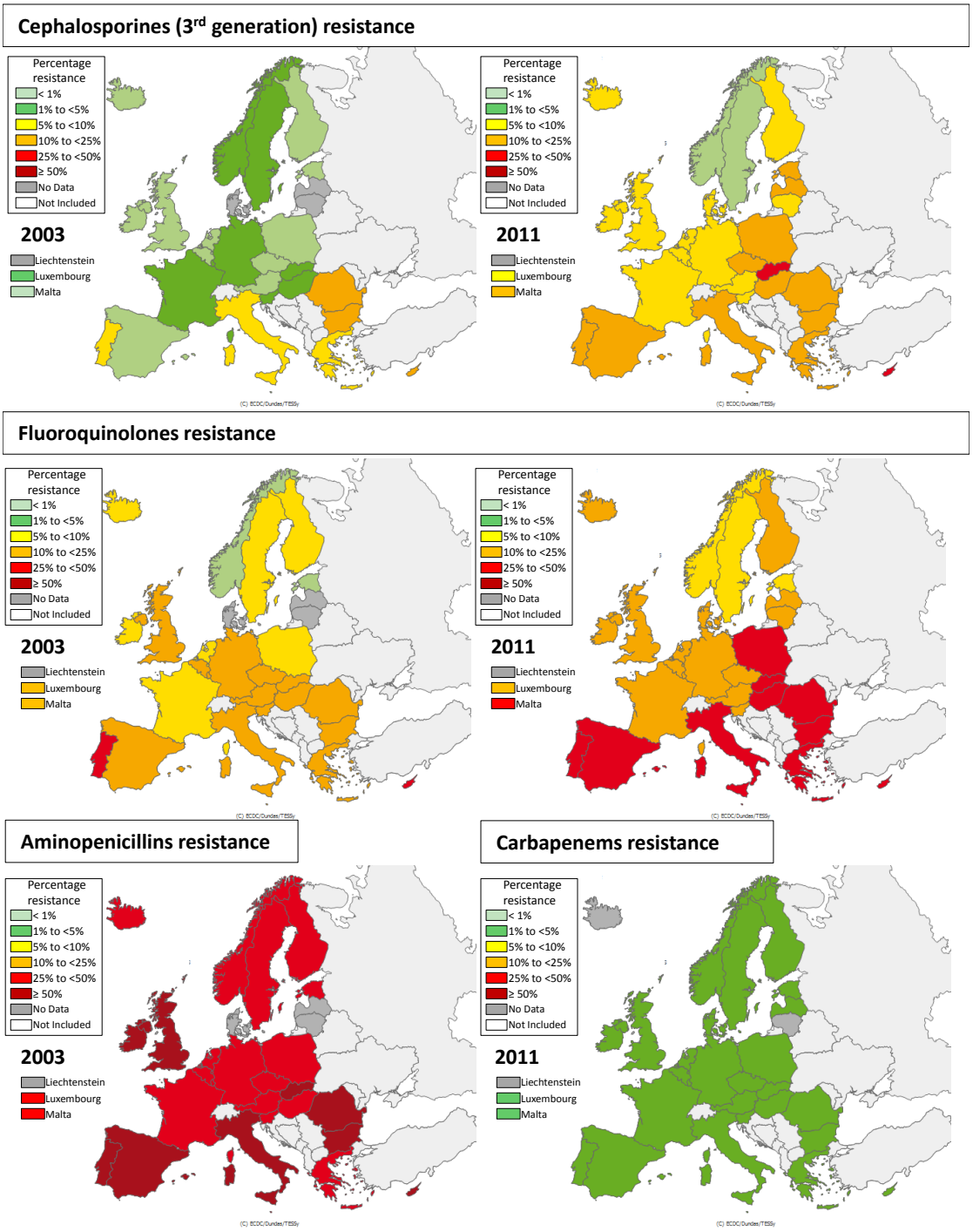

FIGURE 1.1: Resistance to fluorquinolones, cephalosporines, aminopenicillins and carbapenems of *E. coli* isolates to. Data collected from states that participate in the EARS-net study over the years 2003 and 2011. The survey and data were updated in 2012. In the legend: "No Data" refers to an insufficient amount of isolates. Figure adapted from [10]

In this thesis the attention to the rising threat generated by Gram negative bacteria has been engaged through the analysis of two processes occurring during a

bacterial infection. One research focus of this investigation aims to understand the role of the bacterial outer membrane (OM) component lipopolysaccharide (LPS) in protecting against the membrane perturbing activity of specific peptide antibiotics. The second research focus aims to study the efficacy of these potential antibiotics as effective molecules against the toxic activity of the same LPS component.

1.2 The lipopolysaccharides of Gram negative bacteria.

In common with other types of microorganisms, Gram negative bacteria have evolved several mechanisms to resist the action of antibiotic molecules. These mechanisms include enzymatic degradation, enzymatic modification and inactivation of the antibiotic molecule, alteration of the molecule's target in the bacteria, active transport that reduces the intake of the drug and reduced access of the drug into the cell due to the presence of a physical barrier, which is a non-specific, broad-spectrum, intrinsic mechanism against several type of antibiotics drugs [18, 19]. The cell envelope of Gram negative bacteria depicted in Figure 1.2 is composed of an inner membrane consisting of a lipidic bilayer with intrinsic proteins surrounded by a thin peptidoglycan layer, further enclosed within the asymmetric bilayer that constitutes the outer membrane (OM). The OM, on its outer leaflet, is composed of the amphiphilic macromolecule LPS which confers a negative charge to the cell envelope, covers up to 75% of the outer membrane surface area [20, 21] and is an essential component for the viability of the bacterial cell [22].

An OM containing LPS is an effective barrier against hydrophobic molecules which would potentially interact with the bacterial plasma membrane, destroy it and kill the bacteria [19, 23]. The low permeability of the outer membrane seems to be due to the rigidity of the acyl chains induced by the intact structure of LPS, in fact truncation of the oligosaccharide moiety of LPS results in a more disordered bilayer of the membrane and a higher susceptibility to hydrophobic antibiotics [24–26]. Hence the outer membrane permeability is strongly dependent on the structure of the oligosaccharide headgroup of LPS.

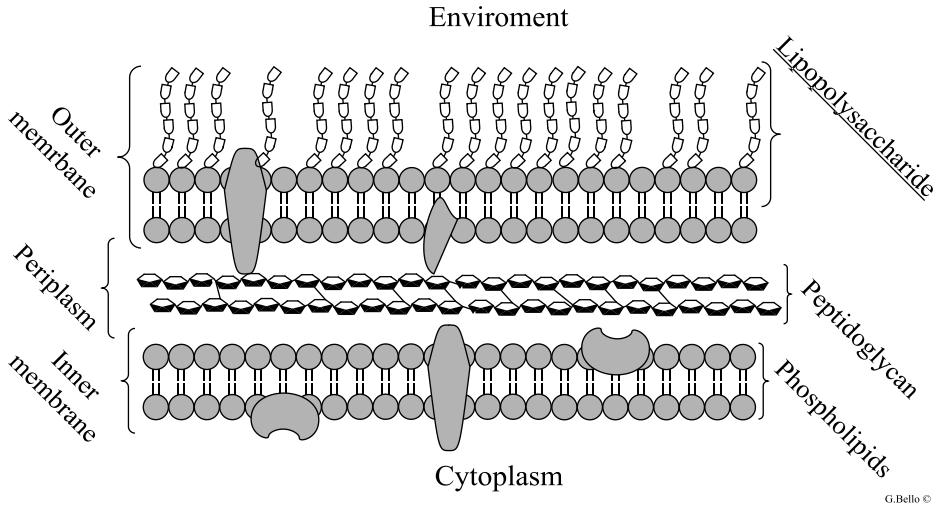

FIGURE 1.2: Representation of the cell envelope of Gram negative bacteria.

1.2.1 Structure of Lipopolysaccharides.

An intact LPS molecule is defined as being a smooth chemotype and consists of a high-molecular-weight heterogeneous macroamphiphile composed of three domains: the lipid A, the oligosaccharide core region (sub-divided into the inner and outer core) and the polysaccharide O-antigen (Figure 1.3).The lipid A region is a highly conserved moiety of LPS which anchors the whole molecule to the OM of the bacterium via its hydrophobic chains. It is covalently linked with the core oligosaccharide which has several lateral substitutions and it is bound by a glycosidic bond to the highly polydisperse O-antigen moiety, which consists of repeating short oligosaccharide units (up to 40 times).

The absence of the O-antigen due to mutations in the bacterial genome produces so-called rough chemotypes of LPS (Figure 1.3). Within the rough chemotype group, specific mutations can lead to the expression of LPS with even shorter core regions. Rough chemotypes of LPS are designated as Ra, Rb, Rc, Rd and Re according to the length of their core region (Figure 1.3).

Inter-species variation exists in each of the three structural domains of LPS and is characterized by differences in length of the poly-oligosaccharide chains, the number and type of constituent sugars, the number and type of substituent groups, and the number and length of the acyl chains found on the lipid A moiety. The heterogeneity of the LPS structures also occurs between different strains of the same species [27–31]. In this thesis attention has been focused on the well studied

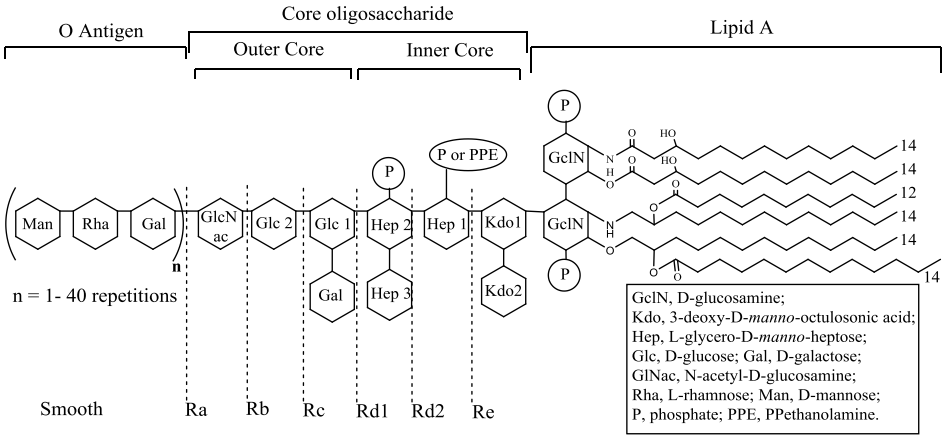

FIGURE 1.3: Schematic representation of the structure of smooth and rough chemotypes of LPS. The labels Ra to Re depend upon the length of the oligosaccharidic core region.

LPS from *E. coli* [29, 32–35] and in particular from the mutants of the strain K12 [31, 36], and the strains 0111B4, EH100 and J5 [37–41].

1.2.1.1 Structure of the lipid-A from *E. coli*.

The lipid A region of LPS is the hydrophobic anchor to the OM and the centre of its endotoxic activity. The most conserved structure of lipid A from enterobacteria such as *E. coli* consists of a bisphosphorylated Glucosamine (GlcN) di-saccharide, whose monomers are connected $\beta - 1,6$ by a O-glycosidic bond [42]. The disaccharide is acylated by four residues of (R)-3-hydroxytetradecanoic acid (14:0) in positions two and three of each GlcN monomer [43], a basic structure which is highly conserved amongst many genera of Gram negative bacteria [44]. Further non-stoichiometric acylation may be present by the formation of ester bonds with the acyl chains of the basic structure, as shown in Figure 1.4, and other specific variations on the appendages X and Y of the phosphate groups and phosphoethanolamine (PEtn) or phospho-phosphoethanolamine (PPEtn) groups, may vary between different species [29]. The lipid A from *E. coli* possesses a hexa-acylated hydrophobic region with the possibility of a further phosphorylation in position Y (Figure 1.4). The lipid A region is connected to the core oligosacharide moiety by a β O-glycosidic bond in position 6 of the distal GlcN with the first 3-deoxy-D-mannooctulosonic acid (Kdo) residue of the inner core.

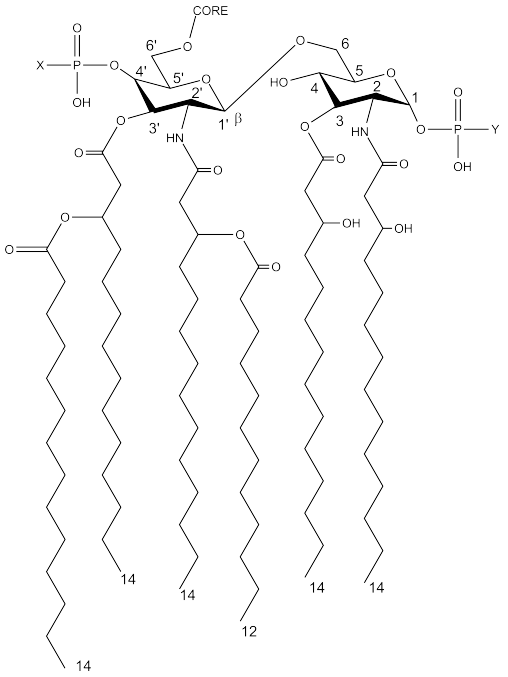

FIGURE 1.4: Conserved structure of the lipid A moiety of LPS from *E. coli* and other enterobacteriae. X and Y refer to possible substitutions on the phosphate groups.

1.2.1.2 Structure of the core oligosaccharide of LPS from the Rough *E. coli* K12, D21 mutants.

E. coli K12 is a rough strain of the bacterium which does not express an O-antigen region, but possesses an intact core oligosaccharide [45]. *E. coli* K12 produces several glycoforms of lipopolysaccharide with minor differences on the number and type of carbohydrates and phosphate substitutions [35, 42]. The D21 mutant of K12, whose core structure is described by Banoub *et al.* [46], is an ampicillin-resistant mutant [47–49] of the wild type *E. coli* K12 which produces an identical core region to the parental strain [50]. The LPS produced by this mutant is a full core Ra chemotype which is named LPS D21 in this thesis (see Table 1.1). The mutant D21 is quite distinctive from other strains of *E. coli* , as it expresses a L-rhamnose (Rha) substitution on the second Kdo residue of the inner core of its LPS [47]. The mutant D21e19 carries a mutation on the *lpsB* gene and produces a Rb cemotype of LPS which retains some of the Rha substituents of the chemotype D21 and has very little galactose (Gal) residues linked to the first outer core D-glucose (Glc) I [47]. The Rc mutant D21e7, also defined as LPS E7 in this thesis (see Table 1.1), possesses a mutation at the *rfaP* gene which gives no phosphorylation at the heptose (Hep) I and II, coupled with absence of the lateral Hep III

[51] (Figure 1.5). A mutation, presumably involving the *rfaY* gene, gives noRha at the Kdo II level and seems to be coupled with the modification at the level of the heptoses as well[52]. Additionally the LPS E7 does not possess phosphates, PEtns or other lateral substituents at Kdo II level [45, 47, 49]. The mutant D21e7 is the parental strain of the glucose-deficient mutant D21f1 and heptose-deficient mutant D21f2 which produce a Rd and Re LPS chemotypes respectively [48, 51]. Both these strains lack phosphate substituents on their inner core region and do not possess Rha or PEtn substituents in the Kdo II [50].
The LPS chemotypes of interest in this thesis will be those produced by the mutants D21 and D21e7 (together with those described in the next Section 1.2.1.3) whose structures are depicted in Figure 1.5 . For the sake of clarity the codes used in this thesis to refer to these two LPS chemotypes are respectively D21 and E7, as reported in Table1.1.

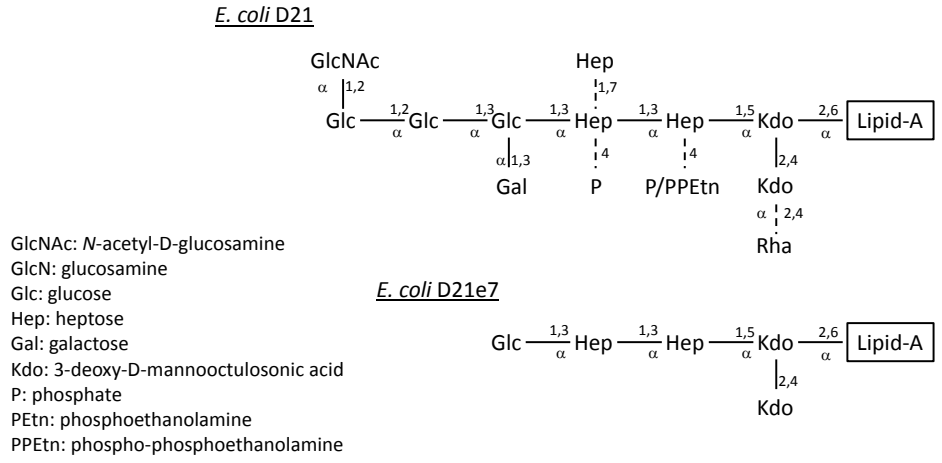

FIGURE 1.5: The core structures of LPS D21 and D21e7. The dashed lines refer to non-stoichiometric substitutions.

1.2.1.3 Structure of the core oligosaccharide and O-antigen of LPS from *E. coli* 0111B4,EH100 and J5

The lipopolysaccharide from the smooth *E. coli* 0111B4 and the rough chemotypes from *E. coli* Eh100 and *E. coli* J5 were investigated and their structures reported in Figure 1.6. The smooth LPS [41] produced by the *E. coli* 0111B4 has an intact O-antigen and core regions which differ from the LPS D21 and EH100. The core region of the smooth LPS 0111B4 possesses a Gal in the place of the Glc II, further substituted by a N-acetyl-D-glucosamine (GlcNac), and the replacement

of the lateral GlcNac with a Glc at the Glc III level. The J5 mutant is derived from the parental strain 0111B4 and is an Rc chemotype, named LPS J5, which possesses different core species, the main product of which is reported in Figure 1.6 [39, 40]. The LPS J5 has a similar core region to the LPS E7 but retains all the phosphate substitutions at the heptose level and it has the Hep III group which is further substituted with a GlcN. The core of the lipopolysaccharide expressed by *E. coli* EH100 is described by different authors [37, 38, 41] and its structure is similar to the LPS D21 with the additional presence of a PEtn and a Gal substitutions at the Kdo II level. For the sake of clarity the codes used in this thesis to refer to these three LPS chemotypes are respectively 0111B4, EH and J5, as reported in Table1.1.

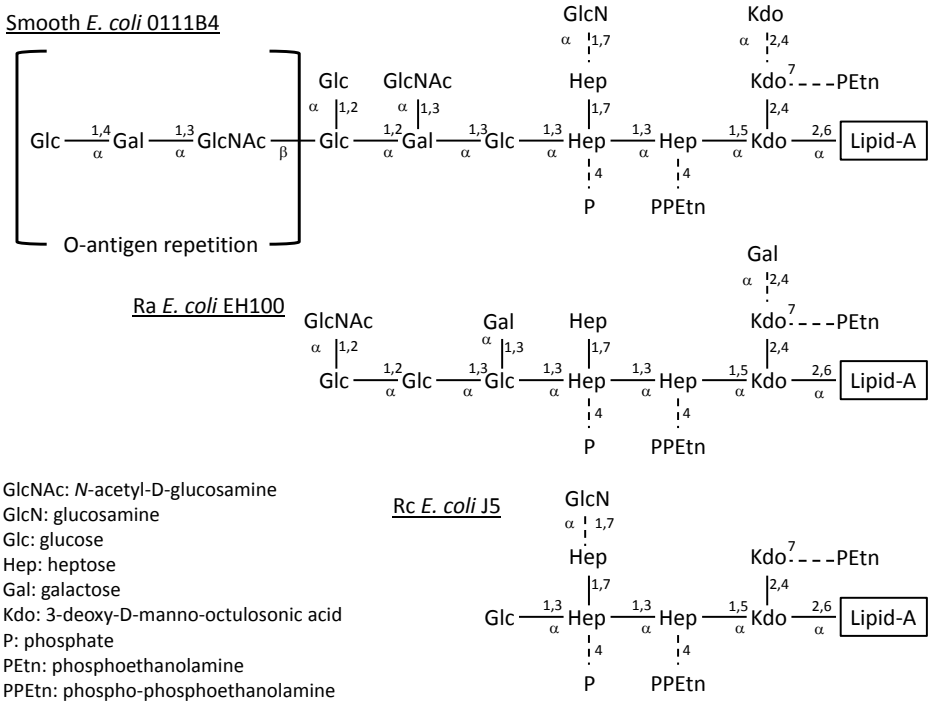

FIGURE 1.6: The core and O-antigen structures of LPS 0111B4, Eh100 and J5. The dashed lines refer to non-stoichiometric substitutions.

1.2.2 The role of LPS in the packing of the outer membrane.

The low permeability of the outer membrane to hydrophobic molecules may be due to the structure-dependent ordering effect of LPS molecules on the outer leaflet.

TABLE 1.1: Nomenclature of lipopolysaccharide chemotypes used in this thesis.

E. coli K12 mutants	Acronyms in the thesis	Chemotype
0111B4	0111B4	Smooth
D21	D21	Ra
D21e7[i]	E7	Rc$^-$
EH100	EH	Ra
J5	J5	Rc

[i] phosphate-free in the heptose region

The intact structure of the smooth LPS has a high gel to liquid phase transition temperature for the acyl chains (above 37°C) [53] in the presence of divalent cations such as Mg^{2+} . This means that the smooth LPS at physiological human body temperature increases the ordering and the rigidity of the membrane [54] thus reducing the permeation of hydrophobic molecules and preventing their insertion into the bilayer [55]. The modified rough LPS from the Ra to the Re chemotypes exhibit, in the presence of divalent cations, transition temperatures which decrease from 37°C to 30°C with the reduction of the length of the oligosaccharide chain [53, 56], hence at physiological human body temperature the acyl chains of these LPS chemotypes are likely to be in their fluid phase increasing the likelihood of permeation of hydrophobic molecules [24, 26]. LPS has a high affinity for divalent cations such as Mg^{2+} and Ca^{2+} [57] the presence of which increases the order state of all the LPS increasing the rigidity of the acyl chains [53, 56, 58, 59]. The divalent cations may act as bridges between the negative charges of the LPS headgroup explaining the importance of such ions to the stability of the OM [20, 60].

1.2.3 The toxic activity of LPS from Gram negative bacteria in humans.

LPS is released from bacteria during cell multiplication, death and lysis [22] and is responsible for the major toxic manifestations of serious Gram negative infections [61], giving rise to its alternative name endotoxin. The pathological effects of a severe Gram negative bacterial infection are, in reality, the result of an unregulated physiological response to endotoxins. Endotoxins stimulate the mammalian

immune system which reacts, in a balanced physiological immunoreaction, producing several inflammatory mediators and small molecules in order to promote the antimicrobial defence mechanisms designed to eliminate the cause of the infection (*e.g.* increase of the body temperature, reduced oxygen species, etc.). Elevated concentrations of LPS in the body, as in the case of severe sepsis, over-stimulates the immune system and the unbalanced levels of inflammatory mediators may lead to septic shock syndrome resulting in high fever, hypotension, thrombosis, organ failure and other pathological life, threatening conditions [61].
Macrophages/monocytes and neutrophils cell types are of particular interest because they are the primary target cells that react towards LPS due their constitutive expression of the membrane protein CD14 (mCD14) and toll-like receptor 4 (TLR4) , and are sensitive to picomolar quantities of endotoxin (*i.e.* 1-10 pg/mL) [61]. Nevertheless many other host cell types such as endothelial and muscle cells, fibroblasts and dendritic cells, are responsive to LPS thanks to the activation of their immune response induced by soluble protein CD14 (sCD14) instead [62]. The

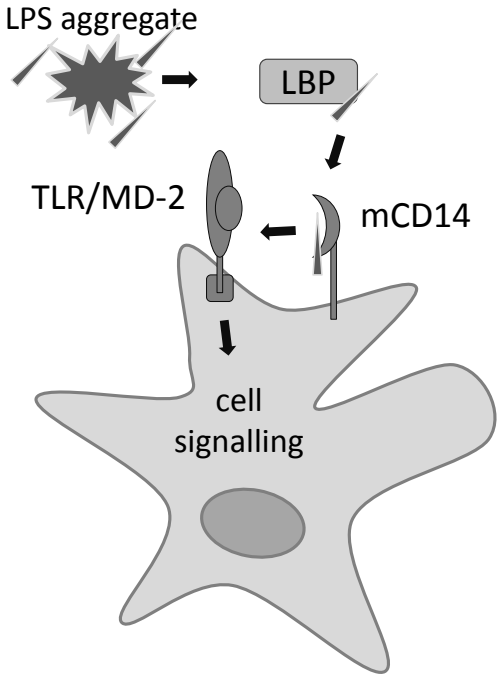

FIGURE 1.7: Activation of a macrophage cell by a LPS aggregate. The Single LPS monomer is transferred from the aggregate to the CD14 by the LBP protein. CD14 associates with the TLR/MD-2 receptor which triggers the cell signaling.

first step for the cellular activation is the recognition of LPS aggregates by the serum circulating lipopolysaccharide binding protein (LBP) [63] which, at low concentrations, acts as carrier of a single LPS monomer taken from an LPS aggregate

and presented to the CD receptor on the immune system cells membrane [64] . Only aggregates of LPS exert toxic activity whereas monomers of rough LPS and lipid A have proved to be inefficient in stimulating the release of tumor necrosis factor alpha (TNF-α) from human monocytes *in vitro* in the presence of LBP [65]. LBP is essential for an efficient immune system activation against LPS and mutations of this protein increase the mortality of patients with sepsis [66]. LBP binds specifically the negative charges of the lipid A portion of LPS by electrostatic interaction with three cationic amino acid residues (Arg 94,Lys 95 and Lys 99) at the N-terminal of the protein [67] and site mutations in this region result in loss of binding with the LPS monomer [67]. Recent experiments [68] suggest that LBP may also partition into cell membrane models thus suggesting the aid of the fusion of LPS with the lipid bilayers, which when occurring in macrophages, would enhance the activation of the cells [69]. On the other hand a high concentration of circulating LBP neutralizes LPS reducing the cellular activation [69], possibly due to a modification of the LPS aggregates' morphology (Section 1.2.3.1). More recent investigations suggest that LBP could be already present in the membrane of cultured human macrophages even after washing of the culture media [70].
LBP interacts by its C-terminal region [71] with mCD14 and sCD14 forming a ternary LPS/LBP/CD14 complex with an ideal 1:1:2 stoichiometry, and transfers the LPS monomer allowing the formation of a CD14/LPS complex [72, 73]. The CD14 receptors seem to form a hydrophobic region with a β-sheet conformation able to accommodate the acyl chains of lipid A and possess cationic residues which would interact with the negative charges on LPS as well [63] and possibly also with the carbohydrates of the core and O-antigen region [74]. CD14 presents the LPS monomer to the essential TLR4 associated protein (MD-2) associated to the final TLR4 receptor, which is responsible for the intracellular signaling cascade [62, 63] (Figure 1.7). The receptor MD-2 , as monomer, binds directly monomers of LPS [75, 76] by a delimited amphiphilic region which seems to recognize the amphiphilic properties of LPS. The structure of MD-2 contains a hydrophobic region [77] and hydrophillyc lysines [78] which could interact respectively with the acyl chains and the negative charges of LPS. Moreover the number of acyl chains of LPS influences the activity of MD-2 as signal transducer, in fact the hexa-acylated LPS/MD-2 complex activates more TLR4 than the tetra- or penta-acylated LPS/MD-2 complex [75].
The signal transduction pathway that is initiated by the activation of the TLR4 receptor leading to the release of inflammatory mediators is described in detail

elsewhere [79]. The ultimate purpose of such signal amplification is the release of prostaglandins, cytokines and other small molecules such as the anion superoxide (O_2^-), radicals ($^{\bullet}OH$) and nitric oxide (NO) [61]. A central role in the inflammatory response of the macrophages is played by the mediators TNF-α and interleukin 1 (IL-1) which facilitates many of the pathological features of the LPS-induced shock [80].

1.2.3.1 Structure-activity relationship of LPS aggregates.

LPS is an amphiphilic glycolipid which forms (like phospholipids) colloidal aggregates in an aqueous environment above its critical micellar concentration (CMC). The CMCs of different LPS have not been precisely determined due to their polydispersity and the complexity of their structures. However it is reasonable to assume that the CMC of smooth and rough LPS chemotypes is in the picomolar range of concentration, in consideration of atomic force microspcopy data from the literature which showed the formation of aggregates already in the pM range [81]. The type of aggregate that any amphphiles can form in solution has been described by Israelachvili [82, 83] by a geometric model which relates a dimensionless shape parameter S to the ratio of the effective hydrophile hydrophile cross-sectional area (a_o) and the hydrophobe cross-sectional area (a_h) according to

$$S = \frac{a_h}{a_o} = \frac{V}{a_o \cdot l_c} \tag{1.1}$$

where the other parameters are the molecular volume of the hydrocarbon's region V and the hydrophobe chain length (l_c). The shape parameter S is an indicator of the possible supramolecular aggregate structure formed by various amphiphiles dependent upon the state of order of the acyl chains. The order parameter is a physico-chemical property inversely correlated to the fluidity of the chains, which can adopt two type of states, or phases: the highly ordered gel phase (Lβ) and the disordered liquid-crystalline phase (Lα). The transition between the two phases takes place at the so-called phase transition temperature (T_m). The shape parameter, state of order and phase transition temperature depend on molecular properties, such as the length of the acyl chains, degree of saturation, headgroup conformation, charge density and charge distribution, but they are also influenced by the environmental conditions, *i.e.* ionic strength of the solution, type of ions

present, temperature and pH .

The morphology of the aggregates of LPS in solution, which is related to the

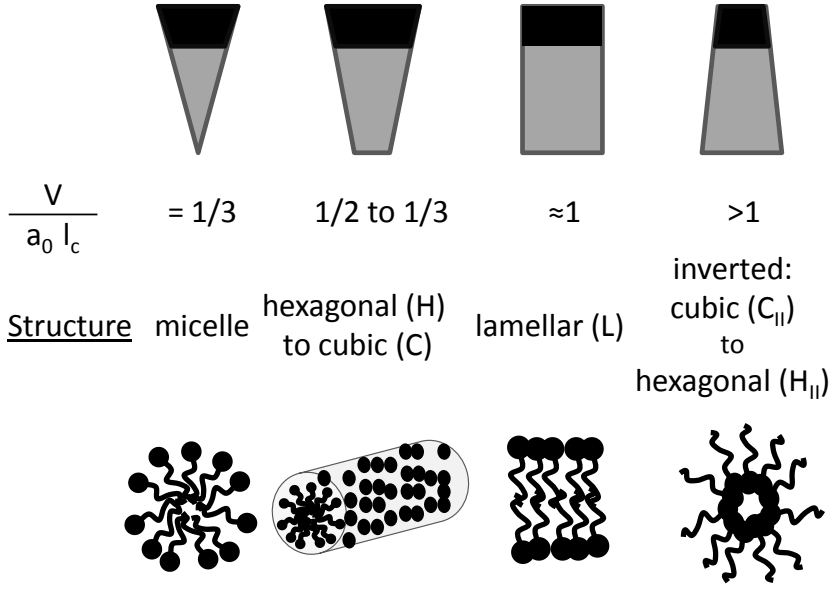

FIGURE 1.8: Amphiphile molecular structure shape parameter and related aggregate structures.

shape parameter of each single monomer, is thought to be related to its toxic activity as proposed in the "conformational concept of endotoxicity" [84]. Previous investigations on synthetic phospholipid-like compounds provided an understanding of the structure-activity relationship of LPS [85]. The toxic synthetic analog of lipid A , compound 506, studied by FT-IR at a minimal concentration of 40 mg/mL, possesses a disordered acyl chains state and a T_m of 44°C [53], forms non-lamellar cubic/inverted hexagonal structures (S>1) similarly to the lipid A from *E. coli* [86]. Whereas the non-toxic synthetic tetraacylated compound 406, an antagonist of lipid A possessing more ordered acyl chains and a T_m of 20°C , was found to form micellar or lamellar structures (S<1) [86]. When the compound 406 is mixed in a defined ratio with compound 506, it loses its antagonistic effect and the mixed aggregates showed even higher capacity to stimulate the production of TNF-α by human mononuclear cells than aggregates composed of pure compound 506 [65]. This suggests that the toxic/non-toxic feature of lipid A derivatives depend on the morphology, or shape parameter, of the molecule within the aggregate rather than the value of T_m.

Many investigations have been performed by means of X-ray diffraction in the presence of Mg^{2+} with different chemotypes of rough LPSs and with lipid A with

a water content above 90% to resolve the structural polymorphism of different endotoxin chemotypes [56, 58, 59, 87, 88]. Ra, Rc, Rd, Re LPS and lipid A from *Salmonella minnesota* (*S. minnesota*) at a minimal concentration of 18 mg/mL formed lamellar structures below 37°C and non-lamellar structures above the phase transition temperature, whereas the addition of Mg^{2+} induced the coexistence of lamellar and non-lamellar strucutres and reduced the fluidity of the acyl chains [56, 59, 89]. The ordering effect of Mg^{2+} is most expressed in lipid A and the Re LPS and to a lesser extent in rough chemotypes with a more complete oligosaccharide core, suggesting that the negatively charged phosphates at the heptose level might reduce the effect of divalent ions which otherwise would interact with the phosphates at the glucosamine level of lipid A inducing a stronger ordering effect upon the acyl chains [53]. The divalent cation Mg^{2+} reduced the chain mobility of LPS and produced a decrease in the toxicity levels due to the favoring of a lamellar state [90]. The biological role of LPS is also connected to the interdependence of the molecular conformation and the molecular charge of the lipid A [91]. To summarise LPSs in the lamellar state with a cylindrical shape parameter and absent or reduced negative charges seem to be non-toxic whilst LPS aggregates in the non-lamellar state whose monomers possess an inverted cone shape parameter (S>1) and have four negative charges exert the highest toxic activity [84, 91, 92].

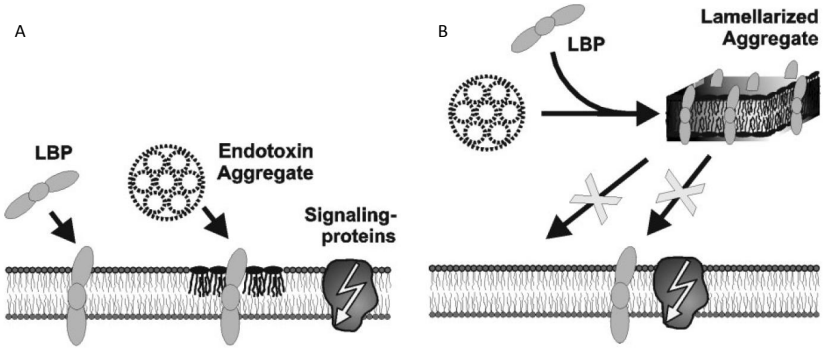

FIGURE 1.9: Model of cell activation by LPS adapted from [70]. (A) Recognition of non-lamellar structures of LPS by membrane bound LBP and cell activation. (B) Aggregates of LPS in the lamellar state pre-treated with LBP do not stimulate the cells.

The proposed mechanism of endotoxic activity suggested by the group of Klaus Brandenburg can be summarized as follows (Figure 1.9). The LBP associated to the membrane of the immune cells such as human mono-nuclear cells [68, 69] recognizes the aggregates of LPS in the non-lamellar state and facilitates the incorporation of endotoxin in the membrane of the host cell [93]. The incorporated

LPS molecule is allowed to interact with the membrane-bound acceptors and initiate the immunostimulatory signal [69]. The presence of LPS in the lamellar state would not allow the recognition of the aggregates and the stimulation of the immune system would not occur [84].

1.3 Cationic antimicrobial peptides (CAP).

The increasing prevalence of multi-drug resistant Gram negative bacteria and the lack of new antimicrobial drugs on the market (Section 1.1), necessitates the need for the investigation of feasible alternatives to the use of classical antibiotics. The support for cationic antimicrobial peptides as possible replacements or adjuvants to common treatments for bacterial infections has been extensively discussed [94–97]. Currently the number of recognized cationic antimicrobial peptides (CAPs) in the literature amount to almost two thousand peptides [98, 99] which can be divided in the following classes (a) α-helical, (B) β-sheet, (c) cysteine-rich, (d) unusual composition and (e) unusual amino acids [100].
Several CAPs of diverse natural origin with different structures and physicochemical features have been investigated [101, 102] and despite their structural diversity, most of them share some important features required for their activity including a net positive charge and an amphiphilic character [103]. The central mechanism of antimicrobial activity of CAP is the selective interaction of the peptides with the negatively charged envelopes of Gram negative bacteria [94, 100, 104, 105]. The initial electrostatic interaction of CAPs with biological membranes is followed by the permeabilization of the membrane [105]. The most plausible mechanisms of membrane disruption involve the formation of pore-like structures such as the 'barrel-stave model' or the 'toroidal model' [106], or the so-called 'carpet model' by which the lipid bilayer is destroyed in a detergent-like manner [107]. All these mechanisms of action rely on the achievement of a cooperative threshold peptide concentration on the surface of the membrane. Once that the bacterial physical barrier has been compromised, the peptides may be internalized into the cytoplasm of the cells and interact with intracellular targets such as nucleic acids and proteins, strongly affecting the bacterial viability [108–110]. The function of CAPs may not be confined to bactericidal activity, in fact human cathelicidins and defensins showed additional activities in processes such

as chemotaxis and wound repairing [111–113]. In addition to these latter activities, an emerging interest is arising for the anti-inflammatory role of antimicrobial peptides of synthetic [114] and natural origin [115, 116].
This thesis investigates the functions of the two CAPs, LL37 anf LFb , as membrane active compounds against models of Gram negative bacterial membranes containing different chemotypes of LPS and as potential anti-endotoxic molecules by the use of biophysical and biological techniques.

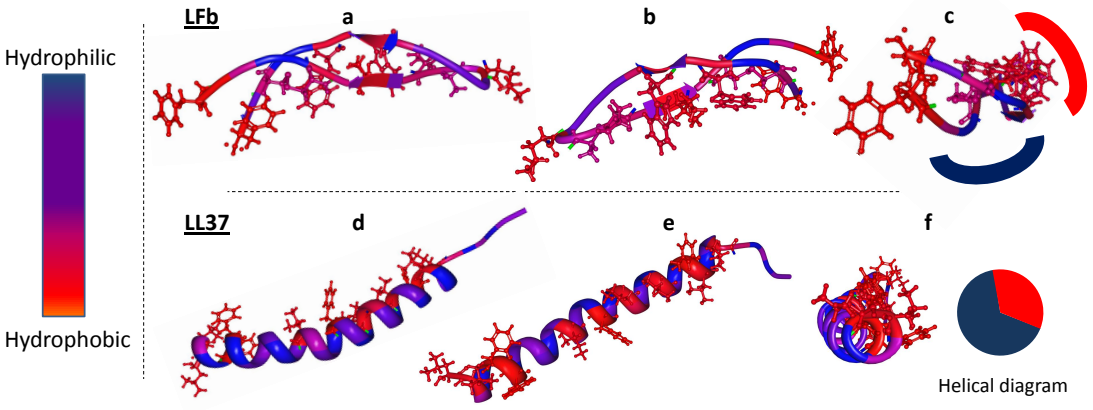

FIGURE 1.10: Structures of LL37 and LFb with the hydrophobicity scale on the left. LFb (A) hydrophilic side, (B) hydrophobic side and (c) the diagram of the axial view of the peptide that shows the hydrophobic and hydrophilic regions. LL37 with the (d) hydrophilic side, (e) hydrophobic side and (f) diagram of the axial view of the peptide and the relative helical diagram. Image generated from the PDB structures of LL37 (PDB code 2k60) and LFb (PDB code 1lfc).

1.3.1 Bovine lactoferricin (LFb).

Lactoferricin B (LFb) is a 25-residue antimicrobial peptide derived from the bovine lactoferrin protein by pepsin cleavage [117] with a positive net charge of +8 at neutral pH. LFb consists of an amphiphilic β-sheet conformation with one disulfide bond between the Cys 3 and Cys 20 residues, which does not seem to be necessary for its antimicrobial activity [118], and it forms a loop which bares two distorted anti-parallel β-sheets domains [119]. The peptide presents one hydrophobic strip surrounded by the side chains of hydrophilic or positively charged residues [120, 121]. The structure of LFb depicted in Figure 1.10 shows different views of the peptide with the side chains of the hydrophobic residues Phe 1, Cys 3, Trp 6, Trp 8, Leu 13, Ala 15, Pro 16, Ile 18 and Cys 20, which form the apolar

face of the peptide. From the figure it is possible to note the amphiphilic character of the peptide with the identification of the hydrophobic (red) and hydrophilic (blue) regions (Figure 1.10 C). Bovine lactoferricin's structure differs from that of human lactoferricin, which possesses a partial α-helical conformation, [122] and its antimicrobial activity is more potent than its human analog against a wide range of bacteria [123]. Sequence and details of the peptide are provided in Appendix B.

LFb interacts with the outer membrane of *E. coli* causing blebbing and it is possibly internalized increasing the cytoplasmic debris [124, 125]. The possible intracellular targets of LFb have been little investigated, however Yu *et al.* [126] revealed that LFb affects several metabolic processes of *E. coli* . LFb interacts with phosphatidylglycerol (PG) mono- and bilayers through the electrostatic interaction with the negative charges, adsorbing parallel to the plane of the interface below the lipid layer. The depth of the insertion is related to the order state of the acyl chains, in fact the more ordered acyl chains of dipalmitoylphosphatidylglycerol (DPPG) prevent the insertion of the peptide compared to the more fluid chains of palmitoyl-oleoylphosphatidylglycerol (POPG) lipids [127]. Umeyama *et al.* supported, by NMR investigations, the evidence that LFb is attracted by negatively charged lipids and they also suggest that it possibly forms pores in bilayers containing acidic lipids [128].

The susceptibility of *E. coli* to the minimal active sequence RRWQWR at the N-terminal of LFb , necessary to build up an amphiphilic structure, is highly dependent on the structure of LPS [129]. The presence of negative charges in the core of LPS allows for a strong electrostatic interaction of the minimal sequence, reducing the minimal bactericidal concentration (MBC) of the peptide, whereas the removal of part of LPS's core containing the negative charges, despite a reduced shielding effect, decreases the electrostatic attraction with a consequent increase in the MBC; exception is made for the case of the deep rough LPS which allows a direct hydrophobic interaction of the peptide with the acyl chains, increasing the bacteria's susceptibility [129] . This suggests a two-step mechanism where the initial electrostatic interaction with the core of LPS disorganizes the membrane structure [127, 130] allowing the interaction of the hydrophobic residues of LFb with the acyl chains and subsequent membrane disruption. Despite such relevant evidence of the dependency on the LPS's structure of the antibacterial activity of LFb , interaction studies in the presence of different chemotypes of endotoxin are absent from the literature.

A sequence similarity investigation by means of the RCSB PDB protein comparison tool [131] which applies two sequence alignment algorithms, the Smith-Waterman (SM) and Needleman-Wunsch (NW), has been carried out matching the sequence of LFb with the whole sequence of LBP (PDB identification code 4M4D). The algorithms produced a high degree of similarity with only one mismatched residue (G and W) between the minimal LFb sequence $_{5}$RWQWRMKK $_{12}$ and the LBP's sequence $_{92}$RGKWKVRK $_{99}$ which is the best docking sequence for LPS [132]. The competition of antimicrobial peptides with LBP for the binding to the endotoxin may be a very specialized and effective way to reduce or impede the LPS-induced inflammatory response, as suggested by the investigation of Scott *et al.* on several CAPs [133]. Moreover LFb presents a stronger affinity for LPS than its human analog [134] and the LPS-binding activity has been established for other similar peptides such as the cyclic β-sheet peptide tachyplesin I [135]. The interaction of a specific sequence in the loop of LFb with LPS molecules is the basis of the anti-endotoxic role of the bovine lactoferrin protein [136] and may explain the *in vitro* anti-inflammatory effect of LFb on disc tissues from humans and other mammals [116]. All this evidence supports the rationale for the investigations carried out in this thesis on the mechanism of anti-endotoxic activity of LFb .

1.3.2 Human cathelicidin LL-37 (LL37).

The LL37 peptide, sometimes called Cap-18, is a 37-residue antimicrobial peptide derived from the proprotein hCAP-18 stored in neutrophils and epithelial cells [137]. It is unfolded at low concentration in an aqueous environment [138] whereas it adopts an α-helical conformation in the presence of sodium dodecyl sulphate (SDS) micelles and lipid membranes [139] with a bend between the residues 14 and 16 and a disordered C-terminus from the residue 32 to 37. The peptide also folds up at higher peptide concentrations (over 0.1 μM) due to the formation of oligomers which protect the peptide from proteolytic degradation [140, 141] . LL37 possesses a positive net charge of +6 at pH 7.4 and an amphiphilic nature produced by the defined hydrophobic and hydrophilic facets formed in the folded state, shown in Figure 1.10. Sequence and details of the peptide are provided in Appendix B.

LL37 has a wide range of antimicrobial and immunomodulatory bioactivities such

as binding and transport activity of DNA, a complex role in carcinogenesis, chemotaxis and cell signaling [142–147]. In this thesis the attention is focused on the interaction of LL37 with Gram negative model bacterial membranes and LPS aggregates. LL37 binds LPS and reduces its toxic activity *in vitro* and *in vivo* [148] decreasing the production of the inflammatory mediators TNF-α and NO by macrophages [149].

The mechanism of action of LL37 against Gram negative bacteria involves the interaction of the peptide with the outer membrane and its permeabilization. LL37 interacts with negatively charged lipids covering the surface of the bilayer in a carpet-like mode and, upon the achievement of a threshold concentration, the peptide penetrates the bilayer as an oligomer forming a toroidal pore and crossing the outer membrane [138, 145, 150, 151]. Oren *et al.* suggested that upon disruption of the outer membrane of the bacteria, LL37 dissociates into monomers and disintegrate the inner membrane through a similar carpet-like action [140]. The disruption of the Gram negative envelope induces leakage of the cell contents and possible interaction of the peptide with intracellular targets [138, 145]. The mechanism of detoxification of LL37 has been investigated by Rosenfeld *et al.* [115] who tested the peptide in cultures of murine macrophages in the presence of smooth LPS 0111B4. The peptide strongly dissociates LPS aggregates in a linear dose-dependent manner, inhibiting the binding of the endotoxin to the macrophages; the peptide also binds LPS molecules already bound to the macrophages' membrane and competes with the receptor CD14 to the binding of LPS. The result of all these bioactivities is a reduction of the secretion of cytokines and TNF-α by the macrophages. In the same study the bioactivity of LL37 with other α-helical peptides is compared and they suggested that the binding of the peptides to LPS is not related to their detoxification capacity.

LL37 diminishes the pro-inflammatory response of mouse bone marrow macrophages stimulated with smooth LPS 0111B4 by reducing the level and transcription of TNF-α and NO in a time-dependent manner; the peptide has a greater anti-inflammatory effect when it is pre-mixed with LPS before the addition to the cells. The inhibition of NO production by LL37 is dose-dependent and 20 μg/mL of peptide reduced the NO concentration by almost 90% [149]. The anti-inflammatory effect of LL37 is probably due to a combination of the binding capacity for LPS and its immunomodulatory role. It is evident the importance of the affinity of LL37 for the endotoxin molecules, which modulates the anti-sepsis activity of the pepetide; in fact the detoxification activity of LL37 (*i.e.* reduction of TNF-α and

NO in macrophages) can be improved by substituting with Leu and Lys specific residues within sequence 15 to 32, increasing the affinity for LPS by tuning the cationic and hydrophobic features of the peptide [152].
In the light of the capacity of both peptides to interact with LPS molecules and their anti-endotoxic role, certain for LL37 and partially unresolved for LFb , the work described in this thesis aims to determine if the mechanism of interaction with aggregates of several chemotypes of LPS follows the rationale described in the 'conformational concept of endotoxicity' (Section 1.2.3.1).

1.4 Techniques used for characterizing aggregates, monolayers and bilayers of LPS.

1.4.1 Neutron scattering techniques.

Diffraction techniques involving photons (light, electrons, X-ray and neutrons) are used in spectroscopy to analyse, to different extents, the structure of soft matter. The different electromagnetic incident beams have diverse properties (*i.e.* wavelength and energy, magnetic field, charge) and therefore may be selected according to the nature of the sample under investigation and the information required from it. In principle, all the photons are scattered by matter, but some of them are more penetrating than others (Figure 1.11) and give detailed dimensional and structural information about molecules and their assemblies within the matter itself. Electrons are negatively charged particles that are repelled electrostatically by the cloud of electrons around the atoms that compose the first layers of matter. This probing method is therefore used to study the surface of solids in techniques such as transmission electron microscopy and scanning electron microscopy; the result is a very detailed image of the matter at nano-scale resolution. X-ray photons penetrate matter more deeply than electrons and interact with its inner atoms. X-rays are uncharged high energy electromagnetic waves (with an approximate wavelength of 1 Å) influenced by the electromagnetic field of the orbital of the atoms. The bigger the atomic number (Z) of the atoms constituting the material, the higher its scattering properties; therefore X-rays are sensitive to heavy nuclei that compose the molecules and selective atomic substitution in the molecules can aid the investigation and highlight particular groups within the structure.

Neutrons are neutral particles which are not affected by the atomic orbital and penetrate deeply into the matter. They interact directly with the nuclei of the molecule that constitute the sample and are scattered due to the presence of the strong nuclear forces within the atoms (Figure 1.11). All these techniques share

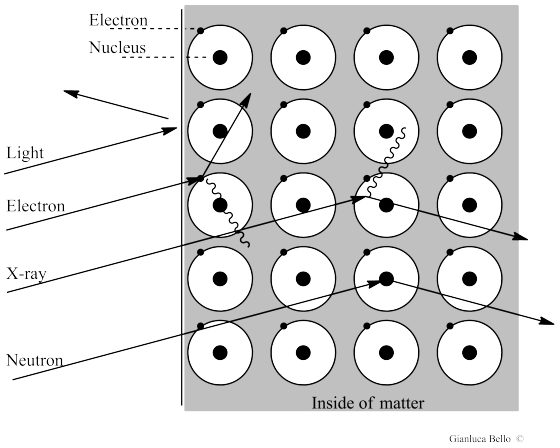

FIGURE 1.11: Schematic illustration of the diffraction of different photons and neutrons by a material.

some theoretical aspects but in this section the attention is focused on the basic theory behind neutron scattering. In particular the application of small-angle neutron scattering (SANS) and neutron reflectivity (neutron reflectivity (NR)) techniques is discussed as analytical tools used to probe the properties of aggregates, monolayer and bilayers of amphiphlies (*i.e.* lipopolysaccharide molecules and lipids) and their interaction with small CAPs.
The neutron scattering techniques described in this chapter will be additionally used in this thesis to carry preliminary investigations on the interaction of CAPs and LPS. The LPS systems under study may be composed of aggregates of pure LPS in solution (Chapter 3), monolayers of LPS at the air/liquid interface or asymmetric bilayer of DPPC/LPS supported by silicon blocks (Chapter 4).

1.4.1.1 The properties of neutrons and elastic neutron scattering.

The neutron is an uncharged particle with a spin and a mass m_n that behaves according to the quantum mechanic rule of wave-particle duality of photons described by Planck and de Broglie [153, 154]. According to Planck's hypothesis, an oscillating wave of frequency ν is associated with a defined packet ('quantum') of energy E shown in the Equation 1.2 and proportional to the Planck's constant h.

For periodic waves the frequency ν is related to the wavelength λ and the velocity v of the wave by $\lambda\,\nu = v$, therefore Planck's equation becomes the Equation 1.3

$$E = h\,\nu \qquad (1.2) \qquad\qquad E = \frac{h\,v}{\lambda} \qquad (1.3)$$

The hypothesis of De Broglie associates a particle-like behaviour to an oscillating wave of wavelength λ, according to the equation

$$\lambda = \frac{h}{p} = \frac{h}{m_n\,v} \qquad (1.4)$$

where p is the momentum of the particle defined by the vectorial factor between the mass m_n and velocity v of the neutron. Taking into account the equation 1.4, the particle-like behaviour of the neutron is linked to its kinetic energy E_k by

$$E_k = \frac{1}{2}\,m_n\,v^2 = \frac{h^2}{2\,m_n\,\lambda^2} \qquad (1.5)$$

.

The kinetic energy of a beam of neutrons is thus related to the wavelength of the periodic neutron wave. The energy of the neutron is also dependent upon the temperature T by a simplified relationship

$$E = k_B\,T \qquad (1.6)$$

in which k_B is the Boltzmann's constant.

1.4.1.2 Elastic neutron scattering and differential cross section.

The scattering of a neutron by a material, as depicted in Figure 1.12, is characterized by a modification of the momentum p and the energy E of the neutron. This modification is expressed by the momentum transfer P as

$$P = \frac{h}{2\pi}\,(Ki - Ks) = \frac{h}{2\pi}Q \qquad (1.7)$$

and by the energy transfer

$$E = \frac{h}{2\pi}(\omega i - \omega s) \tag{1.8}$$

in which Ki and Kf are the wavevectors, ωi and ωs are the angular frequencies of respectively the incident and the scattered neutron. In an ideal simple scattering experiment, the scattering is elastic and therefore there is no energy transfer to be considered. The scattering event is restricted to the wavevector transfer $Q = Ki - Ks$. The condition of "no energy exchange" ($Ei = Es$) between the neutron and the sample implies that there is no modification of the λ of the neutron (according to Equation 1.3) and in consideration of the relation of K with the speed of the neutron v and the frequency ω as $K \cdot v = \omega$, the energy transfer is equal to *zero* and is expressed as

$$E = \frac{|h\,Ki|^2}{4\pi\,m_n} - \frac{|h\,Ks|^2}{4\pi\,m_n} \tag{1.9}$$

which, according to the Equations 1.3 and 1.4, is simplified as relation between the vectors

$$|Ki| = |Ki| = \frac{2\pi}{\lambda} \tag{1.10}$$

In consideration of the Equations 1.9 and 1.10, the wavevector transfer Q is simplified by the equation [153–156]

$$|Q| = \frac{4\,\pi\,sin\theta}{\lambda} \tag{1.11}$$

Making it dependent only on the scattering angle θ and the wavelength λ of the incident beam.

The scattering of a neutron occurs in a three dimensional system therefore the position of the scattered wavevector Ks is defined by a second angle ϕ, as reported in Figure 1.13. As a consequence of this implementation, the Q value is also expanded to a three dimensional system described by the equation [153]

$$|Q| = \frac{4\,\pi\,sin\theta}{\lambda}\,(-cos\theta cos\phi, -cos\theta sin\phi, sin\theta) \tag{1.12}$$

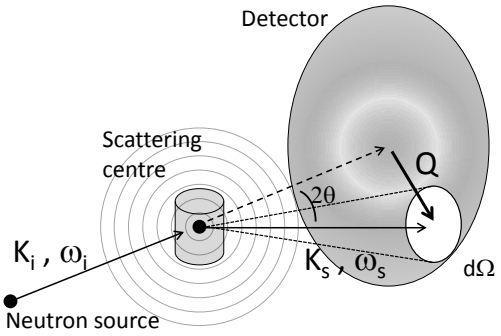

FIGURE 1.12: Scattering of a neutron beam from a single point material. For each scattering angle θ, the neutrons are collected by the solid angle $d\Omega$, partial areas (in white) that compose the detector.

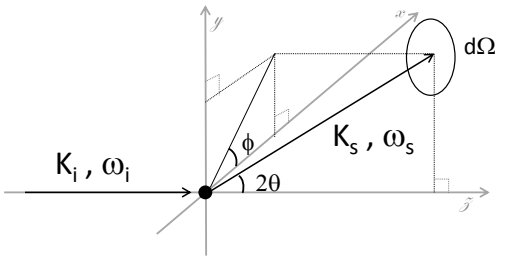

FIGURE 1.13: Scattering geometry of the neutrons' wavevectors with three dimensional coordinates. The position of the solid angle $d\Omega$ is now described by the two angles θ and ϕ.

Differential cross section. The number of scattered neutrons by an atom is defined by the scattering cross section (σ) which is directly proportional to the scattering length (b) of the atom, or more precisely of the isotope. The number of scattered neutrons in all directions per second divided by the incident flux of neutrons (I_0) that hits the scattering center is defined as the total cross section σ_{tot}. The scattered neutrons are collected by a detector which is divided in areas called solid angles $d\Omega$ (Figure 1.12). In a neutron diffraction experiment the actual intensity recorded by the instrument taking into account the spherical polar coordinates 2θ and ϕ, is the differential cross section

$$\frac{d\sigma}{d\Omega} = \frac{number\ of\ neutron\ per\ sec\ in\ d\Omega\ (2\theta, \phi)}{I_0\ d\Omega\ N} \tag{1.13}$$

where N is generic term to define the number of scattering units of interest [153].

Scattering from assemblies of atoms. In a sample containing several scattering centers, the total differential cross section for the coherent elastic scattering of N number of scattering centers is

$$\frac{d\sigma}{d\Omega} = \left| \sum_{j}^{N} b_j \, exp(iQ \cdot r_j) \right| \tag{1.14}$$

where b_j is the scattering length of the isotope in the position r_j of the space defined by the coordinates x, y, z, which produces a wave scattered in the direction Kf [155]. The atom in position r_j is referred to an arbitrary center $r_j = 0, 0, 0$.

1.4.1.3 Nuclear scattering length and contrast matching.

The strength of the neutron scattering induced by a particular isotope depends upon the value of its b [154, 156, 157]. The b value is isotope-specific, does not vary simply with Z of the atom and depends upon the spin of the nuclei. In Table 1.2 the scattering lengths of the H and D atoms are reported [158]; these atoms have two b values because of their non-zero atomic spin [153, 157]. The two scattering lengths are then combined to determine the average scattering length ($\langle b \rangle$) [153]. The rate of neutrons scattered by an atom or molecule is defined by

Table 1.2: Neutron scattering lengths of H and D according to their spin quantum number (b^+ and b^-). Averaged values of the scattering length $\langle b \rangle$ and their standard deviation Δb.

	b^+ (x10^{-14}m)	b^- (x10^{-14}m)	$\langle b \rangle$ (x10^{-14} m)	Δb[i]	σ_{coh} (barns)	σ_{incoh} (barns)
H	1.085	-4.75	-0.374	2.527	1.76	80.27
D	0.953	0.098	0.668	0.403	5.59	2.05

[i] standard deviation of b calculated as $\Delta b = \sqrt{\langle b^2 \rangle - \langle b \rangle^2}$ [157]

the scattering cross section σ, as mentioned in the previous section. The value of sigma is proportional to the scattering length b of each atom, taken b as if it was the radius of the nucleus as seen by the neutron. Using H and D atoms as an example, they present two values of σ each defined as coherent (σ_{coh}) and incoherent (σ_{incoh}) scattering cross section. The σ_{coh} and σ_{incoh} are defined by the equations

$$\sigma_{coh} = 4\pi \langle b \rangle^2 \qquad (1.15) \qquad \sigma_{incoh} = 4\pi (\Delta b)^2 \qquad (1.16)$$

The coherent scattering is the scattering that carries most of the information about the matter, whilst the incoherent scattering is a sort of variance of the σ_{coh} and adds a featureless background signal [153, 157]. The difference of the scattering cross sections between H, D and other atoms (*e.g.* N, O, P,C) is at the basis of the contrast matching variations applied in neutron experiments.
From the $\langle b \rangle$ it is possible to calculate the parameter scattering length density (ρ), for a particle or material, which is the sum of the scattering lengths of the constituent atoms per unit volume, calculated according to the equation

$$\rho = \sum \frac{\delta N_A}{m} \langle b \rangle \qquad (1.17)$$

of which the parameters are the atomic mass of the material m, the density (δ) and N_A is Avogadro's number.

1.4.1.4 Contrast variation.

One of the key advantages of using neutrons for the analysis of complex structures is the possibility to selectively label a molecule, or part of it, with isotopes that have different ρ (also referred with the acronym SLD) and thus allow the neutron beam to highlight or block specific regions of the molecules. One of the most used contrast variations is between H and D, and it is extensively used to aid the investigation of biological samples such as DNA, lipids and proteins [159–161]. The substitution of H with D within a molecule introduces limited chemical modifications but the scattering length densities of these two isotopes are markedly different (see Table 1.2). Other naturally occurring isotopes such as ^{14}N,^{16}O,P,^{32}S and ^{12}C have a positive $\langle b \rangle$ and can be exploited in neutron scattering experiments. As an example, if fully hydrogenated lipid liposomes are dispersed in pure D_2O , which has an scattering length density (SLD) of 6.35×10^{-6} Å^{-2} , the total scattering intensity is given by the liposomes whereas the solvent has very low scattering properties (Figure1.14) [157]. The different simplified contrast variation examples reported in Figure1.14 are implemented by the possibility to match the SLD of a mixture of H_2O andD_2O to the scattering length density of specific biological molecules. For instance a mixture of approximately 40-45% D_2O in H_2O (v/v) matches the SLD of proteins whereas a mixture of 13% D_2O in H_2O (v/v) would

match the SLD of hydrogenated lipids. The matched molecules would not contribute to the neutron scattering and the scattering profile contains no information regarding these molecules. In some experiments (see Section 1.4.2) it is convenient to use a 8% D_2O in H_2O (v/v) solution which has no scattering (SLD=*zero*) [162]. This is identical with that of air and therefore the solution is called air contrast matched water (ACMW).

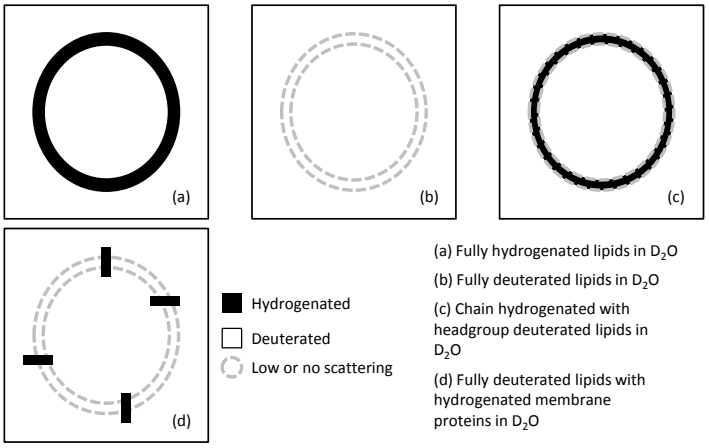

FIGURE 1.14: Schematic illustration of simplified contrast variation options in a neutron scattering experiment carried out on lipid liposomes and membrane proteins.

1.4.2 Neutron reflectivity (NR).

A reflectivity curve defined as $R(Q)\,vs\,Q$ is obtained from the specular reflection of an incident neutron beam with a wavevector Ki that occurs at the angle θ, or above, on a planar sample (Figure1.15). The planar samples of interest in this thesis can be either monolayers of lipids at the air/water interface or bilayers supported on a silicon block. The neutron SLDs of the layers are invariant on the x and y plane but they change through the z axis, due to the presence of layers of different materials. Specifically the neutron refractive indices in a NR experiment are defined by the scattering length density SLD of each layer [153, 157]. The neutron beam hits the layers and is reflected to different extents (*i.e.* intensity or $R(Q)$) according to the specific scattering length density of the material that is crossing. The reflectivity value $R(Q)$ is obtained from the relation [153, 162]

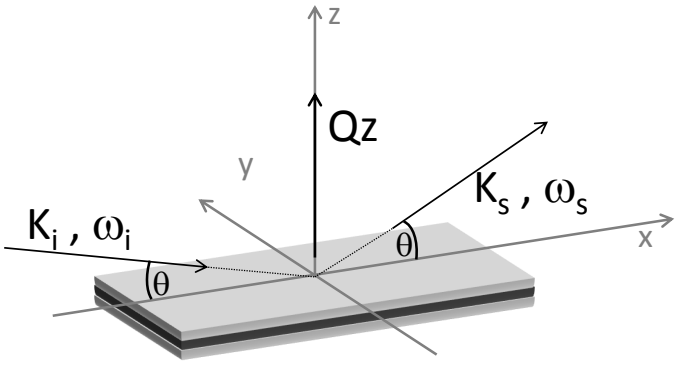

FIGURE 1.15: Schematic illustration of the specular reflectivity of a neutron beam from the surface of layered samples at an angle θ respect to the x plane.

$$R(Q) \propto \frac{16\,\pi^2}{Q^2} \left| \int_{-\infty}^{\infty} \rho z\, e^{-i\,z\,Q}\, dz \right|^2 \tag{1.18}$$

where ρz is the ρ of the layer in the z position along the z axis. The reflectivity is a function of the wavevector transfer Qz which is described in Equation 1.11. According to the geometry of the instrument and the type of neutron source, the value of Qz varies modifying the angle of incidence of the beam or its wavelength (as it occurs on pulsed sources [156]).

As an example, Figure 1.16 reports a simulation of the reflectivity profile of an arbitrary lipid bilayer on a silicon block. Most of the interfacial information can be obtained by the fitting of the reflectivity profile to obtain an SLD profile of the layers (Figure 1.16 b). The SLD profile is directly related to the distance (Å) along the z axis and gives information about the thickness, roughness and solvation of a particular layer. The use of contrast variation is essential in NR experiments in order to obtain as much information as possible for each layer, and produce a more reliable mathematical fit which would provide a more accurate interpretation of the SLD profile. The material from which the layer is composed can be either hydrogenated or deuterated, or a mixture of the two. In this thesis partially deuterated lipids will aid the investigation of the monolayers or bilayers formed by the amphiphile LPS in conjunction with the contrast matching (Section 1.4.1.4) in order to gain an insight into the structure and interaction of specific regions of the LPS layer.

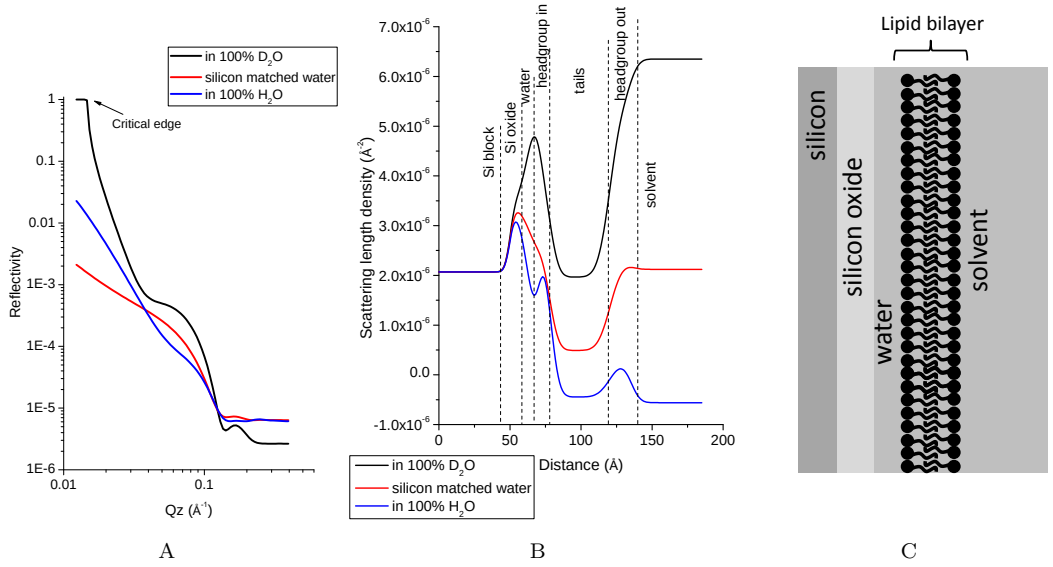

FIGURE 1.16: Neutron reflectivity simulation of a lipid bilayer on a silicon block: (A) the reflectivity profile, (B) the SLD profile divided according to the different layers, (B) schematic representation of the layers.

1.4.3 Small-angle neutron scattering (SANS).

The SANS technique is one of the most popular neutron scattering methods to study a wide range of materials, including biological structures, [157] with a resolution in real space from 10 to 1000 Å. The main advantages of the neutron small angle scattering technique over that of X-rays reside in its lower beam energy (for an equivalent wavelength) which reduces the radiative damage given to the sample, and the possibility of isotope contrast matching. A simplified scheme illustrating the set-up of a SANS experiment is shown in Figure 1.12.

The SANS technique allows one to ascertain the dimension, the shape and the orientation of an ensemble of particles in solution through the measurement of the intensity of the coherent radiation scattered in an elastic way by the atoms constituting the aggregates. The intensity of the scatter is dependent only upon the Q value and is described by the generalized expressions

$$I(Q) \propto \frac{d\sigma}{d\Omega} = N V^2 \Delta\rho^2 P(Q) S(Q) \tag{1.19}$$

$$\Delta\rho = \rho_p - \rho_s \tag{1.20}$$

where N is defined as the number of particles of volume V, the form factor ($P(Q)$) and the structure factor ($S(Q)$), whereas the $\Delta\rho$ is the contrast defined as the difference between the scattering length of the particle and the solvent, respectively ρ_p and ρ_s [154, 155, 157]. The term $P(Q)$ describes the shape of the particles and its mathematical expressions exist for many different shapes (rods, spheres, ellipsoids) which will be described in more detail in Section 3.2.4. The term $S(Q)$ takes into consideration the inter-particle interactions and distances. In the case of very dilute systems the structure factor is often considered equal to *one* and therefore is neglected during the analysis of the SANS data [155, 159]. The scattered radiation is collected by the two dimensional detector and its intensity is radially averaged and processed through a Fourier transform method to obtain the classical small angle scattering profile $I(Q)$ *vs* Q. The scattering curve can be mathematically described by fitting appropriate models and approximations (see Section 3.2.4) to obtain structural information on the particles or aggregates in dispersion. At small values of Q the scattering pattern retains information on the large scale dimensions such as tens of hundreds of nanometers, whilst at higher values the information pertains to small scale dimensions in the order of angstroms.

1.4.4 Neutron sources and instruments.

The neutron scattering experiments described in this thesis have made use of a reactor source and a pulsed accelerator source [155, 156]. The reactor source used for the reflectivity experiments under description is the high-flux reactor at the *Institut Laue-Langevine* (ILL) in Grenoble (France) which produces a continuous flux of neutrons. The pulsed accelerator source used for the small-angle neutron scattering and neutron reflectivity experiments is the synchrotron accelerated ISIS source at the Rutherford Appleton laboratory in Oxfordshire (United Kingdom) in which, due to the initial pulsed nature of the colliding proton beam, the flux of neutrons is pulsed as well. In both cases the outgoing high energy neutron flux is moderated by passing through a medium (water, heavy-water, liquid hydrogen, methane, graphite) which modifies its initial kinetic energy and determines the wavelength of the flux according to the Equation 1.5. These neutrons referred to as cold neutrons [154] are useful in studying biological materials due to their wavelength, low energy and a subsequent reduced radiation damage inferred to

the sample.

1.4.5 Monolayer at the air/liquid interface formed by lipids and amphiphiles.

The physical properties of lipids and other amphiphiles have been extensively characterized using monomolecular films formed at the interface between air and an aqueous subphase. This study is ordinarily achieved with the use of a Langmuir-Blodgett (LB) trough. A standard LB trough consists of a trough made of a hydrophobic material such as polytetrafluoroethylene (PTFE), which contains the aqueous subphase. Two movable barriers made of polyoxymethylene (POM) are controlled by the instrument's software via a computer interface and move across the surface of the subphase and can be closed at a controlled speed. The amphiphiles are deposited at the interface after first being dissolved in an organic solvent, such as chloroform, and spread onto the clean subphase with the barriers open at their maximum area. The evaporation of the solvent leaves the lipid molecules arranged far apart from each other on the surface with the hydrophilic region in contact with the aqueous phase and the hydrophobic region directed upward to the air (Figure 1.17). A microbalance allows the measurement of the surface pressure (Π) through the suspension of a Wilhelmy plate made of chromatographic paper into the subphase, so that any surface active agent present on the surface will modify the Π. The barriers are closed at a constant speed expressed in cm^2/min, forcing the lipid molecules to get closer and closer (Figure 1.17); this results in an increase of Π which is recorded by the microbalance as a downward force (F) expressed in mN/m^2, which acts on the Wilhelmy plate. The F is determined by the equation

$$F = (\delta_P\, g\, l\, w\, t) + 2\,\gamma\,(t + w)\, cos\theta - (\delta_S\, g\, l\, w\, t\, h) \tag{1.21}$$

.

where the Wilhelmy plate's dimension are given by w (width), l (length) and t (thickness). The density δ_P of the material used to prepare the plate (in this case absorbant filter paper) and the density δ_S of the subphase are included. The depth of the immersion of the plate is represented by h and the surface tension is γ, g

is the gravitational constant and θ is the contact angle between the plate and the subphase's surface [163]. The surface pressure of the monolayer is generated by the increasing pressure of the monolayer on the surface γ_m opposed to the pressure of the clean surface γ_0 according to

$$\Pi \; = \; \Delta\gamma \; = \; \gamma_0 - \gamma_m \tag{1.22}$$

.

Considering that the dimensions and the depth of the plate remain constant and that the plate is completely wetted by the subphase ($cos\theta = 1$) [163], the relationship between the change in force ΔF and the change in surface tension $\Delta\gamma$ derived from Equation 1.21 is now simplified as

$$\Delta F \; = \; 2\Pi \tag{1.23}$$

.

thus the change in force, in m/mN, is equal to twice the change in surface pressure [163].
The LB trough is used to compress a monolayer of lipids at a constant temperature while the surface pressure is monitored, producing what is called a $P - Area$ (Figure 1.17). The number of molecules spread onto the surface must be known in order to associate the surface area of the trough with the area per molecule (Λ) giving the plot $P - Area$.

When the barriers of the LB trough are fully open the molecules are separated by large distances and they behave like a two dimensional gas, hence this phase is called the gas phase. The compression of the barriers forces the molecules together reducing their intermolecular distances and the interaction becomes stronger, increasing Π: the molecules pack tighter and tighter until they reach the liquid phase. Further compression leads to the formation of a condensed or solid phase in which the amphphiles are highly organized, oriented normal to the subphase and the area per molecule is reduced as they are compressed together. A compression over the solid phase causes the collapse of the monolayer due to mechanical destabilization [164] and its organization is lost, resulting in the loss of material into the subphase and a sudden drop of surface pressure. During the condensed phase it is possible to determine the limiting area per molecule through the interpolation (dotted line

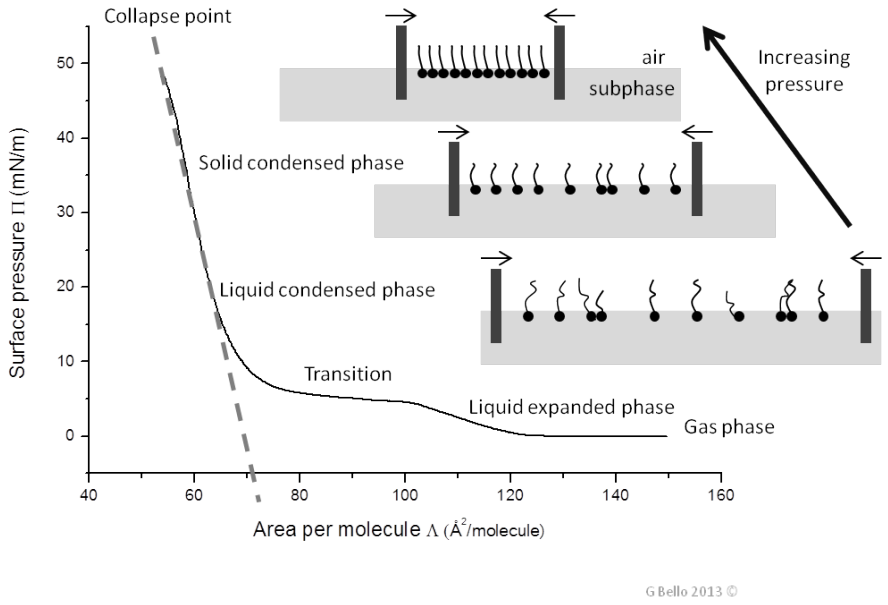

FIGURE 1.17: Surface pressure - area isotherms of a phospholipid film and molecules in different phases. Dotted line: interpolation for the calculation of the limiting area per molecule.

in Figure 1.17) of the $P-Area$ graph at a constant pressure within the range 30-35 mN/m, which has been chosen as it is the approximate lateral pressure of a lipid bilayer [165]. The limiting area per molecule of different amphiphiles varies widely and results from steric factors as well as attractive and repulsive forces between adjacent molecules and the molecules and the subphase [163]. Salts and counter ions present in the subphase affect the intermolacular interactions in addition to the intrinsic properties of the amphiphiles (headgroup charge and steric properties, saturation and number of the hydrophillic chains, particular groups present in the molecule) [166–168]. Monolayers formed on the Langmuir trough provide a good model for the behaviour of bilayers, since the surface pressure and the area per molecule are comparable between the monomolecular film and the membranes [169, 170]. Lipid monolayers at the air-water interface are an invaluable tool for the characterization of films of amphphiles and the interaction with antimicrobial peptides, especially in combination with other biophysical techniques such as neutron reflectivity and Brewster angle microscopy [164, 171–173]. Limited information are available regarding the characterization of monolayers composed of LPS [21, 174] despite its central role as permeability barrier on the OM of Gram negative bacteria (see Section1.2.2). Previous studies determined the role of increasing concentrations of rough Re and smooth chemotypes of LPS in monolayer composed of DPPC [175, 176] suggesting a fluidizing effect on the lipid at 25°C and

and an attractive interaction between the two molecules. Recently this technique has been used in connection with other biophysical techniques (X-ray and neutron reflectivity) in order to investigate the properties of LPS within a monolayer model of the Gram negative bacterial outer membrane [21, 177].

1.5 Techniques used for studying the interaction between LPS and CAPs.

1.5.1 Tryptophan fluorescence

The amino acid tryptophan (Trp) possess the strongest fluorescence intensity and highest quantum yield compared to the other two aromatic amino acids phenylalanine (Phe) and tyrosine (Tyr) [178]. The emission spectrum of Trp reaches its maximum when the amino acid is excited at 295 nm. The wavelength of the maximum emission of Trp and its intensity are strongly influenced by the polarity of the surrounding environment (Figure 1.18). In a non-polar environment (*i.e.* the hydrophobic chains within a lipid membrane or the hydrophobic core of a protein) the peak fluorescence intensity increases and it undergoes a hypsochromic shifts towards a wavelength of approximately 300 nm.

If the Trp residues are exposed to a highly polar environment such as aqueous buffers (Figure 1.18 B case 3), the emission spectrum possesses a lower maximum intensity peak at longer wavelength (Figure 1.18 A) at approximately 350nm. The alteration in the emission peak is due to the presence of the indole group in the side chain of the amino acid. The indole presents two electronic emission states (T1 and T2) which contribute to the overall emission anisotropy of Trp. In a non-polar environment the transition T2 is dominant because has a lower energy state and contributes for the most of the emission, which occurs at shorter wavelength and high intensity (blue shift). The presence of polar solvents induces the formation of hydrogen bonding with the imino group of the cyclic molecule, reducing the emission energy state of the transition T1, which now will contribute the most to the emission; this results in red shifts (higher wavelength) of the emission spectrum. The sensitivity of tryptophan towards the polarity of the environment has been extensively used in order to study the interaction between lipid membranes and peptides [179]. More interestingly the interaction between CAPs and models

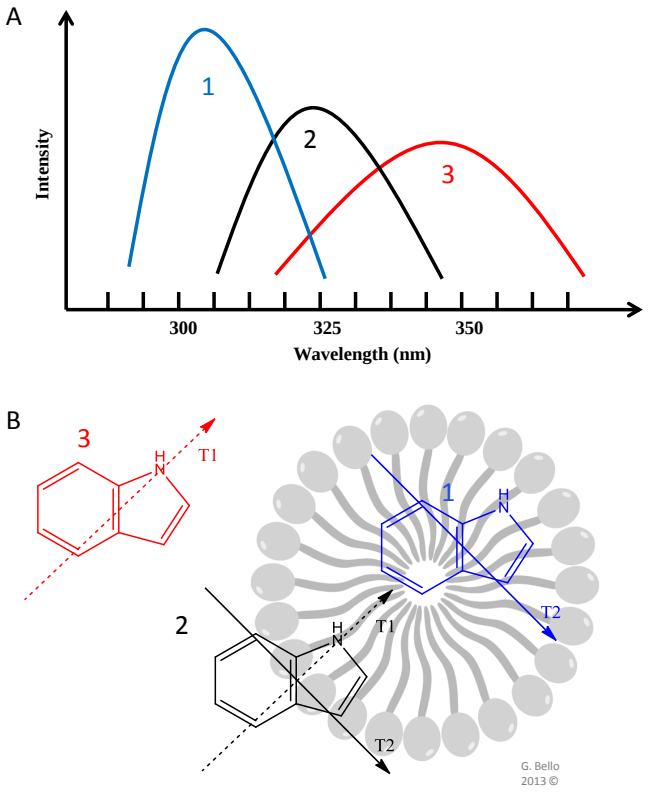

FIGURE 1.18: (A) Emission spectra of indole in different environments: red in a nonpolar, blue at the interface and black in a polar environment. (B) Transitions T1 and T2 involved in the indole emission in different environments, example with a micelle.

of bacterial membranes has been investigated to understand the depth of insertion of the peptides into the bilayers [180–182]. The environment polarity - dependent emission of Trp amino acids within the primary structure of peptides and proteins is used to study the interaction between the antimicrobial peptides LL37 and LFb and liposomes composed of mixtures of hydrogenated dipalmitoylphosphatidylcholine (hDPPC) and LPS . It is possible to relate the shift of the fluorescence spectra of the Trp residues with the penetration of the peptides into the bilayer as described above. The modified LL37 peptide used in this experiment has a substitution of the original amino acid phenylalanine in position 17 with a tryptophan residue; this substitution has negligible effects on the structure and potency of the peptide relative its wild type [182] therefore it is a good representative of the original peptide. The multifunctional antimicrobial peptide LL37 interacts and disrupts natural and model bilayers driven by the electrostatic interaction with negatively charged lipids [183, 184]. The wild type antimicrobial peptide LFb possesses two tryptophans in its primary structure [117] located

within the six residues that comprise its active antimicrobial center and which are located in the loop formed by the disulphide bridge [120]. Fluorescence studies on the whole LFb peptide and the active hexapeptide, suggest that they preferentially disrupt vesicles composed of negatively charged lipids upon insertion into the bilayer [181]. Considering the LPS binding activity of LL37 and LFb (Section 1.3), this technique may aid the investigation of the insertion process of these two peptides and its modulation in the presence of different chemotypes of LPS which present a different core structure. Hence some information could be obtained on the modulation of the LPS's shielding role by the diverse oligosaccharidic compositions.

1.5.2 Solid state ^{2}H NMR.

The ^{2}H NMR technique is well suited to acquire information about the dynamic (*i.e.* the degree of order of the lipid chains) of the lipid bilayer and the influence on the lipid organization due to the interaction of membrane perturbating peptides [185]. The selective isotopic modification, as in the case of lipid tail deuterated D_{62}DPPC , allows one to study the deuterium energy and resonance spectrum and its perturbation induced by the surrounding carbon atoms in the acyl chains. The ^{2}H-C bond orientation is derived from the analysis of the ^{2}H signal splitting due to the intensity of the quadrupolar interaction with Carbon [186]. The lipid dynamics are important in the case of membrane lipid hence the spectra are mostly recorded for bilayers above the lipid T_m, when they are in the fluid phase [186] and their mobility is maximized. The signal from the randomly oriented bilayers, such in the case of multilamellar vesicles, is deconvoluted into a signal from an oriented bilayers through a procedure called depakeing of the ^{2}H NMR powder spectra [187].

Figure 1.19 A shows a ^{2}H NMR spectrum for a mixture of D_{62}DPPC /hDPPC in Tris HCl 10 mM pH 7,4, 1 mM $MgCl_2$ at 45°C and the deconvoluted (or dePaked) spectrum of the D_{62}DPPC acyl chains allowing for the resolution of the signal into well defined splittings; the splittings from the ^{2}H of the carbons close to the headgroup presents the largest value of residual quadrupolar splitting $\Delta\nu_Q$, with a progressive reduction of frequence width along the chains towards to the bilayer centre. The ^{2}H NMR signal for D_{62}DPPC containing bilayers below the T_m would provide a powder spectra with no visible doublet splitting whereas the increase in temperature over the T_m results in higher mobility of the acyl chains and more

defined doublet splitting in the powder spectrum, as shown in Figure 1.19 A [188]. The increase in order of the acyl chains reduces the degree of freedom of the flexible lipids producing the broadening of the dePaked spectrum, *i.e.* an increase in the $\Delta\nu_Q$ frequency (Figure 1.19 A) [189]. The $\Delta\nu_Q$ is directly related to a S_{CD} in a convenient way [185, 189] according to the equations

$$\Delta\nu_Q = \frac{3}{4}\frac{e^2qQ}{h} S_{CD} \tag{1.24}$$

and

$$S_{CD} = \left\langle \frac{1}{2}\left(3\, cos^2\theta - 1\right) \right\rangle \tag{1.25}$$

where e^2qQ/h is the quadrupole coupling constant (167 kHz for ^{2}H in a ^{2}H-C bond), h is Planck's constant and θ is the angle between the D-C bond and the bilayer normal [185, 190]. The calculation of the S_{CD} allows us to obtain the profile reported in Figure 1.19 B which expresses the order parameter as a function of the acyl position for D_{62}DPPC . The S_{CD} profile provides a straightforward interpretation of the acyl chain order within the bilayer, and the increase in S_{CD} indicates an increase in their order [186]. This technique is ideal to study the perturbation induced on membrane mimetic multilamellar liposomes by peptides with different function, origin and structure which can either increase [191] or reduce [192] the order parameter S_{CD} of the bilayers. In this thesis, specifically, the solid state ^{2}H NMR technique is used to resolve the effect of antimicrobial peptides on a liposome model of the Gram negative bacterial membrane [193–195]. Previous investigations did not consider the presence of the LPS in the composition of the membrane models hence these preliminary studies aim to address this issue.

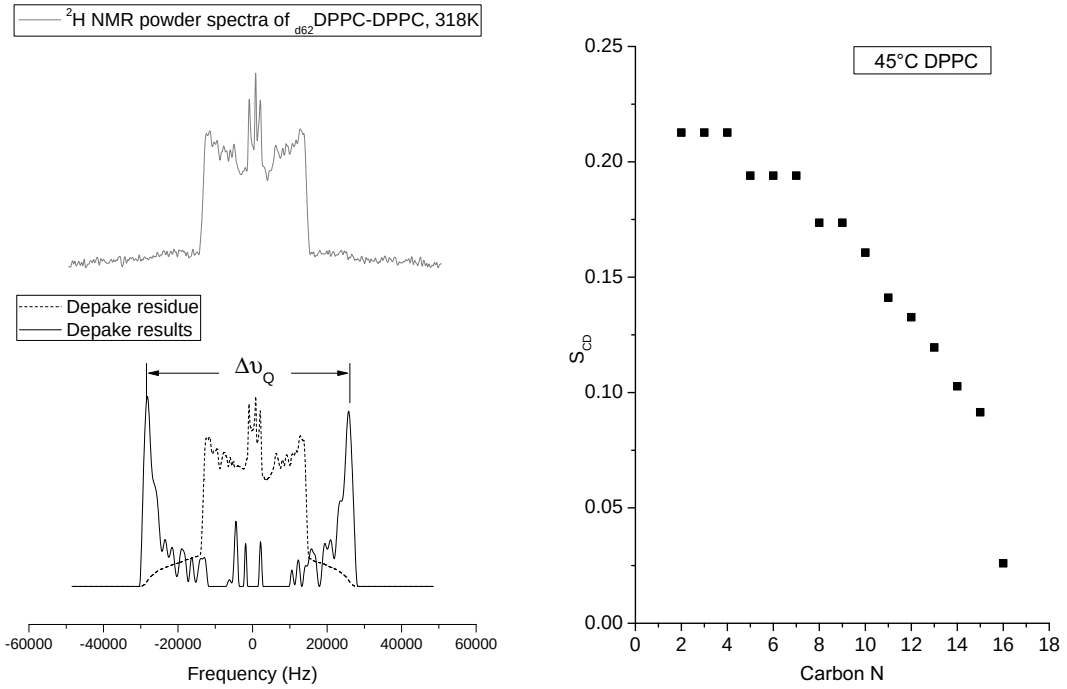

A B

FIGURE 1.19: d_{62}DPPC-hDPPC in Tris HCl pH 7.4, 1 mM $MgCl_2$ at 45°C . (A) Deuterium powder spectrum with the relative dePaked and the residual spectra. (B) Example of the smoothed order parameter profile obtained from the dePaked ^{2}H NMR powder spectra.

1.6 Aims of the project.

In the light of the theoretical background, employing the methods described in this Chapter, the aims of the project can be summarised thus:

- To test the inflammatory activation of cultured murine macrophages in the presence of different concentrations of several LPS chemotypes to determine the changes in bioactivity according to the structure of the endotoxins.
- To ascertain the possible anti-endotoxic role of LL37 and LFb in biological experiments by stimulation of the cultured murine macrophages with premixed solutions of different LPS chemotypes and peptides, either LL37 or LFb , at different concentrations.
- To study the colloidal structures formed by several LPS chemotypes in aqueous suspension by cryo-transmission electron microscopy (cryo-TEM) and

SANS and investigate the effect of the addition of either LL37 or LFb on the morphology of the LPS aggregates. These results will be examined in the context of the theories of the conformational concept of endotoxicity and the preliminary biological studies carried out on cultured murine macrophages.

- To study, at the molecular level, the interaction of LL37 and LFb with LPS-containing membrane models by the use of fluorescence spectroscopy, solid state NMR and neutron reflectivity. The study will focus on the understanding of the kinetics and the mechanism of peptide/LPS interaction. These data will provide insight into the effect of the physico-chemical features of the diverse LPS chemotypes and peptides on the binding with the models.

- The combination of all the biophysical data to elucidate the mechanisms of the respective peptide/LPS interaction.

Chapter 2

Preliminary study of cell activation by endotoxins and the effect of LL37 and LFb peptides.

2.1 Introduction.

LPS released from Gram negative bacteria stimulates a strong inflammatory response in mammals by the activation of cells of the immune system such as monocytes, macrophages and neutrophils, in addition to tissue cells such as endothelial cells and fibroblasts [62]. The cell activation induces the release of inflammatory mediators such as citokines, chemokines, prostaglandins and small molecules *e.g.* anion superoxide (O_2^-), radicals ($^\bullet OH$) and NO [62], all of them aimed at the eradication of infection. The result of a severe Gram negative infection may lead to an extensive release of LPS in the body fluids which would over-stimulate the immune system above the limits of a normal physiological response, causing a life-threatening pathological condition called septic shock which exacerbates into high fever, hypotension and eventual organ failure [61] (Section 1.2.3).

Both smooth and rough chemotypes of LPS stimulate the expression of surface receptors on neutrophils and monocytes in whole human blood [196] and induce the release of citokines (TNF-α, interleukines) [197] escalating the inflammatory state. The degree of inflammatory stimulation may be related to the structure of LPS in the light of the fact that whole and partial structures of LPS exhibit different toxicities in terms of cytokine release from cultured human peripheral

blood mononuclear cells [198]. Different LPSs of synthetic and natural origin have also exhibited either agonistic or antagonistic toxic activities on cultured J774.1 murine macrophages, depending on the structure of the endotoxin [22, 199]. With the introduction of the "conformational concept of endotoxicity" (Section 1.2.3.1), additional evidence has accumulated to support the structure-activity relationship of lipid A , the endotoxic principle of LPS [84]. The molecular conformation of lipid A determines the toxic or non-toxic effect of LPS, with a lamellar conformation eliciting less toxicity than inverted cubic or hexagonal conformations (see Section 1.2.3.1). Naturally occurring endotoxins (rough or smooth chemotypes) contain, in addition to the lipid A , the core oligosaccharide and the O-antigen regions, which modulate the toxicity of the whole LPS molecule *in vitro* [200]. Although a number of studies have concentrated on the immunostimulatory effects of natural lipid A and synthetic derivatives [53, 86], very few investigations have focused on the comparison of the biological activity of rough and smooth chemotypes of LPS [196].

Nitric oxide (NO) is a multifunctional modulator of the inflammation, produced by macrophages, which is involved in the antimicrobial response of the immune system [201–203]. As a consequence of the role of NO as an immuno-modulator, the *in vitro* inflammatory activation of J774.1 murine macrophages cells by LPS can be quantified by the dose-dependent production of NO [204, 205]. The same biological model can also be used to measure the inhibitory effects of diverse molecules on the LPS-induced activation of the macrophages [204, 206]. Thus measuring NO production by cultured macrophages can be employed as a screening method for investigating natural and synthetic CAPs with possible combined antimicrobial and anti-endotoxic roles, by determining their ability to reduce the inflammatory response of immune cells *in vitro* [114, 152, 207].

In this study the release of nitric oxide from J774.1 cells was investigated in the presence of different concentrations of several chemotypes of LPS, specifically smooth 0111B4, rough Ra EH100, rough Rc J5 and deep rough Re lipid A-2Kdo , in order to determine any difference in the inflammatory response in relation to their relative structure. The same LPS chemotypes were challenged with different concentrations of the cationic antimicrobial peptides (CAP) LL37 and LFb to determine their potential anti-endotoxic activity (see Section 1.3).

2.2 Materials and methods

2.2.1 Materials

Rc LPS from *E. coli* J5 (purity: protein 1.4%, nucleic acid 0.340%, phosphate 7.3%, Kdo 5.9%), smooth LPS from *E. coli* 0111B4 (purity: protein 1.6%, nucleic acid 1.7%, phosphate 2.8%, Kdo 1.5%) were obtained from Merck KGaA (Darmstadt, Germany) and used without further purification. Ra LPS from *E. coli* EH100 was obtained from Sigma-Aldrich Ltd. (Dorset, UK) and used after purification following the method described in Section 3.2.2. Re LPS lipid A-2Kdo was obtained from Avanti Polar Lipids (Alabaster, USA) and was used without further purification. Phenol red free Dulbecco modified eagle medium (DMEM), fetal bovine serum (FBS), L-glutamine, antibiotic formulation containing 5 mg/mL streptomycin and 5000 unit/mL penicillin, 75 cm^2 Cellstar® polystyrene culture flasks, Trypan Blue dye, 96-well polystyrene plate Cellstar® either transparent or black suitable for fluorescence measurement, 3-(4-5-dimethylthiazol-2-yl)-2-5 diphenyltetrazolium bromide (MTT), SDS and dimethyl formamide were all purchased from Sigma-Aldrich Ltd. (Dorset, UK). Interferon gamma (IFN-γ) was purchased from PepproTech (London, UK). Phosphate buffered saline (PBS) was purchased from Gibco life technologies (Paisley, UK). Details of the peptides LL37 and LFb are reported in Appendix B.

2.2.1.1 Culturing of J774.1 macrophages.

Murine macrophages of the semi-adherent cell line J774.1 were maintained in a humidified incubator at 37°C in a 5% CO_2/95% air atmosphere. The culture medium consisted of phenol red-free DMEM, supplemented with 10% heat inactivated FBS, 2 mM of L-glutamine and antibiotic formulation at a final concentration of 100 μg/mL streptomycin and 100 unit/mL penicillin. All the cell culture experiments were carried out in phenol red free cell culture medium to avoid any interference with the nitric oxide fluorescence assay (Section 2.2.1.3).
The cells were cultured in 75 cm^2 flasks and the confluent cell monolayer (90% viability) was removed for passages and for experiments by scraping. Cell viability was evaluated with Trypan Blue exclusion dye which selectively traverses the membranes of dead cells, resulting in a blue colour, whereas it does not pass through the membrane of viable cells, which are not coloured. With the use of a

microscope it is therefore possible to count the ratio of viable and dead cells and evaluate the confluence of the cell monolayer [208]. In order to perform the MTT or the NO experiments, the cells were seeded in transparent 96-well tissue culture plates with 200 μL of cell culture medium, at a density of 5×10^4 cells per well and incubated for 24 hours to allow for cell attachment. The cells were pretreated with IFN-γ at a final concentration of 500 unit/mL for a further 24 hours before further experimentation, in the light of the evidence that IFN-γ primes the cells by causing over-expression of mCD14 and TLR4 receptors [198, 209].

2.2.1.2 MTT cell viability assay.

The MTT assay was performed to assess the percentage cell viability upon treatment with different LPS chemotypes or peptides (either LL37 or LFb). This test is based on the reduction of the soluble yellow MTT compound to an insoluble purple formazan dye by the NAD(P)H-dependent oxidoreductase enzymes, allowing the quantification of viable cells. The formazan crystals, collected from the supernatant of the cell culture, were then solubilized by the addition of SDS; the intensity of the absorption at 570 nm of the resulting purple solution is correlated to the cell viability [210]. For the proliferation assays, after the initial stimulation with IFN-γ, the cells were treated either with each LPS chemotype at concentrations of 1, 10, 100 and 1000 ng/mL, or with the peptides, either LL37 or LFb , at concentrations of 0.01, 0.1, 1, 10 and 50 μM. After 24 hours of incubation, the old media was removed and replaced by serum-free media containing 12,5% (V/V) of MTT obtained from a 5 mg/mL sterile stock solution in PBS. The plates were incubated for a further two hours before the addition of 100 μL of 10% SDS solution in 50% dimethyl formamide and incubated for 4 hours to dissolve the dark-blue formazan crystals. Finally the absorbance at 570 nm was measured with a plate reader spectrophotometer SpectraMax 190 (Molecular devices, Sunnyvale, Ca, USA), recording the absorbance at 630 nm as a reference wavelength. All the tests were carried out in at least triplicate and compared with control wells in which untreated cells were cultured. The percentage of viable cells was calculated using the equation:

$$cell\ viability\ \% \ = \ \frac{Avg\ Abs\ exp}{Avg\ Abs\ control} \ \times \ 100 \tag{2.1}$$

where the numerator is the average absorbance of the experimental groups and the denominator is the average absorbance of the control group.

2.2.1.3 Cell inflammatory activation: nitric oxide assay.

The stimulation of the production of NO induced by the LPS chemotypes 0111B4, EH100, J5 and lipid A-2Kdo was investigated. The J774.1 macrophages were cultured in the same conditions as described above (Section 2.2.1.1) and, after stimulation with IFN-γ for 24 hours and removal of the stimulus, each LPS chemotype was added in fresh cell culture medium at the final concentration of 1, 10, 100 and 1000 ng/mL of LPS.
The possible anti-endotoxic role of the peptides LL37 and LFb was assessed by the measurement of NO production from J774.1 cells stimulated by LPS. The cells were treated with 100 ng/mL of each LPS chemotype pre-mixed in the cell culture medium with either LL37 or LFb at increasing final peptide concentrations of 0, 0.01, 0.1, 1, 10 and 50 μM. The LPS/peptide mixtures were incubated at room temperature for at least one hour prior to their addition to the plates. After 24 hours incubation at 37°C , the 96-well plates were spun down at 1500 rpm for 5 min and the supernatants were collected and stored at -80°C before the analysis of the nitrite concentration.
NO levels were determined using a fluorimetric assay performed in black 96-well plates suitable for fluorescence measurements. Aliquots of 100 μL of each sample supernatant were transferred into the black plates, mixed with 10 μL of a 0.3 mM solution of 2-3 diaminonaphthalene (DAN) in 0.62 M HCl and incubated at room temperature with continuous mild shaking for 15 minutes. Post incubation, 20 μL of a 3 M NaOH stop solution was added and the plate was read in a plate reader fluorimeter using an excitation wavelength of 365 nm and an emission wavelength of 410 nm. The amount of nitrite in each sample was calculated from a linear calibration curve of known nitrite concentrations, made up in the same medium used for the test samples.

Statistical analysis All the data were collected from at least three independent experiments. The values are presented as means±SD (standard deviation) and were analyzed using two-way ANOVA test and T-test by the use of the software

Graph Pad Prism (version 5) . Values with P <0.05 were considered statistically different compared to untreated cells.

2.3 Results

2.3.1 MTT assay.

The first analysis performed on J774.1 macrophages concerned the cell viability upon addition of the different LPS chemotypes or peptides (Figure 2.1A and B). The most cytotoxic activity was exerted by the LPS chemotype EH100 which produced a reduction of cell viability to 84% at 100 ng/mL and the lowest viability value amongst all the LPS chemotypes tested with a value of 61.7% at the 1000 ng/mL concentration. The second most cytotoxic LPS seemed to be LPS J5 with a value of cell viability of 82.9% at the highest concentration of 1000 ng/mL. The LPS 0111B4 and the lipid A-2Kdo had a cell viability above 89 % for all the concentration tested. The LPS EH100 only showed a significant cytotoxicity compared to the control (P<0.05) at 1000 ng/mL.
The MTT assay was also performed on the macrophages in the presence of the peptides alone, either LL37 or LFb (Figure 2.1 B). LL37 is clearly more cytotoxic than LFb , with a reduction of cell viability to 55.3% and 10.3% respectively at the concentrations of 50 and 100 μM; whereas LFb showed the largest reduction of cell viability to 59.8% at the highest concentration of 100 μM. Apart from the LL37 case at the concentration of 50 μM , the cell viability below the concentration of 50 μM was above 88% for both peptides. Only LL37 at 50 and 100 μM and LFb at 100 μM were significantly cytotoxic compared to the control (P<0.001).

2.3.2 Nitric oxide assay.

The production of NO induced by LPS is related to the inflammatory activation of J774.1 cells. In the same way the production of NO was measured in the presence of the peptides alone to assess any inflammatory stimulation they might elicit. The chemotype EH100 is possibly the most endotoxic LPS amongst all, showing the highest production of NO already at the concentration of 1 ng/mL (Figure 2.2 A). The least endotoxic chemotype is lipid A-2Kdo which presented a rather regular

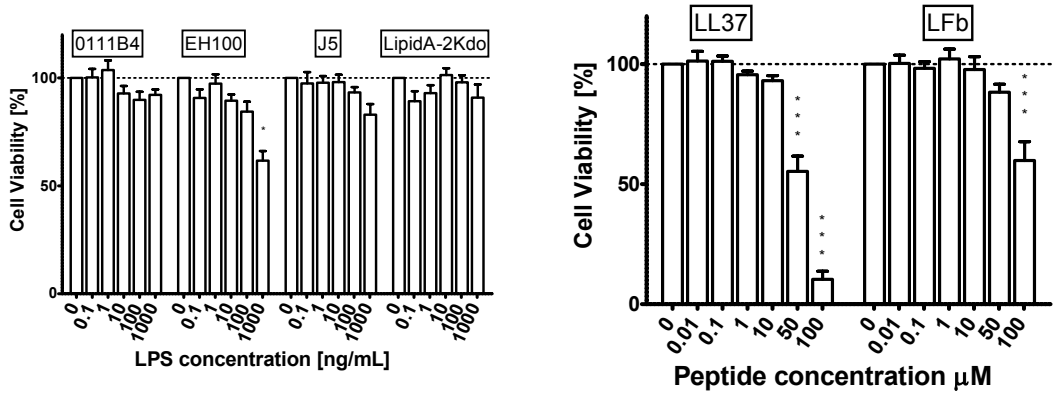

A B

FIGURE 2.1: Cell viability measurement by MTT assay in the presence of (A) different LPS chemotypes and (B) the peptides LL37 or LFb. "*" P<0.05. "**" P<0.01. "***" P<0.001.

increase of NO production proportional to the LPS concentration (Figure 2.2 A). The chemotypes 0111B4 and J5 showed a rapid formation of NO production which plateaued above the 10 ng/mL concentration. The amount of NO elicited by LPS EH100 was significantly higher from 0111B4 and lipid A-2Kdo at concentrations up to 10 ng/mL (P<0.05) whereas the amount of NO elicited by LPS EH100 was significantly lower than LPS 0111B4 and higher than lipid A-2Kdo above the concentration of 100 ng/mL (P<0.05). The amount of NO elicited byLPS EH100 was not significantly different from the NO induced by LPS J5, excluding the 1 ng/mL and 100o ng/mL concentrations (P<0.001) in which the NO production was respectively higher and lower. The NO production induced by LPS 0111B4 was significantly higher than the NO induced by lipid A-2Kdo at the concentrations of 10 and 100 ng/mL (P<0.01) whereas it was significantly lower than the NO induced by LPS J5 only at 1 ng/mL concentration (P<0.001.). LPS J5 nitric oxide production is significantly higher than the NO induction by lipid A-2Kdo at 1,10 and 100 ng/mL concentrations (P<0.001.).

The 100 ng/mL concentration for each LPS chemotype had been chosen to be tested with either LL37 or LFb to identify any anti-endotoxic, anti-inflammatory activity of the peptides. The statistical analysis of this data set revealed that the LPSs 0111B4, EH100 and J5 are not significantly different between each other in terms of endotoxicity but they are all significantly more endotoxic than lipid A-2Kdo (P<0.01).

Neither of the peptides LL37 or LFb induced, at any concentration, a statisti-

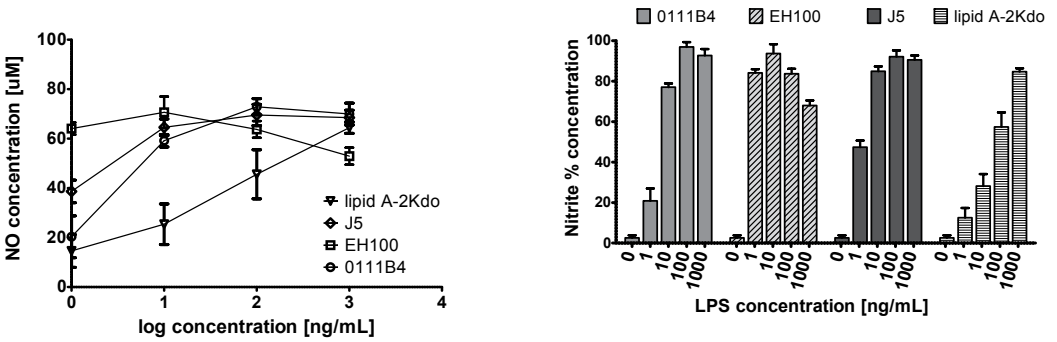

A B

FIGURE 2.2: Nitric oxide production of J774.1 cells in the presence of (A) different chemotypes of LPS and (B) the peptides LL37 and LFb.

cally significant reduction of NO production in the presence of any LPS chemotypes tested. The poor statistics outcome could be due to the high variability that affected the measurements. Hence the trend observed in the data was not be supported by any statistical test. Nevertheless it was possible to notice some differences between the activity of the two peptides. The peptide LFb did not induce visible reduction of NO production at any concentration, in the presence of all the LPS chemotypes tested; moreover the peptide itself did not show an inflammatory stimulation of the macrophages, reporting a maximum nitrite production of 5 μM, equal to the value of the untreated cells. On the other hand LL37 induced an inflammatory stimulation of the J774.1 cells at the highest peptide concentration of 50 mM and a consequent production of 16 μM of nitric oxide, three times the basal NO production (Figure 2.3 A). LL37 's increasing concentrations seemed to reduce the production of NO of the macrophages stimulated with 0111B4 and EH100 LPSs, whereas it did not have a visible effect in the case of cells stimulated with lipid A-2Kdo; the peptide seemed to increase the production of NO in cells treated with LPS J5 up to the peptide concentration of 1 mM, and induced a decrease of inflammatory stimulus above the peptide concentration of 10 mM.

2.4 Discussion

The activation of the immune system by endotoxins is not only related to the molecular conformation of the lipid A part of LPS, the endotoxic principle, which showed toxic activity in the negatively charged cubic or hexagonal inverted state and non-toxic activity in the lamellar state [91, 199]. In fact naturally occurring

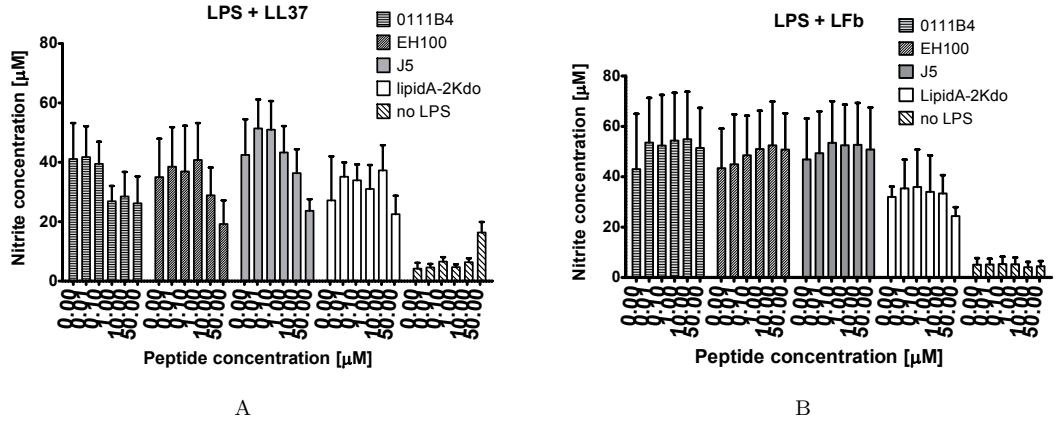

A B

FIGURE 2.3: Nitric oxide production of J774.1 cells stimulate with 100 ng/mL of different LPS chemotypes in the presence of different concentrations of (A) LL37 and (B) LFb peptides.

LPS is composed of the lipid A part connected to the core and O-antigen regions which have been shown to influence the molecular shape of LPS modulating its toxicity [198]. As revealed by X-ray diffraction experiments, a longer core region, such as the one of Ra and Rc chemotypes, favors the lamellar conformation while a shorter core region, such as the one of the Re chemotype, determines the formation of a cubic/hexagonal conformation [56]. The limitation of these data resides on the fact that the experiments were carried out with non-physiological water content and in the absence of solutes whereas the structure of LPS is affected by both solvation and the solutes contained in the medium.

A detailed comparison of the pro-inflammatory activity of naturally occurring smooth and rough LPS chemotypes with different structures is limited. Previous investigations of Gomes *et al.* showed that the presence of 100 ng/mL of either smooth or Re LPS from *S. minnesota* induced significant NO release from human monocytes, but these data lack any comparison with other chemotypes or any effect of different concentrations [196]. Schromm *et al.* investigated the LPS-induced cytokine IL-6 release from human mononuclear cells and showed that smooth LPS from *Salmonella friedenau* (*S. friedenau*) has a stronger pro-inflammatory activity than the Re LPS and lipid A from *E. coli* [199].

The preliminary biological experiments conducted in this study aimed to compare the diversity of the pro-inflammatory activity of different chemotypes of LPS in relation to their structure, by the measurement of the NO produced by LPS-stimulated J774.1 murine macrophages. At the LPS concentrations tested, the

chemotypes smooth 0111B4, Ra EH100 and Rc J5 produced a dose-response stimulation of the macrophages characterized by the formation of a plateau of NO concentration whereas the lipid A-2Kdo showed an exponential trend of the curve (Figure 2.2 A) . In consideration of an ideal dose-response sigmoidal curve, the first three chemotypes may have reached the final part of the sigmoid whilst the lipid A-2Kdo may be still at the initial exponential phase of the sigmoid. This suggests that the smooth, Ra and Rc chemotypes may have a more potent immunostimulatory effect than the Re lipid A-2Kdo .

The anti-endotoxic activity of antimicrobial peptides and their derivatives had been subject of several investigations such as the work of Gutsmann et. al. [114] which synthesized various peptides which inhibit the cytokine production induced by different chemotypes of LPS by the induction of a lamellar phase of the endotoxin aggregates. A similar activity was suggested for LBP on the release of TNF-α from human mononuclear cells stimulated with Re LPS from *E. coli* [69]. Nagaoka *et al.* [250] studied derivatives of LL37 and their anti-inflammatory activity reporting a reduction of expression of TNF-α and mCD14 induced by the peptides in cultured RAW 264.7 murine macrophages stimulated by LPS 0111B4. The preliminary data presented in this study compared the antimicrobial peptides LL37 and LFb and their anti-inflammatory role on LPS-stimulated macrophages. Despite the poor statistics, the data show that LFb is not as active as LL37 on the modulation of the inflammatory response of the cells stimulated by several chemotypes of LPS. Neither of the peptides induce a significant production of NO below 10 mM concentration and LL37 showed a slight reduction in nitric oxide production from cells stimulated with LPS 0111B4, EH100 and J5, whilst LFb had no anti-inflammatory activity at this concentration.

The data were not sufficient to draw any definitive conclusion. The J774.1 cell line system is a simple and yet useful tool to test the inflammatory activity of LPS nevertheless it may substantially differ from other cell lines or techniques used in the literature . Other biological assays, such as tests from whole blood, may complement the data presented in this chapter and give a more realistic model of the system in consideration of the fact that *in vitro* cell culture tests may lack components of the immune system response such as LBP (partially de-activated in FBS), which is present in the blood. The anti-endotoxic role of the two peptides tested could not be supported or rejected and further analyses are needed. These preliminary investigations however suggested that these biological tests are

great challenges for the peptides in consideration of the amount of interactive compounds present in the culture medium. More sensitive detection techniques, such as the use of antibodies for cytokines and mediators of the inflammatory response, may help to reduce the uncertainty of these tests.

Chapter 3

Interaction of the cationic antimicrobial peptides LL37 and LFb with aggregates formed by different chemotypes of Lipopolysaccharide from *E. coli* in solution.

3.1 Introduction

The outer membrane component lipopolysaccharide (LPS) of Gram negative bacteria is one of the most potent activators of the human immune system and the ability to induce an uncontrolled inflammatory reaction which can worsen into severe septic shock syndrome and organ failure [62, 198]. The biological activity of LPS is attributed to the membrane-anchoring moiety of LPS, the lipid A, which is the 'endotoxin principle' of LPS [211].The common architecture of lipid-A consists of the highly conserved glucosamine disaccharide connected to two phospates and usually six fatty acid acyl and hydroxyacyl chains with 12 or 14 carbons [44], but the fine structure can change according to the different bacteria and the environmental conditions [212, 213]. LPS is a macroamphiphilic glycolipid which forms

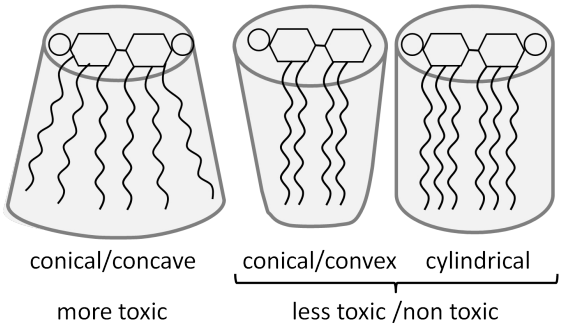

FIGURE 3.1: Representation of the possible conformations assumed by lipid A and relative toxicity.

colloidal aggregates in aqueous environments, the morphologies of which are determined by the conformation of the lipid-A and the headgroup region (Figure 3.1). Studies carried out on the lipid-A moiety [199] showed that in a conical/-concave conformation of lipid-A with a critical packing parameter (CPP) > 1 [83], the hydrophobe volume (acyl chain's volume) is bigger than the hydrophobe area (the optimal headgroup area) and the immune system activation is greater than a cylindrical or conical/convex conformation which has a CPP < 1 : the relationship between molecular conformation of lipid Aand its toxic effect, developed the notion of the "conformational concept of endotoxicity" [84]. These earlier investigations, that gave rise to the structure-toxicity relationship, were limited to the lipid-A structure without taking into consideration the influence of a more complex headgroup on the packing behavior of a whole LPS molecule, as in the case of rough and smooth chemotypes of LPS.

More recent studies reported that rough LPSs and lipid A are not active as a monomers, but exert their toxic function only if they are in an aggregated form [65, 70] which interacts with the membrane of the immune system's cells such as macrophages and monocytes, but also with endothelial cells, fibroblasts and muscular cells [62]. Biophysical investigations on several rough chemotypes of LPS, as well as lipid-A, were carried out [56, 87] to determine the structural polymorphism of endotoxin aggregates by X-ray diffraction in the presence of $MgCl_2$ at different levels of hydration and at different temperatures. These and more recent investigations [84, 85] suggest that cubic and non-lamellar aggregate morphologies of LPS exhibit greater toxicity than lamellar. The concept of morphology-dependent toxicity of LPS aggregates introduced new possibilities for the study and development of anti-endotoxic agents which interact with LPS aggregates. An emerging therapeutic approach to reducing the LPS-mediated inflammation focuses on the investigation of the anti-endotoxic role of CAPs. In addition to their anti-infective

role [96], CAPs interact with LPS in a way which results in a reduced toxicity of the aggregates [214–216].

In particular, the CAP LL37 is an amphiphatic α-helical peptide of human origin, a member of the cathelicidin family [138], which is released by neutrophils and epithelial cells upon digestion its pro-protein hCAP-18 [137]. LL37 shows multi-functional properties including antimicrobial activity against Gram negative and Gram positive bacteria [144, 146], binding and transport activity of DNA [142], cell signaling [147, 217] and the capacity of binding LPS, which results in reduced immune system response both *in vitro* and *ex-vivo* [115, 152, 218, 219].

The cationic peptide lactoferricin (LF) is derived from the N terminus of both human and bovine lactoferrin proteins [117]. The bovine LF (LFb) has an amphiphilic β-sheet structure [119] which allows an interaction with *E. coli* membranes [125] resulting in a bactericidal activity [118] highly dependent on the structure of LPS in terms of size of the oligosaccharidic moiety and number of negative charges in the core region [129]. Despite the fact that α-helical peptides seem to have more potent anti-endotoxic activity than β-sheet analogs [220], LFb peptide showed strong anti-inflammatory activity against LPS-stimulated cells *ex-vivo* [116]. The human analog of LFb neutralizes the LPS from *E. coli* 0111B4 *in vitro* and *in vivo* [221] hence interaction studies were performed to understand its possible anti-endotoxic role [207, 222]. Despite the stronger affinity for LPS of the bovine lactoferricin LFb [134] these types of the interaction studies are absent, neglecting its possible antiseptic function. The comparison between the peptides LL37 and LFb would help to explain the mechanism of action of CAPs as anti-endotoxic agents and the higher efficacy of α-helical conformation.

Studies on aggregates of LPS in solution have previously been conducted using several biophysical techniques such as X-ray diffraction, electron microscopy, infrared and fluorescence spectroscopies, as well as biological toxicity tests. In order to achieve a good scattering pattern from the sample during an X-ray experiment, the concentration of lipid A or LPS has to be very high, up to approximately 100 mg/ml. High intensity difractometers allow the reduction of LPS concentration down to 10-20 mg/ml. Alternative techniques such as SANS can be also used to perform similar experiments at even lower concentrations of LPS than those used in X-ray experiments, allowing for the use of more physiologically relevant concentrations of endotoxin.

Previously only two groups, Hayter *et al.* [223] and Labischinski *et al.* [224], used SANS to determine the structure of colloidal LPS aggregates in solution. These

two studies presented data for fully hydrated Lipid-A and Re LPS. The amount of amphiphile in solution was as low as 1 mg/ml, a value which is more physiologically relevant than the concentrations used in X-ray experiments. Labischinski *et al.* found that fully hydrated lipid A at neutral pH above and below the T_m forms lamellar structures of about 50 Å in thickness with interdigitation of the acyl chains. Previous X-ray data for free lipid-A in the presence of low concentrations of $MgCl_2$ confirmed the presence of lamellar structures [59]. Furthermore, at temperatures above 37°C , the scattering curves showed Bragg reflections characteristic of a coexisting cubic and lamellar phases. Hayter found that 10 mg/ml of fully hydrated Re LPS in its NaCl salt form, at neutral pH (25°C), builds up tubular micelles with a diameter of approximately 100 Å which seem to stiffen and form pairs above pH 9.0. More recently, small-angle X-ray diffraction of Re LPS at 24 mg/ml in the presence of $MgCl_2$ at temperatures up to 55°C confirmed the formation of lamellar structures for this chemotype of LPS [59]. A direct comparison of these different studies is not possible due to the different conditions and salt concentration used, which strongly affect the packing of LPS and thus the morphologies of the aggregates [25].

Electron microscopy techniques are useful in order to visualize colloidal aggergates and aid the interpretation of data obtained from small angle scattering experiments. Cryo-TEM can be combined as a complementary technique to SANS experiments. Previously, electron microscopy investigations have been carried out in order to understand the structure of LPS in solution [225–227]. Effects of salts [57] and peptides [228, 229] on LPS aggregates have been analyzed using transmission electron microscopy (TEM), cryo-TEM and freeze fracture transmission electron microscopy (ff-TEM). The diversity of the conditions applied makes it difficult to compare the results of these studies therefore a generalized conclusion from the literature cannot be drawn easily.

The experiments presented in this chapter investigate the suprastructure of three diverse chemotypes of LPS in solution : a smooth chemotype of LPS from *E. coli* 0111B4 (LPS 0111B4), a rough full-core chemotype from *E. coli* K12 D21 (LPS D21) and a deep rough LPS from *E. coli* K12 D21e7 (LPS E7), which structures are reported in Figure 1.5. SANS experiments and cryo-TEM methods are combined to gain further insight into the structure of LPS aggregates. The same techniques are used to study the interaction of two CAPs, LL37 and LFb , with the aggregate of the LPS chemotypes. The aim is to define the morphological changes induced by the peptides and to relate these changes to their putative

anti-endotoxic activity.

3.2 Materials and Methods

3.2.1 Materials

LB broth, Kimax® boro-silicate centrifuge tubes, liquefied phenol ≥ 96% pure , deuterium oxide D_2O 99.990 atom % D and magnesium chloride anhydrous were all purchased from Sigma-Aldrich Ltd. (Dorset, UK). The ultrapure water at 18.2 $M\Omega \cdot cm$ was produced by a Purelab Ultra machine from ELGA process water (Marlow, UK). The Spectra/Por 6 dialysis membrane with a MWCO of 1000 Da was purchased from Spectrum Laboratories (Houston, USA). LPS 0111B4 was purchased from Merck KGaA (Darmstadt, Germany). Petroleum ether (40-60 degree) was obtained from VWR International (Soulbury, UK). Chloroform and diethyl ether were obtained from Fisher Scientific (Loughborough, UK). Details of the peptides LL37 and LFb are reported in Appendix B.

3.2.2 Extraction of rough LPS from *E.coli*

The liquid phenol-chloroform-petroleum ether (PCP) extraction of Galanos et. al. [230] is the extraction method best suited for rough chemotypes of LPS such as LPS D21 and D21E7. However contaminants remain present at the end of the PCP extraction especially nucleic acids which co-partition in the same phase as LPS [231]. SDS-gel electrophoresis showed that proteins were still present after PCP extraction (see Appendix A) and the spectroscopic quantification of nucleic acids through the absorbance at 260 nm, revealed up to 29.1% (by weight) of nucleic acid in the final extract of LPS D21 (data from two extraction). Therefore in order to achieve a higher degree of purity, a few additional steps adapted from the Darveau LPS extraction method [232] were added to the Galanos method.
The *E. coli* K12 mutants D21 and D21e7 were incubated at 37°C in a 100 mL pre-culture of LB media in the presence of 15 μg/mL ampicillin under continuous mild shaking at 100 rpm. The optical density of the pre-culture was checked by the use of a Jenway 6300 spectrophotometer (Bibby Scientific, Staffordshire, UK)

until the mid-logarithmic phase was reached, corresponding to an $O.D._{600}$ of ~ 1. Pre/culture aliquots of 20 mL each were then transferred into four 1.25 L flasks containing LB media with 15 μg/mL ampicillin and incubated at 37°C for 8 to 10 hours under constant agitation at a speed of 170-200 rpm. After inoculation, the bacterial pellet was collected by centrifugation at 9000 rpm for 15 minutes at 15°C by the use of a Beckman J2-HS centrifuge (Beckman Coulter Inc, Pasadena, USA) before being washed with 400 mL of deionized water and recentrifuged twice to remove the excess LB media. The wet pellet was then transferred into one 50 mL polypropylene vials and washed with ethanol followed by acetone. To aid the re-suspension of the cell pellet during this washing step a homogenizer was used. Subsequently the pellet was centrifuged bu the use of a Boeco U-320 bench centrifuge (Boeco, Hamburg, Germany) at 1000 rpm for 20 minutes at 4°C , then it was frozen thoroughly in liquid nitrogen and lyophilized with a Heto Powerdry LL3000 freeze dryer (Thermo Scientific, Wilmington, USA). The resultant dry product weighed approximately 1000-2500 mg.

Each gram of lyophilized pellet was homogenized in a 10 mL mixture of phenol, chloroform and petroleum ether (2:5:8 v/v/v), followed by mixing on a magnetic stirrer for two hours in a fume hood. The suspension was then centrifuged by the use of a Beckman J2-HS centrifuge (Beckman Coulter Inc, Pasadena, USA) in 35 mL Kimax® boro-silicate centrifuge tubes at 5.000 rpm for 15 min and the supernatant containing the LPS was collected in a 250 mL glass round bottom flask. This extraction from the addition of the PCP mixture to the dry pellet was repeated twice, homogenizing the residual pellet and finally combining the supernatants from each replicate. Ether and chloroform were removed from the supernatant on a rotary evaporator at 40°C . During this process it is possible that some water from the phenol solution is also evaporated, causing the crystallization of the phenol. If this happens a small amount of water has to be added until the crystallized phenol returns to its liquid state. The concentrated phenolic phase, which should be of a pale, transparent yellow color, was transferred back into a clean glass tube and ultrapure water was added dropwise until the LPS started to precipitate. This suspension was allowed to sediment overnight at room temperature. The precipitate was centrifuged at 3000 rpm for 40 minutes yielding in a white pellet containing LPS which was carefully washed three times with diethyl ether to remove any excess phenol. The pellet was then suspended in 50 mL of ultrapure water and dialyzed overnight in 30-32 cm Spectra/Por 6 dialysis membrane against 10 L of ultrapure water to further reduce the quantity of residual

phenol.
The aqueous suspension of LPS was lyophilized and then resuspended in 25 mM Tris HCl , 10 mM $MgCl_2$ at pH 7.4. An enzymatic digestion was performed in order to remove the residual nucleic acids and proteins by adding sufficient enzymes to give a final concentration of 50 μg/mL RNAse and 30 μg/mL DNAse. The suspension was kept at 37°C for 5-6 hours under constant agitation. Subsequently proteinase K was then added to reach a final concentration of 50 μg/mL of enzyme and incubated for 12 hours at 37°C under constant agitation. After the enzymatic digestion, the mixture was deactivated in a water bath at 60°C for 1.5 hours followed by further dialysis against ultrapure water before finally being lyophilized. Another PCP extraction was then performed to remove the residual enzymes and any digestion products which would partition into the supernatant. The pellet containing the LPS was collected upon centrifugation, resuspended in ultrapure water and dialyzed thoroughly. The suspension was then spun down with a Beckman L8-M ultracentrifuge (Beckman Coulter Inc, Pasadena, USA) at 42000 rpm for 4.5 hours at 14°C . The resulting pellet had a transparent-yellow color and contained the purified LPS. This pellet was re-suspended in the appropriate volume of ultrapure water and lyophilized.
The purity of the extracted LPS was verified spectrophotometrically using a a Nanodrop 1000 spectrophotometer (Thermo Scientific, Wilmington, USA). The protein content was measured using a bicinchoninic acid (BCA) Pierce protein assay kit (Thermo Scientific, Wilmington, USA) while the measurement of the nucleic acid content was performed by recording the absorbance at 260 nm. The purity of the LPS 0111B4 was measured following the same method. LPS 0111B4, D21and E7 had an average protein content of respectively 2%, 2% and 1.6% while the nucleic acid content was calculated to be respectively 1.95% 2.22% and 2.52%. The average yield of the extraction for LPS D21 and E7 was approximately 0.36% and 1.91% respectively according to the total mass of the dry bacterial pellet.

3.2.3 Cryo-transmission electron microscopy (Cryo-TEM)

The samples for cryo-TEM, prepared according to the technique described in the next section (Section 3.2.4), were processed and analysed as follows. The cryogenic transmission electron microscopy (cryo-TEM) investigations were performed by collaborators in the group of Prof. Katarina Edwards in the Department of Chemistry of the University of Uppsala using a Zeiss Libra 120 (Carl Zeiss NTS,

Oberkochen, Germany). The microscope was operating at an accelerating voltage of 80kV and in zero loss bright-field mode. Digital images were recorded under low dose conditions with a slow-scan CCD camera (TRS GmbH, Moorenweis, Germany) and iTEM software (Olympus Soft Imaging Solutions GmbH, Mnster, Germany). An under-focus of 1-2 μm was used to enhance the image contrast. The cryo-TEM specimen preparations were performed in a custom-built climate chamber at 25°C and approximately 98-100% relative humidity. A small drop ($\sim$1 μl) of sample was deposited on a copper grid covered with a carbon reinforced holey polymer film. Excess liquid was thereafter removed by means of blotting with a filter paper, leaving a thin film of the solution on the grid. Immediately after blotting the sample was vitrified in liquid ethane, held just above its freezing point of 182°C . Samples were kept below -165°C and protected against atmospheric conditions during both transfer to the TEM and examination, where representative images for the samples were acquired. Full details of the technique are described in Almgren *et al.* [233].

3.2.4 Small-Angle Neutron Scattering (SANS)

The SANS measurements presented in this chapter was carried out on the LoQ instrument at the ISIS pulsed neutron source at the Rutherford-Appleton Laboratory (Oxon, UK) [234]. This instrument produces an incident neutron beam with wavelengths of 2.2 - 10 Å in time of flight mode. The instrument has a very broad range in scattering vector resulting in wide Q range of approximately 0.01 - 0.34 $Å^{-1}$; this can be achieved in one single measurement without the need of changing the settings of the instrument (*i.e.* the position of the detector). The beam is collimated into the sample after being framed at a defined beam size. The 64 cm^2 active area of the detector is placed at 4.1 meters from the sample into a vacuum tube. A second detector placed at a closer position records the scattering at higher Q [235].

The aggregates of LPS were prepared for SANS using the thin film hydration method and re-suspension in D_2O containing 1mM $MgCl_2$ as counter ions for the charges present in the endotoxin's headgroups. The experiments concerning the effect of the dilution on the scattering pattern of LPS were carried using LPS concentrations of 4, 6, 8 and 10 mg/ml. For the interaction study with the peptides LL37 or LFb , an LPS concentration of 6 mg/ml was used and each peptide was added at the LPS/peptide ratios (w/w) of 50/1 and 10/1. The peptides were

allowed to interact with the LPS for at least one hour prior to measurement in the neutron beam. The samples were placed in cleaned quartz cells of 1 mm path length and the scattering pattern was recorded at 37°C with an acquisition time of at least one hour. The transmission and background scattering from the saline solution and solutes were subtracted from the samples prior to analysis.

3.2.4.1 Data analysis

Analysis of the SANS data was performed via the simple observation of the characteristic features of the scattering pattern, but also with the manipulation of the scattering curves by means of mathematical approximations of SANS data, which apply particular plotting in order in order to determine sample parameters by approximating the characteristic scattering patterns from defined colloidal morphologies. This type of data manipulation is implemented together with a more detailed analysis of the scattering curves which required the use of specific software in order to apply complex mathematical modeling to the SANS data. These models yielded more detailed information on the aggregate morphologies. However, in some cases, the sample contained numerous complex morphologies and therefore both the simple approximations and the more complex model fitting must be considered as providing only approximate parameters.

Analysis of elongated objects The first type of manipulation implemented for the study of scattering data was the Guinier approximation. This analysis is more suitable for spherical form factors, nevertheless this it can be modified for the analysis of elongated particles such as rigid rods. The Guinier approximation for an assembly of identical particles is

$$\frac{\partial \Sigma}{\partial \Omega}(Q) \approx N V^2 (\Delta\rho)^2 exp\left(-\frac{Q^2 R_g^2}{3}\right) \tag{3.1}$$

where $(\Delta\rho)$ is the SLD difference between the solute and the solvent, V is the volume of one scattering centre and N is the number of scattering centres, R_g is the radius of gyration of the object. The Equation 3.1 is implemented with

$$R_g^2 = \frac{L\,M}{6\,M_L} \tag{3.2}$$

$$NV^2 = \frac{\phi\,M}{N_A\,\delta} \tag{3.3}$$

where the parameters are the molecular weight of the object M, the volume fraction (ϕ), Avogadro's number N_A, the length L and δ as the density of the molecule in g/cm^3. The plot $ln[(\delta\Sigma/\delta\Omega)(Q)]\ vs\ Q^2$ would result in a straight line at small values of Q^2 for a limit of $Q \times R_g < \sqrt{3}$. The straight line at small Q^2 values can be related to the R_g and the Mass M of the aggregates according to the equations:

$$slope\ =\ -\frac{R_g^2}{3} \qquad (3.4) \qquad intercept\ =\ \frac{\phi\,(\Delta\rho)^2\,M}{N_A\,\delta} \qquad (3.5)$$

However this approximation has some limitations. The anisometry of the scattering centres and the inhomogeneous distribution of their SLDs require an alternative analysis. Moreover the rigid rods approximation is possibly not the most accurate representation of more flexible objects. Therefore the Kratky-Porod worm-like chain model [153, 236, 237] is used to describe elongated particles of L length by the form factor

$$\frac{\partial\Sigma}{\partial\Omega}(Q)\ =\ N\,V^2\,(\Delta\rho)^2\,\left[\frac{2}{Q\,L}\left(S_i\,(Q\,L) - \frac{(1-cos(Q\,L))}{Q\,L}\right)\right] \qquad (3.6)$$

and S_i is expressed by:

$$S_i(Q\,L)\ =\ \int_0^{Q\,L}\frac{sin(x)}{x}dx \qquad (3.7)$$

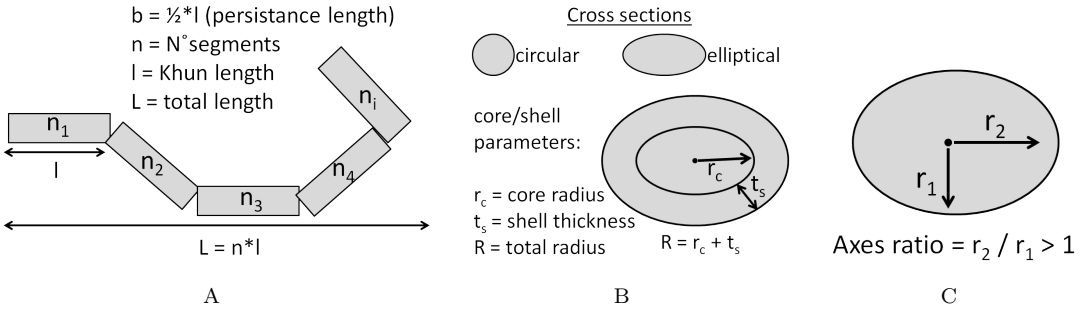

FIGURE 3.2: (A) Representation of a worm-like chain formed by n segments of length l. (B) Possible cross sections for elongated objects with description of the core/shell cross section. (C) Axial ratio in the case of an elliptical cross section.

Figure 3.2 A shows a schematic representation of an elongated object of number of segments (n), Khun length (l) and contour length (L) which are the same parameters described by the Kratky-Porod model. Figures 3.2 B and C describe

also the possible cross sections that an elongated object can have. The cross sections can be either cylindrical or ellyptical depending upon the ratio between the X and Y radii of the section; a cross section can be also formed by an inner core and an outer shell distinguished by a core radius (r_c) and a shell thickness (t_s). The Equation 3.6 is simplified for infinitely long chains in the intermediate-high Q range with limits of $Q > b^{-1}$ where b, the persistence length, is half of the l factor (see Figure 3.2 A), hence it becomes

$$\frac{\partial \Sigma}{\partial \Omega}(Q) \approx \frac{\pi\, c\, (\Delta\rho)^2}{N_A\, \delta^2} \times \frac{M_L}{Q} \tag{3.8}$$

where M_L is the mass per unit length equal to M/n and c is the concentration of solute in g/ml. In order to incorporate the cross sectional radius of gyration ($R_{g,xs}$) as finite parameter, the expression is extended considering a Guinier-like factor:

$$\frac{\partial \Sigma}{\partial \Omega}(Q) \approx \frac{\pi\, c\, (\Delta\rho)^2}{N_A\, \delta^2} \times \frac{M_L}{Q} \times \overbrace{exp\left(-\frac{Q^2\, R_{g,xs}^2}{2}\right)}^{Guinier\, factor} \tag{3.9}$$

Following the Equation 3.9, the linear plot of $ln[Q \times (\delta\Sigma/\delta\Omega)(Q)]\; vs\; Q^2$ gives

$$slope = -\frac{R_{g,xs}^2}{2} \tag{3.10}$$

$$intercept = ln\left(\frac{\pi\, c\, (\Delta\rho)^2\, M_L}{N_A\, \delta^2}\right) \tag{3.11}$$

This approximation is valid if it is linear at high Q^2 values and for a limit of $Q \times R_{g,xs} < 1.1$; the value of $R_{g,xs}$ allows the calculation of the radius of the elongated object $R = \sqrt{R_{g,xs}}$. In addition the intercept can be used to determine the mass per unit length M_L [238] in Da/Å as

$$M_L = \frac{1000\, intercept\, \delta^2\, N_A}{\pi\, C\, (\rho_{worm} - \rho_{solvent})^2} \tag{3.12}$$

where C is the concentration in g/L.

Following the data approximation it is logical to try to apply a more defined mathematical model to fit the scattering curve in order to maximise the amount of extractable information from the SANS data. The Kratky-Porod theory is at the base of the Kholodenko worm-like chain models [239] used in the FISH software

and applied to elongated flexible objects. Two different Kholodenko models are available whether the chain is considered as having a uniform SLD or differing SLDs between the core and the shell region (see Figure 3.2 B). The model with the uniform SLD presents the scale factor:

$$scale \;=\; 10^{-24}\,\phi\,(\rho_{worm} - \rho_{solvent})^2 \tag{3.13}$$

while the core/shell model presents a scale factor of

$$scale \;=\; 10^{-24}\,\phi_{core}\,(\rho_1 - \rho_2)^2 \tag{3.14}$$

and a contrast of

$$Contrast \;=\; \frac{(\rho_2 - \rho_3)}{(\rho_1 - \rho_3)} \tag{3.15}$$

where ρ_1, ρ_2, ρ_3 are respectively the core, shell and solvent scattering length densities in cm^{-1}.

Analysis of lamellar aggregates A lamellar aggregate is considered to be formed by at least one bilayer of amphiphiles in which the core hydrophobic region contains the acyl chains and the shell hydrophilic region is composed of the headgroups, in contact with the aqueous bulk. Such a structure could be repeated indefinitely to form stacks defined by the space in between the bilayers (d-spacing) with a core thickness (t_c) and a t_s (Figure 3.3). In our specific case the core of the lamellae consists solely of the hydrocarbon chains of LPS while the shell of the bilayer is composed of the the Core region and eventually the O-antigen region of the oligosaccharide headgroup.

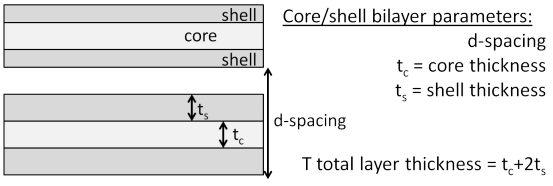

FIGURE 3.3: Representation of bilayer structure with shell/core/shell features. Shell and core have different SLDs.

Again a Guinier approximation can be used as a first attempt in order to obtain some dimensional information. In this case the Guinier factor of Equation 3.1 becomes:

$$exp\left(-\frac{Q^2\,R_g^2}{1}\right) \tag{3.16}$$

and the total thickness T of the bilayer is related to radius of gyration (R_g) by the function

$$R_g^2 \;=\; \frac{T^2}{12} \tag{3.17}$$

.

The plot $ln[Q^2 \times (\delta\Sigma/\delta\Omega)(Q)]$ vs Q^2 allows for the calculation of R_g as $R_g = \sqrt{-2 \times slope}$. In this case the criteria for the validity of the approximation are $0.41 < Q \times R_g < 0.92$.

In the mathematical model provided by the fitting software used for the fitting of neutron scattering data as monodisperse oriented sheet with a shell/core/shell feature (Figure 3.3), the neutron scattering intensity IQ is calculated as:

$$I(Q) \;=\; I(Q) + Scale \cdot L_N(Q) \cdot f^2(Q) \tag{3.18}$$

where Scale is the scale factor defined by the model, $L_N(Q)$ is a Lorentzian factor which considers a random orientation of the sheets and $f(Q)$ is the molecular form factor for such a model [240]:

$$f(Q) \;=\; t_c\,\frac{sin(Qt_c/2)}{Qt_c/2}\;2t_s\,\frac{\rho_2-\rho_3}{\rho_1-\rho_3}\,cos(Q(t_c+t_s)/2)\,\frac{sin(Qt_s/2)}{Qt_s/2} \tag{3.19}$$

in which l_1 and t_s are respectively the core and the shell thickness, therefore the total thickness (T) is $T = t_c + 2t_s$; ρ_1 and ρ_2 are the scattering length densities of respectively the hydrophobic and the hydrophilic regions of the LPS molecule (Appendix D), whilst ρ_3 is the solvent scattering length density. The main parameters for this model are t_c and t_s, $R\sigma$ which is a parameter that describes the uniformity of an object, the contrast is expressed as

$$Contrast = \frac{(\rho_2 - \rho_3)}{(\rho_1 - \rho_3)} \tag{3.20}$$

and the scale factor

$$Scale\ factor = 10^{-32} \cdot \Pi \cdot (\rho_1 - \rho_3)^2 \cdot S \cdot (R\sigma)^2 \tag{3.21}$$

where S is the area of sheet per unit volume of sample in cm^{-1}. S is also expressed as the function

$$S = \frac{\phi}{10^{-8} t_c} \tag{3.22}$$

in the case of a truly infinite sheet; it is therefore possible to calculate back the ϕ in order to check the validity of its calculated value.

3.3 Results

3.3.1 Cryo-TEM

The analysis of Cryo-TEM micrographs of the three LPS chemotypes 0111B4, D21 and E7 at the concentration of 6 mg/ml in the absence or presence of peptides LL37 and LFb at a weight ratio of LPS/peptide 10/1 in 1mM $MgCl_2$ saline solution revealed diverse populations of aggregates (Figures 3.4 and 3.5 to 3.10), the morphologies of which differed according to the LPS chemotype and the peptide added.

3.3.1.1 Cryo-TEM of LPS 0111B4 and peptides

LPS 0111B4 at a concentration of 6 mg/ml in saline solution containing 1mM $MgCl_2$ forms elongated worm-like micelles (Figure 3.4 A) with an approximate diameter of 150 Å; it must be considered however that the precise diameter value can not be calculated directly from the micrograph because of the low resolution of the image and the possibility that the micellles are flattened or twisted. However it is

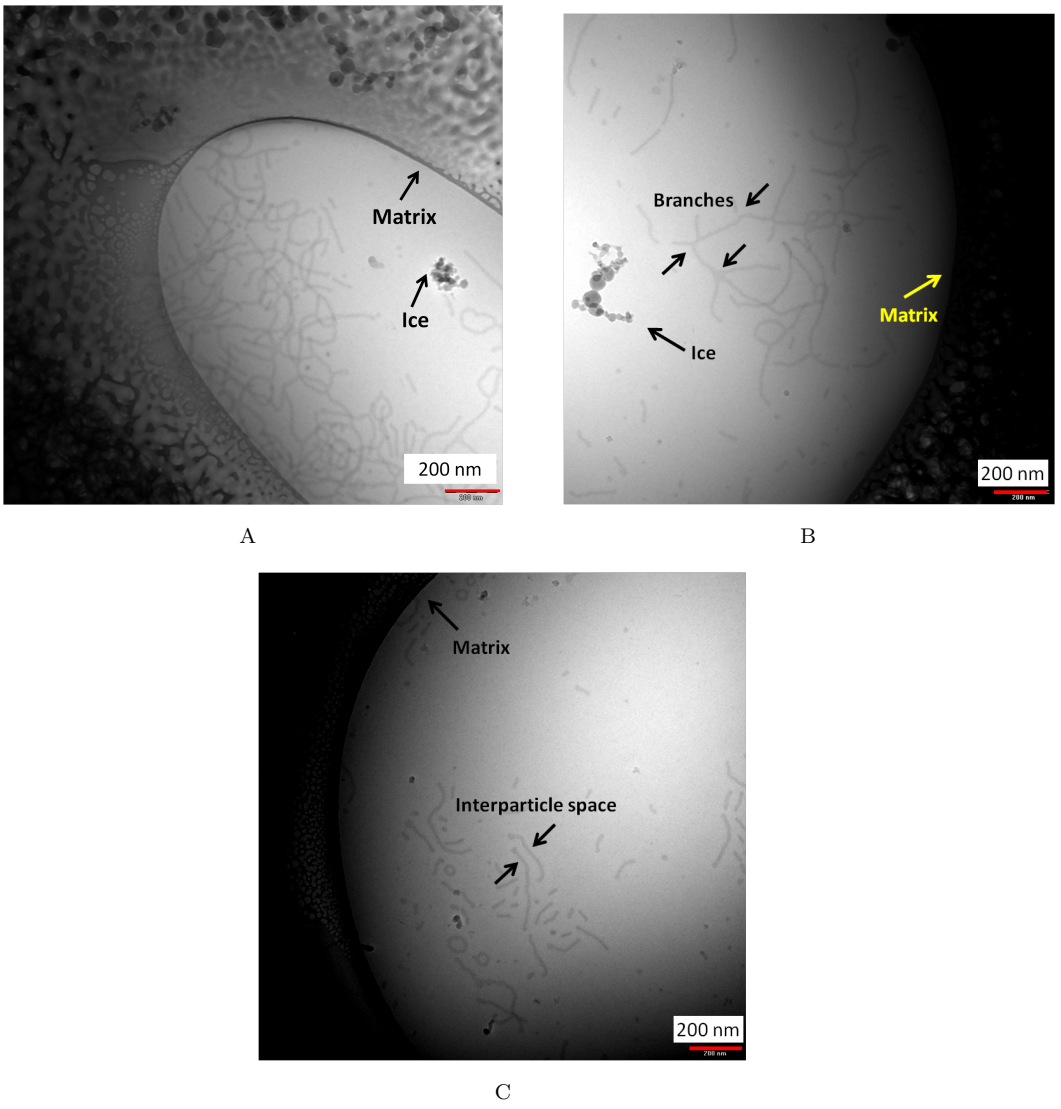

FIGURE 3.4: (A) Cryo-TEM micrographs of smooth LPS 0111B4 at 6 mg/mL in aqueous solution containing 1 mM $MgCl_2$ at 37°C forming elongated micelles (black box). (B) and (C): the arrows show details of the structures such as branches and interparticles spaces.

possible that the O-antigen is not truly visible and therefore the measured diameter is an underestimation of the actual one. Nevertheless the diameter seems to be realistic in consideration of the dimensions of the whole molecule. The micelles are branched (Figure 3.4 B) and have the tendency to form connected structures which could be described as torroidal or torroids, depicted in Figure 3.6, which resemble loops of regular or irregular shape and different sizes. Smaller particles are also present which could be either the product of the disruption of larger micelles, or could represent new micelles in formation. Being a two dimensional image of a three dimensional system, the orientation which the particles can assume has

to be taken into consideration. Some smaller particles may actually be visual artefacts made of the axial view of elongated micelles. When the micelles are not connected there are large inter-particle spaces (around 400 Å, see Figure 3.4 C) the dimensions of which can be measured between two parallel micelles.

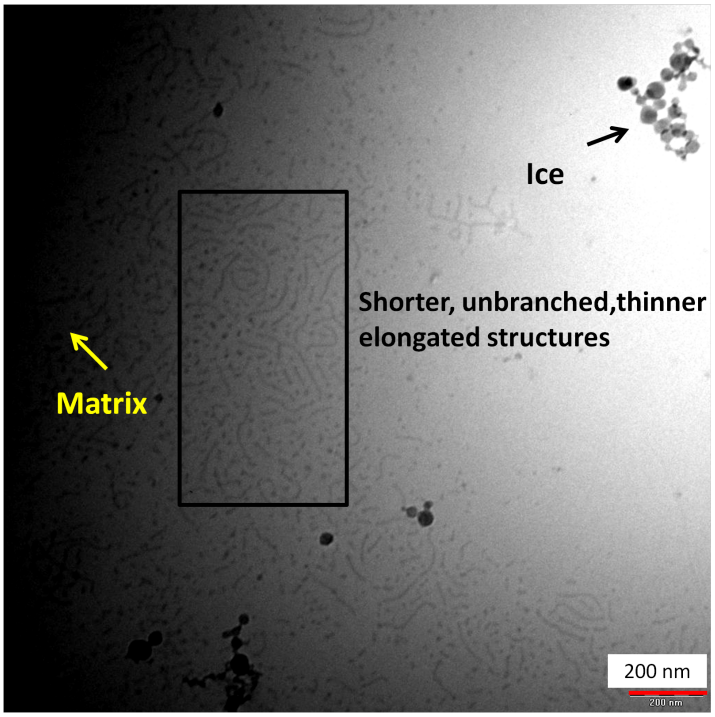

A LPS 0111B4 with LL37

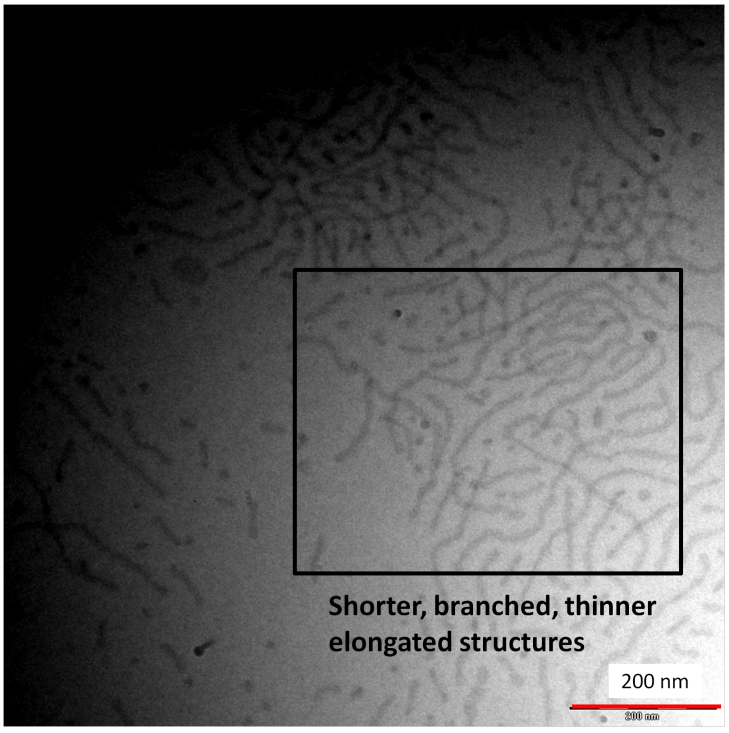

B LPS 0111B4 with LFb

FIGURE 3.5: Cryo-TEM micrographs of LPS 0111B4 at 6 mg/mL in aqueous solution containing 1 mM $MgCl_2$ at 37°C with addition of the peptides at a LPS/peptide ratio of 10/1. The addition of LL37 (A) or LFb (B) reduces the length, diameter and the number of branches of the micelles.

The addition of LL37 peptide to LPS 0111B4 (Figure 3.5 A) prevented the formation of toroids and connections between the elongated micelles and the number of branched structures decreased in comparison to the LPS alone. The peptide appeared to halve the diameter of the chains to approximately 80 Å. The peptide LL37 also shortened the length of LPS 0111B4 micelles, augmented the number of small objects and reduced the inter-particle space. The peptide LFb induced a smaller reduction of the diameter of the micelles, to 115 Å LFb had a lesser impact on the length of the particles than LL37 (Figure 3.5 B) and it seemed to cause a closer packing of the aggregates, with a visible reduction of the inter-particle spaces. Frequently the micelles appeared connected and branched even in the presence of LFb peptide but there are no sign of toroidal structures or loops. LFb peptide as well as LL37 increased the number of smaller structures or fragments, probably due to the detergent-like activity of the peptides in disrupting the micelles.

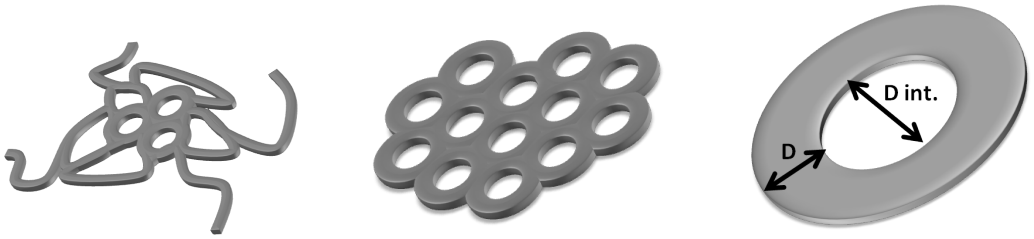

A B C

FIGURE 3.6: Diverse type of toroids: (A) irregular and (B) regular. (C) Dimension of the toroid with the toroidal internal diameter *D Int.* and the diameter of the micelle *D*.

3.3.1.2 CryoTEM of LPS D21 and peptides

The LPS D21 at a concentration of 6 mg/mL in saline solution containing 1 mM $MgCl_2$ forms mainly sheet-like structures distributed as single lamellae, possibly coexisting with toroids as outlined in the black boxes in Figure 3.7. The resolution of the micrographs does not allow a more precise definition of such a structure, which in this case could be mistaken for ripples or undulations of the lamellae. In the micrograph the presence of small white holes, or dots, in the sheets is due to the effect of radiation damage on the sample; they can be easily distinguished

from toroids and pores because of their white clear background.

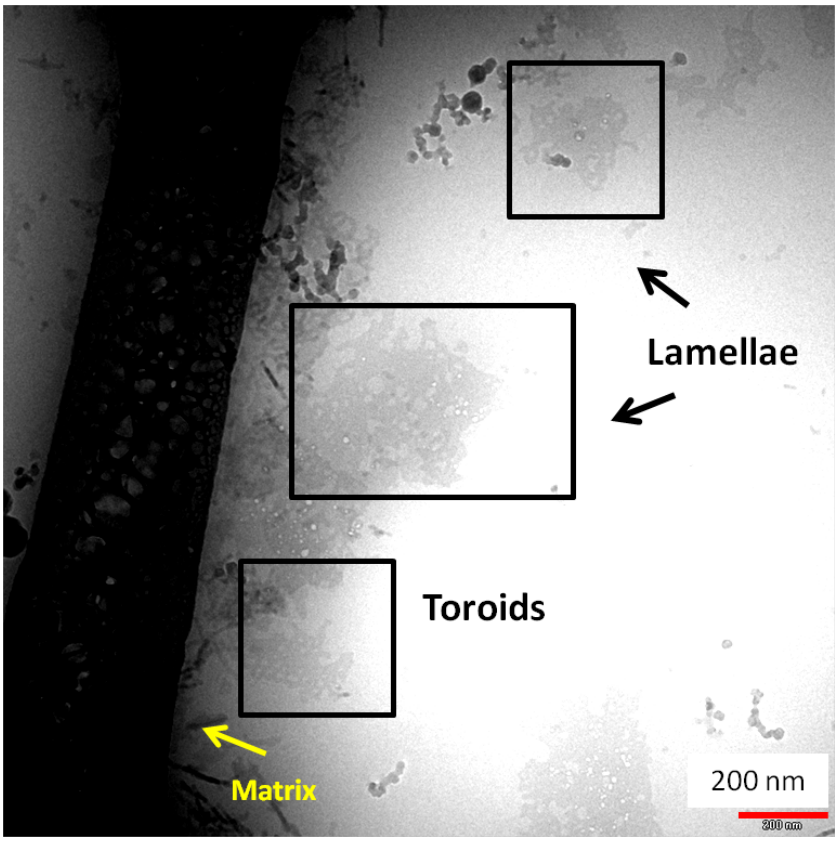

FIGURE 3.7: Cryo-TEM of LPS D21 at 6 mg/mL forming sheet-like structures (upper black boxes) coexisting with toroids (lower black box) in aqueous solution containing 1 mM $MgCl_2$ at 37°C .

The peptide LL37 induced the formation of a mixture of organized and irregular toroids (Figure 3.6 A and B) opening up into elongated micelles. The micelles forming the toroids had a diameter (D) of ∼77 Å, however it was not possible to measure the inner diameter of the toroids because of the wide range of sizes and shapes. Toroidal structures were the most commonly visible structures with patches of uneven shapes and others with a more regular and ordered structure; some micelles were visible free from the network and formed elongated structures. The situation in the presence of LFb peptide (Figure 3.6 B) showed a much more regular structure than in the presence of LL37 . The toroids formed appeared much more uniform in terms of shape and dimensions, with an homogeneous toroidal pattern; the micelles forming the toroids had a diameter of approximately 82 Å and the toroidal internal diameter was approximately 78 Å; this structure resembles lamellae which have been perforated by closely packed pores.

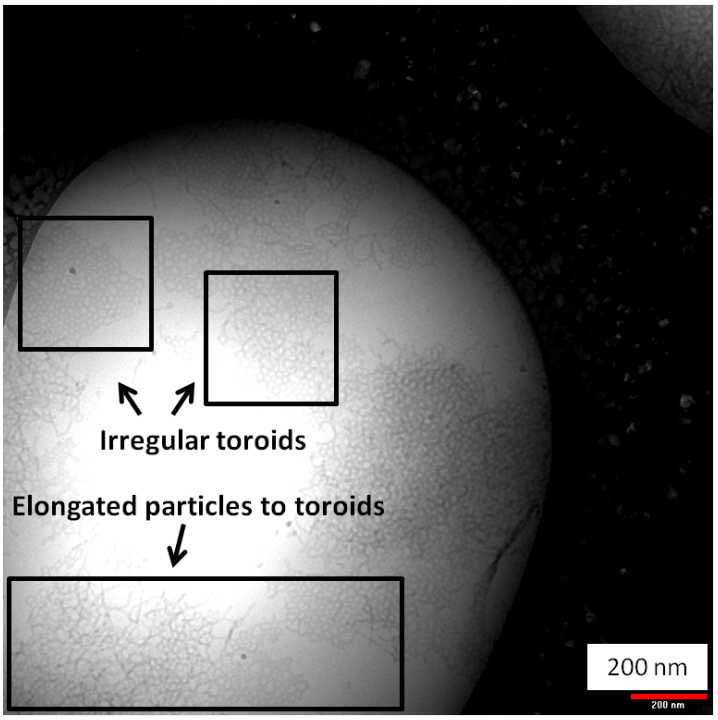

A LPS D21 with LL37

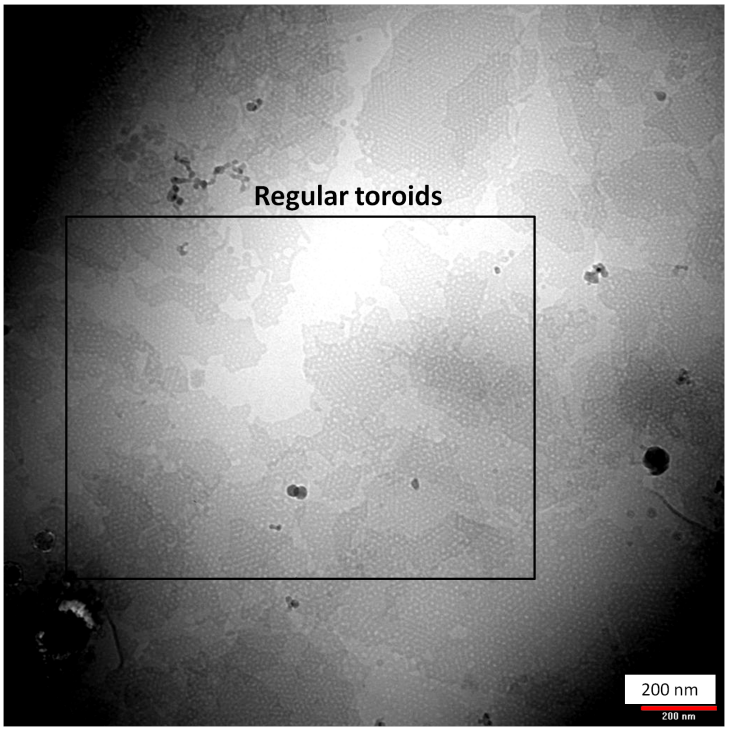

B LPS D21 with LFb

FIGURE 3.8: Cryo-TEM micrographs of LPS D21 at 6 mg/mL in aqueous solution containing 1 mM $MgCl_2$ at 37°C with addition of peptides at a LPS/peptide ratio of 10/1. (A) addition of LL37: formation of elongated particles closing up into irregular toroids (black boxes). (B) addition of LFb: regular toroids.

3.3.1.3 Cryo-TEM of LPS E7 and peptides

The LPS E7 at a concentration of 6 mg/mL in aqueous solution containing 1 mM $MgCl_2$ forms irregular sheets with an undulating surface (Figure 3.9); possible toroidal structures are highlighted in the black boxes on the micrograph, however these could be artefacts due to the irregular surface of the bilayer. The addition of the peptide LL37 caused the formation of mixed sheet-like structures together with irregular toroids and elongated micelles, the latter having an approximate diameter of 90 Å (Figure 3.10 A). LFb peptide added to LPS E7 induced the formation of mixed irregular sheets and very thin elongated structures for which the inter-particle space was not clearly distinguishable and it was not possible to measure the diameter of these chains from the micrographs (Figure 3.10 B). The micrographs showed a few patches of possible toroidal structures, which are highlighted within the black boxes.

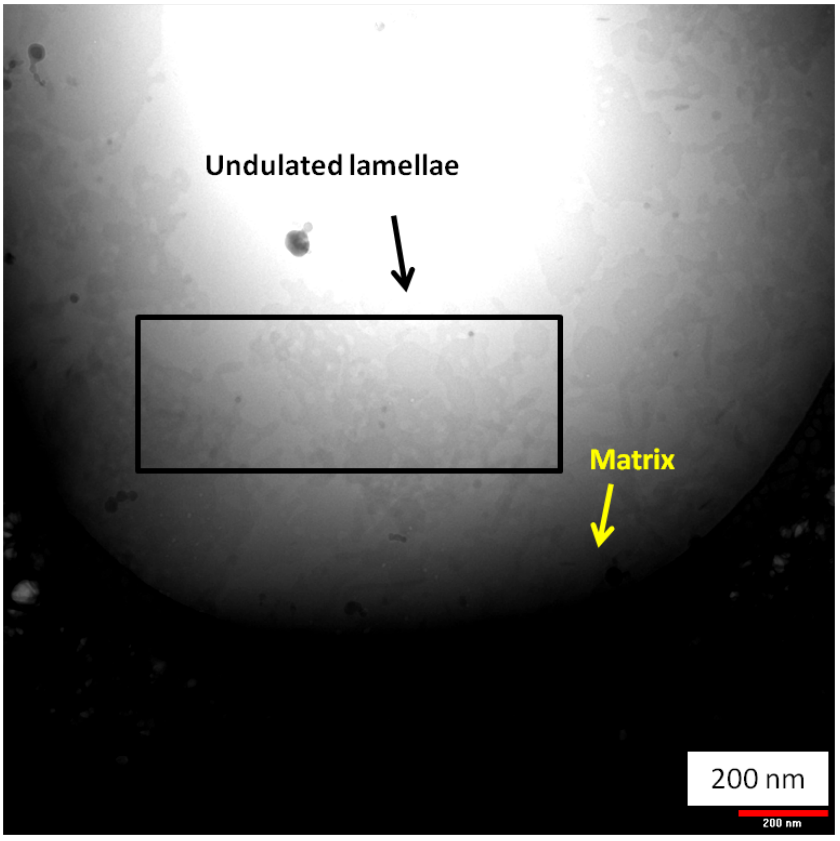

FIGURE 3.9: Cryo-TEM of LPS E7 at 6 mg/mL in aqueous solution containing 1 mM $MgCl_2$ at 37°C forming undulated lamellae (black box).

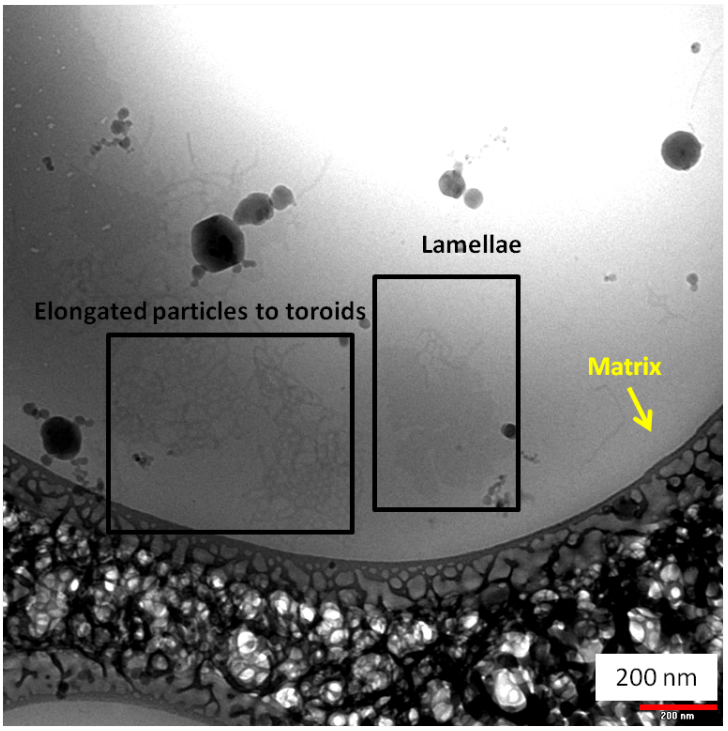

A LPS E7 with LL37

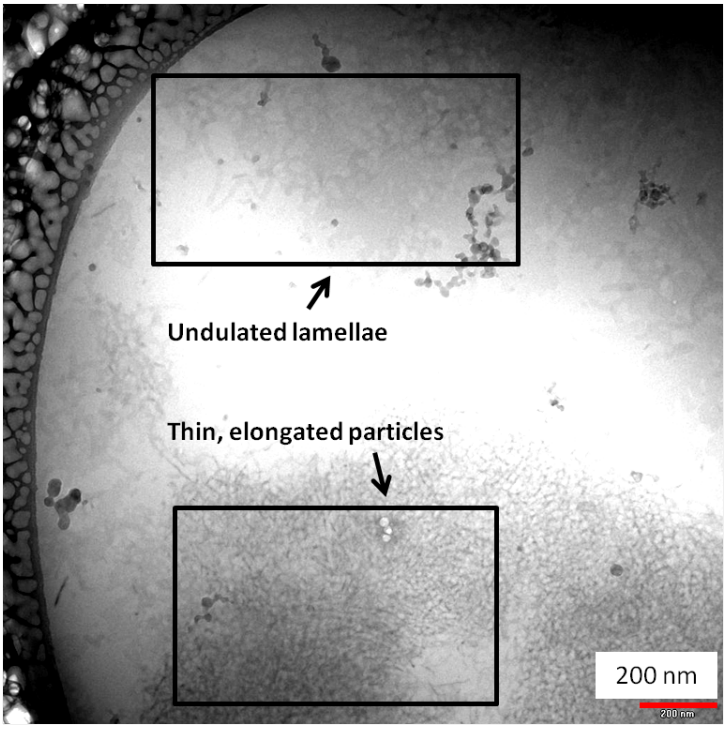

B LPS E7 with LFb

FIGURE 3.10: Cryo-TEM micrographs of LPS E7 at 6 mg/mL in aqueous solution containing 1 mM $MgCl_2$ at 37°C with addition of peptides at LPS/peptide ratio of 10/1. (A) addition of LL37: formation of elongated particles closing into toroids and lamellae (black boxes). (B) addition of LFb: formation of mixed thin elongated particles and lamellae (black boxes).

3.3.2 Small-angle neutron scattering

The SANS investigation of the samples described above (Section 3.2.4) required specific model fitting for each system investigated. During the modeling process of the raw data, some initial parameters such as the SLD and the ϕ are required. Usually the value of SLD can be calculated back from the fitting of the data but in this case, being a highly polydisperse molecule, the calculation of an SLD value for each LPS chemotype was more complex. Therefore the SLD values were estimated by calculations based on the theoretical molecular structure of each LPS chemotype reported in Section 1.2.1 and implemented at the beginning of the model fitting process. The calculated SLD values are reported in the Table D.1 of Appendix D. Each SLD value has been checked for consistency by employing the calculation for the scale factor of each model. The modeling process was carried out using a combination of the FISH and the SansView software programs. SANS dilution studies of all three LPS chemotypes were carried out at LPS concentrations of 4 mg/mL, 6 mg/mL, 8 mg/mL, 10 mg/mL in order to ascertain whether any change in the scattering patterns could be attributed to LPS concentration. In the studies involving the challenge by LL37 or LFb peptides, an LPS concentration of 6 mg/mL was used at LPS/peptide weight ratios of 50/1 and 10/1.

3.3.2.1 LPS 0111B4 scattering data

The data from LPS 0111B4 experiments were plotted in a $log_{10}Iq\,vs\,log_{10}Q$ graph in order to obtain the Q dependency of the scattering intensity from the slope of the linear parts of the curve. The representative example data for LPS 0111B4 at 6 mg/ml alone and in the presence of either LL37 or LFb peptides at a ratio of 10/1 are shown in Figure 3.11. In all the three cases, the scattering patterns do not present features indicative of rigid rods, as characterized by a slope of 1, and the the experimental data deviates from the theoretical model (dashed lines). Possibly the structure which could approximately fit the curve of LPS 0111B4 6 mg/ml in the Porod region is the collapsed coil (solid grey line with slope equal to 3 in Figure 3.11) even though other features are also present (Figure 3.11 A); the addition of the two peptides (Figure 3.11 B and C) seems to increase this evidence and the theoretical model (solid grey line) more closely follows the scattering curve. Therefore the Guinier and the Kratky-Porod analysis for elongated particles were applied in order to have a better idea of the dimensions of these particles.

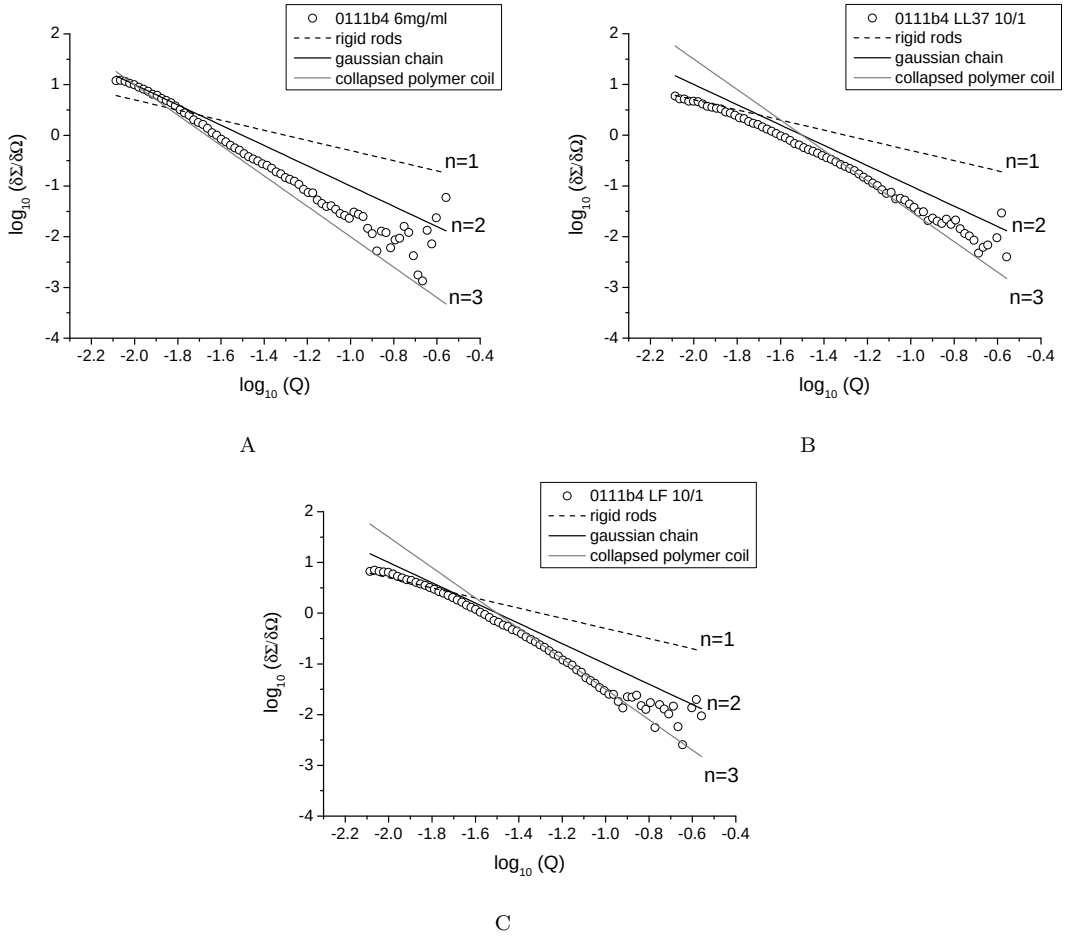

FIGURE 3.11: Scattering curves showing the Q dependency of the intensity of LPS 0111B4 at 6 mg/mL in 1 mM $MgCl_2$ saline solution at 37°C alone (A) or in the presence of the peptides LL37 (B) and LFb (c) at a LPS/peptide weight ratio of 10/1. n is the slope of the straight lines.

The Guinier plot $ln[(\delta\Sigma/\delta\Omega)(Q)]\, vs\, Q^2$ of the dilution data of LPS 0111B4 in 1mM $MgCl_2$ saline solution is reported in Figure 3.12 A, and it shows the dependency of the scattering intensity on the concentration of the solute. From the linear fitting of the plot at low Q in Figure 3.12 B, it is possible to define some parameters as expressed by the Equations 3.4 and 3.5. Table 3.1 shows the calculated values obtained from the linear fits of the Guinier plot over the low Q range 0.015-0.032, equivalent to a Q^2 range of 0.00024-0.00103.

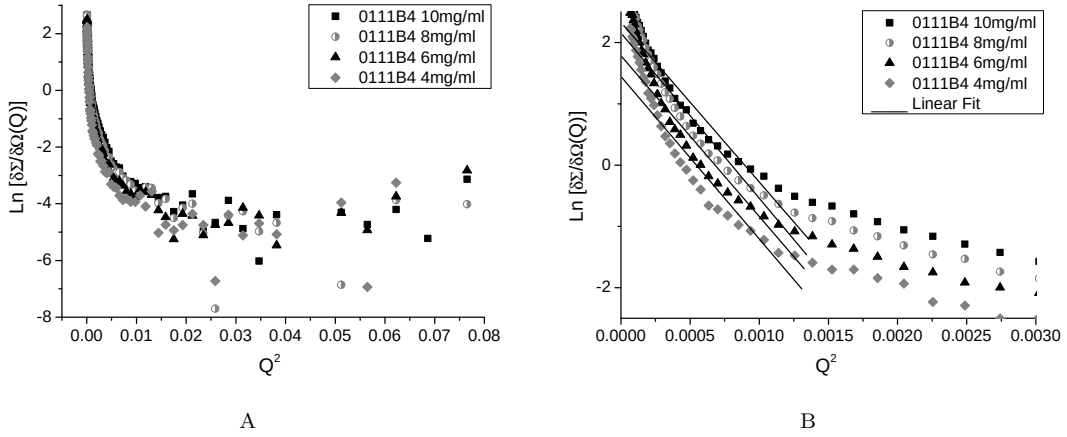

FIGURE 3.12: (A) Guinier plot of scattering data of LPS 0111B4 dilutions in 1 mM $MgCl_2$ saline solution at 37°C . (B) Linear curve fitting of the expanded low Q^2 range of 0.000-0.003 of the Guinier plot.

TABLE 3.1: Values from the linear fitting of Guinier plot of LPS 0111B4 dilutions in 1 mM $MgCl_2$ saline solution at 37°C at the low Q range of 0.015-0.032.

0111B4	R^2 fit[i]	$Q * R_g$ value[ii]	Rg (Å)
10 mg/ml	0.959	2.75	86.5
8 mg/ml	0.964	2.87	89.3
6 mg/ml	0.955	2.89	90.0
4 mg/ml	0.944	2.91	90.5

[i] coefficient of determination [ii] limit $Q * R_g < \sqrt{3}$

The Guinier approximation requires values of $Q * R_g < \sqrt{3}$, which are not complied by any of the samples analyzed. Thus it is not possible to make further use of these data other than to make superficial speculations on the intrinsic changes of the sample in relation to an increasing concentration of LPS. It is clear, however, that the radius of gyration R_g of the rod is not significantly affected by the dilutions at the three lowest LPS 0111B4 concentrations, with very little value fluctuation between 89 and 91 Å, whilst the 10 mg/mL concentration presents a lower R_g equal to 86.5 Å.

The Kratky-Porod approximation might be more useful for analysing data from particles which are more flexible than simple rods. Hence the data for the LPS 0111B4 dilution study was plotted as $ln[Q \times (\delta\Sigma/\delta\Omega)(Q)]$ *vs* Q^2 in Figure 3.13. The linear fitting of the data in the intermediate-high Q range 0.032-0.067 (equivalent to a Q^2 range of 0.00103-0.00447) allowed the calculations of the parameters reported in Table 3.2, as described by the Equations 3.10 and 3.11. Additionally

the plot allows the calculation of the mass per unit length M_L in Da/Å according to the Equation 3.12; in this calculation the parameters considered are the particles SLD ρ_{worm} of 1.57*10^{10} cm^{-2}, the solvent SLD $\rho_{solvent}$ of 6.35*10^{10} cm^{-2} and a density of LPS equal to 1.4 g/cm^3 as reported by Ulevitch [241].

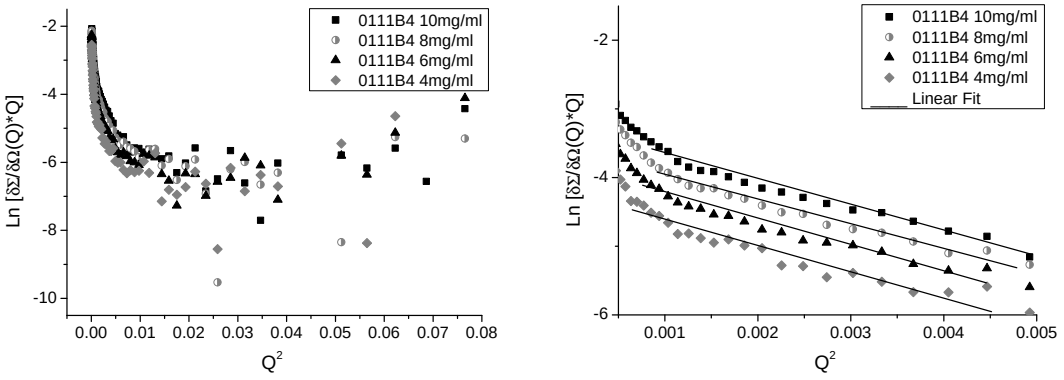

FIGURE 3.13: (A) Kratky plot of scattering data of LPS 0111B4 dilutions in 1 mM $MgCl_2$ saline solution at 37°C . (B) Linear curve fitting of the expanded intermediate-high Q^2 range of 0.001-0.005 of the Kratky plot.

TABLE 3.2: Values from the linear fitting of Kratky plot of LPS 0111B4 dilutions at intermediate-high Q range of 0.032-0.067.

0111B4	R^2 fit	$Q * R_g$ value[i]	R_g	$R = \sqrt{2} * R_g$ (Å)	M_L (Da/Å)
10 mg/ml	0.982	1.74	26.0	37	55'124
8 mg/ml	0.977	1.74	26.1	37	74'282
6 mg/ml	0.973	1.69	25.2	36	108'855
4 mg/ml	0.921	1.64	24.5	35	180'744

[i] limit $Q * R_g < 1.1$

As found with the Guinier approximation, the Kratky analysis applied to these dilutions experiments does not meet the requirement $Q*R_g < 1.1$. Nevertheless we can estimate that the radius of the worm-like micelle is not changing significantly and maintains values between 35 and 37 Å. Being inversely proportional to the concentration of the solute, M_L incresaes with decreasing concentration and can be used to estimate the amount of molecules present over the length of the micelle. Unfortunately being a structurally polydisperse molecule, makes it is difficult to calculate this number for LPS but according to Aurell *et al.* [242] the average molecular weight is estimated to be 10000 Da. Therefore we can see how the number of molecules per micelle increases as the concentration decreases. The

Guinier plot of LPS011b4 6mg/ml with and without peptides at LPS/peptide ratios of 50/1 (data not shown) and 10/1 (Figure 3.14) was fitted to a straight line at low Q range as described before. The values of $Q * R_g$ and R_g obtained from the linear fits are reported in Table 3.3. The $Q * R_g$ value does not meet the requirement for the reliability of the approximation but it is still possible to approximate a radius of gyration of the elongated particles: LL37 and LFb seem to slightly decrease R_g of the particles especially at the higher peptide concentration. This change is probably not significant considering the un-reliability of the rod approximation.

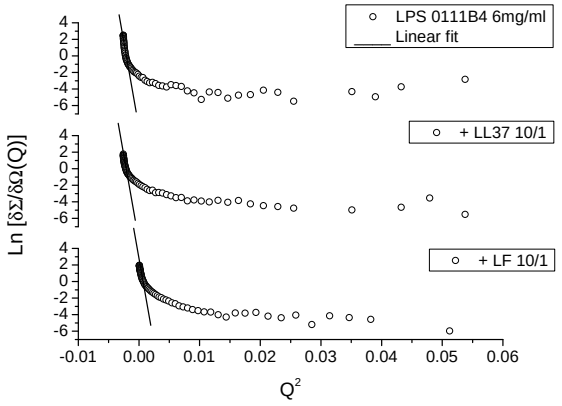

FIGURE 3.14: Guinier plot of scattering data of LPS 0111B4 (6 mg/mL) in 1 mM $MgCl_2$ saline solution at 37°C alone and with the addition of peptides LL37 or LFb at a LPS/peptide ratio of 10/1. The linear fit was applied at the low Q^2 range of 0.000-0.003.

TABLE 3.3: Values from the linear fitting of the Guinier plot of LPS 0111B4 6 mg/mL in 1 mM $MgCl_2$ saline solution at 37°C alone and following challenge by the peptides LL37 or LFb at a low Q range of 0.015-0.032.

Sample	R^2 fit	$Q * R_g$ value[i]	R_g
0111B4 6mg/ml	0.955	2.89	90.0
+ LL37 50/1	0.958	2.84	88.4
+ LL37 10/1	0.985	2.39	74.4
+ LFb 50/1	0.969	2.83	87.9
+ LFb 10/1	0.977	2.50	77.9

[i] limit $Q * R_g < \sqrt{3}$

Because of the poor fit of the Guinier approximation to the SANS data from LPS 0111B4 6 mg/mL in the presence of the peptides, the Kratky-Porod model was

applied instead. In Figure 3.15 only the fitting for the 10/1 LPS/peptide ratio is depicted as example. The linear fit at the intermediate-high Q range gave the values for $Q * R_g$, R_g and R, listed in Table 3.4. The data show that similar to the Guinier approximation, the fit does not meet the $Q * R_g$ value requirement. The radius radius (R) values are much smaller than the values calculated with the Guinier approximation and a significant reduction in R_g was not observed except for the sample containing the highest concentration of LL37 peptide (ratio 10/1). No modification of M_L was observed in the presence of the two peptides.

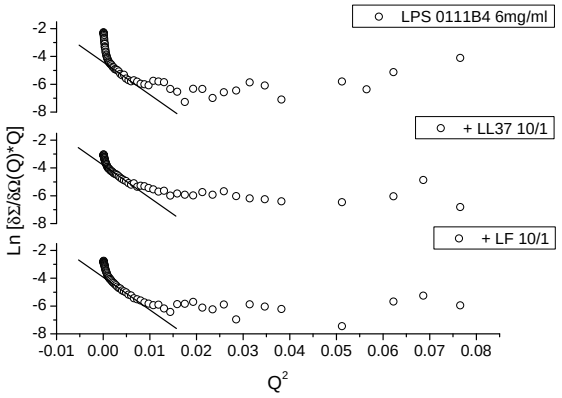

FIGURE 3.15: Kratky plot of LPS 0111B4 (6 mg/mL) in 1 mM $MgCl_2$ saline solution at 37°C alone and with the addition of peptides LL37 or LFb at a LPS/peptide ratio of 10/1. The linear fit was applied at the intermediate-high Q^2 range of 0.003-0.005.

TABLE 3.4: Values from the linear fitting of Kratky plot of LPS 0111B4 (6 mg/mL) in 1 mM $MgCl_2$ saline solution at 37°C alone and following challenge by the peptides LL37 or LFb at the intermediate-high Q range of 0.032-0.067.

Sample	R^2 fit	$Q * R_g$ value[i]	R_g	$R = \sqrt{2} * R_g$ (Å)	M_L (Da/Å)
0111B4 6mg/ml	0.973	1.69	25.2	36	108'855
+ LL37 50/1	0.974	1.66	24.9	35	104'677
+ LL37 10/1	0.995	1.50	22.5	32	101'600
+ LFb 50/1	0.979	1.70	25.4	36	102'703
+ LFb 10/1	0.985	1.70	25.4	36	96'710

[i] limit $Q * R_g < 1.1$

Both the Guinier and the Kratky approximation failed to provide trustworthy information about the systems, therefore, in order to obtain more details and to have a more reliable fitting, structural models from the fitting software programs

FISH and SansView were used to extract as much information as possible. These models are more complex than the simple Guinier and Kratky approximations and allowed a closer fit to the scattering curves across the entire Q range. The fitting attempts of the sample containing LPS 0111B4 at a concetration of 6 mg/mL in 1 mM $MgCl_2$ saline solution at 37°C are here reported as being representatives of the analysis of the other samples not mentioned in this section. Based on the Cryo TEM micrographs a range of models for elongated objects were attempted. The first attempts were made using a simple rod model number 18 in FISH software (attempts not reported) and it proved to be unsuccessful for the fitting of the curves. This particular model considers the scattering objects as rigid rods, probably too rigid for such apparently flexible particles. Attempts to fit the data with models for flexible cylinders with and without elliptical cross sections (Figure 3.2) were made, where the number of elements n and their length l are given in order to approximate the flexibility of the objects, in addition to the radial dimensions of the particles. Unfortunately these further attempts at fitting the data did not result in a good outcome. First the FISH software has been used running a Kholodenko worm-like chain model [239] with a circular cross section. The cylinder can have either an homogeneous SLD or a core/shell feature, with two different SLDs for the inner part and the outer part of the worm-like micelle, both alternatives were attempted with similar results. The fitting of LPS 0111B4 at a concentration of 6 mg/ml as core/shell flexible cylinder is depicted in Figure 3.16.

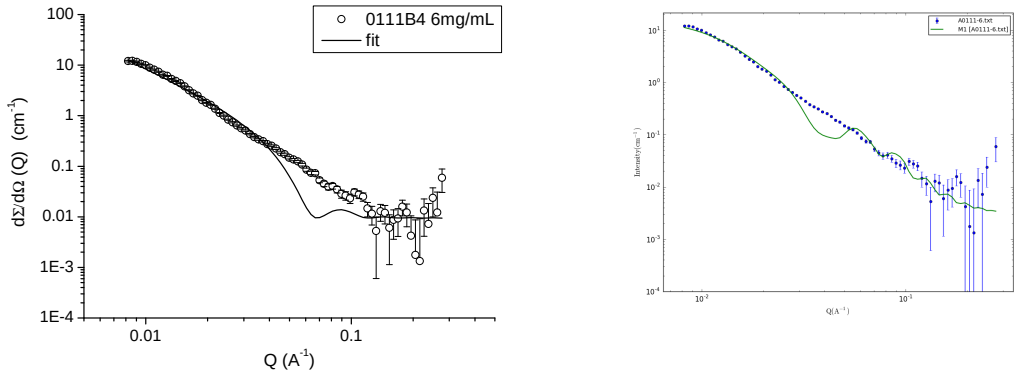

A B

FIGURE 3.16: LPS 0111B4 (6 mg/mL) fitting as (A) core/shell flexible cylinder in FISH software and (B) as elliptical flexible worm in SANSview software.

As mentioned above, the value of the contrast has been entered from the calculated SLDs of the molecule (contrast Equation 3.15). The Kholodenko model provided

TABLE 3.5: Parameters for the fitting in FISH software of LPS 0111B4 (6 mg/mL) (Figure 3.16A).

Parameter	Value	Unit
Scale	4.52E-07	
n	-1.08E+02[i]	Å
l	1.29E+02	Å
r_c core	3.70E+01	Å
t_s shell	2.15E+01	Å
contrast	8.24E-01	

[i] unreal negative value

TABLE 3.6: Parameters for the fitting in SANSview software of LPS 0111B4 (6 mg/mL) (Figure 3.16B).

Parameter	Value	Unit
Axis ratio	2.4701	
l	64.981	Å
L	12.286[i]	Å
$r1$	88.973	Å
scale	0.00426	

[i] unreal value comapred to l

by the FISH software would give as an output the n and the l of each segment composing the flexible cylinder, the r_c and the t_s; therefore the total radius of the cross section $R = r_c + t_s$ can be calculated. As an example for the fitting of LPS 0111B4 at a concentration of 6mg/mL in saline solution containing 1 mM $MgCl_2$ (Figure 3.16) , the number of segments is unrealistically negative (Table 3.5) but if the parameters are restrained inputting a reasonable number, another parameter would subsequently be calculated as negative.

The second model used in other attempts, including the example reported here (Figure 3.16) for LPS 0111B4 at 6 mg/mL, was a flexible cylinder with elliptical cross section model provided by the fitting software program SANSview, the parameters of which are reported in Table 3.6 and described in Figure 3.2. The *axes ratio* is the ratio between the major radius $r2$ and the minor radius $r1$ and has to be > 1; other parameters of the model are the l and L, the latter being defined as the total length of the object. The scale in this case is equal to the ϕ of the LPS in solution. From the values of Table 3.6 it is possible to note an irregularity in the length values because $L < l$, which is theoretically impossible (the length of a single segment cannot be bigger than the total length of the object). If the length was restrained in order to have reasonable values, the *axes ratio* becomes < 1 which is not possible according to the limits of the model. Equivalent results were found for all the models attempted during the analysis of the dilutions of

LPS 011B4 and its interaction with the peptides LL37 and LFb .

3.3.2.2 LPS D21 and peptides LL37 and LFb.

The first data analysis carried out for LPS D21 dilutions in saline solution containing 1mM $MgCl_2$ scattering curves is the Guinier approximation for lamellar structures. In Figure 3.17 the approximation for the dilution experiment are depicted with the linear fitting at intermediate-high Q of 0.01973-0.05236 (equal to a Q^2 range of 0.000389-0.002741). The thickness T of the bilayer (Table 3.7) does not change considerably with the increasing concentration and the value is stable between the range 72-74 Å. The approximation almost satisfies the requirements (limit $0.41 < Q * R_g < 0.92$) therefore we can consider these calculations to be valid. A more precise characterization of the scattering curves can be achieved applying a lamellar model using a scattering data fitting software. LPS D21 dilutions

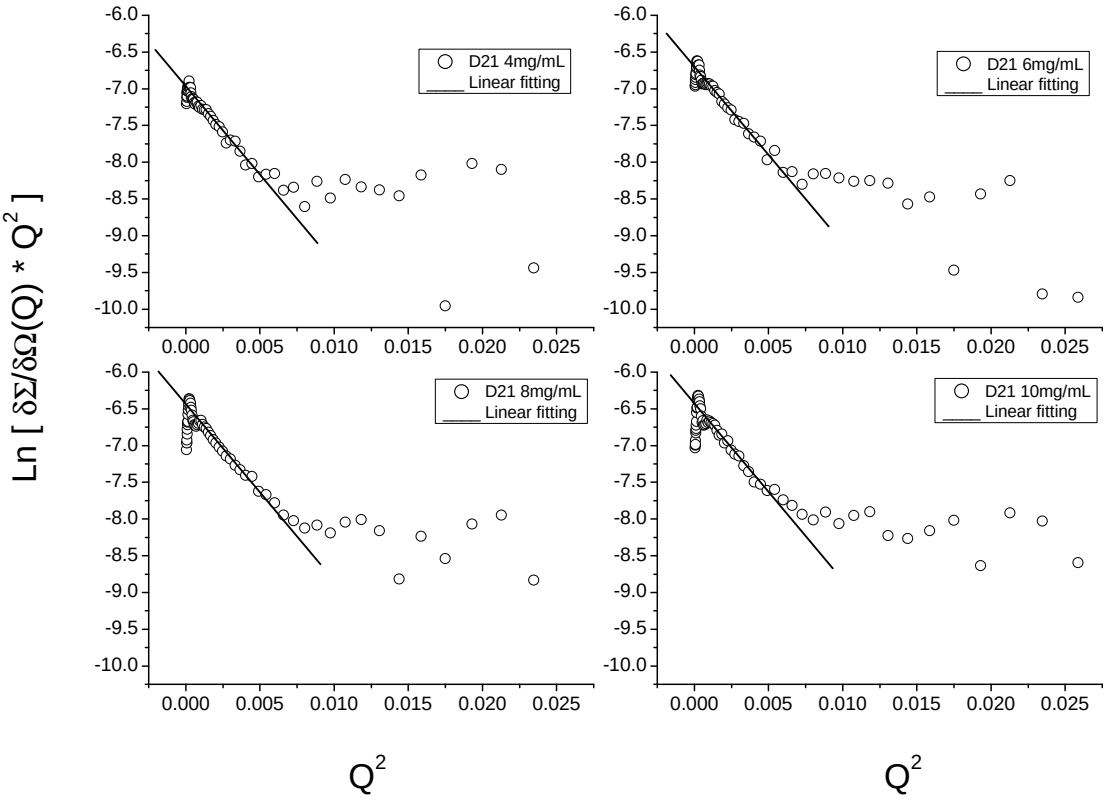

FIGURE 3.17: Guinier approximation for lamellar structures of the scattering data of LPS D21 dilutions in 1 mM $MgCl_2$ saline solution at 37°C and relative linear fitting at intermediate-high Q^2 range of 0.0004-0.003.

were fitted as a monodisperse oriented sheet with a shell/core/shell feature (Figure 3.3). In this case the shell was considered as being formed by the hydrophilic regions of LPS (the core of LPS), and the core being composed of the hydrophobic

TABLE 3.7: Values from the linear fitting of the Guinier approximation for lamellar structures of LPS D21 dilutions in 1 mM $MgCl_2$ saline solution at 37°C at the intermediate-high Q range of 0.02-0.052

D21	R^2 fit	$Q * R_g$ value[i]	R_g	$T = \sqrt{12} * R_g$ (Å)
10 mg/ml	0.878	1.08	20.81	72.08
8 mg/ml	0.910	1.09	20.80	72.04
6 mg/ml	0.941	1.09	20.83	72.16
4 mg/ml	0.964	1.12	21.41	74.18

[i] limit $0.41 < Q * R_g < 0.92$

acyl chains of the lipid A region. The fitting of the data reported in Figure 3.18 shows the scattering curves of D21 at different concentrations. At 4 mg/ml and 6 mg/ml the mono-disperse oriented sheet fitting is acceptable, while at higher concentrations (8 mg/ml and 10 mg/ml) the sheet features are lost and the model gives a less precise fit. It is interesting to note the formation of three shoulders at high concentrations which are not visible in the scattering curve at 4 mg/ml; these might be Bragg reflections from a multi-lamellar structure. If these reflections are grouped in equidistant ratios of the lamellar repeat *d*-spacing we can approximate the value of the distance repeat as $d = \frac{2\Pi}{Q}$; the resulting d-spacing values between bilayers, calculated at high Q range (Q value of the first reflection on the right) for D21 at 6 mg/mL, 8 mg/mL and 10 mg/mL are respectively 70.6 Å, 57.7 Å and 59.6 Å; the ripples at lower Q values are separate from the first reflection by a ratio of respectively 0.41 ± 0.05, 0.40 ± 0.09 and 0.41 ± 0.09 which suggests a repeated distance of 1/2.5. While the first reflection at high Q suggests a spacing between two bilayers, the other reflections might represent the spacing between lamellae present in a stack of bilayers rather than a space between two lamellae. However, the formation of ripples might also suggest the formation of different populations of objects which could be either sheets with different thickness or alternatively particles with diverse morphologies. This might explain the steadiness of the middle reflection (Q 0.032) which would describe one population that does not change with the dilutions, together with other populations described by the other ripples at diverse Q values. Due to the complexity of the system, an adequate model to fit is not available, although several attempts to mix different form factors have been made unsuccessfully. The output parameters of the monodisperse oriented sheet shell/core/shell model provided by the FISH software are reported in the Table 3.8. The contrast value was fixed in the model and was calculated to be 0.904 for LPS D21, according to the Equation 3.15. The values of the bilayer's

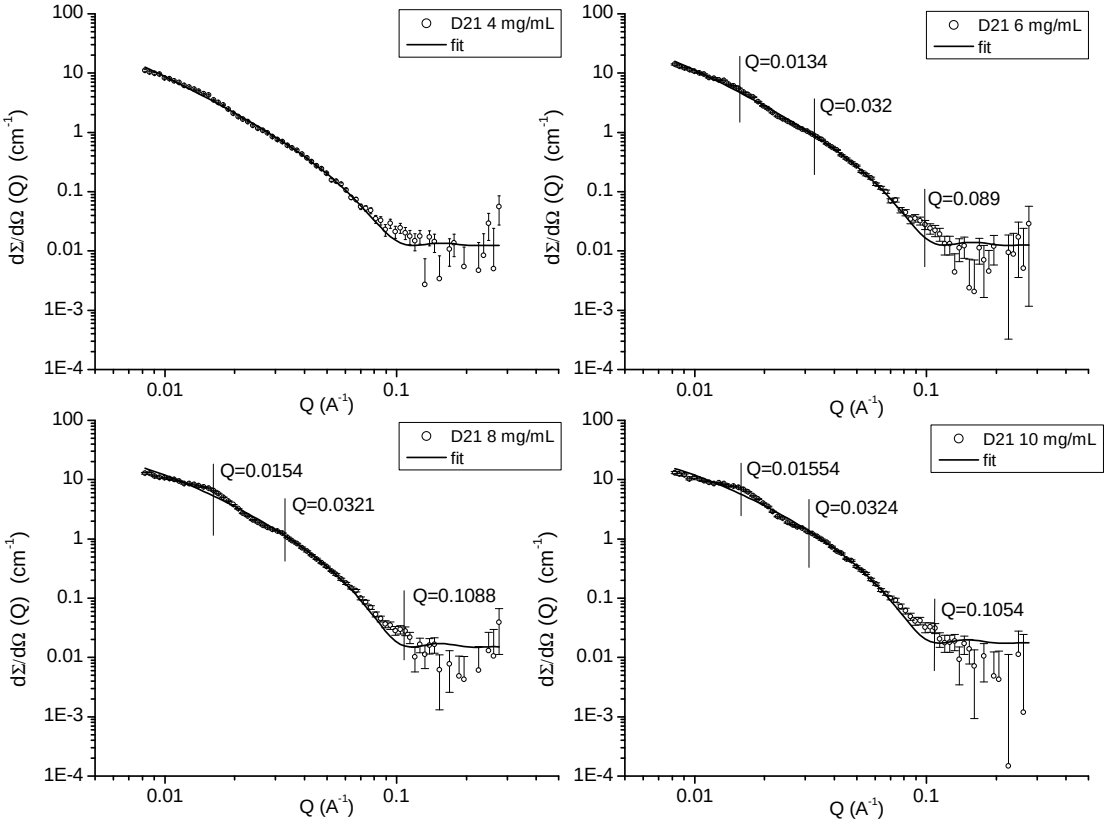

FIGURE 3.18: SANS data for LPS D21 dilutions in saline solution containing 1 mM $MgCl_2$ at 37 °C fitted as monodisperse oriented sheet shell/core/shell provided by the FISH software. The Q values reported have been considered of interest.

TABLE 3.8: Parameters obtained from the fitting of LPS D21 dilutions with the monodisperse oriented sheet shell/core/shell model provided by the FISH software.

D21	4mg/ml	6mg/ml	8mg/ml	10mg/ml
Scale	0.042	0.039	0.016	0.014
t_c (Å)[i]	22.91 ±0.00	23.05 ±0.01	23.38 ±0.01	23.28 ±11.5
t_s (Å)[ii]	16.96 ±0.00	16.68 ±0.01	18.05 ±0.01	17.17 ±5.55
T[iii](Å)	56.83	56.41	58.04	57.62
$R\sigma$ (Å)	503.06	408.47	228.53	211.12

[i] core thickness [ii] shell thickness [iii] Total thickness $T = 2 * t_s + t_c$

shell and core thickness did not change with the increasing concentration of LPS, therefore the T is similar at all the dilutions (between 55 and 58 Å). The scale factor decreased because it is proportional to the power of $R\sigma$.

The Kratky-Porod approximation for elongated objects of the scattering curves of the LPS D21 (6 mg/mL) in saline solution containing 1mM $MgCl_2$ at 37°C with

peptides LL37 or LFb at the LPS/peptide ratios of 50/1 and 10/1 is shown in Figure 3.19. The linear fitting of the intermediate-high Q values was carried out for all the scattering curves over the Q range 0.032-0.067 (equivalent to a Q^2 range of 0.00103-0.00447). The parameters obtained from the calculations for this approximation are reported in Table 3.9.

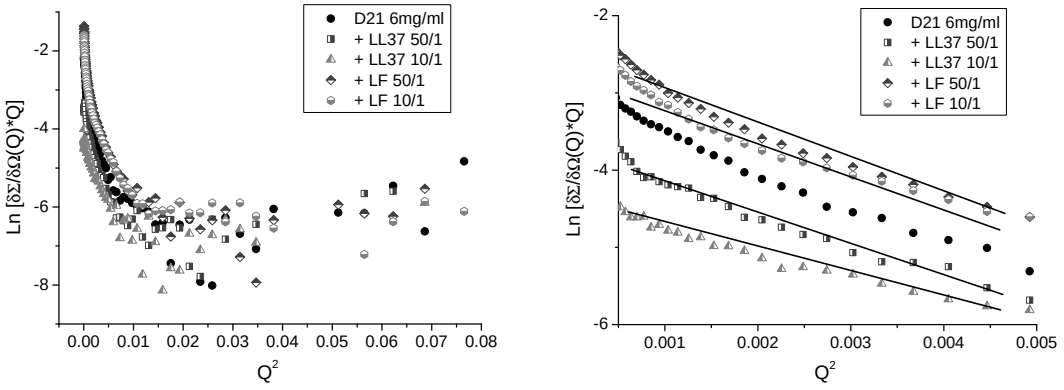

FIGURE 3.19: (A) Kratky plot of LPS D21 6 mg/mL in saline solution containing 1mM $MgCl_2$ at 37°C alone and following challenge with the peptides LL37 or LFb at LPS/peptide ratios of 50/1 and 10/1. (B) Linear fitting of the Kratky plot expanded over the Q^2 range of 0.0005-0.005.

TABLE 3.9: Parameters obtained from the linear fitting of the Kratky plot of LPS D21 6 mg/mL in saline solution containing 1mM $MgCl_2$ at 37°C with the peptides LL37 or LFb at the LPS/peptide ratios of 50/1 and 10/1.

D21 6mg/ml	R^2 fit	$Q * R_g$ value[i]	R_g	$R = \sqrt{2} * R_g$ (Å)	M_L (Da/Å)
+ LL37 50/1	0.979	1.85	27.7	39	78'053
+ LL37 10/1	0.983	1.59	23.8	34	67'821
+ LFb 50/1	0.987	1.95	29.3	41	39'597
+ LFb 10/1	0.978	1.83	27.5	39	43'514

[i] limit $Q * R_g < 1.1$

Despite the fact that the approximation does not fully comply with the prescribed Q range limits for the Kratky approximation, it is possible to observe different effects of LL37 and LFb peptides on the aggregates of LPS D21 from these curves. The R_g value did not change considerably with the addition of the two peptides at different ratios. The M_L values are different when comparing the samples with LL37 and the samples with LFb peptide. From the observation of the CryoTEM

micrographs of LPS D21 with LFb (Figure 3.8 B) it seems that D21 forms perforated lamellae or regular toroidal structures rather than tightly packed elongated structures. This might suggest that the Kratky approximation is not correct for this system, a fact that is corroborated by the highest $Q * R_g$ values of the data set (Table 3.9). The thickness of lamellae of the sample containing LPS D21 challenged by LFb peptide was calculated using the Guinier approximation for lamellar structures plotting the scattering curve as $ln[Q^2 \times (\delta\Sigma/\delta\Omega)(Q)]\, vs\, Q^2$ (Figure 3.20 A). The linear fitting of the Guinier plot (Figure 3.20 B) over the intermediate Q range 0.016-0.043, equivalent to a Q^2 range of 0.00026-0.00186, allowed for the calculation of the parameters shown in Table 3.10. The Guinier approximation

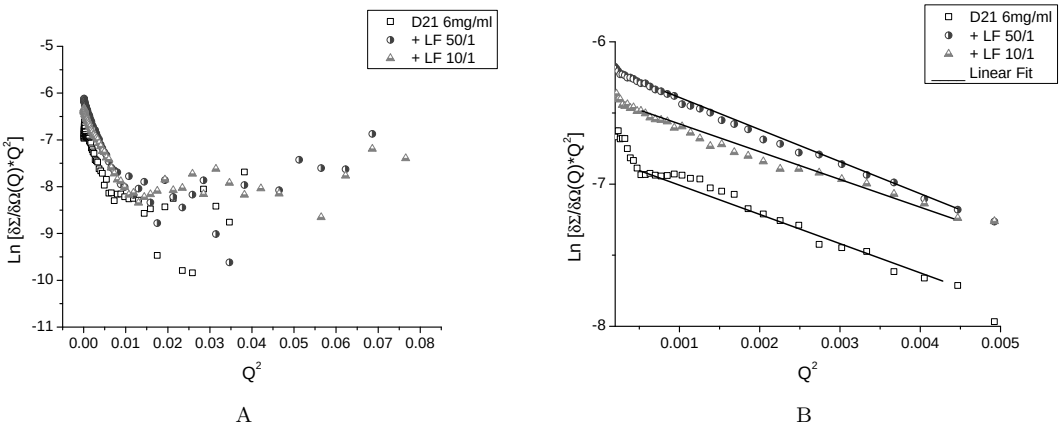

FIGURE 3.20: (A) Guinier approximation for lamellar structures of LPS D21 (6 mg/mL) in saline solution containing 1mM $MgCl_2$ at 37°C alone and with the peptide LFb at LPS/peptide ratios of 50/1 and 10/1. (B) Linear fitting of the Guinier plot over the expanded intermediate-high Q^2 range of 0.0002-0.005.

TABLE 3.10: Output values of the Guinier approximation for lamellar structures of LPS D21 with LFb peptide at 50/1 and 10/1 LPS/peptide ratios.

D21	R^2 fit	$Q * R_g$ value[i]	R_g	$T = \sqrt{12} * R_g$ (Å)
6 mg/ml	0.941	1.09	20.83	72.16
+ LFb 50/1	0.996	0.92	22.38	77.53
+ LFb 10/1	0.987	0.90	22.03	76.33

[i] limit $0.41 < Q * R_g < 0.92$

fits correctly the data of LPS D21 with LFb peptide and the $Q * R_g$ limit is respected; there was an increase of the layer thickness upon addition of LFb to the sample. The thickness of the bilayer was comparable to the radius of the elongated particle found with the previous Kratky approximation. Following the findings of

the approximations, the LPS D21/LL37 and LPS D21/LFb samples were fitted to respectively a Kholodenko flexible cylinder model and a monodisperse sheet shell/core/shell model with the use of FISH software. LPS D21/LL37 fitting is shown in Figure 3.21 and the resultant parameters are reported in Table 3.11. The value of the contrast is 8.17e-01 (see Equation 3.15) . The number of segments n

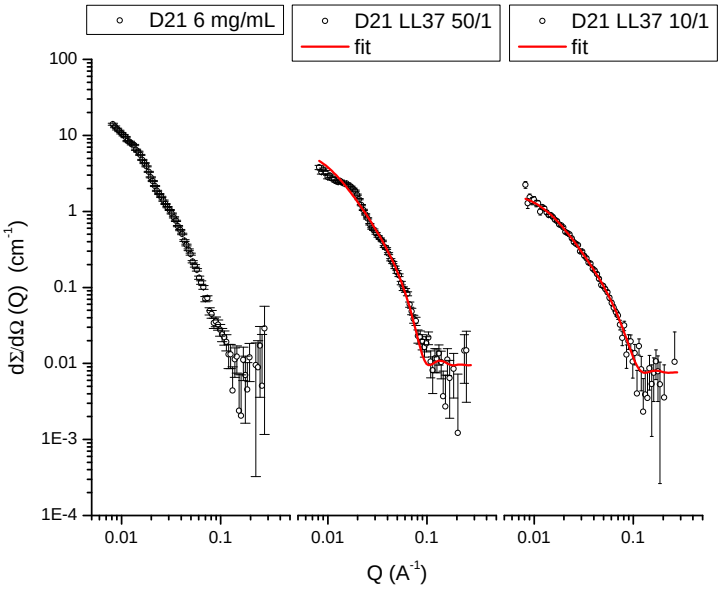

FIGURE 3.21: Kholodenko flexible cylinder model fitting of LPS D21 (6 mg/mL) in saline solution containing 1mM $MgCl_2$ at 37°C with the peptide LL37 at LPS/peptide ratios of 50/1 and 10/1.

TABLE 3.11: Kholodenko flexible cylinder model parameters of the fitting of LPS D21 at 6 mg/mL in saline solution containing 1mM $MgCl_2$ at 37°C with the peptide LL37 at LPS/peptide ratios of 50/1 and 10/1.

D21 6mg/ml	+ LL37 50/1	+ LL37 10/1
Scale	4.58 e-07	2.18 e-07
ϕ^{i}	1.39 e-04	6.60 e-05
n	12.8 ±6.8	7.9 ±2.1
l (Å)	109.0 ±36.1	103.0 ±17.1
total L (Å)	1397.05	816.23
r_c core (Å)	20.7 ±1.1	13.4 ±0.5
t_s shell (Å)	17.4 ±2.5	16.9 ±0.8
total R (Å)	38.1	30.3

[i] calculated volume fraction from the *Scale* according to Equation 3.14

appeared to reduce upon addition of more LL37 peptide, whilst the Khun length l seemed scarcely affected. Overall the total length of one single particle reduced at higher concentration of LL37 . The core radius r_c decreased from the peptide

ratio 50/1 to 10/1, whilst the shell thickness t_s was not influenced by the increased concentration of peptide. The contrast value was constant and introduced into the fitting as explained above. The volume fraction for each sample was also calculated from the *Scale* value, and they did not match the theoretical value for LPS D21 alone which is 0.004267; this is consistent with the presence of the peptide within the micelle which is likely to alter the density and the SLD of the aggregates.

The scattering curves of LPS D21/LFb peptide were fitted with the lamellar

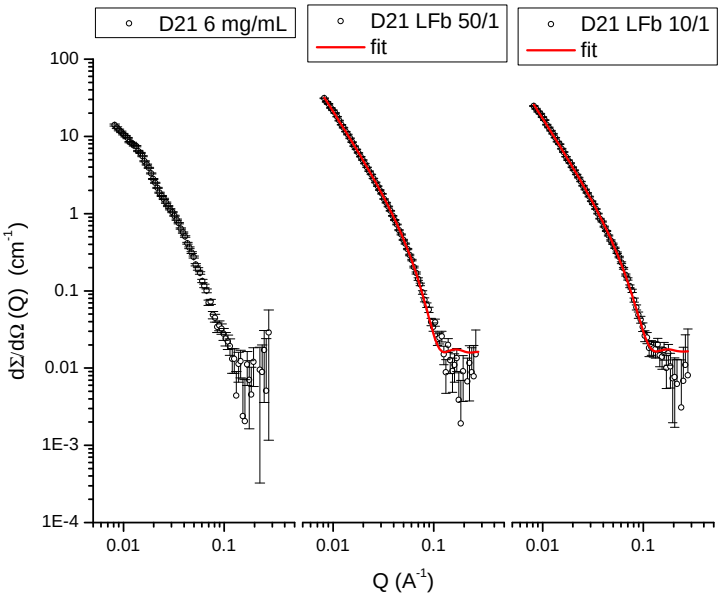

FIGURE 3.22: Monodisperse sheet shell/core/shell model fitting of LPS D21 at 6 mg/mL in saline solution containing 1 mM $MgCl_2$ at 37°C alone and with the peptide LFb at LPS/peptide ratios of 50/1 and 10/1.

TABLE 3.12: Monodisperse sheet shell/core/shell model parameters obtained from the fitting of LPS D21 at 6 mg/mL in saline solution containing 1 mM $MgCl_2$ at 37°C alone and with the peptide LFbat LPS/peptide ratios of 50/1 and 10/1.

	D21 6mg/ml	+ LFb 50/1	+ LFb 10/1
Scale	0.039	4.771	0.838
ϕ^{i}	0.00157	0.00273	0.00277
t_c (Å)	23.05 ±0.01	21.66 ±0.00	25.69 ±0.00
t_s (Å)	16.68 ±0.01	15.72± 0.00	12.52 ±0.00
T (Å)	56.41	53.10	50.73
$R\sigma$	408	330	210

[i] calculated volume fraction from the *Scale* according to Equation 3.21

model described previously. As with the LPS D21/LL37 sample, the contrast

value input into the model was fixed; the model provides a close fit to the scattering curves (Figure 3.22) and the resulting values for the parameters are presented in Table 3.12. At the LPS/peptide ratio of 50/1, t_c and t_s values did not change considerably compared to the LPS D21 alone, with a reduction of both core and shell thickness of approximately 1-1.5 Å each; increasing the concentration of the peptide to a LPS/peptide ratio of 10/1, the core thickness increased while the shell layer became thinner. In this case the overall T of the bilayer reduced by ∼10% compared to the bilayer without the presence of LFb . The volume fraction ϕ values increased with the addition of the peptide at both the LPS/peptide ratios.

3.3.2.3 LPS E7 and peptides LL37 and LFb.

The scattering curves of LPS E7 dilutions were approximated with a Guinier plot (Figure 3.23) for lamellar structures at the intermediate-high Q range of 0.01624-0.04308 (equal to a Q^2 range of 0.000264-0.001856). The parameters presented in Table 3.13 show that the approximation is reliable since the value of $Q * R_g$ is within the limit range of $0.41 < Q * R_g < 0.92$. The thickness of the bilayer formed by LPS E7 is constant, for each dilution, at ∼60 Å, suggesting that there is no effect of dilution on the packing of the lamellae.
The fitting of LPS E7 dilutions (Figure 3.24) as monodisperse sheet shell/core/shell was accurate and the output parameters (Table 3.14) confirm that the concentration did not change the lamellar thickness. In detail both the shell and the core thickness, t_s and t_c respectively, are similar for each dilution; the value of $R\sigma$ does not change significantly except for the LPS E7 sample 8 mg/mL. The scattering curve of LPS E7 retained the same shape for each concentration; the scattering intensity increases, as expected, with the increase in LPS concentration.

The LPS E7 (6 mg/mL) in saline solution containing 1 mM $MgCl_2$ at 37°C was challenged with the peptides LL37 or LFb at the LPS/peptide ratios of 50/1 and 10/1, and the scattering data were analysed with different models and approximations due to the complexity of the system. The addition of peptide LL37 to samples containing LPS E7 (6 mg/mL) was first analysed plotting the Q dependency of the intensity of the scattering curves as reported in Figure 3.25. The curves show how the scattering pattern of LPS E7/LL37 suggests the presence of a Gaussian chain feature at low Q (slope $n = 2$) and a polymer coil behavior at intermediate-high

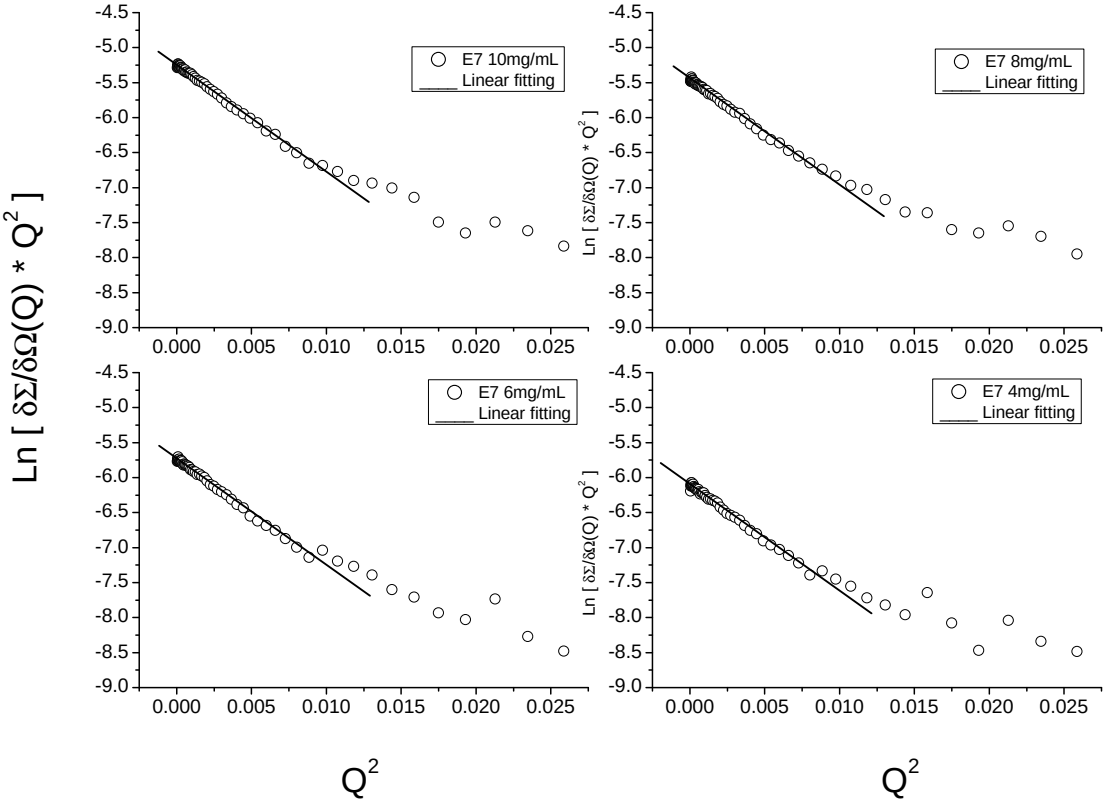

FIGURE 3.23: Guinier approximation for lamellar structures for the scattering data of LPS E7 dilutions in saline solution 1 mM $MgCl_2$ at 37°C and relative linear fitting at intermediate-high Q^2 range of 0.0003-0.0019.

TABLE 3.13: Parameters of the linear fitting of the Guinier approximation for lamellar structures of LPS E7 dilutions in saline solution 1 mM $MgCl_2$ at 37°C at the intermediate-high Q range of 0.02-0.04

E7	R^2 fit	$Q * R_g$ value[i]	R_g	$T = \sqrt{12} * R_g$ (Å)
10 mg/ml	0.983	0.76	17.63	61.09
8 mg/ml	0.989	0.74	17.16	59.44
6 mg/ml	0.978	0.75	17.45	60.46
4 mg/ml	0.971	0.74	17.26	59.81

[i] limit $0.41 < Q * R_g < 0.92$

Q values (slope $n = 3$); therefore the Guinier approximation for rigid rods was excluded and the data were processed using the Kratky approximation for elongated particles. The data concerning the addition of the peptide LFb were approximated with a $ln[Q \times (\delta\Sigma/\delta\Omega)(Q)]\, vs\, Q^2$ plot fitted linearly over the intermediate-high Q range of 0.03215-0.06683 , equal to a Q^2 range of 0.001033-0.004466 (fitting not shown).

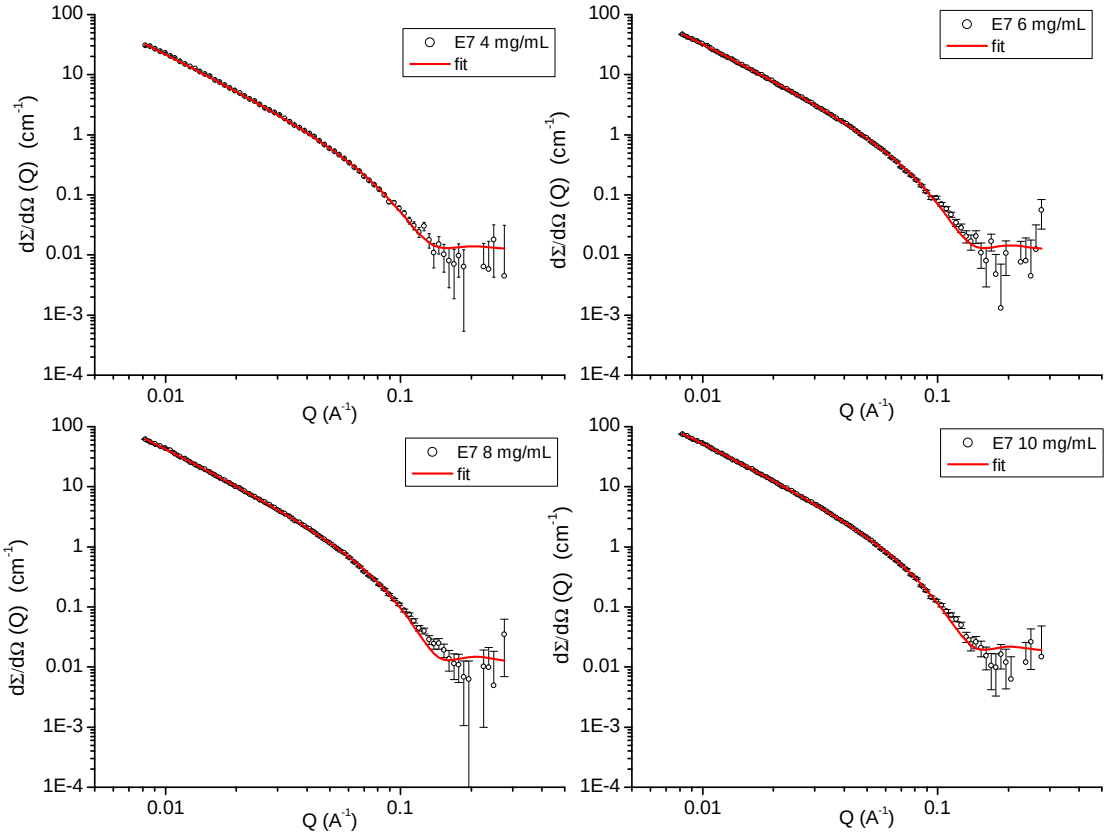

FIGURE 3.24: Monodisperse oriented sheet shell/core/shell model fitting of LPS E7 dilutions in saline solution containing 1 mM $MgCl_2$ at 37 °C .

TABLE 3.14: Parameters obtained from the monodisperse oriented sheet shell/-core/shell model fitting of LPS E7 dilutions in saline solution containing 1 mM $MgCl_2$ at 37 °C .

E7	4mg/ml	6mg/ml	8mg/ml	10mg/ml
Scale	0.042	0.423	1.107	0.885
t_c (Å)[i]	17.25 ±7.67e-17	17.25 ±4.83e-17	17.04 ±1.43e-17	17.24 ±4.79e-14
t_s (Å)[ii]	13.02 ±4.88e-17	13.02 ±3.08e-17	12.63 ±9.08e-18	12.93 ±3.05e-14
T[iii](Å)	43.29	43.29	42.30	43.10
$R\sigma$ (Å)	769.85	769.85	875.82	716.09

[i] core thickness [ii] shell thickness [iii] Total thickness $T = 2 * t_s + t_c$

The values of the parameters for the Kratky approximation are listed in Table 3.15. The approximation does not comply with the requirement of the fitting in all the cases, however it shows the approximate values of the radius R and the parameter M_L for the elongated particles. The addition of more LL37 peptide slightly decreases the radius of the micelle and increases the mass per unit length of the objects. It should be pointed out that, compared to the 50/1 ratio, the highest concentration of LL37 at 10/1 ratio seems to provide a closer fit (lower

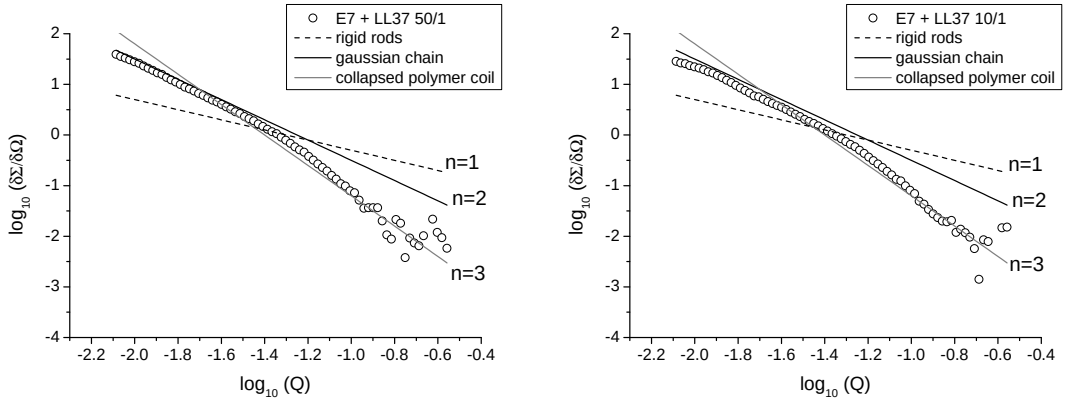

A B

FIGURE 3.25: Q dependency of the intensity of LPS E7 (6 mg/mL) in saline solution containing 1 mM $MgCl_2$ at 37 °C with the peptide LL37 at a LPS/peptide ratio of (A) 50/1 and (B) 10/1. n is the slope of the straight lines.

TABLE 3.15: Parameters obtained from the linear fitting of Kratky plot of LPS E7 (6 mg/mL) with the peptides LL37 and LFb at 50/1 and 10/1 LPS/peptide ratios at the intermediate-high Q range of 0.03215-0.06683.

E7 6mg/ml	R^2 fit	$Q * R_g$ value[i]	R_g	$R = \sqrt{2} * R_g$ (Å)	M_L (Da/Å)
+LL37 50/1	0.988	1.80	26.9	38.1	61'730
+LL37 10/1	0.992	1.72	25.7	36.4	65'721
+LFb 50/1	0.987	1.80	26.9	38.1	67'357
+LFb 10/1	0.983	1.77	26.5	37.5	67'536

[i] limit $Q * R_g < 1.1$

R^2 value) and presents a $Q * R_g$ value closer to the limit, although still not satisfactory. Regarding the addition of the LFb peptide, both the values of R_g and the mass per unit length (M_L) do not show relevant differences between the two ratios, suggesting a weak LFb effect upon increase of its concentration.

Subsequently the Kholodenko model was applied to the data in order to obtain more detailed parameters relevant to elongated objects. The scattering curves for the samples challenged with LL37 and LFb are presented in Figure 3.27. The E7 scattering data in the presence of the peptides were additionally plotted with a Guinier approximation for lamellar structures, considering the possibility of a mix of diverse structures. The plot $ln[Q^2 \times (\delta\Sigma/\delta\Omega)(Q)]$ vs Q^2 was fitted linearly in the intermediate-high Q range of 0.01624-0.04308 (equal to a Q^2 range of 0.000264-0.001856). In Table 3.16 the data obtained from the plot clearly show that the addition of increasing amount of LL37 peptide reduces the thickness of

the bilayer proportionally. While the addition of LFb peptide initially seemd to decrease T at the ratio 50/1, followed by an increase of thickness at the higher LFb concentration. All the approximations respect the the $Q * R_g$ limits, therefore the values can be considered reliable; moreover the thickness magnitude seems to be reasonable according to previous analysis of the data set. It is worth higlighting that the highest concentration of LL37 drags the trend line away from an ideal linearity value, with a poor value for the coefficient of determination.
Since it is likely that the samples contained a mixture of structures, a number of

TABLE 3.16: Parameters obtained from the linear fitting of the Guinier approximation for lamellar structures of LPS E7 at 6 mg/mL in saline solution containing 1 mM $MgCl_2$ at 37 °C , alone and with the addition of the peptides LL37 or LFb at LPS/peptide ratios of 50/1 and 10/1 LPS/peptide ratios, at the intermediated-high Q range.

Sample	R^2 fit	$Q * R_g$ value[i]	R_g	$T = \sqrt{12} * R_g$ (Å)
E7 6mg/ml	0.978	0.75	17.45	60.46
+LLL37 50/1	0.953	0.67	15.59	54.01
+LL37 10/1	0.659	0.46	10.76	37.28
+LFb 50/1	0.975	0.69	16.08	55.71
+LFb 10/1	0.973	0.73	17.02	58.97

[i] limit $0.41 < Q * R_g < 0.92$

different models are applied to the data for LPS E7 at 6 mg/mL concentration in saline solution containing 1 mM $MgCl_2$, at 37°C , with the addition of the peptides LL37 or LFb at LPS/peptide ratios of 50/1 and 10/1, using both a lamellar structure model and a flexible cylinder structure model.
The application of the monodisperse shell/core/shell model is shown in Figure 3.26 A and B, respectively, for LL37 and LFb peptides. The model fitted closely the scattering curves and produced the parameters reported in Table 3.17. The peptide LL37 reduced the overall thickness of the lamellae relatively to an increase in the peptide concentration. This effect is mostly concentrated on the shell part of the bilayer, as a matter of fact the thickness of the core is almost unchanged at the highest concentration of peptide (ratio LPS E7/LL37 of 10/1). The value of $R\sigma$ was halved exclusively at the highest concentration of peptide, compared to the value of LPS E7 alone. The volume fraction remains rather constant for all the three samples within the LL37 group. The addition of LFb peptide has a more irregular effect on the bilayer (see parameters in Table 3.17). Compared to the

sample without peptide, the data for LPS/LFb ratio of 50/1 presents a mere total thickness reduction coupled with a noteworthy increase of the core thickness t_c at the expenses of a decrease of the shell thickness t_s. At the highest concentration of LFb (ratio 10/1) there is a drop of total thickness of $\sim$3 Å mainly due to a reduction of the core thickness t_c, this effect contrasts with the effect noted at lower LFb concentration at the LPS/peptide ratio of 50/1. The value of $R\sigma$ has undergone a slight reduction upon addition of the peptide LFb , and it is constant for both peptide ratios. LFb seems to induce a low reduction of the volume fraction, compared to the less pronounced effect on ϕ of the peptide LL37 .

The LPS E7 alone forms lamellar structures, therefore a direct comparison with

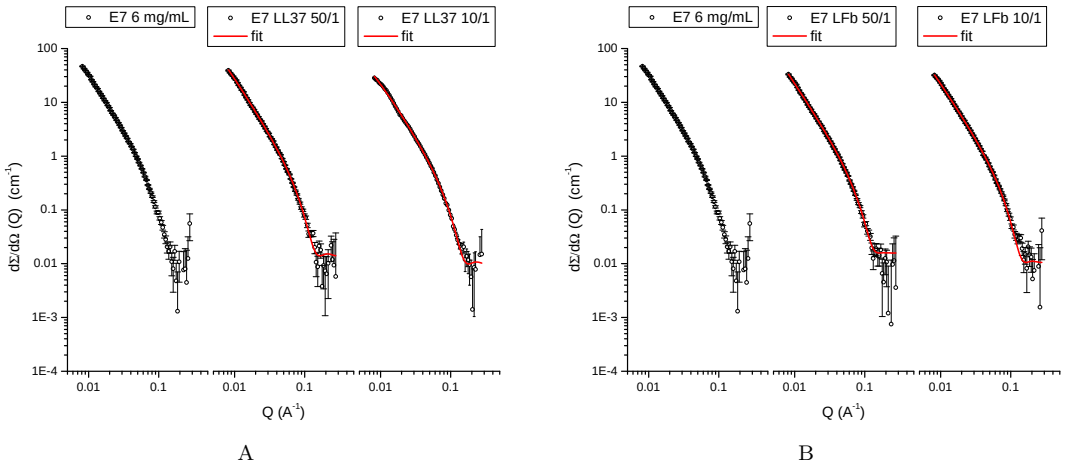

FIGURE 3.26: Monodisperse sheet shell/core/shell model fitting of LPS E7 at 6 mg/mL in saline solution containing 1 mM $MgCl_2$ at 37°C with (A) LL37 peptide and (B) LFb peptide at LPS/peptide ratios of 50/1 and 10/1.

TABLE 3.17: Parameters obtained from the monodisperse sheet shell/core/shell model fitting of LPS E7 at 6 mg/ml in saline solution containing 1 mM $MgCl_2$ at 37°C alone and with the peptides LL37 or LFb at LPS/peptide ratios of 50/1 and 10/1.

	E7 6mg/ml	+LL37 50/1	+LL37 10/1	+LFb 50/1	+LFb 10/1
Scale	0.623	0.527	0.136	0.365	0.406
ϕ^{i}	0.00468	0.00415	0.00432	0.00408	0.00338
t_c (Å)	17.25 ±0.00	16.43 ±0.17	17.05 ±2.48	21.33 ±1.31	15.60 ±0.00
t_s (Å)	13.02 ±0.00	12.52 ±0.10	10.64 ±1.24	10.40 ±0.66	12.63 ±0.00
T (Å)	43.29	41.46	38.34	42.14	40.85
$R\sigma$ (Å)	770	734	372	702	695

[i] calculated volume fraction from the *Scale* according to Equation 3.21

the samples containing the two peptides fitted using the Kholodenko model (Figure 3.27) is not possible. From the parameters obtained from the fitting reported in Table 3.18 it is possible to observe that the scale factors and the volume fractions for all the samples are unchanged. Concerning both LL37 and LFb added it is striking to note the value of n and l, where both peptides induced the formation of a large number (ranging form 4000 to 48000) of very short segments of micelles of approximately 8 to 11 Å. In the case of LL37 peptide, the highest peptide concentration (ratio 10/1) revealed a ten-fold reduction of n compared to the 50/1 ratio, while the l value is reduced from 8 to 10 Å. However the large errors must be considered. The core radius and the shell thickness have not undergone major changes apart from a reduction of r_c from 9 to 8 Å and the total radius of the objects is set between 23-24 Å. The peptide LFb induced a six-fold reduction of n and a l decrease from 11 to 8 Å probably because it affects mostly the headgroup region of the LPS.

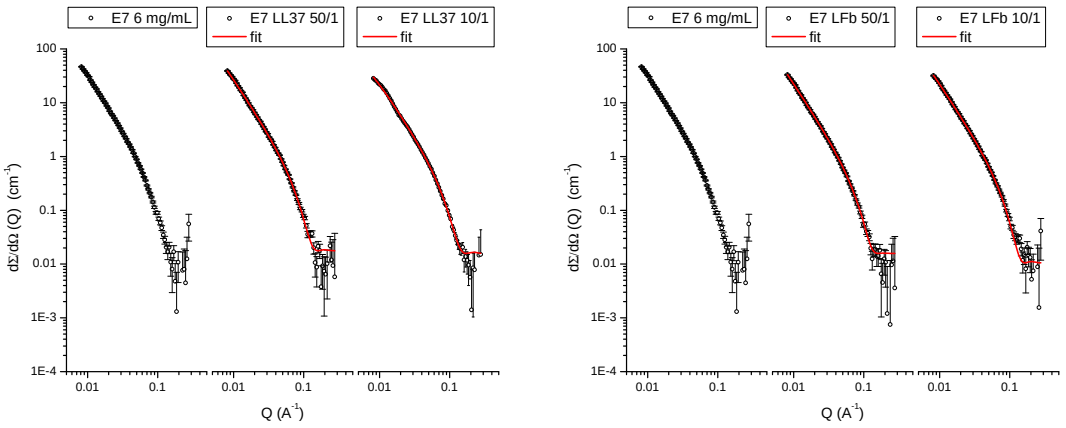

A B

FIGURE 3.27: Kholodenko flexible cylinder model fitting of LPS E7 at 6 mg/mL in saline solution containing 1 mM $MgCl_2$ at 37°C (A) LL37 peptide or (B) LFb peptide at LPS/peptide ratios of 50/1 and 10/1.

3.3.2.4 Calculation of the volume fraction

From the fitting of the scattering curves of the dilution experiments it was possible to calculate back the ϕ through the *Scale* parameter of each model. The equations to be considered are Equation 3.21 and Equation 3.22. Table 3.19 compares the calculated volume fraction for each concentration of LPS D21 and D21E7 and the

Table 3.18: Parameters from the Kholodenko flexible cylinder model fitting of LPS E7 at 6 mg/mL in saline solution containing 1 mM $MgCl_2$ at 37°C (A) LL37 peptide or (B) LFb peptide at LPS/peptide ratios of 50/1 and 10/1.

Parameter	+LL37 50/1	+LL37 10/1	+LFb 50/1	+LFb 10/1
Scale	2.02E-07	2.18E-07	2.19E-07	2.09E-07
ϕ^{i}	6.11E-05	6.59E-05	6.62E-05	6.33E-05
n	48698 ±25330	4877 ±1687	61979 ±8877	13788 ±3653
l (Å)	8.38 ±0.50	10.04 ±1.68	8.46 ±0.40	11.27 ±0.41
total L (Å)	407915	48948	524625	155352
r_c (Å)	9.30 ±0.37	8.05 ±0.79	10.82 ±0.34	8.36 ±0.20
t_s (Å)	15.52 ±0.31	15.00 ±0.72	14.12 ±0.27	15.67 ±0.19
total R (Å)	24.82	23.06	24.94	24.03

[i] calculated volume fraction from the *Scale* according to Equation 3.14

relative ϕ values obtained from the fittings. Only data concerning the dilution experiments of the pure LPSs (without peptides) were considered. The reliability of the calculations depends upon the closeness of the model fits therefore data from the model fitting of LPS E7 as monodisperse sheet shell/core/shell could be considered more representative than the data from the fitting of LPS D21. Nevertheless the calculations are valid and show that the ϕ calculated values and the obtained values from the fitting are comparable. The volume fraction for LPS 0111B4 could not be obtained because of the inability to closely match the data to a valid model.

Table 3.19: Calculated and theoretical volume fractions for LPS E7 and D21

Sample	Calculated ϕ	ϕD21	ϕE7
4mg/ml	0.00285	0.00318	0.00389
6mg/ml	0.00427	0.00468	0.00529
8mg/ml	0.00568	0.00635	0.00688
10mg/ml	0.00709	0.00768	0.00707

3.4 Discussion

In this study the TEM, combined with the SANS technique, allowed the scattering data modelling to be informed by observation of the micrographs, thus producing models with greater relevance to the samples' morphologies. The diverse molecular

structure of each LPS chemotype induces the formation of various colloidal aggregates (Figure 3.28) which are affected by the presence of the peptides LL37 and LFb . The modifications to the LPS aggregates induced by the peptides (Figure 3.28) depended upon the peptides' physico-chemical characteristics such as conformation, charge and hydrophobicity, as well as to the molecular structure and physico-chemical features of the LPS chemotype studied.

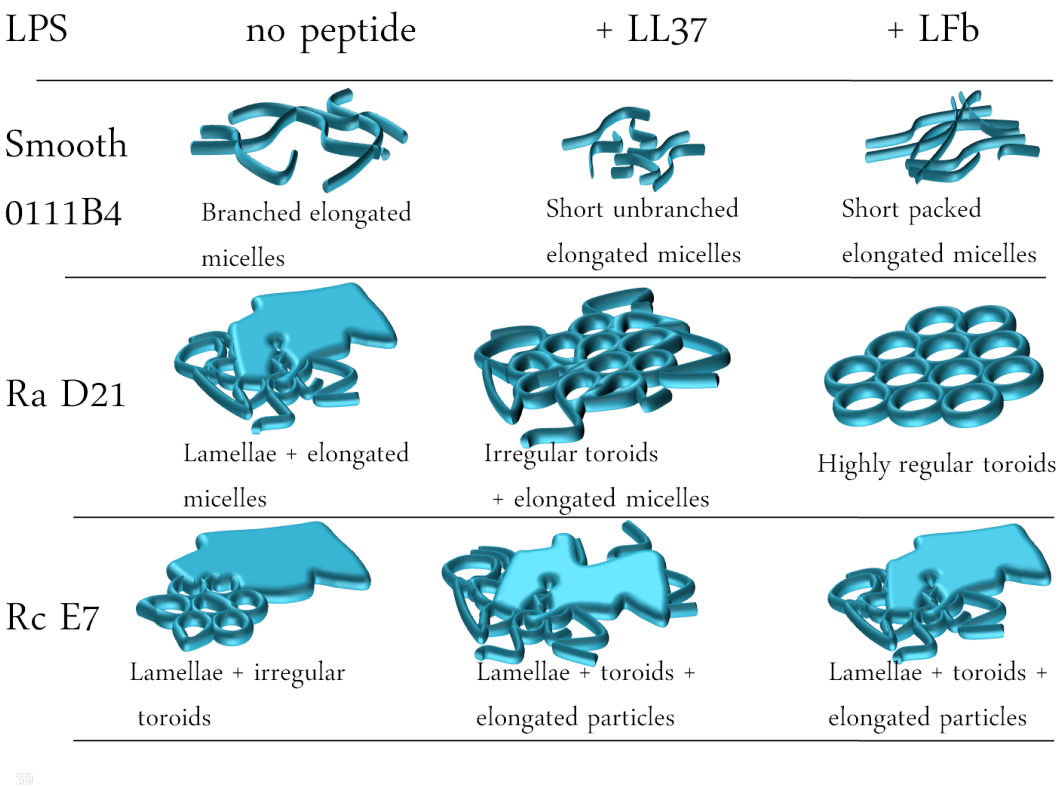

FIGURE 3.28: Representation of the aggregate structures formed by various LPS chemotypes and the effect of the peptides LL37 and LFb on the morphology of the aggregates.

3.4.1 LPS 0111B4 and peptides

Previous ff-TEM and cryo-TEM analysis of the LPS 055B5 smooth chemotype in PBS buffer solution containing only mono-valent cations reported the formation of spherical aggregates in solution [226, 243]. The effect of mono- and di-valent cations on the aggregates of LPS is different [25] therefore, considering the paucity of data regarding the structure of smooth LPS in the presence of divalent cations, the aggregation of smooth LPS 0111B4 was investigated in the presence of 1 mM

$MgCl_2$. Cryo-TEM of LPS 0111B4 showed the formation of worm-like micelles with wide inter-particle distances. The SANS data analyzed by the Kratky approximation for elongated particles confirmed the presence of worm-like micelles.

Despite the changes observed from the TEM, the neutron scattering data suggest a minimal effect of both peptides on the aggregates of LPS 0111B4 (Figure 3.28). The electrostatic attraction between CAP and the negative charges present on lipid or LPS headgroups (specifically the phosphates present in the core oligosaccharide and lipid A of the endotoxin) is the dominant driving force of the interaction [183], but in the case of the smooth LPS 0111B4, these negative charges are shielded by the LPS O-antigen chains. Recent investigations on the interaction between the α-helical antimicrobial peptide magainin and liposomes made of mixed hDPPC , dipalmitoylphosphatidylglycerol (DPPG) and the negatively charged ganglioside molecule (GM1), showed that the peptide is trapped into the sugar region of GM1, which might resemble the core region of LPS with its negative charges [244]. The presence of a long polymeric chain such as the O-antigen of LPS shields the negative charges in the core oligosaccharide and the lipid-A from the cationic peptides. Previous evidence suggests that the steric hindrance of large polymeric headgroups such as the one of poly(ethylene glycol) (PEG), reduces the fibrinogen protein interaction with mixed liposomes made of several lipids (zwitterionic and negatively charged) and pegylated phosphatidylethanolamine [245]. It may therefore be assumed that most of the interaction of the peptides LL37 and LFb is concentrated on the O-antigen part of the LPS molecule resulting in a lower penetration of the peptides in the innermost core of the micelles. This would be consistent with the protective role of the O-antigen oligosaccharidic headgroup of LPS on the outer membrane of the bacteria where the charged groups, which the peptides would be expected to interact with, are buried in the core of the LPS headgroup and the peptides are sterically hindered from access by the long oligosaccharidic chains. The SANS technique is more sensitive to changes in the core region of the micelles therefore the lack of modifications to the scattering pattern upon addition of the peptides suggests that both LL37 and LFb are not penetrating the O-antigen barrier of LPS thus are not allowed to bind to the negatively charged phosphates on the core region and the lipid-A headgroup of the LPS. In addition, the unmodified values of mass per unit length obtained from the analysis of LPS 0111B4 SANS data even in the presence of the peptides, suggests that there is no modification of the packing of the micelles, hence no interaction with the innermost part of

the particles. The packing effect induced by both peptides on LPS 0111B4 aggregates reported by cryo-TEM could be the result of the modifications caused to the outermost hydrophilic region of the particle. The peptides interacting with the O-antigen region, induce the collapse of the oligosaccharidic chains and therefore the steric repulsion between different micelles, resulting in smaller spaces between the micelles and their consequent tighter packing.

3.4.2 LPS D21 and peptides

The Cryo-TEMs of LPS D21 at a concentration of 6 mg/ml in saline solution containing 1 mM $MgCl_2$ at 37°C show the formation of very complex lamellar structures in agreement with the negative stain TEM performed by Coughlin, Haug and McGroarty on the same LPS D21 Ra chemotype [57]. More recently Richter *et al.* [227] found that Ra LPS from *S. minnesota* R60 in 20 mM HEPES buffer, analyzed by ff-TEM and cryo-TEM, forms elongated fibrilles made up by two tightly packed bilayers. The apparent discrepancy between the data reported in the current study and those reported by Richter *et al.* can be explained by the tendency of Mg^{2+} to induce a higher order state of Ra LPS and an increase in the "lamellarity" of the aggregates [56].
The analysis of SANS data for the dilution of LPS D21 confirmed the presence of lamellar structures (Figure 3.28), the thickness of which is not affected by LPS concentration. The formation of fringes in the scattering curve at higher LPS concentration, suggests that the lamellae are becoming more ordered and rigid in response to increasing concentrations of LPS.
The addition of LL37 peptide to the LPS D21 at the concentration of 6 mg/mL in the presence of 1mM $MgCl_2$, caused the formation of elongated particles, closing up into packed irregular toroids as shown by cryo-TEM micrographs (Figure 3.28). A consistent result in terms of radii values of the elongated particles was obtained from the Kratky approximation of the SANS data set. The number of LPS molecules per unit length of the micelles decreases upon addition of LL37 , suggesting that the peptide acts on the innermost core oligosaccharide region of the LPS D21, and possibly on the lipid-A region as well, affecting its packing within the aggregate and probably displacing LPS molecules. The Kholodenko worm-like micelle model fit of the SANS data in the presence of LL37 suggests the formation of elongated objects composed by numerous segments of 100-110 Å in

length, each of which has radius values in agreement with those obtained from the TEM micrographs. The elongated structures formed by LPS D21 in the presence of LL37 may be rather flexible and the forming chains may close up into irregularly shaped toroids, as seen from the cryo-TEM micrographs.

LPS D21 treated with LFb peptide forms tightly packed, extremely regular toroids which resemble a bilayer perforated by pores (Figure 3.28). Such a complex system could not be analyzed, as with the previous samples, as a flexible micelle model therefore a better description of this structure might be given through the approximation of the system as a bilayer. The Guinier approximation of the SANS reports a little increase in the bilayer thickness upon the addition of LFb peptide, evidence corroborated by the data fitting with the monodisperse sheet shell/-core/shell model. The model shows that most of the changes in thickness induced by LFb occur at the shell level which decreases upon addition of the peptide. Less consistent conclusions can be drawn when observing the core thickness of the bilayer, which decreases at the lower peptide concentration and increases again at the highest LFb concentration, in comparison to the untreated LPS E7.

Previous investigations showed that LFb peptide partitions into the lipid bilayer in the presence of negatively charged lipids [128, 246] but at a physiological membrane lateral pressure (*i.e.* 30 mN/m [165]), as could be expected in the aggregates of Ra LPS, the peptide does not partition into the bilayer but lays parallel at the bulk solvent/lipid interface [127], as suggested by the experiments reported in this thesis as well (Chapter 2). As proposed by Ulvatne *et al.* [130] LFb has no penetrating properties on the cytoplasmic membrane of the bacteria but acts on the surface of the membrane depolarizing it and causing the bilayer to curl on itself. The regular structures observed in the cryo-TEM micrographs formed by LPS D21/LFb could be the result of the curling effect of the peptide on the LPS D21 lamellae.

It is clear that the removal of the O-antigen and the exposure of the negatively charged phosphate groups in the heptose level of the core region and in the lipid-A headgroup level of the LPS D21, allows for a stronger interaction of both peptides with the core part of the LPS aggregates. LL37 influences more than LFb the core of the objects, which corresponds to the hydrophobic part of the LPS structure (the lipid-A acyl chains). LL37 , as other peptides with an α-helical conformation, presents amphiphilic properties which allow for an effective interaction and a deep penetration into the lipid membranes [105, 247]. The ability of LL37 to partition effectively in monolayers and bilayers composed of LPS Ra is reported

in Chapter 2. The drastic change of morphology of LPS D21 lamellae into elongated micelles/toroids could be due to the effect of LL37 on the critical packing parameter (CPP) of the LPS aggregates as a result of a deeper interaction. The change in the aggregation number observed from the SANS data induced by LL37 , suggests that the peptide modifies the curvature of the bilayer, an effect that has already been shown by the α-helical peptide magainin [248] on model membranes. It may be assumed that the cylindrical molecular shape of the untreated LPS D21 in the bilayer ($CPP \sim 1$) has been extensively modified to a conical shape ($1/3 < CPP < 1/2$) which favors the formation of elongated micelles. On the other hand the weaker interaction of the peptide LFb with the bilayer formed by LPS D21, could not modify broadly the critical packing parameter of the LPS. This resulted in LPS maintaining its cylindrical molecular shape with exception of areas, probably at high peptide concentrations, in which the bilayer is curved, or curled, into pore-like structures due to a local modification of the CPP of LPS.

3.4.3 LPS E7 and peptides

The cryo-TEM micrographs for LPS E7 in solution at the concentration of 6 mg/ml in the presence of 1 mM $MgCl_2$ show the formation of complex lamellar structures with some areas characterized by toroids (Figure 3.28). Former cryo-TEM analysis Rc LPS from *S. minnesota* in HEPES buffer reported the formation of elongated particles [228] while more recent ff-TEM investigations of the same system suggest the presence of spherical liposomes and planar bilayers [227]. The latter findings and the data presented in this chapter are supported by X-ray diffraction of Rc LPS from *S. minnesota* in the presence of Mg^{2+} [56]. The Kratky approximation and the data model fitting as monodisperse sheet shell/core/shell of the SANS data for the LPS E7 dilution experiment show no concentration effect on the lamellar structures formed by the LPS. The high values of the $R\sigma$ describes a system without a rigid geometry, probably due to lamellae placed very far away, or due to a heterogeneous population of lamellae or due to high undulation of the bilayers, which results in the smoothing of any long-range structure between the lamellae and therefore the absence of fringes in the scattering curves.

The cryo-TEM micrographs for LPS E7 with LL37 peptide suggest the formation of a mixed population of lamellae, toroids and worm-like micelles (Figure 3.28). The SANS data set for LPS E7/LL37 samples were analyzed as lamellar structure

through the Guinier approximation and data modelling monodisperse sheet shell/core/shell revealing that LL37 affects the shell thickness rather than the core of the aggregates. Despite the heterogeneous population of structures observed at the higher LL37 concentration, the value of $R\sigma$ suggests a controversial increase of the order of the system, confirmed by the appearance of fringes in the scattering curve, which had no explanation.The same SANS data set analyzed as worm-like micelles reports the formation of elongated objects with no detectable changes in the number of molecules per unit length. The elongated particles seem to be be formed by a high number of very short segments suggesting the presence of very flexible structures which easily can close up into toroids. The thickness of the lamellae shell of the untreated LPS E7 is comparable to the shell thickness of the worm-like micelles but most of the modifications occurred at the core level, reporting a radius of the micelle which is almost half of the lamellae core thickness. The addition of LFb peptide to the aggregates of LPS E7 caused similar morphological changes as seen for the addition of LL37 by the observation of the cryo-TEM micrographs (Figure 3.28). As for the previous case, the SANS data were analyzed both as lamellae and elongated particles. LFb induced a general decrease in the lamellae thickness but interestingly the lowest LFb concentration (LPS/peptide ratio of 50/1) has a bigger impact than the 10/1 ratio when the values of t_c and t_s are compared. This unexpected result might be due to the limitation of the model when it comes to analysis of such a complex system. The analysis of LPS E7 challenged by the LFb peptide as elongated objects revealed that increasing concentrations of peptide do not affect the radius and the mass per unit length of the particles.

Both LL37 and LFb peptides interact with the aggregates of LPS E7 to such an extent that the system became extremely complex and the intricacy data interpretation reflects such complexity. The inhomogeneity of the aggregates formed did not allow for a defined and precise analysis of the SANS data. What is clear is that the removal of the steric shielding of part of the core of LPS and the phosphates at the heptose level allows for a deeper interaction of the peptides with the negatively charged phospahte groups at the lipid-A level of the LPS E7. This deeper interaction of both peptides resulted in the modification of the innermost part of LPS E7 aggregates culminating in mixed complex structures. The higher number of LPS E7 molecules in the samples, compared to the experiments carried out with LPS 0111B4 and D21, may result in the sequestration of the peptide in areas in which the peptides could exert their activity, and other areas

in which there is a limited presence or total absence of peptide, explaining the lack of uniformity of the samples. In those area of peptides' activity the extent of the modification induced by LL37 is qualitatively comparable to the case of LPS D21. The peptide LL37 already proved to interact efficiently with the LPS D21 aggregates and the removal of part of the core oligosaccharide, as in the LPS E7, allowed for a stronger modification of the packing parameter of LPS resulting in defined elongated structures and toroids. On the other hand LFb induced different morphologies (elongated structures) on LPS E7 aggregates when compared to the LPS D21 case (pore-like structures in a bilayer of LPS). This could be explained by the absence of the phosphate groups in the heptose level of the core of LPS E7, which allowed the peptide LFb to partition more effectively into the aggregate, acting directly with the negatively charged groups of the lipid-A region and perhaps interacting with the hydrophobic chain region as well . This deeper interaction resulted in a stronger curvature effect on the LPS E7 bilayer, resulting in the formation of elongated micelles favored by a change in the LPS E7 molecular shape to a CPP value of $1/3 < CPP < 1/2$.

3.5 Conclusion

The data presented in this chapter show that LL37 and LFb peptide are not able to modify the aggregates of smooth LPS 011B4 due to the steric shielding of the O-antigen part of the LPS molecule. The removal of such a barrier, as seen on the data set for LPS D21, allowed a stronger interaction of the peptides with the LPS aggregates. LPS D21 retains some shielding properties due to the core oligosaccharidic region of LPS therefore LL37 is more effective than LFb peptide in the modification of the core of the aggregates most likely due to its propitious physico-chemical properties. The further removal of some of the core LPS shielding as in the case of LPS E7, uniformed the effect of LL37 and LFb which produced a comparable modification. Considering the theory of the conformational concept of endotoxicity [84], both peptides failed to modify the aggregates of smooth, Ra and Rc LPS from *E. coli* K12 into a lamellar, less toxic form, as reported previously for other peptides [207, 215, 228, 249]. LL37 could exert its anti-endotoxic role with different mechanisms of action than the modification of the morphology of LPS aggregates as speculated in previous investigations: it can reduce the recognition of LPS aggregates by the LBP and other mediators of the immune system [250] and

it can decrease the cell activation induced by LPS acting as an immunonodulatory molecule [152, 251]. Previous studies on peptides with a β-sheet conformation [135, 252] showed the potential of such molecules as interacting agents with LPS. Peptides derived from human LF [207] are able to reduce LPS toxicity inducing the lamellarization of the aggregates. The data presented in this chapter suggest that LFb does not reduce LPS toxicity through the lamellarization of the aggregates and its anti-endotoxic role [221] could be the result of the interaction and sequestration of LPS molecules as speculated in previous investigations [129, 222].

Chapter 4

Interaction of LL37 and LFb peptides with monolayers and bilayers composed of DPPC and Lipopolysaccharide.

4.1 Introduction.

The OM of Gram negative bacteria is an asymmetric bilayer, the external leaflet of which is mainly composed of lipopolysaccharide (LPS). The outer membrane gives structure and stability to the whole bacterial cell and is the first line of defence against environmental perturbations (*e.g.* unfavorable temperature, ionic strength, pH), competitive microorganisms and, in the case of symbiotic bacteria, defence against host defense immune system reaction. The protective role of the OM affects also the microbicidal activity of antibiotic drugs used in the treatment of bacterial infections in humans (Section 1.2). The consequences of a reduced susceptibility of Gram negative bacteria to common treatments promoted the investigations of new, more efficient antiseptic molecules [94, 253]. For this reason particular attention has been given to the class of cationic antimicrobial peptides (CAPs) as possible therapeutics or adjuvant treatments for highly resistant microbial infections [95].

In this chapter the interaction of the antimicrobial peptides LL37 and LFb and monolayers and asymmetric bilayers composed of mixtures of hDPPC and the Ra

LPS EH100 or the Rc LPS J5 was investigated. Despite not being a natural membrane component, the introduction in the mixture of the zwitterionic hDPPC lipid, which presents two saturated acyl chains with a T_m of 41°C [254], allowed the stabilization of LPS liposomes and it was chosen in the light of the relative low interaction of CAPs with membranes composed of lipids which are in the gel phase state and have a neutral headgroup charge at physiological pH and temperature [121, 183, 255]. Exploiting the theoretical noninterference of hDPPC , the studies are focused on the role of different LPSs on the structure of the outer membrane and the interaction with CAPs, by the use of biophysical techniques. The diversity of the active conformations adopted by the peptides LL37 and LFb would shed light on the different putative mechanisms of action of CAPs which have shown binding properties towards bacterial endotoxins [129, 152, 207, 222] and Gram negative bacterial membranes [130, 144]. The ordered structure of D_{62}DPPC within a lipid membrane allows the highlighting of the role of LPS molecules in the packing of the bilayer, thus identifying the structural role of the endotoxin in the cytoplasmic membrane of the bacteria.

Both monolayers and bilayers are used to study different aspects of the peptide-LPS interaction. The Langmuir Blodgett (LB) technique is used to study the physico-chemical properties of the mixed monolayers of amphiphiles at the air-water interface and their interaction with the antimicrobial peptides of choice, implemented with NR experiments of the same monolayers at the air-water interface and asymmetric bilayers supported by a silicon crystal. The subphase injection of amphiphiles below lipid monolayers at the air/liquid interface is a good method to study the CAP/LPS interaction because it resembles the biological membranes [165, 172, 256] and is well suited for NR experiments (Section 4.3.4). In consideration of the fact that the Gram negative bacterial outer membrane is an asymmetric bilayer in which the outer leaflet is composed almost exclusively of LPS (Section 1.2) this study reports NR investigations on asymmetrical bilayers, supported by silicon crystals, consisting of an inner leaflet of hDPPC and an outer leaflet of either the Rc LPS J5 or the Ra LPS EH100 (Section 4.3.5). Recently the very same system has been investigated by Clifton et. al. [161] which suggested further interaction studies with antimicrobial peptides and DPPC/LPS asymmetric bilayers to study the permealizing activity of CAPs on the OM of the bacteria. The experiments presented in this study are focused on such an aim and bilayers composed of either Ra LPS EH100 or Rc LPS J5 and DPPC were challenged by

the antimicrobial peptides LL37 and LFb to shed light on the mechanism of interaction of CAPs with membrane models containing LPS.
In addition, tryptophan fluorescence spectroscopy experiments carried out on vesicles containing mixtures of hDPPC and either Rc LPS J5 or Ra LPS EH100 is used to compare the depth of the bilayer penetration by the peptides in relation to their physico-chemical properties, in order to understand how the binding activity of CAPs with different conformations is affected by the structure of LPS. The same lipid/LPS mixtures were analyzed by solid state ^{2}H NMR in order to examine the contribution of the two LPS chemotypes on the packing of the bilayer, and the effect of the interaction of the peptides on the chain order of the vesicles.

4.2 Materials and methods

4.2.1 Materials

Rc LPS from *E. coli* J5 (purity: protein 1.4%, nucleic acid 0.340%, phosphate 7.3%, Kdo 5.9%), was obtained from Merck KGaA (Darmstadt, Germany) and was used without further purification. LPS from *E. coli* EH100 was obtained from Sigma-Aldrich Ltd. (Dorset, UK) and used after purification following the method described in Section 3.2.2. Deuterium oxide D_2O 99.990 atom % D, L-tryptophan and $MgCl_2$ anhydrous were also obtained from Sigma Aldrich Ltd. The lipids hDPPC andD_{62}DPPC were obtained from Avanti Polar Lipids (Alabaster, USA) and used without further purification. Chloroform and methanol were obtained from Fisher Scientific (Loughborough, UK). Ethanol 99% was obtained from VWR International (Lutterworth, UK). All the organic solvent used were of analytical grade or better. The ultrapure water at 18.2 MΩ·cm was produced by a Purelab Ultra machine from ELGA Process Water (Marlow, UK). Whatman chromatographic paper No.1 from Merck KGaA (Darmstadt, Germany) was used to produce the Wilhelmy plates used for monolayer surface pressure measurements. Details of the peptides LL37 and LFb are reported in Appendix B.

4.2.2 Tryptophan fluorescence measurements.

Liposomes were prepared containing the same formulations of hDPPC and LPS used in the LB experiments (Section 4.2.4) according to the formulations reported

in Table 4.1. The vesicles composed of pure hDPPC will henceforth be referred to as DPPC, those with a composition of 20% Rc LPS J5 and 80% hDPPC (molar ratio) will be named J5-20 whereas those composed of 20% Ra LPS EH100 and 80% hDPPC (molar ratio) will be referred to as Eh-20.

TABLE 4.1: Composition of the lipid/LPS mixtures used in the Langmuir-Blodgett experiments and tryptophan fluorescence experiments.

Monolayer ID	Description[i]
PC	pure hDPPC
Eh-20	20% EH100 - 80% hDPPC
J5-20	20% J5 - 80% hDPPC
lipid A-2Kdo-20	20% lipid A-2Kdo- 80% hDPPC

[i] for all the mixtures the components' ratio is expressed in molar percentage.

The thin lipid film hydration method was used to produce the liposomes [257] whereby the lipid components were mixed in chloroform, according to the required formulation, in a 5 mL round bottomed flask. The organic suspension was bath-sonicated at room temperature with an Elmasonic P ultrasonic bath (Elma Hans Schmidbauer GmbH & Co. KG, Singen, Germany) to ensure the homogenization of the lipids. The chloroform was removed through the use of a Buchi rotovapor system R-210 (Buchi Labortechnik AG, Flawill, Switzerland) connected to a KNF Lab Neuberger Laboport Diaphragm Vacuum Pump UN840.3 FTP (KNF Neuberger UK, Witney, UK) and equipped with a Buchi waterbath at 40°C . The dry thin film produced by solvent evaporation was rehydrated in an aqueous buffer containing 10 mM Tris pH 7.4, 1 mM $MgCl_2$ to ensure a final lipid concentration of 500 μM and was vortex mixed followed by 10 minutes of bath-sonication at room temperature until the entire film was detached from the sides of the flask. The resultant lipid suspension was sonicated for 30 minutes with a Soniprobe model 7535A (Lucas Dawe Ultrasonics, London, UK) in an ice bath to prevent over-heating of the sample.

The static tryptophan fluorescence measurements were recorded at 37°C in a 10 mm × 4 mm dual path length cell (Hellma analytics, Mllheim, Germany) with a Cary Eclipse spectrofluorimeter (Varian Ltd, Oxford, UK) equipped with a

temperature-controlled water bath, allowing for 5 minutes of temperature equilibration before data acquisition. The tryptophans were excited with a monochromated incident beam at 290 nm wavelegnth and the emission spectrum was recorded between 300 nm and 450 nm, averaging 5 measurements for each sample. Each liposome formulation at a concentration of 500 μM was challenged with 5 μM (lipid/peptide ratio 100/1) and 10 μM (ratio 50/1) of either LL37 or LFb , which was allowed to interact for 5 minutes prior to data acquisition. Correction measurements were employed in order to compensate for the effect of light scattering by the vesicles [179] which affects the intensity of the fluorescence emission from the Trp residues. The correction involves the measurement of the emission from a solution of the amino acid L-tryptophan in buffer (I_{trp}) and in the presence of the vesicles (I_{trpV}) at a concentration equal to the molarity of Trp present in the relevant samples with the peptides. The background spectra of samples containing only vesicles (I_V) were subtracted from the emission spectra of samples with vesicles, giving the fluorescence intensities of the samples containing either the peptides (I_{pepV}) or L-Tryptophan (L-Trp) (I_{trpV}) only. The corrected value for the fluorescence of the peptide (I_{pepC}) was calculated according to the equation

$$I_{pepC} = \frac{I_{trp}}{I_{trpV}} \cdot I_{pepV} \tag{4.1}$$

where I_{trp} is the intensity of the L-Trp without vesicles, I_{trpV} is the emission of L-Trp with then vesicles and I_{pepV} is the emission of the peptides with vesicles. The influence of any inner-filter effect was avoided by adjusting the concentration of fluorophore in order to maintain an optical density below O.D. 0.05 [179]. The tryptophan fluorescence intensity was plotted against the wavelength of the emission (range 300-400 nm) to produce the fluorescence spectrum. From the same spectrum it was possible to estimate the depth of the insertion through the blue shift (hypsochromic shift) of the emission by following the wavelength and the intensity of the maximum emission peak [179]. The emission peak wavelength was calculated through the maximum intensity of the emission curve by the software Spekwin32 [258].

4.2.3 Solid state ^{2}H NMR measurements.

The lipid/LPS mixtures used to produce the multilamellar liposomes for the ^{2}H NMR experiments contained 30 or 40% D_{62}DPPC in lieu of the equivalent amount of hDPPC . The various liposome mixtures used in these experiments are reported in Table 4.2 with their appropriate acronyms, and these were designed to match the formulations used for the tryptophan fluorescence experiments and the LB monolayer at the air-water interface experiments to maintain consistency across all the techniques. A total of 4 mg of each lipid and LPSs mixture was prepared

Table 4.2: Composition of the LPS-lipid mixtures used in the solid state NMR experiments.

Liposome mix ID	Composition (% molar ratio)
DPPC	60% hDPPC - 40% D_{62}DPPC
Eh-20	20% EH100 - 30% D_{62}DPPC - 50% hDPPC
J5-20	20% J5 - 30% D_{62}DPPC - 50% hDPPC

according to the formulations reported above (Table 4.2), by combining stock solutions of each pure lipid dissolved in chloroform at known concentration in a 25 mL round bottomed flask. Where necessary, at the mixing stage, the peptides were added to the lipid mixture solutions at a final lipid/peptide molar ratios of 50:1 or 100:1, from solutions prepared in ethanol . The organic solvents were evaporated to form a thin film using the same methodology described in Section 4.2.2. The flask containing the thin film was placed overnight (minimum 12 hours) under vacuum in a dessicator chamber to ensure that all the chloroform and ethanol were removed from the thin film. The dry lipid/LPS and lipid/LPS/peptide films were resuspended in 4 mL of 10 mM TRIS, 1 mM $MgCl_2$, pH 7.4 buffer to give a final total lipid concentration of 1 mg/mL. At this stage, to ensure the complete resuspension of the thin film, the flasks were placed at room temperature in an Elmasonic P ultrasonic bath (Elma Hans Schmidbauer GmbH & Co. KG, Singen, Germany) for 10 minutes. In order to produce multilamellar vesicles the lipid suspension was subjected to 5 cycles of freeze/thawing by the use of liquid nitrogen followed by immersion in a water bath at 40°C . The suspension was transferred into centrifuge tubes and centrifuged at 15000 g for 30 min with a Heraeus Biofuge Pico (Thermo Scientific, UK) to obtain a dense white pellet containing the vesicles.

The pellets were transferred in a Bruker 4 mm MAS rotor. ^{2}H quadruple echo

experiments on a Bruker advance 400 NMR spectrometer were performed at 61.46 MHz using a 4 mm MAS probe. The spectral width of 100 KHz was used with recycle delay of 0.25 s, echo delay of 100 μs, acquisition time of 2.6 ms and 90°C pulse lengths 3 μs. Experiments were performed at 45°C which is above the hDPPC phase transition temperature of the lipids and LPSs, to ensure that the acyl chains were in the fluid phase. Spectra were symmetrized and dePaked by the Amix software (Bruker) using mixed Gaussian-Lorentian fitting to determine the quadrupolar splittings [187] and then fitted with the software PeakFit (fitting r^2>0.997) to obtain the S_{CD} plotted against the carbon number in the chain [194].

4.2.4 Langmuir-Blodgett monolayers at the air-liquid interface

$P - Area$ isotherms measurements were carried out at the temperature of 22 $\pm$ 3°C on a Nima Langmuir trough 602A (Nima Technologies Ltd., Coventry, UK) fitted with a Nima PS4 surface pressure microbalance (0-240 mN/m range, 0.1 mN/m resolution) controlled by a PC equipped with the Nima IU4 computer interface unit software. The microbalance was calibrated with a 10 mg standard weight and the area enclosed by the barriers was calibrated. Prior to use, the PTFE surface of the trough was extensively cleaned with ethanol and chloroform in order to remove any impurities. A clean Whilelmy plate made of Whatman Grade 1 chromatography paper, 1cm width (GE Healthcare life sciences UK, Little Chalfont, UK) was attached to the microbalance and dipped into the subphase made of a 1 mM $MgCl_2$ solution in ultrapure water. The subphase surface was cleaned of dust and contaminants prior the experiment, by repeated compression of the barriers and suction of the surface using a glass pipette attached to a vacuum pump. The subphase was considered clean when, upon compression, the surface pressure would not exceed 0.2 mN/m.

The pure lipid or lipid/LPS mixtures were reconstituted by sonication in pure chloroform at a total concentration of 1 mg/mL producing a homogeneous suspension. For each isotherm, approximately 70 μL of lipid suspension was added dropwise to the subphase surface using a Hamilton syringe (Hamilton Co. Europe, Bonaduz, Switzerland), with the barriers open at their maximum. Ten minutes were allowed for the solvent to evaporate, then the barriers were closed at a constant rate of 35 cm^2/min while the changes in surface pressure were constantly recorded and the

monolayer was compressed until its collapse point was reached.
The limiting molecular area for each monolayer was calculated from the $P - Area$ isotherm from the intercept on the X-axis of the tangent to the curve at the pressure of 30 mN/m, as reported in Section 1.4.5. Since the monolayers were formed by mixtures of lipids and LPSs, the additive area per molecule rule was employed according to the equation

$$A_{tot} = A_1 \cdot N_1 + A_2 \cdot N_2 + A_n \cdot N_n \ldots \tag{4.2}$$

where A_{tot} is the area per molecule of the mix whilst A_n and N_n are respectively the area per molecule and the molar ratio of each single component within the mixture. Table 4.1 reports the acronyms used in this experiment for each monolayer and their composition in mixed monolayers, where the ratio between the components is expressed in molar percentage.

4.2.4.1 Brewster angle microscopy.

A direct qualitative analysis of the macroscopic properties of a film at the air-water interface can be addressed with the Brewster angle microscopy (BAM) microscopy technique. The BAM technique exploits the property of interfaces (gas, liquids and solid) to reflect and refract an incident beam of polarized radiation according to the refractive index and the angle formed between the surface normal and the incoming radiation for each interface. The system composed of a lipid film spread on a water subphase, is a system consisting of three different layers, *i.e.* air, lipid film and water, each of them having different refractive indexes. A polarized He-Ne Laser hitting a LB monolayer at the Brewster angle would be reflected and captured by a CCD detector pointed toward the surface, specular to the incident beam. The incident polarized laser beam that hits a clean water surface will be reflected differently if a monolayer is present at the interface because the monolayer changes the reflectivity of the interface. The maximum change in reflectivity happens when the laser beam is at the Brewster angle θ_B calculated to be approximately 53° from the normal of the surface for the air-water interface [259] according to the equation:

$$\theta_B = arctan \frac{n_1}{n_2} \tag{4.3}$$

where n_1 and n_2 are the refractive indexes of the different media (air and water) that the light propagates through. If the lipid monolayer is in a coexistence state between two phases (*e.g.* the gas and liquid phases) these two phases would have different reflectivities. The image that the CCD camera produces might have brighter regions formed by lipid in a denser phase such as liquid-condensed or solid phases, and darker regions consisting of less dense phases such as those in the gas or liquid-expanded phases. A homogeneous image without domains or patches corresponds to a homogenous phase monolayer in a uniform ordered state. The BAM measurements were performed at the Soft Matter facility at the *Institut Laue-Langevine* (ILL) by the use of a custom made BAM apparatus fitted on a Nima/KSV Spot LB trough (Nima/KSV Ltd., Espoo, Finland). The monolayers were spread according to the methodology described in the previous section (Section 4.2.4).

The BAM technique has been extensively used in order to study monolayers of lipids [260–262] as well as monolayer composed of Rc LPS from *E. coli* [21] qualitatively and to investigate the insertion of proteins into films [263, 264]. This technique would help the characterization of the LB isotherms in terms of attractive/repulsive forces between the molecules in the film. The visualization of the domains of a lipid monolayer would shed light on the effect of exogenous components, *i.e.* LPS, on the packing behavior of a well characterized film of hDPPC .

.

4.2.4.2 Interaction studies of LL37 and LFb peptides and the mixed DPPC/LPS monolayers.

A variation of the LB trough technique was used to investigate the interaction of the peptides LL37 and LFb and the mixed monolayers hDPPC /LPS described above (Table 4.1). The experiment was performed at 22°C using the Nima PS4 surface pressure microbalance with a 50 mm diameter Petri dish made out of fluorinated ethylene propylene (FEP) (Welch fluorocarbon Inc., Dover, UK) and placed over a magnetic stirring plate. The Petri dish was filled with filtered ultrapure water containing 1 mM $MgCl_2$ giving a final subphase volume of 15 mL. A small magnetic stirrer was placed into the subphase into which a Whilelmy plate attached to the pressure sensor was dipped. A small disposable plastic syringe of 1

mL volume (BD biosciences UK, Oxford, UK) containing a solution of 250 μg/mL of peptide was clamped into a stand close to the dish and the gauge inserted into the subphase below the surface. The surface was cleaned from contaminants by suction with a vacuum pump and the mixtures of LPS and lipid in chloroform was spread dropwise on the subphase until a surface pressure of approximately 32 mN/m was reached. The surface pressure was recorded at constant slow stirring of the subphase, with the magnet speed set at its minimum in order to avoid a variation of pressure greater than 0.2 mN/m. The monolayer was allowed to equilibrate until it reached a plateau before carefully injecting 100 μL of peptide solution into the subphase. The change in pressure was plotted against time and the binding isotherms produced were fitted with a simple exponential equation $y = A(1 - e^{-k(x)})$ to obtain kinetics parameters for A the maximum change in pressure and k the rate of pressure increase.

4.2.5 Neutron reflectivity of mixed LPS/DPPC monolayers at the air/liquid interface and their interaction with antimicrobial peptides.

The NR measurements were carried out on mixed monolayers composed of the LPS chemotypes Rc J5 or Ra EH100 and hydrogenated hDPPC or tail-deuterated D_{62}DPPC described in Table 4.3 spread onto a water subphase containing 1 mM $MgCl_2$ at 22°C , before and after the subphase injection of the peptides LL37 or LFb , were performed on the FIGARO beam line at the ILL high-flux reactor in Grenoble (France). A reduced area custom-made Teflon® Langmuir trough (50 mL subphase volume) was placed on an active anti-vibration movable table for which the height could be controlled by the user or automatically set up by the instrument. The alignment of the instrument beam and the detector was achieved by the use of a laser hitting the subphase; the same laser was used during the NR experiment to automatically align the beam to the interface. The incoming neutron beam had a wavelength between 2 Å and 30 Å and grazed the subphase from above. The specularly reflected beam was collected by a movable two dimensional detector.

The mixed monolayers under study contained either hDPPC or D_{62}DPPC depending upon the desired isotopic contrast, and the relative acronyms for each monolayer

Table 4.3: Composition of the lipid/LPS mixtures used in the NR air/liquid interface monolayer experiments.

Monolayer ID	Description[i]
Eh-20	20% EH100 - 80% hDPPC
J5-20	20% J5 - 80% hDPPC
d-Eh-20	20% EH100 - 80% D_{62}DPPC
d-J5-20	20% J5 - 80% D_{62}DPPC

[i] for all the mixtures the components' ratio is expressed in molar percentage.

used during the experiments are reported in Table 4.3. The tail deuterated DPPC was mixed with the LPS chemotypes to be used with either D_2O or ACMW (8% D_2O in water v/v) subphase in order to highlight the properties of the hydrogenated headgroups and the hydrophobic region of the monolayers, respectively. The hydrogenated DPPC was used on D_2O subphase to focus on the properties of the whole monolayer. Both D_2O and ACMW subphases always contained 1 mM $MgCl_2$.

The monolayer mixtures were suspended in chloroform after extensive sonication in a Elmasonic P ultrasonic bath (Elma Hans Schmidbauer GmbH & Co. KG, Singen, Germany) and were spread on a clean subphase free of contaminants (see Section 4.2.4) using a Hamilton syringe (Hamilton Co. Europe, Bonaduz, Switzerland). The chloroform was allowed to evaporate for 10 minutes and the barrier were closed at a constant rate of 15 cm^2/min in order to compress the monolayer until the lateral pressure of 30 mN/m was reached. The barriers were then kept fixed at a constant area and the monolayer was allowed to equilibrate and reach a stable pressure, determined by the formation of a plateau on the $P - Area$ isotherm (Figure 4.1). A concentrated peptide solution of either LL37 or LFb was carefully injected into the subphase by the use of a small syringe to transfer a total amount of 300 μg of peptide into the subphase. The interaction between the peptides and the monolayer was allowed to progress until a surface pressure plateau was reached, as shown in Figure 4.1.

The acquisition of the NR spectra was performed during the plateau phases of the monolayers defined by the $P - Area$ isotherms and the reflectivity data was collected at two different angles to achieve the full Qz range. The NR profiles for each monolayer mixture with diverse isotopic contrast in the absence or presence

of either LL37 or LFb peptides were reduced and the data from the different contrast were simultaneously fitted with the RasCAL analysis software, the fitting being considered acceptable when the Chi-square value was lower than 60.

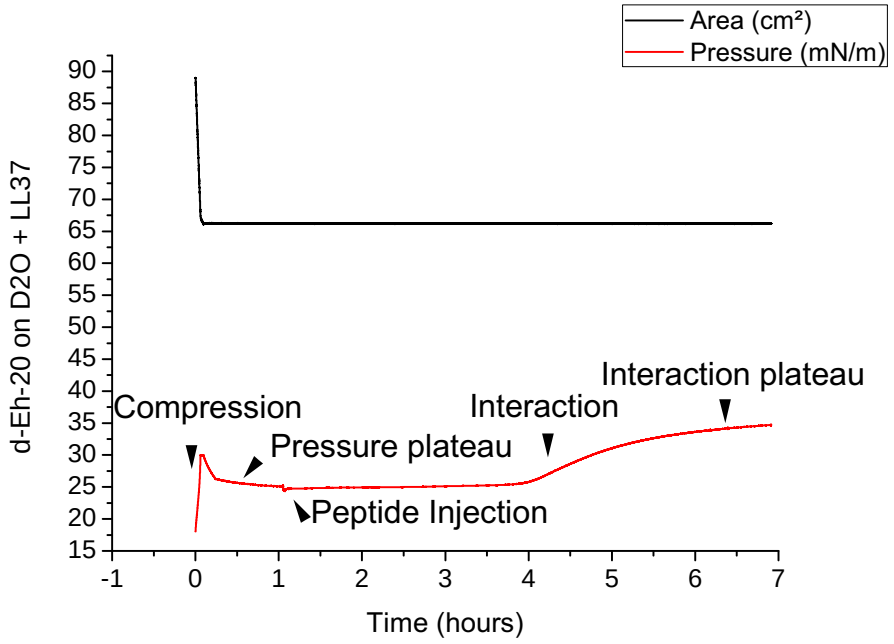

FIGURE 4.1: Isotherm of the monolayer d-Eh-20 on D_2O with the injection of the peptide LL37. The area and the pressure of the monolayer are reported over time.

The chain region was considered to be composed of the hydrophobic acyl chains only, whilst the inner headgroup was taken to be composed of the glucosamine (GlcN) and the Kdo residues of LPS together with the headgroup of hDPPC . The carbohydrates constituting the core of the LPS over the Kdo residues were considered to form the outer headgroup of the monolayer. Some additional parameters were implemented into the fitting program and kept constant, these included the amount of solvent present in the chain region, which was considered to be negligible, and the SLD of the fully hydrogenated and mixed hydrogenated/deuterated chains. The calculation of the total SLD of the chains considered the ratio between the lipid (D_{62}DPPC or hDPPC) and the hydrogenated LPSs (respectively 80 to 20, molar ratio) and their relative SLDs. It was found that the total SLDs of the fully hydrogenated and mixed H/D chain regions were respectively -1.34×10^{-7} and 6.10×10^{-6} $Å^{-2}$.

4.2.6 Neutron reflectivity of asymmetric bilayer of DPPC and LPS and interaction with antimicrobial peptides.

The Langmuir-Schaefer technique was used for the deposition of the bilayer on a clean polished silicon single-crystal block by the use of a LB Nima/KSV trough (Nima/KSV Ltd., Espoo, Finland). The block was submerged into the ultrapure water subphase containing 1mM $MgCl_2$ kept at 4°C and the water surface was cleaned thoroughly by suction to remove the superficial impurities. A monolayer of hDPPC was spread at the interface and compressed slowly to a constant surface pressure of 30 mN/m. The submerged silicon block was lifted through the air-water interface at a speed of 3 mm/min and the barrier of the trough were allowed to close in order to maintain the surface pressure at 30 mN/m (close to the natural membrane lateral pressure [165]). The silicon block, now covered with a homogeneous hDPPC layer with the headgroup adsorbed to the silicon block and the hydrophobic tails facing the environment, was attached to a holder above the water surface with the acyl chains pointed downward toward the interface. The surface was cleaned and a monolayer of LPS was spread until the surface pressure of 30 mN/m, which was kept constant. A built-in laser equipped device attached to the LB trough was used to level the surface of the crystal to make it parallel with the interface. The silicon block was lowered at a speed of 3 mm/min through the interface in order to allow the lipid monolayer on the block to match the LPS monolayer on the subphase via the hydrophobic chains, producing a bilayer. The block was then allowed to continue moving downwards until the bottom of the trough was reached where a customised sample cell made of PTFE was placed. The sample cell and silicon block were placed in a custom made metal holder to ensure the bilayer was fully contained and sealed inside the small water chamber of the sample cell, for which total volume was 3 mL.

The specular NR measurements were carried out using the CRISP instrument at the Rutherford Appleton Laboratory (Oxfordshire, UK) which utilizes a neutron beam wavelength λ from 0.5 to 6.4 Å to hit the sample at the incident angles θ of 0.35°C , 0.8°C and 1.8°C on a special adjustable anti-vibration table. The intensity of the reflected beam was measured as a function of the momentum transfer $Q_z = (4\pi sin\theta)/\lambda$ (Section 1.4.1). The sample holder was fitted with a L7100 HPLC pump (Hitachi/Merck, Germany) which allowed for the automated control of the exchange of the different isotopic contrast solvents and their flow, directly from the same software (OpenGENIE) used to run the command script

that controlled the CRISP instrument. For each isotopic contrast the reflectivity was measured after the bulk phase was equilibrated at the temperature of 37°C by the use of a Julabo water bath (Julabo GmbH, Seelbach, Germany) connected to the sample holder and controlled by the instrument's software. In the case of the experiments in the presence of LL37 and LFb , the peptides were dissolved directly into the bulk phase solvent to produce a solution with a concentration of 250 μg/mL and were injected into the sample cell's chamber and allowed to equilibrate for 30 minutes before data acquisition. During the experiments all the isotopically matched bulk phases contained 1 mM $MgCl_2$.

In order to highlight the different components of the hydrogenated bilayer of DPPC/LPS, the three different isotopic contrasts used were 100% D_2O , silicon matched water (SMW) (38% D_2O) and 100% H_2O , producing three different reflectivity profiles. The three contrasts allowed the determination of structural parameters of the layer model described in Figure 1.16 by the use of the reflectivity fitting software RasCAL, which simultaneously fitted the three different reflectivity profiles by the calculation of the common parameters obtained from datasets of multiple contrasts. The calculated SLDs for the subphases D_2O , SMW and H_2O were respectively 6.38×10^{-6} Å^{-2} , 2.08×10^{-6} Å^{-2} and -0.55×10^{-6} Å^{-2} . The limited number of contrasts used in this study did not allow a sensitive discrimination between the silicon oxide layer and the adjacent water layer hence the fitting model considered those two layers as a single layer named oxide layer, the parameters of which were determined by the best fit produced by the software. The best fits allowed the calculation of the parameters of the inner headgroup, tails and outer headgroup layers, as well as the bilayer roughness which considers the imperfections of the surface of the bilayer. The tail SLD value for the bilayers in the absence of peptides was kept constant at -3.9×10^{-7} Å^{-2} as previously calculated [265] whereas the percent of tail hydration was calculated from the fitting. The values of the SLD of the inner and outer headgroup layers were calculated separately for each contrast applied by the fitting software. For each layer, the thickness was calculated in order to determine any structural changes induced by the presence of the peptides.

4.3 Results

4.3.1 Tryptophan fluorescence spectra.

Tryptophan fluorescence measurements were conducted using vesicles composed of pure hDPPC , Eh-20 and J5-20 (see formulations reported in Table 4.1). The tryptophan emission spectra of the peptides were acquired and these, together with the spectra for the lipid/peptide ratio 50/1, are plotted in Figure 4.2 as an example, whilst the emission peak wavelengths and the emission peak intensity for both the ratios 100/1 or 50/1 are reported in Table 4.4.

TABLE 4.4: Parameters obtained from static fluorescence emission measurements of the tryptophan emission from the peptides LL37 and LFb in the presence of hDPPC, Eh-20 or J5-20 liposomes at 37°C in 10 mM Tris pH 7.4, 1 mM $MgCl_2$. Lipid/peptide ratios 100/1 and 50/1.

	Peak Wavelength (nm)		**Peak intensity (a.u.)**	
	Lipid/peptide ratio 100/1			
Vesicle	LL37	LFb	LL37	LFb
no vesicles	350.0	353.5	192.3	174.5
DPPC	346.5	349.0	193.8	157.3
J5-20	325.0	341.0	623.1	288.9
Eh-20	326.0	339.5	508.2	316.0
	Lipid/peptide ratio 50/1			
Vesicle	LL37	LFb	LL37	LFb
no vesicles	348.5	353.0	366.5	318.5
DPPC	347.0	351.5	344.0	292.7
J5-20	326.0	342.5	718.5	501.1
Eh-20	324.5	340.0	1105.0	552.1

At the lower peptide concentration, ratio 100/1 (Table 4.4), LL37 peptide does not effectively penetrate the hDPPC vesicles, since the position of the emission peak and intensity are very similar to the ones obtained from the peptide alone. The fluorescence emission in the presence of vesicles composed of the mixtures Eh-20 and J5-20 showed a significant hypsochromic shift of the peaks and an increase of the intensity, suggesting that LL37 interacts and partitions into the membrane in the presence of LPS. The peak shift of the emission of LL37 's tryptophans

between the two LPS-containing liposome compositions is comparable whereas the peak intensity is higher in the case of the J5-20. This may suggest that despite a similar penetration depth, more peptides are bound to the J5-20 vesicles than Eh-20 vesicles. As for the case of LL37 peptide, LFb at a lipid/peptide ratio of 100/1 does not interact effectively with hDPPC vesicles and it seems that the peak intensities are reduced compared to the peptide alone. This could be due to a possible aggregation of the peptide which forms apolar domains assembled from the hydrophobic facets of each monomer and that bury the tryptophans slightly shifting the fluorescence peak; such behavior was hypothesized by Haukland and Vorland [266]. The emission of LFb in the presence of either J5-20 or Eh-20 vesicles produced a comparable hypsochromic wavelength shift. The higher peak intensity detected in the presence of Eh-20 may suggest a greater amount of peptide close to the hydrophobic chains when LPS EH100 is present in the bilayer, compared to the intensity peak obtained from the sample containing the vesicles J5-20. Compared to LL37 , LFb appears to interact less with the vesicles containing either LPS at the lipid/peptide ratio of 100/1.

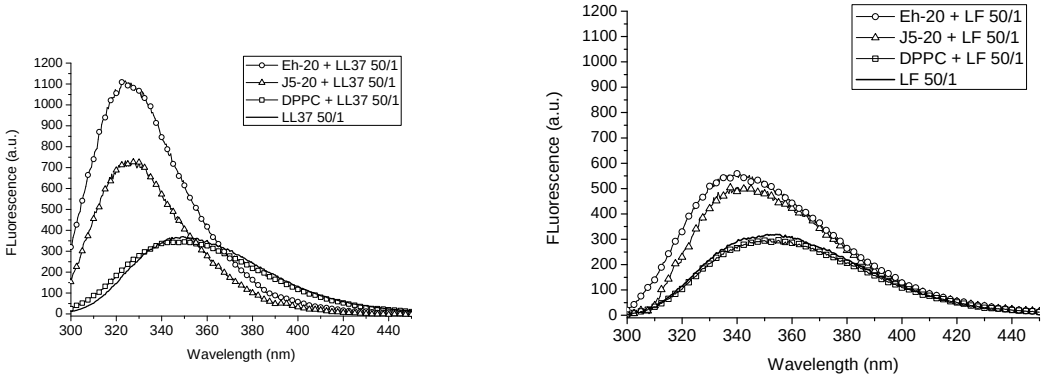

A B

FIGURE 4.2: Interaction of LL37 (A) and LFb (B) peptides with liposomes of pure hDPPC, Eh-20 and J5-20 mixtures at 37°C in 10 mM Tris pH 7.4, 1 mM $MgCl_2$ at a lipid/peptide ratio of 50/1.

Even at the higher LL37 peptide concentration (ratio 50/1), in the presence of hDPPC vesicles, there is no hypsochromic shift of the emission peak suggesting that the peptide does not penetrate effectively into the bilayer of these vesicles. In the presence of both J5-20 and Eh-20 vesicles the wavelength shift of LL37 emission peak is comparable to the one at the lower peptide concentration of the 100/1

ratio, but the peak intensity increased especially in the presence of Eh-20 vesicles. The intensities of the peaks are increased in both cases perhaps due to a greater presence of LL37 into the bilayer. At this concentration LL37 has a greater affinity for Eh-20 vesicles, in contrast with the findings at a lower peptide concentration. LFb behaves in a similar way to LL37 concerning the interaction with hDPPC liposomes, showing a similar emission peak wavelength and a slight lower peak intensity. The presence of either EH100 or J5 LPSs in the mixtures increased significantly the emission peak intensity maximum, concurrently with a hypsochromic shift of the emission peak. The LFb emission peak intensities increased with the increasing concentration of the peptide although there was no modification of the peak position for the two peptide/liposome ratios studied.

4.3.2 Solid state ^{2}H NMR.

The measurement of the S_{CD} profile for a lipid bilayer provides a quantitative estimation of the order state along the chain length of the lipids by the measurement of the molecular motion within the chains (details are provided in Section 1.5.2). The profile consist of a plateau in the S_{CD} order values in the carbons proximal to the interface of the bilayer, followed by a magnitude decrease toward the chain's terminal carbon [267]. The ^{2}H NMR quadrupole splitting allows a description of the dynamic and conformation of acyl deuterated lipid within a bilayer and registers any perturbation of the order parameter induced by the addition of CAPs or other membrane perturbing molecules [185, 194, 268]. Solid state ^{2}H NMR experiments were carried out on vesicles of pure DPPC and mixtures Eh-20 and J5-20 as reported in the formulations of Table 4.2. The addition of the two LPS chemotypes induced a limited broadening of the ^{2}H NMR spectrum of hDPPC (Figure 4.3 A) suggesting the conferring of an ordering effect on the lipid bilayer above the T_m of hDPPC . The ordering effect induced by J5 LPS is of greater magnitude than the effect induced by EH100 LPS, as shown by the smoothed order parameter S_{CD} in Figure 4.3 B. The J5-20 bilayer induces an ordering effect which is be distributed along the carbon chains of D_{62}DPPC , from the distal carbons to the ones closer to the heagroup. EH100 LPS influence on the ordering of D_{62}DPPC chains is more subtle and it is mostly limited to the carbons closer to the headgroup region.

The effect of the peptides LL37 and LFb on the order state of the bilayers at a lipid/peptide molar ratio of 50/1 was investigated in the same conditions mentioned above.

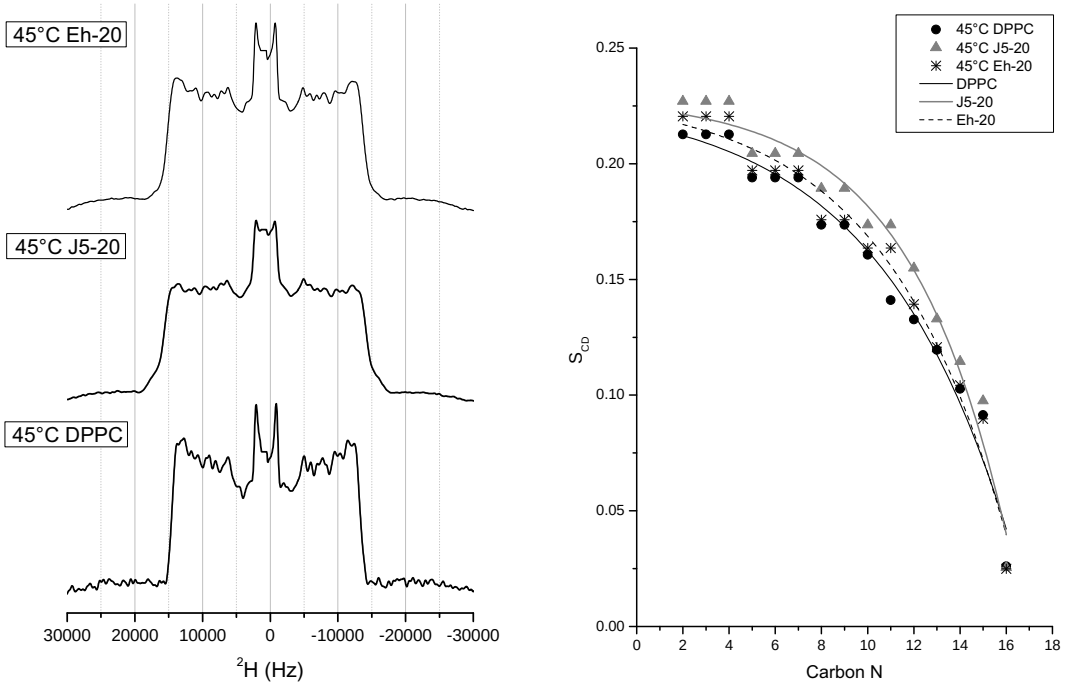

FIGURE 4.3: ^{2}H NMR analysis at 45°C of the pure DPPC , Eh-20 and J5-20 vesicles.(A) DePaked powder spectra of D_{62}DPPC signal. (B) Smoothed order parameter (S_{CD}) plot versus the carbon position of the D_{62}DPPC NMR spectra.

LL37 scarcely modifies the ^{2}H NMR spectrum of the Eh-20 vesicles, whereas it induces more significant changes in the J5-20 vesicles with an appreciable broadening of the powder spectrum of D_{62}DPPC (Figure 4.4 A). The S_{CD} plot shows that Eh-20 order parameter is not modified by the presence of LL37 , whilst J5-20 signal in the presence of the peptide produced a decrease in order of the distal carbon of the chains (Figure 4.4 B) suggesting a disordering effect on the bilayer.

The LFb peptide had no noticeable effects on the ^{2}H NMR spectrum of the Eh-20 bilayer and the modifications induced to the ^{2}H NMR spectrum of J5-20 are less marked than the LL37 case. The S_{CD} profiles of the Eh-20 vesicles in the absence or presence of the peptide LFb at a lipid/peptide molar ratio of 50/1 are identical (Figure 4.5 B). A detailed observation of the smoothed order parameter of J5-20 bilayer in the presence of LFb shows that the peptide induces a slight ordered state of the bilayer at the carbons closer to the headgroup region.

For a comparison the DPPC vesicles were challenged by the peptides LL37 and LFb at the same conditions. LFb at the lipid/peptide ratio of 50/1 reduced noticeably the S_{CD} values of DPPC vesicles; the disordering effect was marked on the carbons closest to the headgroup region (Appendix C). LL37 did not allow the formation of vesicles when mixed with the hDPPC /D_{62}DPPC lipids; even at

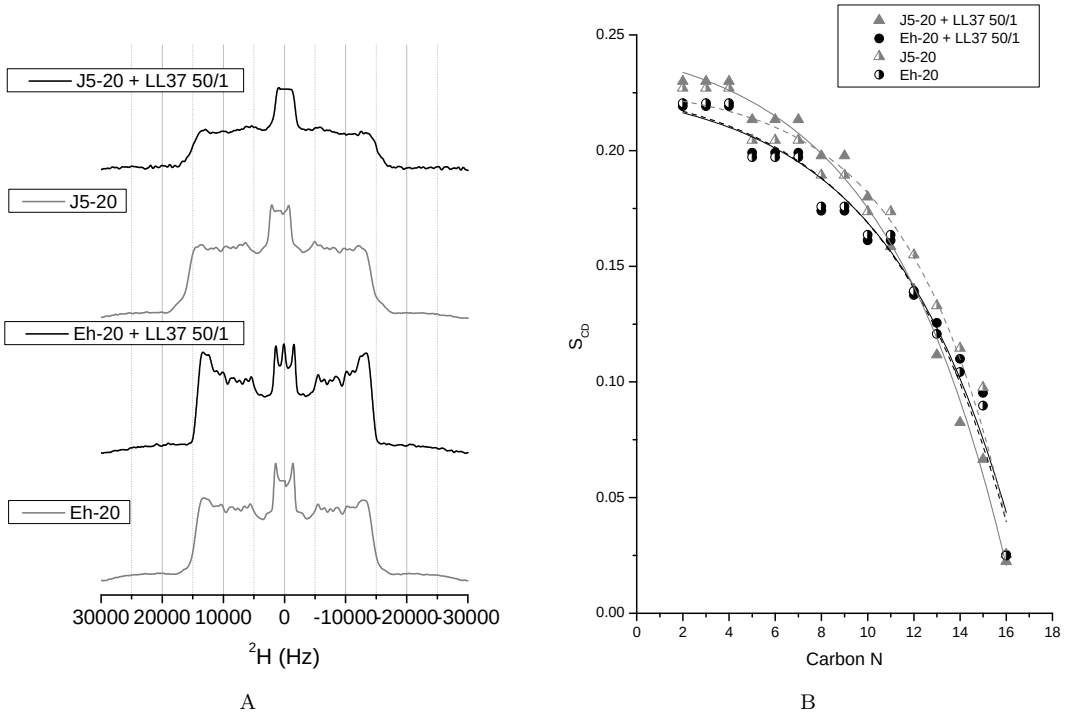

FIGURE 4.4: ^{2}H NMR analysis at 45°C of Eh-20 and J5-20 vesicles in the presence or absence of the peptide LL37 at a lipid/peptide molar ratio of 50/1. (A) DePaked powder spectra of D_{62}DPPC signal. (B) Smoothed order parameter (S_{CD}) plot versus the carbon position of the D_{62}DPPC NMR spectra.

lower peptide concentration it was not possible to obtain a liposome pellet.

4.3.3 Langmuir-Blodgett monolayers of mixed Ra and Rc LPS and DPPC.

Surface pressure-area per molecule isotherms ($P-Area$) were used to characterize the mixed monolayers of lipids and LPS and to calculate the area per molecule of each LPS chemotype. The $P-Area$ isotherms of pure hDPPC and mixed monolayers containing molar ratios of 80% hDPPC and 20% of either LPS EH100 or LPS J5 on water subphase of 1 mM $MgCl_2$ solution at 22°C , are shown in Figure 4.6 whilst the values of the area per molecule of each component are reported in Table 4.5. The total area per molecule of the mixed monolayers containing the LPSs is greater than the one of pure hDPPC , due to the presence of the bulky headgroup of the LPS. In consideration of the additive rule for the area per molecule within a mixed monolayer described by Equation 4.2 in Section 4.2.4 it is possible to

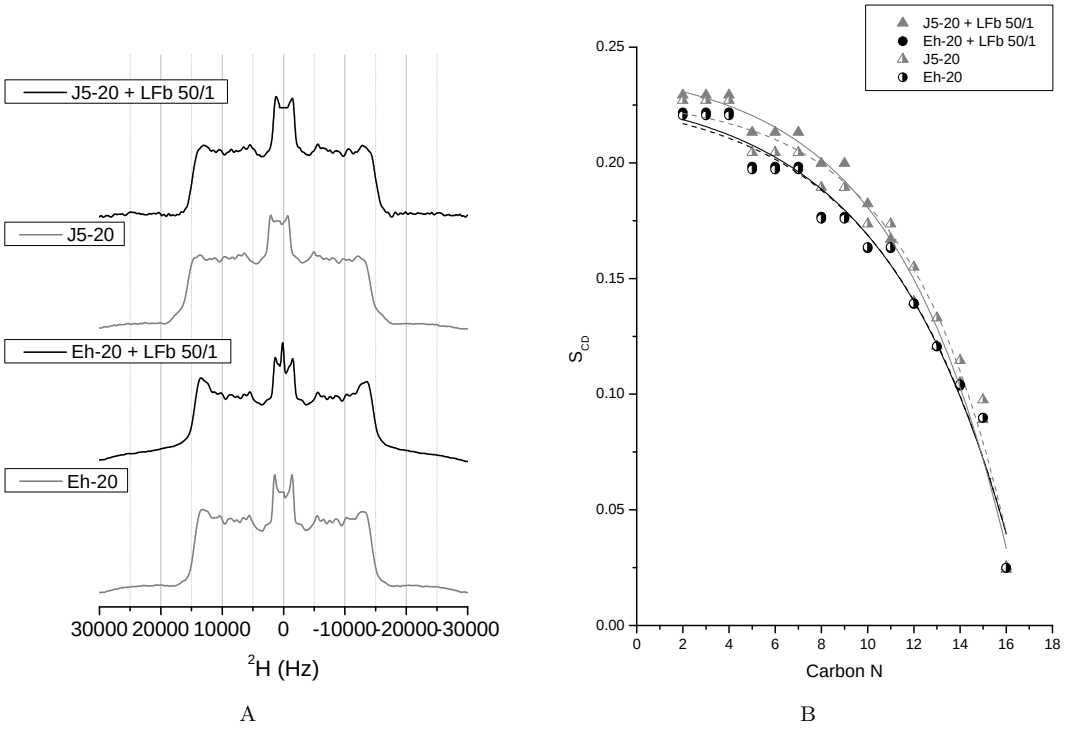

FIGURE 4.5: ^{2}H NMR analysis at 45°C of Eh-20 and J5-20 vesicles in the presence or absence of the peptide LFb at a lipid/peptide molar ratio of 50/1. (A) DePaked powder spectra of D_{62}DPPC signal. (B) Smoothed order parameter (S_{CD}) plot versus the carbon position of the D_{62}DPPC NMR spectra.

calculate back the area per molecule of each single component; the resultant area per molecule of EH100 LPS and J5 LPS are thus respectively 175.1 and 119.7 Å^2 which are in accordance with the relative sizes of the headgroups. The isotherms for pure hDPPC obtained in this experiment are comparable with those observed in previous experiments [269] and present the characteristic liquid expanded (LE) to liquid condensed (LC) phase transition occurring below 10 mN/m in the presence of Mg^{2+} ions [270, 271]. The addition of 20% molar ratio of either LPS EH100 (Eh-20 monolayer) or LPS J5 (J5-20 monolayer) to hDPPC monolayers removed the LE-LC phase transition of hDPPC and the shape of the curve from the gaseous to the solid phase is gradual (Figure 4.6); this effect has already been observed in monolayers containing hDPPC and either smooth or Re LPSs at different hDPPC /LPS ratios [175, 176]. A detailed observation of the three isotherms (Figure 4.6) in the liquid condensed phase, between ∼10 and ∼20 mN/m, shows that the LC phase of the hDPPC isotherm is steeper than the LC phase of the curves of the monolayers containing LPS, suggesting that in this phase the pure hDPPC monolayer is less compressible while the addition of the LPS chemotypes

makes the film more fluid and elastic. In the region of the LC-solid phase, at surface pressures above 20 mN/m, thehDPPC monolayer and the Eh-20 monolayer present a steeper isotherm curve compared to the monolayer containing Rc J5 LPS, suggesting that during this phase only J5 LPS has a greater fluidizing effect on the hDPPC monolayer.

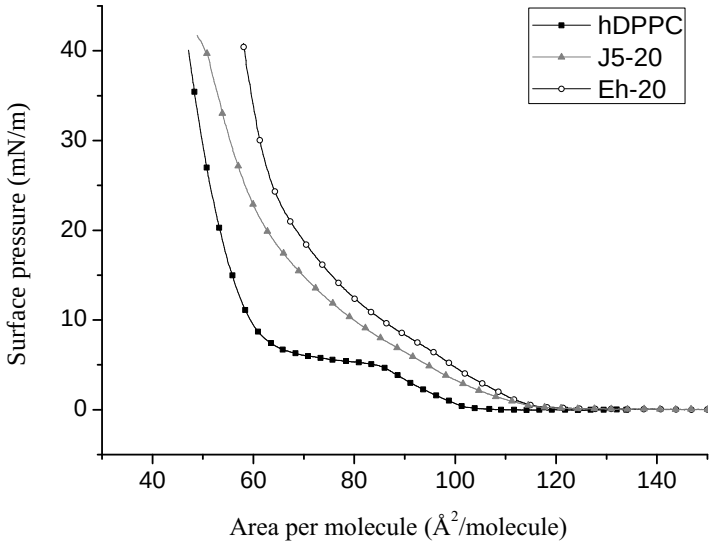

FIGURE 4.6: Surface pressure-area per molecule isotherms at 22°C on subphase of 1 mM $MgCl_2$ solution of pure hDPPC, J5-20 and Eh-20 monolayers.

TABLE 4.5: Area per molecule of hDPPC and LPSs calculated according to Equation 4.2.

Molecule	Area per molecule (Å²/molecule)	Standard deviation
hDPPC	57.5	2.4
LPS J5	119.7	7.3
LPS EH100	175.1	13.0

The calculation of the surface compressional modulus from the isotherms allows a better understanding of the compressibility of the monolayers and the effect of the addition of LPS to hDPPC films. The compressibility modulus (E_S) is derived from the reciprocal of the monolayer's compressibility modulus (C_S) according to the equation [174, 272]

$$E_S = \frac{1}{C_S} = -A\left(\frac{d\pi}{dA}\right) \tag{4.4}$$

where A is the area per molecule and $d\pi/dA$ is the slope of the isotherm at a defined surface pressure. A liquid condensed state is characterized by E_S values within 100-250 mN/m whereas a solid state is characterized by E_S values above 250 mN/m. [273]. The plot E_S *vs* surface pressure allows an appreciation of the effect of the addition of 20% of either EH100 or J5 LPS in hDPPC monolayers (Figure 4.7) [274]. Pure hDPPC monolayers enter the liquid condensed state right above the surface pressure of 10 mN/m and the rapid E_S increase suggests a low compressibility of this monolayer which reaches the solid state at 30 mN/m pressure equivalent to the the lateral pressure of the biological membranes [165]. The compressibility curves of the mixed monolayers containing 80% of hDPPC and 20% of either EH100 or J5 LPS show a different behavior. Both LPSs decrease the E_S values of hDPPC isotherms allowing the formation of a liquid expanded phase up to the surface pressure of 25 mN/m, the pressure at which the monolayers entered a liquid condensed state. Neither of the mixed monolayers Eh-20 and J5-20 show the formation of a proper solid phase, according to the values of the compressional modulus. This evidence suggests a fluidizing effect of the LPSs on hDPPC monolayers at 22°C , despite the data obtained from the isotherms which indicate the reach of a condensed state. The disordering effect of LPS on hDPPC monolayers has been observed before in LB experiments with hDPPC and smooth LPS [175] and solid state NMR experiments containing hDPPC and rough LPS from *E. coli* , below the T_m of DPPC [275].

TABLE 4.6: Surface compressive modulus E_S for each monolayer at 22°C at 30 mN/m lateral pressure on a water subphase containing 1 mM $MgCl_2$.

Monolayer	Surface compressive modulus E_S (mN/m)
PC	250 ± 45
J5-20	175 ± 38
Eh-20	168 ± 12

A detailed investigation of the curves in Figure 4.7, despite the considerable error bars, shows that over the surface pressure of 30 mN/m (Table 4.6) the compressibility of monolayers containing J5 is lower than the compressibility of monolayers containing EH100, something not apparent from the direct observation of the isotherms.

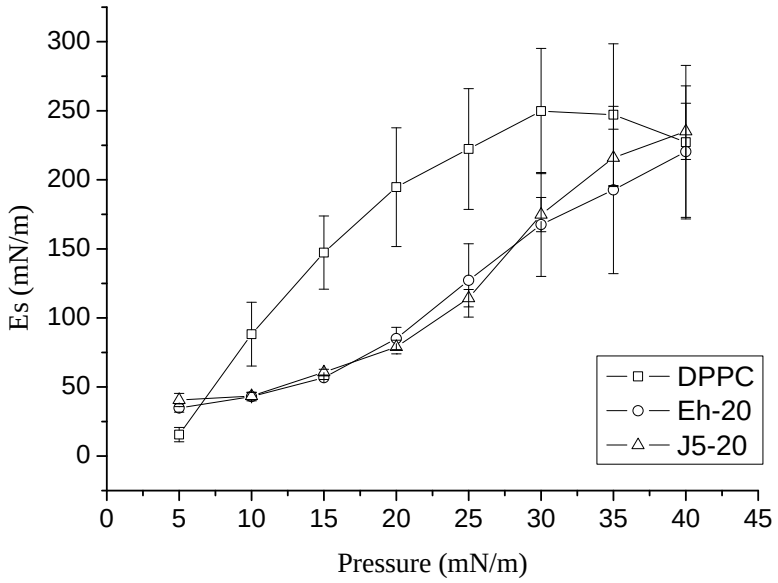

FIGURE 4.7: Surface compressive modulus E_S for hDPPC, 20% J5-80%hDPPC and 20% EH100-80%hDPPC monolayers at different pressure on water subphase containing 1 mM $MgCl_2$ at 22°C .

Stability of mixed monolayers. In order to define the stability of the mixed monolayers composed of 80% DPPC and 20% of either EH100 or J5 LPS at 22°C on water subphase of 1 mM $MgCl_2$ solution, the films were subjected to multiple cycles of compression and relaxation and the surface pressure was continuously recorded. The cycled isotherms of the mixed monolayers do not overlay completely (Figure 4.8 A and B) and show the presence of some hysteresis, caused by the loss of material into the subphase which results in a lower area per molecule at high pressures.

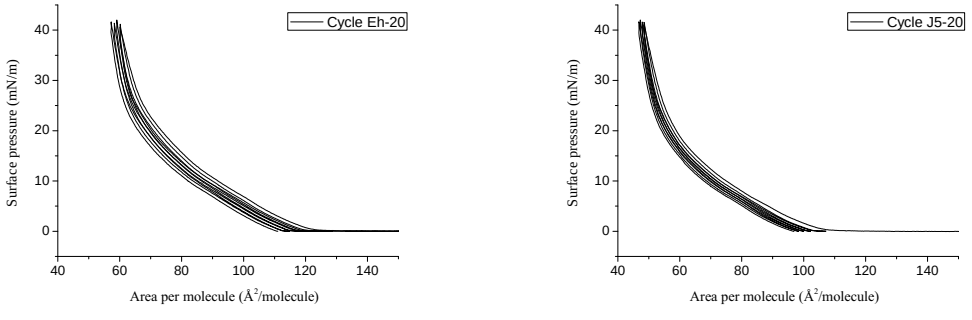

A B

FIGURE 4.8: Eh-20 (A) and J5-20 (B) monolayers cycled up to the target pressure of 40 mN/m at 22°C on water subphase of 1 mM $MgCl_2$ solution.

The monolayer stability in the same subphase conditions at 22°C was studied at a constant surface area measuring the change in surface pressure over time as well.

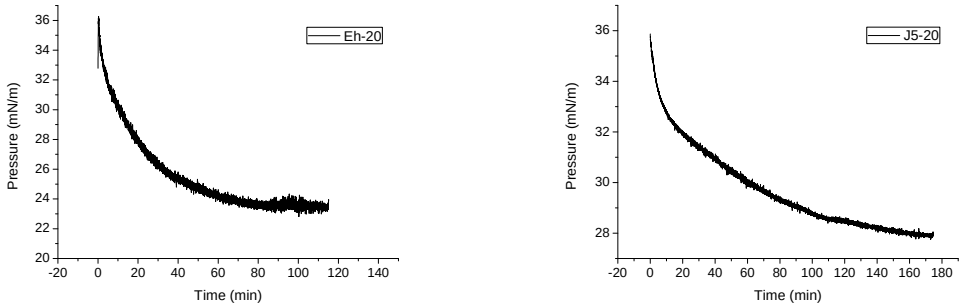

A B

FIGURE 4.9: Eh-20 (A) and J5-20 (B) monolayers stability at constant barrier area over time at 22°C on water subphase of 1 mM $MgCl_2$ solution.

The isotherms reported in Figure 4.9 show that the monolayer Eh-20 reached a final pressure of approximately 24 mN/m were it stabilizes in two hours, whilst the J5-20 monolayer took longer to equilibrate to a final pressure of approximately 28 mN/m in more than three hours.

4.3.3.1 Brewster angle microscopy

BAM images at 22°C on water subphase containing 1 mM $MgCl_2$ were taken for the monolayers hDPPC , Eh-20 and J5-20 in order to investigate the structural modifications induced by the presence of 20% of either EH100 or J5 LPS inhDPPC films. In Figure 4.10 the BAM images of the monolayers at different lateral pressure are reported. The hDPPC monolayer developed the characteristic cluster pattern with the formation of white lobed-like domains of lipids typical of the LE-LC transition state [261]. The compression of the hDPPC monolayer over the LE-LC transition shows the aggregation of the condensed domains until, upon further compression above 14.5 mN/m, they disappear when the film is compressed up to its solid phase. During the solid phase no islands are visible because the repulsive forces between the different clusters are overcome by the lateral pressure and the film presents a homogenous surface.

The J5-20 monolayer (Figure 4.10) at a surface pressure below 15 mN/m presents domains which are probably formed by hDPPC in the liquid condensed state, whereas the remainder of the monolayer is still in a liquid expanded state (Figure 4.7). The presence of LPS J5 modified the shape of the domains of hDPPC

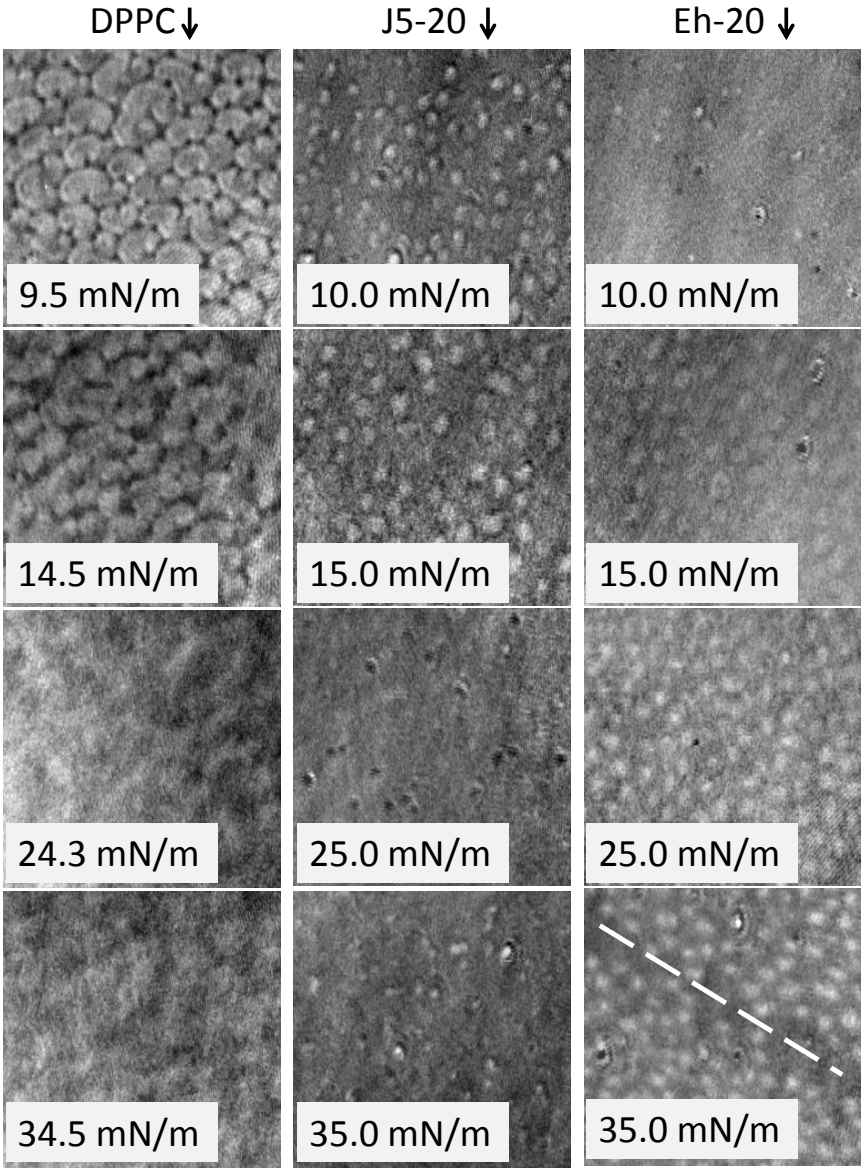

FIGURE 4.10: BAM images of surface pressure-area per molecule isotherms at 22°C on water subphase of 1 mM $MgCl_2$ solution of pure hDPPC, Eh-20 and J5-20 monolayers.

suggesting a close interaction between the amphiphiles. A similar effect was observed for Re LPS and hDPPC monolayers in the presence of Ca^{2+} , using a fluorescence microscopy technique on monolayers at the air-water interface [176]. Above 15 mN/m the film enters the liquid expanded phase and the image becomes more homogeneous, but still some clusters are visible up to 35 mN/m. Probably the existence of domains at every surface pressure suggests that the J5-20 monolayer is in constant coexistence between two phases corresponding to the absence of a defined phase transition of the $P - Area$ (Figure 4.6).

The Eh-20 monolayer is characterized by the absence of domains at low surface

pressure up to 10 mN/m, suggesting a homogeneous gas phase. This homogeneity may suggest that EH100 has a fludizing effect on hDPPC , removing completely the characteristic LC domains of DPPC. The nucleation visible at 15 mN/m suggest the formation of a coexistent LE-LC phase, which is maintained up to 35 mN/m. The actual shift of the phase transition of hDPPC towards higher pressure supports the hypothesis of a disordering effect of EH100 on the hDPPC monolayer. The dashed white line on the picture of Eh-20 monolayer at 35 mN/m highlights a possible rupture of the monolayer, indicating the proximity to its collapse.

4.3.3.2 Interaction studies of LL37 and LFb peptides and the mixed DPPC/LPS monolayers

The mixed hDPPC /LPS monolayers spread on the water subphase containing 1 mM $MgCl_2$ solution at 22°C held at a constant area per molecule were challenged by a subphase injection of the two peptides LL37 and LFb . The resultant changes in surface pressure of the monolayers were recorded and the data plotted in binding isotherm plot of pressure against time (Figure 4.11). The initial lateral pressures of the pure DPPC, Eh-20 and J5-20 monolayers were respectively 29±3 mN/m, 25±4 mN/m and 28±2 mN/m. The curve was fitted as a simple exponential function which parameters k, the rate of the change in the surface pressure, and $PMax$, the maximum change in pressure, describe respectively how quick and efficient is the interaction and the extent of this interaction in terms of surface pressure modifications (Table 4.7).

The presence of 20% of either EH100 or J5 LPS in the monolayer of hDPPC allows for a rapid binding of LL37 , characterized by a linear increase in the surface pressure already in the initial 5 minutes of interaction (Figure 4.11 A); the rate of surface pressure increase k is 0.004 and 0.003 s^{-1} respectively for Eh-20 and J5-20 monolayers, hence the increase of surface pressure induced by LL37 on Eh-20 monolayer is faster than in the case of the J5-20 monolayer. LL37 induces a greater total surface pressure change in Eh-20 monolayer than in J5-20 monolayer, as reported by the $PMax$ values which were respectively 17.3 and 11.2 mN/m. LL37 binds less with the monolayer composed of pure hDPPC (Figure 4.11 A) as revealed by a slow and gradual surface pressure change with a rate (k) value tenfold lower than the value in the presence of LPSs in the mixture; the extent of the surface pressure modification is also lower and the $PMax$ reaches only 4.4 mN/m and

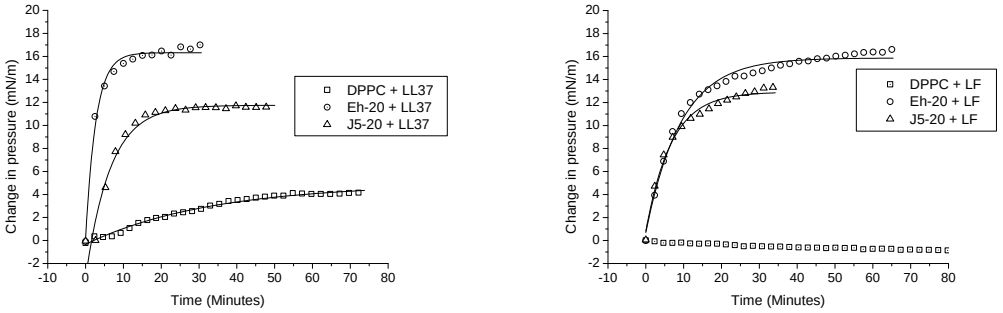

A B

FIGURE 4.11: Binding isotherms of the peptides LL37 (A) and LFb (B) with pure hDPPC, Eh-20 and J5-20 monolayers at 22°C on water subphase containing 1 mM $MgCl_2$ solution.

approaches a plateau after one hour. The LFb peptide injection yields identical k values for both monolayers containing EH100 and J5 LPS (Table 4.7). Whereas the $PMax$ values for the monolayers containing EH100 (14.8mN/m) is slightly higher than for the monolayer containing J5 LPS (12.0 mN/m). LFb showed no interaction with hDPPC , and the monolayer pressure stayed constant.
In general the k and $PMax$ values are lower for the LFb interactions than for the LL37 , suggesting a signficantly weaker binding capacity of LFb with mixed monolayers of hDPPC /LPSs.

TABLE 4.7: Kinetic parameters obtained from the fitting of the binding isotherms of LL37 and LFb peptides and the monolayers at 22°C on water subphase containing 1 mM $MgCl_2$ solution. k is the rate of pressure increase, $P\ max$ is the maximum pressure reached.

	Parameters	DPPC	J5-20	Eh-20
LL37	P Max (mN/m)	4.4 ± 1.6	11.2 ± 1.3	17.3 ± 1.4
	k (s^{-1})	6.0e-04 ± 4.0e-5	3.0e-03 ± 2e-4	4.0e-03 ± 3e-4
LFb	P max (mN/m)	—	12.0 ± 1.6	14.8 ± 1.0
	k (s^{-1})	—	1.0e-03 ± 9e-4	1.0e-03 ± 4e-4

4.3.4 Neutron reflectivity of mixed LPS/DPPC monolayers at the air/liquid interface and interaction with antimicrobial peptides.

Previous interaction experiments were carried out in Section 4.3.3.2 for the same mixed monolayers containing 80% of DPPC and 20% of either Ra EH100 LPS (Eh-20 monolayer) or Rc J5 LPS (J5-20 monolayer). In that case, using a 50 mm diameter circular trough with a significantly smaller volume of subphase, the binding of the peptides LL37 and LFb was much faster than the binding observed with the LB trough used in these NR experiments. The reason of this discrepancy resides in the greater volume of the trough of the NR experiments and the lack of a stirring apparatus which would have more rapidly distributed the peptide throughout the subphase, thus increasing the rate of peptide binding to the monolayers. In the NR experiments the velocity of the binding relied only on the passive diffusion of the peptide in the subphase which was more than three times the volume of the subphase used in the previous experiments. This resulted in a prolonged equilibration time and rather long experiments (Figure 4.13).

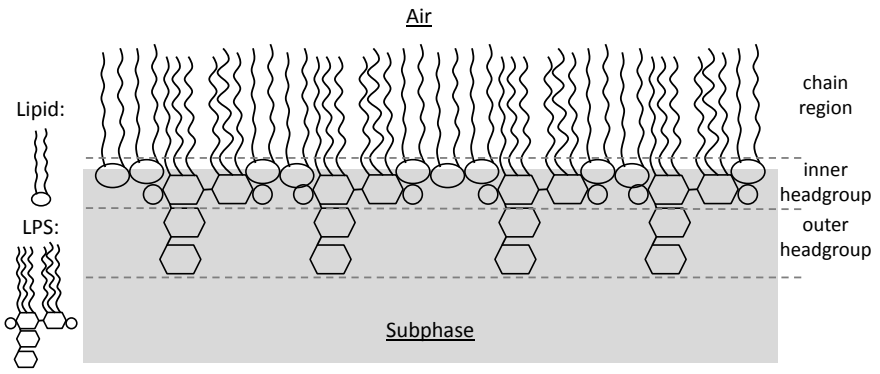

FIGURE 4.12: Scheme of the layers in which the monolayers are divided during the NR data fitting and the parameters obtained from the fitting.

Nevertheless the study of the interaction between CAPs and monolyers containing LPS proved to be remarkably useful and a reliable method to assess the interaction and the permeation capacity of the peptides into Gram negative membrane mimetic systems [172, 256, 276].

Both the peptides LL37 and LFb interacted more rapidly with the Eh-20 monolayer than with the J5-20 monolayer (Figure 4.13 A and B). The LL37 peptide

induced a similar magnitude of change of surface pressure in the monolayers EH-20 and J5-20. It is evident that, compared to LL37 , the peptide LFb shows less interaction with both Eh-20 and J5-20 monolayers. The interaction of LFb with the monolayers seems to be more gradual than the LL37 peptide which suggests a lower binding affinity (Figure 4.13 B). These findings are in agreement with the interaction studies described above in Section 4.3.3.2.

The simultaneous fitting of the NR data from at least two contrasts for each

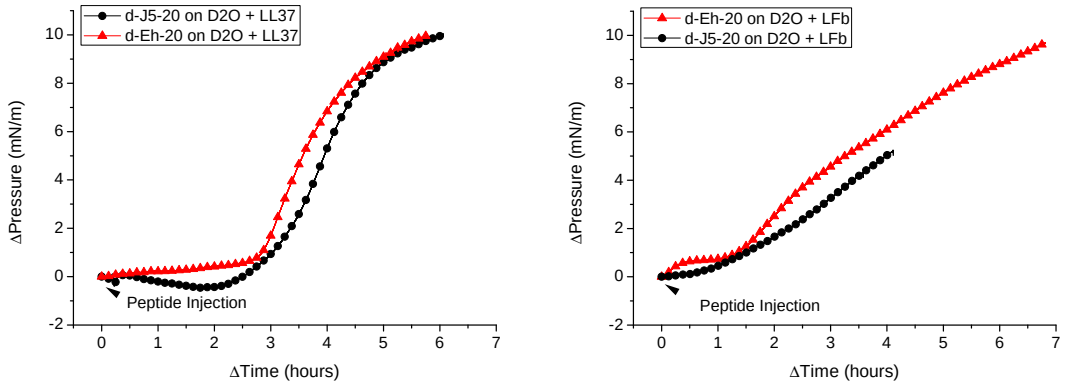

FIGURE 4.13: Examples of kinetics of binding isotherms (pressure over time) of the monolayers Eh-20, J5-20 and lipid A 2Kdo-20 after subphase injection of LL37 and LFb peptides at 22°C on D_2O subphase containing 1 mM $MgCl_2$.

monolayer facilitated the construction of the reflectivity and the SLD profiles of the monolayers Eh-20 and J5-20. The model applied to the reflectivity data considered a monolayer divided into adjacent layers as reported in the scheme of Figure 4.12. The parameters obtained from the data fitting of the NR data of the bilayers Eh-20 and J5-20 in the absence or presence of the peptides, either LL37 or LFb , are reported in Table 4.8. The full range of reflectivity plots are reported in Appendix E.

The reflectivity and the SLD profiles for the monolayers Eh-20 and J5-20 are shown in Figures 4.14 and 4.15 respectively. The chain thickness values obtained for the mixed monolayers Eh-20 and J5-20 were respectively 19.34 Å and 16.76 Å; these values are higher than the thicknesses obtained from experiments carried out on monolayers at the air/liquid interface of pure D_{62}DPPC (16 Å) [277] and pure Rc J5 LPS (12 Å) [21]. The SLD values for the mixed DPPC/LPS chain region of the monolayers were in accordance with previously published data for pure lipids [278] and Rc J5 LPS [21]. The similarity between the values of SLD obtained for the deuterated chain region in both contrasts D_2O and ACMW suggest a limited penetration of solvent in the chain region of the Eh-20 monolayer, as

reported in Table 4.8 and as shown in Figure 4.14. The penetration of solvent was more pronounced in the J5-20 monolayer, as shown by the SLD profiles of Figure 4.15.The values for the inner headgroup thickness, consisting of the headgroup of DPPC and the core region of LPS that includes the GlcN and the Kdo moieties, obtained for the monolayers Eh-20 and J5-20 were respectively 7.00 and 9.98 Å. These values are smaller than expected in consideration of the DPPC headgroup thickness (9 Å) and the Rc J5 LPS inner headgroup thickness (14 Å) previously published [21, 277]. The differences in the SLD values between the two contrasts for both the monolayers may suggest a strong penetration of solvent in this layer. The outer headgroup thicknesses for the Eh-20 and J5-20 monolayers were respectively 26.53 and 20.00 Å. The headgroup thickness of the monolayer containing EH100 LPS was lower than the headgroup thickness value of 31 Å obtained from the NR investigation of asymmetric bilayers composed of DPPC and EH100 LPS [265] whereas the J5 LPS headgroup thickness was in agreement with the data published by the same group. The differences in SLD between the two contrasts obtained for both the monolayers under study suggests a consistent solvation of the outer headgroup region.

The subphase injection of the peptide LL37 under Eh-20 and J5-20 monolayers was investigated (Table 4.8). LL37 increased the chain thickness of the Eh-20 monolayer of ∼3 Å (Table 4.8) and reduced the D chain SLD in ACMW (Figure 4.16) and increased the H chain SLD in D_2O (Figure E.1) which may suggest the penetration of the peptide within the tail region. The peptide reduced the chain thickness of the J5-20 monolayer by 2 Å, increased H chain SLD in D_2O (Figure E.3) and the D chain SLD in D_2O (Figure E.4). This observation suggests a possible penetration of deuterated material such as D_2O , rather than the penetration of the hydrogenated LL37 .The inner headgroup thickness of the Eh-20 monolayer was reduced by LL37 to 5.43 Å and the modification of the SLDs suggests an increased solvation. The inner headgroup thickness of J5-20 monolayer was increased by ∼5 Å and the SLDs modified by the addition of LL37 into the subphase. The peptide increased the outer headgroup thickness of both the Eh-20 and J5-20 monolayers by ∼5 Å with limited modifications on the SLD profiles (Figures 4.16 and 4.17). The minor effect on the SLD may be due to the high solvation of the region which masks the contribution of the peptide to the density of the layer.

The NR data for the interaction of LFb with the Eh-20 and J5-20 monolayers were available only for the deuterated mixed monolayer in either D_2O or ACMW

subphase. The peptide LFb reduces by ∼2 Å the chain thickness of the Eh-20 monolayer with no significant modifications of the SLDs of this region; this is confirmed by the observation of the SLD profile in ACMW (Figure 4.16) which shows a similar maximum of the chain region peak and a reduction of width upo addition of the peptide. LFb induced a minor increase of ∼1.5 Å on the chain thickness of J5-20 monolayer which is hardly recognizable from the SLD profiles (Figure 4.17 and E.3). The peptide increased the inner headgroup thickness of Eh-20 and J5-20 monolayers by ∼7 Å and ∼5 Å respectively, with modifications of the density of the headgroup region (Figures 4.16 and 4.17). LFb reduced the outer headgroup region of the monolayers Eh-20 and J5-20 by ∼-9 and ∼-5 Å .

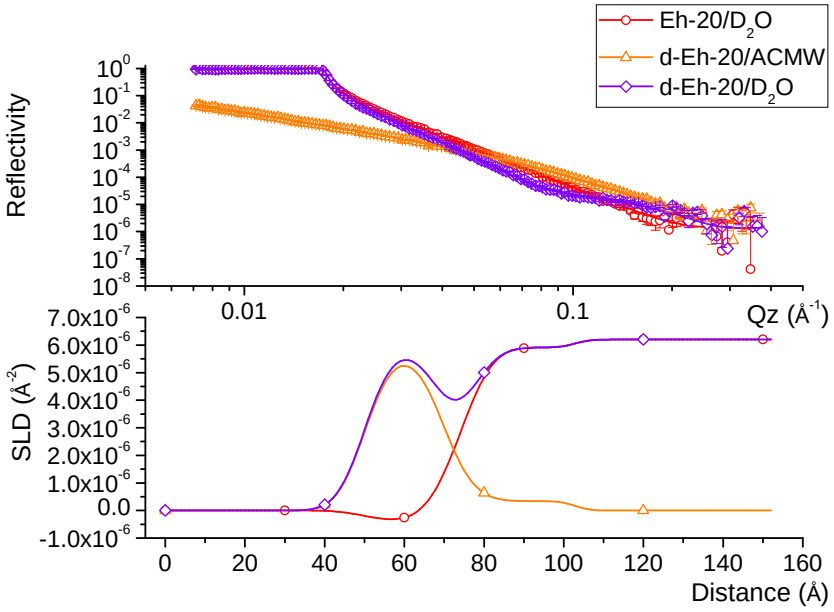

FIGURE 4.14: NR fitted data of either Eh-20 or d-Eh-20 monolayers on two contrasts (D_2O , ACMW) subphase containing 1 mM $MgCl_2$ solution at 22°C . Upper plot: reflectivity profile. Lower plot: SLD profile.

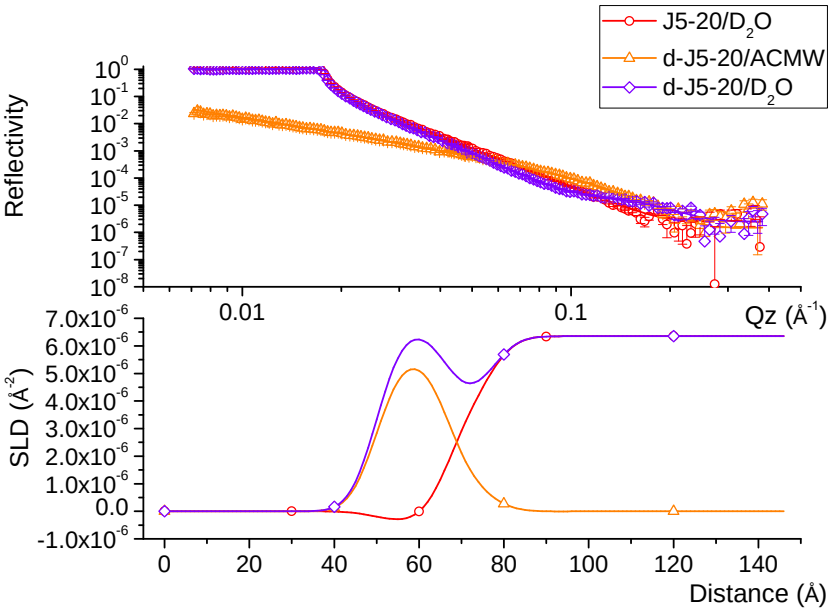

FIGURE 4.15: NR fitted data of either J5-20 or d-J5-20 monolayers on two contrasts (D_2O , ACMW) subphase containing 1 mM $MgCl_2$ solution at 22°C . Upper plot: reflectivity profile. Lower plot: SLD profile.

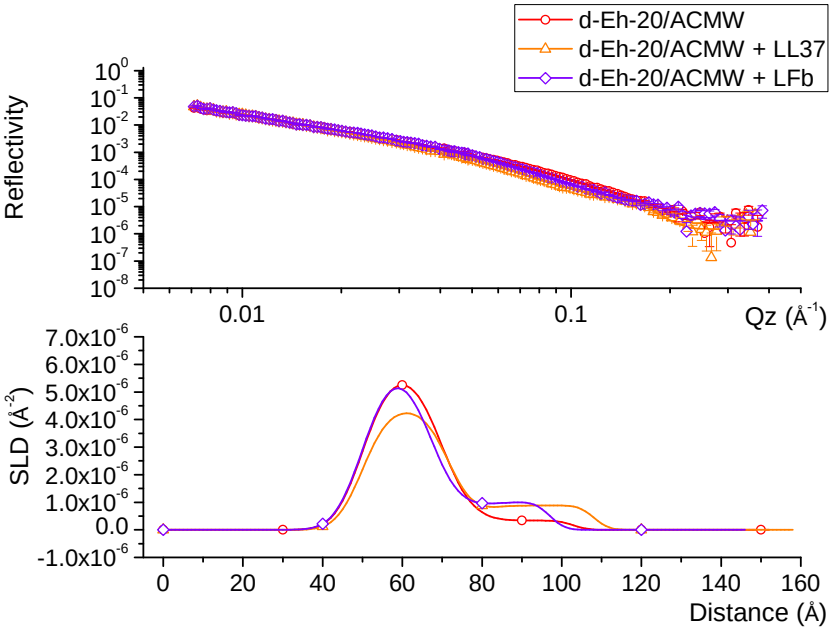

FIGURE 4.16: NR fitted data of d-Eh-20 monolayer on ACMW subphase contianing 1 mM $MgCl_2$ solution at 22°C before and after the subphase injection of the peptides LL37 and LFb. Upper plot: reflectivity profile. Lower plot: SLD profile.

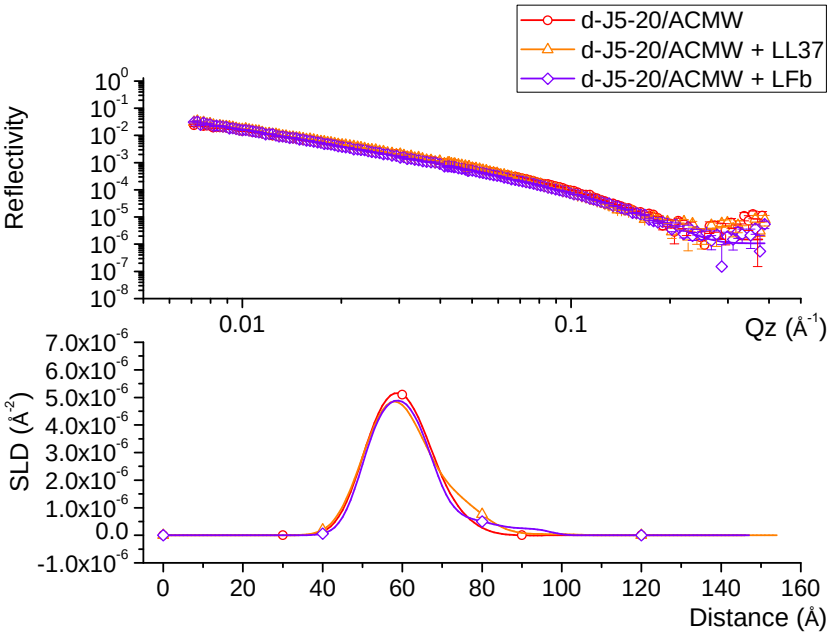

FIGURE 4.17: NR fitted data of d-J5-20 monolayer on ACMW subphase contianing 1 mM $MgCl_2$ solution at 22°C before and after the subphase injection of the peptides LL37 and LFb. Upper plot: reflectivity profile. Lower plot: SLD profile.

TABLE 4.8: Parameters obtained from the fitting of NR data of the mixed Eh-20 and J5-20 monolayers a the air/liquid interface at 22°C in the absence and presence of the peptides, either LL37 or LFb

		Eh-20		+ LL37		+LFb		J5-20		+LL37		+LFb	
Parameter	Unit	value	error	value	error	value	error	value	error	value	error	value	error
Chain h SLD d2o	x10^{-6} (Å^{-2})	-0.39	0.00	0.59	0.05	–	–	-0.39	0.00	-0.28	0.06	–	–
Chain d SLD d20	x10^{-6} (Å^{-2})	5.85	0.05	5.76	0.03	5.98	0.04	6.65	0.05	7.20	0.06	6.15	0.06
Chain d SLD acmw	x10^{-6} (Å^{-2})	5.68	0.02	4.38	0.01	5.83	0.02	5.66	0.03	5.74	0.02	5.14	0.01
Chain Thickness	(Å)	19.34	0.06	22.12	0.05	17.08	0.05	16.76	0.12	14.76	0.01	17.18	0.06
Inner headgroup h SLD d2o	x10^{-6} (Å^{-2})	1.91	0.10	1.00	0.00	3.77	0.00	3.75	0.01	4.10	0.03	4.50	0.05
Inner headgroup h SLD acmw	x10^{-6} (Å^{-2})	1.00	0.00	0.00	0.01	0.86	0.03	1.00	0.04	1.52	0.03	0.61	0.03
Inner headgroup thickness	(Å)	7.00	0.01	5.43	0.07	14.90	0.08	9.98	0.10	14.97	0.01	15.00	0.01
Outer headgroup h SLD d2o	x10^{-6} (Å^{-2})	5.92	0.05	5.80	0.02	5.96	0.05	6.35	0.00	6.08	0.04	6.35	0.01
Outer headgroup h SLD acmw	x10^{-6} (Å^{-2})	0.34	0.01	0.88	0.01	1.02	0.03	0.00	0.00	0.04	0.02	0.25	0.03
Outer headgroup thickness	(Å)	26.53	0.05	30.52	0.20	15.00	0.30	20.00	0.02	24.96	0.04	15.00	0.00
Monolayer roughness	(Å)	5.57	0.05	5.22	0.05	5.64	0.04	5.05	0.12	5.50	0.06	4.40	0.08

4.3.5 Neutron reflectivity of asymmetric bilayer of DPPC and LPS and interaction with antimicrobial peptides.

The asymmetric bilayer composed of an inner leaflet of hDPPC and an outer layer composed of either LPS Ra EH100 or LPS Rc J5, was investigated at 37°C in water subphase containing 1 mM $MgCl_2$ solution in the absence or presence of the antimicrobial peptides LL37 and LFb .

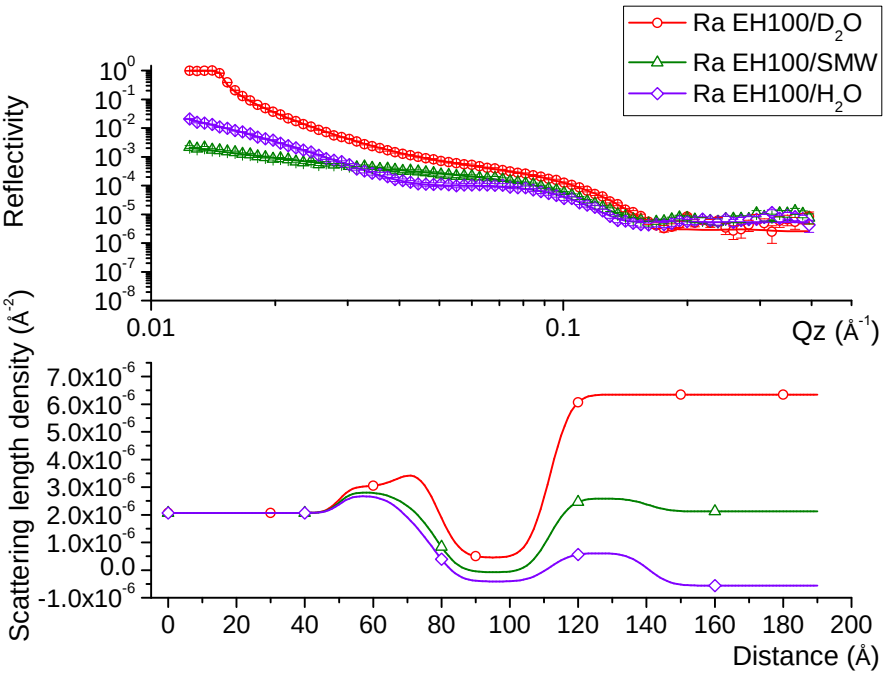

FIGURE 4.18: Reflectivity (upper plot) and SLD (lower plot) profiles of the EH100 bilayer in three contrasts solution containing 1 mM $MgCl_2$ at 37°C .

The fitting of three reflectivity profiles allowed the determination of the bilayer structure parameters reported in Table 4.9. The comparison between the two asymmetric bilayers of LPSs EH100 and J5 revealed an inner headgroup thickness of 10.0±0.01 Å which is lower than previously published data [265]. In particular the thickness of the inner headgroup of the J5 bilayer was significantly different from the thickness of 9.3 Å of the hDPPC headgroup reported in the literature [277]. The hydration of the oxide layer did not significantly change between the two bilayers, even in the presence of the peptides, and the values were considerably lower than previously published data [265]. The SLDs of the inner headgroup of the EH100 and J5 bilayers were comparable with previously published data [265] apart from the SLD in D_2O of J5 bilayer which was considerably higher. The

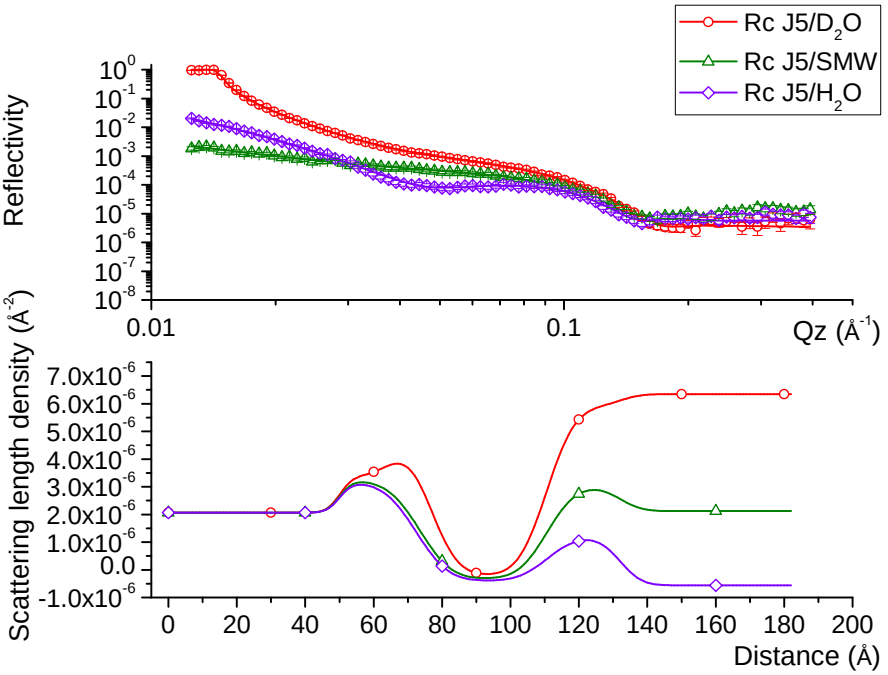

FIGURE 4.19: Reflectivity (upper plot) and SLD (lower plot) profiles of the J5 bilayer in three contrasts solution containing 1 mM $MgCl_2$ at 37°C .

chain thicknesses of the EH100 and J5 bilayers were respectively 32.72±0.12 and 35.77±0.25 Å, in agreement with previous data [265]. The tail hydration values of the EH100 and J5 LPS bilayers were respectively 11.95±0.59 % and 2.83±0.72 %, which suggest a coverage of approximately 88% and 97%, a higher value in respect to the coverage obtained by Clifton *et al.* [265]. The outer headgroup layer thickness for the EH100 and J5 bilayers were respectively 29.49±0.51 and 21.46±0.07 Å, which are in agreement with previously published data [265]. The SLD in D_2O of the outer headgroup for the EH100 bilayer was higher than the relevant values for the J5 bilayer, whereas the SLDs in H_2O and SMW were lower for the EH100 bilayer in respect to the values of the J5 bilayer.

Most of the structural changes occurred in the bilayer EH100 upon addition of the peptide LL37 involved the chain region and the outer headgroup layers which increased respectively by ∼3 and ∼6 Å (Table 4.9), whereas LL37 did not affect significantly these regions in the J5 bilayer. The model fitting applied to both the bilayers did not show any significant modification of the values of the SLD of the tail region (Table 4.9) despite the modification of the SLD profiles in D_2O shown in Figure 4.20 and Figure 4.21) respectively for the EH100 and the J5 bilayer. The hydration of the outer headgroup of the EH100 and the J5 bilayers increased respectively by ∼12% and ∼5% upon addition of LL37 . The values of outer headgroup SLD in each contrasts for both the bilayers were not affected by the presence

of the peptides which is surprising in consideration of the increase in hydration of the layer. The plots of the reflectivity and SLD profiles for other contrasts are reported in Appendix F.

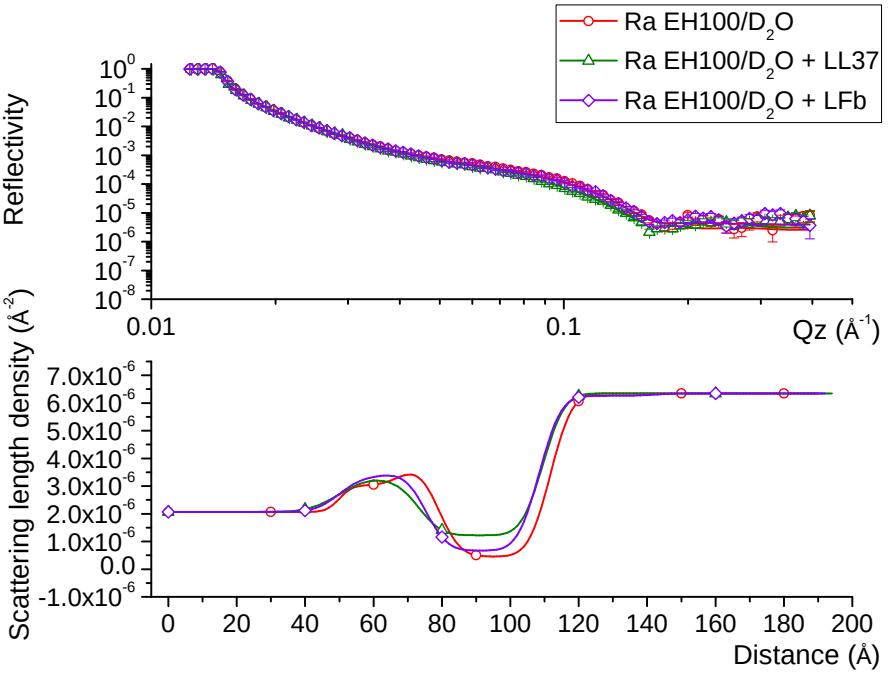

FIGURE 4.20: Reflectivity (upper plot) and SLD (lower plot) profiles of the EH100 bilayer in D_2O solution containing 1 mM $MgCl_2$ at 37°C in the absence or presence of the peptides, either LL37 or LFb.

The addition of the peptide LFb to the EH100 bilayer did not affect significantly the chain region thickness of the bilayer but increased the tails hydration by 6%; such minor increase in solvation did not affect significantly the tails' SLD. LFb increased the outer headgroup thickness by ∼4.5 Å but did not induce any appreciable modification of the SLDs of this layer. In general the peptide LFb did not influence the SLDs of the bilayer, as shown by the SLD profiles in D_2O of Figure 4.20.

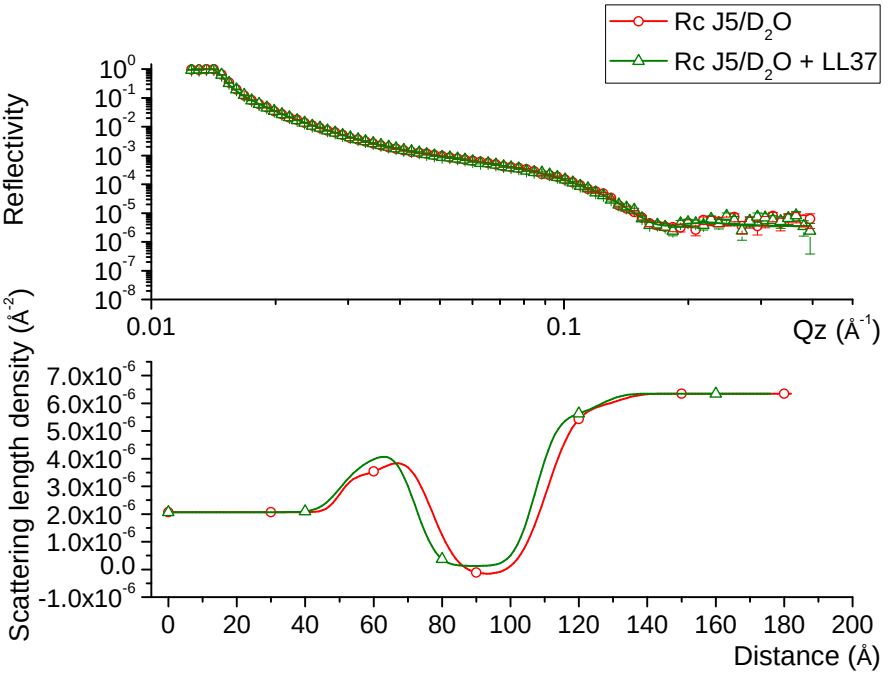

FIGURE 4.21: Reflectivity (upper plot) and SLD (lower plot) profiles of the J5 bilayer in D_2O solution containing 1 mM $MgCl_2$ at 37°C in the absence or presence of the peptide LL37.

TABLE 4.9: Parameters obtained from the fitting of the NR curves for the asymmetric bilayers containing either LPS EH100 or LPS J5 in the absence and in the presence of the peptides, either LL37 or LFb.

		Ra Eh100		+LL37		+LFb		Rc J5		+LL37	
Parameter	Unit	value	error	value	error	value	error	value	error	value	error
Oxide layer thickness	(Å)	18.90	0.23	13.60	0.08	16.37	0.12	18.93	0.27	12.02	0.18
Oxide layer roughness	(Å)	3.00	0.01	7.00	0.02	5.56	0.02	3.00	0.01	4.65	0.01
Oxide Layer SLD	x10^{-6} (Å^{-2})	2.83	0.03	3.37	0.01	3.26	0.02	3.25	0.02	3.65	0.01
Oxide hydration	(%)	3.74	1.34	0.03	0.06	3.33	0.99	2.90	1.34	3.60	1.46
Inner headgroup thickness	(Å)	10.00	0.01	10.00	0.00	8.85	0.07	6.47	0.08	10.00	0.01
Inner headgroup SLD D2O	x10^{-6} (Å^{-2})	3.86	0.03	3.07	0.09	3.56	0.06	6.33	0.02	4.59	0.02
Inner headgroup SLD SMW	x10^{-6} (Å^{-2})	2.12	0.02	2.46	0.02	2.25	0.01	2.07	0.01	2.38	0.02
Inner headgroup SLD H2O	x10^{-6} (Å^{-2})	1.45	0.01	3.00	0.03	1.01	0.01	1.50	0.01	0.98	0.01
Tails thickness	(Å)	32.72	0.12	35.77	0.25	33.21	0.09	35.22	0.22	35.39	0.21
Tails SLD	x10^{-6} (Å^{-2})	-0.39		-0.40	0.00	-0.40	0.00	-0.39		-0.40	0.00
Tail hydration	(%)	11.95	0.59	24.04	0.52	17.97	0.43	2.83	0.72	7.74	0.70
Outer headgroup thickness	(Å)	29.49	0.51	35.49	0.60	34.13	0.33	21.46	0.07	19.01	0.13
Outer headgroup in D2O	x10^{-6} (Å^{-2})	6.05	0.02	6.05	0.00	6.06	0.04	5.89	0.07	5.59	0.08
Outer headgroup in SMW	x10^{-6} (Å^{-2})	2.60	0.01	2.33	0.01	2.32	0.01	3.00	0.02	2.89	0.02
Outer headgroup in H2O	x10^{-6} (Å^{-2})	0.62	0.03	0.73	0.02	0.66	0.03	1.17	0.01	1.19	0.02
Bilayer roughness	(Å)	5.00	0.00	5.00	0.01	5.02	0.03	6.57	0.05	5.01	0.01

4.4 Discussion

4.4.1 Tryptophan fluorescence spectra.

When discussing the results of the study of the fluorescence emission of the Trp residues, the position of this amino acid within the structure of the peptides has to be considered. Figure 1.10 shows the relative locations of the residues and details of the hydrophobicity of the peptides. It is clear that the α-helical structure of LL37 provides a more defined separation between the hydrophilic and hydrophobic facets, which contains the Trp residue. Whereas this clear distribution of hydrophobicity is not as marked in the structure of LFb , yet the Trp residues are contained in an extended hydrophobic region [119]. The emission of the Trp residues depends upon the polarity of the environment, therefore the position of this residue in the LL37 and LFb structure is important. The defined hydrophobic facet of the LL37 helix more likely interacts with the hydrophobic region of the lipid bilayer [279] and probably it would result in a deeper penetration into the bilayer compared to the residues in the structure of LFb . Therefore a higher emission intensity could be expected from the samples containing LL37 despite the lower number of Trp residues.

The presence of negative charges on the surface of the bilayer facilitates the interaction of both LL37 [151, 183] and LFb [128, 246] with lipid bilayers. Previous studies suggest that LL37 penetrates deeply into the bilayer in a concentration dependent way, as reported for other α-helical peptides [151, 280]. On the other hand LFb seems to affect the bilayer more at the interface, rather than at the level of the hydrophobic chains [127, 130]. Certainly the electrostatic interaction between the cationic peptides and the negative charges carried by the LPS is the predominant driving force of their interaction, as revealed by the low binding activity of both LL37 and LFb peptides on the zwitterionic vesicles composed of pure DPPC. Nevertheless the activity of the peptides on vesicles containing Eh100 was greater than on vesicles containing J5 LPS despite their equal theoretical negative charge.

The fluorescence emission experiments were carried out at 37°C which is below the phase transition of hDPPC (41°C) but is slightly above the T_m of the Ra and Rc LPS chemotypes (between 32°C and 36°C [88]). Experiments on mixed hDPPC /LPS monolayers at the air/liquid interface at 22°C (Section 4.3.3) revealed a fluidizing effect of Ra EH100 LPS and Rc J5 LPS on hDPPC , when the

temperature is below the T_m, whereas solid state ^{2}H NMR experiments at 45°C on vesicles containing the same components revealed an ordering effect of LPSs on the bilayers. Hence at the temperature of 37°C it is not straightforward to predict whether the LPSs will be in their gel or fluid phase. A stronger interaction with vesicles containing LPS may be an indication of a more fluid bilayer due to the disordering effect of EH100 and J5 LPSs, whereas a reduced penetration would occur for pure hDPPC vesicles, the bilayer of which is in the gel phase state. The LB experiments on mixed monolayers at the air/liquid interface (Section 4.3.3) revealed a fluidizing effect of both LPS on the DPPC monolayer. The fluidizing effect of EH100 LPS at the lateral pressure of 30 mN/m (the approximate lateral pressure within the natural membranes) was greater than the effect of J5 LPS (Table 4.6), although the error on the values was high. Hence the greater "fluidity" of the vesicles containing EH100 LPS than the ones containing J5 LPS, allowed a deeper penetration of both the peptides into the bilayer.

LL37 does not penetrate into hDPPC vesicles but increasing its concentration favors the accumulation of the peptide at the interface, which may comply with its initial theoretical "carpet model" mechanism of action (Section 1.3.2). The presence of the LPSs, either Ra EH100 or Rc J5, increases significantly the interaction of both peptides with the vesicles. LL37 at the concentrations tested showed the same penetration depth indicating the attainment of an insertion limit into the hydrophobic chains; moreover the depth of insertion is greater than the one exerted by the LFb peptide, supporting the greater propensity for LL37 to interact with the hydrophobic chains. At the lower concentration, LL37 accumulates more at the interface of vesicles containing LPS J5 than LPS EH100; this could be due to the absence of part of the core region in the LPS J5 which would otherwise hinder the interaction, as it happens in the vesicles containing EH100. At the higher concentration, the peptide showed an opposite behavior with a greater binding to LPS EH100 than LPS J5 containing vesicles, perhaps due to the achievement of a threshold concentration which allowed for a greater, additive interaction [145]. LFb , as the LL37 peptide, had no interaction with hDPPC vesicles. LFb , in general, interacts and penetrates to a lesser extent than LL37 all the vesicles containing the LPSs studied, corroborating the hypothesis of its greater activity at the interface rather than at the hydrophobic chains level. The amount of peptide binding to the membranes containing LPS, regardless of the chemotype, is concentration dependent; moreover LFb showed a higher affinity for vesicles containing EH100 LPS at every concentration tested. In general the LL37 peptide penetrates

more effectively into the bilayer containing LPS than the LFb peptide, which acts mostly on the core region of the LPS headgroup.

4.4.2 Solid state ^{2}H NMR

Previous studies regarding ^{2}H NMR experiments performed on mixtures of D_{62}DPPC and LPS from *E. coli* K12 mixtures (1:1 w/w) in buffer containing 10 mM $MgCl_2$ showed that LPS increases the order of DPPC hydrocarbon chains above the T_m of DPPC when the bilayer is in a fluid phase; whereas below the T_m of DPPC, when the chains are more ordered, LPS induces a disordering effect on the chain packing [275]. The ^{2}H NMR experiments in this chapter agree with these observations, suggesting an ordering effect of Ra and Rc LPSs on DPPC bilayers above the lipid melting temperature (41°C). The addition to the D_{62}DPPC vesicles of 20% molar ratio of the Rc J5 LPS induced a higher ordering of the acyl chains, compared to the addition of Ra EH100 LPS. This is in accordance with the FT-IR data reported by Brandenburg *et al.* [89] and the molecular simulations of Wu *et al.* [281] which suggested that a smaller oligosaccharide region of LPS induces a higher order state. Ciesielski *et al.* performed NMR studies on mixtures of DMPC and smooth LPS from *E. coli* , suggesting a weak ordering effect and a reduced bilayer mobility upon addition of the LPS [282].
LL37 pre-mixed with hDPPC /D_{62}DPPC did not allow the formation of vesicles probably because of a solubilizing effect on the membranes, at the concentrations tested in this chapter (lipid/peptide ratio 100/1 and 50/1) . The addition of both J5 and EH100 LPS to DPPC may have helped the aggregation of the lipids because of the ordering effect of LPS. LL37 does not noticeably modify the order parameter of vesicles containing 20% of EH100, but has a disordering effect upon the distal carbons of the vesicles containing LPS J5. Previous ^{2}H NMR experiments on LL37 showed that the peptide effectively inserts into the hydrophobic region of POPC/POPG bilayer driven by the attraction for the negative charges of POPG, thus inducing a disordering effect [279]. The same investigations suggested that disordered chains react to the insertion of LL37 with less modification of their S_{CD} , whereas ordered chains are modified more extensively by the insertion of the peptide [279]. This rational explains the lower disordering effect of LL37 on Eh-20 vesicles, which would be in a more disordered state than J5-20 vesicles, hence more sensitive to the penetration of the peptide. The activity of LL37 is mostly concentrated into the hydrophobic region of the bilayer, due to its greater penetration

activity (Section 4.3.1).
LFb did not modify the order parameter of vesicles containing 20% Ra EH100 LPS but marginally increased the order parameter of the carbons close to the headgroup region of the vesicles containing Rc J5LPS which may be due to its stronger interfacial activity, unlike LL37 which interacts more with the chain region (Section 4.3.1).

4.4.3 Mixed DPPC and LPS monolayers at the air/liquid interface

The LB film technique at the air-liquid interface was used to characterize the mixed hDPPC /LPS monolayers on an aqueous subphase containing 1 mM $MgCl_2$ solution at 22°C and the interaction with the antimicrobial peptides LL37 and LFb . The areas per molecule of the LPS EH100 and J5 were calculated to be respectively 175.1±13 and 119.7±7.3 Å^2. Previous neutron reflectivity experiments at the air-liquid interface for monolayers of pure J5 LPS found an area per molecule of 109 Å^2 [21], which is comparable to the findings of the experiments reported here. Both Ra EH100 and Rc J5 LPSs increased the fluidity of hDPPC lipids in the mixed monolayers Eh-20 and J5-20, reported by a reduction of the E_S value at surface pressures up to 35 mN/m below the T_m of hDPPC . This disordering effect of LPS on hDPPC monolayers is supported by previous investigations on Re rough and smooth LPS [175, 176]. These findings are supported by ^{2}H NMR experiments which showed that below the DPPC T_m rough LPS from *E. coli* has a disordering effect on D_{62}DPPC vesicles [275]. The BAM images confirmed the fluidizing effect of both LPSs on hDPPC monolayers. This disordering effect seems to be more pronounced with EH100 than with J5, which is in accordance with previous FT-IR experiments suggesting a greater disorder of the chains with the increasing size of the oligosaccharide region [89]. The more fluid monolayers containing either Ra EH100 or Rc J5 LPS may allow a stronger binding of the peptides than the more ordered monolayer containing pure hDPPC . The binding of CAPs with the Eh-20 monolayer is greater than the binding with the J5-20 monolayer, in agreement with the higher fluidizing effect of EH100 LPS which allows a stronger peptide interaction.
LL37 peptide interacts more than LFb with all the monolayers tested, supporting the rational by which α-helical peptides are stronger membrane-active agents. The

peptide LL37 interacts more with monolayers containing EH100 than with monolayers containing J5 in terms of the rate of binding and the magnitude of the change of the monolayer surface pressure, moreover LL37 has a reduced binding affinity towards pure hDPPC monolayers. LFb does not bind to hDPPC monolayers and seems to possess a similar rate of binding with both EH100 or J5 LPS-containing monolayers.The peptide shows a greater magnitude of change of pressure for the Eh-20 monolayer.

4.4.4 Neutron reflectivity on LPS/DPPC monolayers at the air/liquid interface.

The chain thickness values obtained in this experiment for the Eh-20 and J5-20 monolayers are higher than the ones observed by others for monolayers of pure Rc J5 LPS [21] or pure D_{62}DPPC [277]. This could be due to an irregular organization of the LPS and DPPC molecules within the monolayer resulting in an uncoordinated acyl chains position, increasing the estimation of the chain thickness. On the other hand the values for the inner headgroup thickness of the monolayers Eh-20 and J5-20 were considerably understimated compared to the headgroup thickness of monolayers composed of pure DPPC or pure Rc J5 LPS [21, 277]. The reason for this discrepancy may reside in the different model used to analyze the reflectivity data and the different monolayer composition used in the experiment presented in this chapter. The outer headgroup thickness of the monolayer composed of EH100 LPS is greater than that of the monolayer composed of J5 LPS, as could be expected in consideration of the relevant core region dimensions. The SLD profiles of the inner and outer headgroup regions of both monolayers suggest a high degree of solvation as it is likely to be for such hydrophilic moieties. The peptide LL37 has conflicting effects on the Eh-20 and J5-20 monolayers and it is difficult to interpret and form definite conclusions on a rational mechanism of action. The peptide seems to increase the chain thickness and outer headgroup of the Eh-20 monolayer, decreasing the value of the inner headgroup thickness. LL37 decreases the chain thickness and increases significantly the thickness of both the headgroup regions of the J5-20 monolayer. A possible interpretation may suggest that LL37 penetrates more the Eh-20 monolayer due to its stronger

interaction with EH100 LPS (Sections 4.3.1 and 4.3.3.2) stretching the chain region, as depicted in Figure 4.22 C, whereas this effect is limited in the case of the J5-20 monolayer. The activity of the peptide LFb is probably concentrated mostly on the headgroup region of the monolayers Eh-20 and J5-20. This evidence is in agreement with previous observation of LFb 's interfacial activity described in Section 1.3.1. The effect of CAPs on monolayers containing EH100 LPS is greater than in the presence of the J5 LPS as observed before in the experiment of Section 4.3.3.2. The reduction of the chain thickness induced to the Eh-20 monolayer may be due to a lateral expansion of the interface by the intercalation of the peptide, followed by the expansion of the tail region (Figure 4.22 B).
The peptide LL37 penetrates more than LFb the chain region of the Eh-20 monolayer reducing the density and expanding the width of the peak as revealed by the profile in ACMW of Figure 4.16. Both peptides insert into the headgroup region (inner + outer region) of the Eh-20 monolayer with the formation of an elongated shoulder on the SLD profile (Figure 4.16). Both LL37 and LFb peptides do not modify the density of the chain region of the J5-20 monolayer (Figure4.17) and induce limited modifications on its headgroup region as well. This evidence are the confirmation of the higher sensitivity of models containing EH100 LPS to the activity of CAPs for the reasons discussed above.

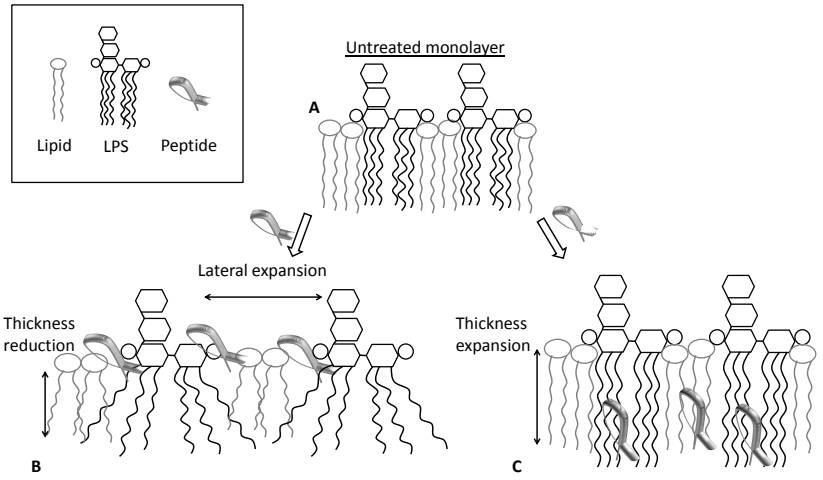

FIGURE 4.22: Possible effects of a generic CAP on the structure of a mixed lipid-LPS monolayer at the air/liquid interface.

The mathematical model used for the analysis of the NR data reported in this Section is clearly not the ideal model which could be applied, but it was the best amongst the models tried (data not shown). A simplified model which consists of two layers, tail region and chain region, reported a headgroup thickness of the

monolayer J5-20 greater than the Eh-20 monolayer which is not possible in consideration of the molecular dimensions of the LPS core regions. Another attempt was made using a model which consisted of three layers, such as the one reported in this Section, with a single SLD value for each layer without considering the two contrasts applied (D_2O and ACMW). As a result of the fitting with such model, the roughness of the monolayers was sometimes exceeding the thickness of the bilayer itself, especially in the case of the J5-20 monolayer (∼20 Å). That would suggest a disruption of the monolayer which was not the case in consideration of the fact that stable monolayers were always formed. The constraint of the parameters such as the monolayer roughness would have forced the fitting program to compensate, generating the modification of other parameters into unreasonable numbers. The analysis of such a complex system certainly requires further investigation in order to optimise the models used in its analysis.

4.4.5 Neutron reflectivity of asymmetric bilayers of DPPC and LPS and interaction with antimicrobial peptides.

The lower values for the inner headgroup thickness obtained in this experiment for both the Ra EH100 and Rc J5 bilayers compared to the data of Clifton *et al.* [265] may be due to a reduced exchange of lipids and LPS between the two leaflets of the bilayers. The data presented in the previous study reported a considerable amount of LPS flipping into the inner leaflet which resulted in an increased inner headgroup thickness. The methodology for the formation of the bilayers used in this study utilised the compression of the DPPC and LPS monolayers at 4°C in the presence of a solution of 1 mM $MgCl_2$ in the subphase. Both conditions may have aided the stability of the outer LPS leaflet reducing the exchange of material between the two layers. This may also explain the lower hydration of the oxide layer because of a thinner inner headgroup which would reduce the water content in this layer. The higher SLD value in D_2O and the lower SLD values in SMW and H_2O of the outer headgroup for the EH100 bilayer in respect to the values for the J5 bilayer may be due to a greater extent of hydration of the former bilayer, as could be expected from the bulkier and wetter headgroup of the Ra EH100 LPS chemotype. The bigger headgroup of the EH100 LPS produced a thicker outer headgroup layer compared to the J5 LPS, in agreement with the molecular dimensions of the relative core region of the LPSs.

The peptide LL37 increases the thicknesses of the outer headgroup and the chain region of the EH100 bilayer whereas it does not modify the J5 bilayer, suggesting a stronger interaction with the Ra EH100 LPS as observed in the experiments reported above and previously in this thesis (Section 4.3.1, Section 4.3.3.2 and Section 4.3.4).The peptide LFb modifies exclusively the thickness of the outer headgroup of the EH100 bilayer suggesting a limited activity confined in the headgroup of Ra EH100 LPS as reported in previous experiments (Section 4.3.1). No NR data are available for the interaction with J5 bilayer but in consideration of earlier evidence (Section 4.3.1, Section 4.3.3.2) it is possible to assume a limited interaction with bilayers consisting of Rc J5 LPS. The interaction of both peptides did not modified the SLD parameters of the tail and the outer headgroup region of the bilayers. This result is unexpected in the light of the fact that the presence of a peptide (which SLDs are reported in Table B.2) in either layers would have modified the density of the layers with consequent modification of the SLD. A qualitative observation of the SLD profiles in the D_2O contrast of the bilayers EH100 in the presence of either LL37 or LFb , and for the bilayer J5 in the presence of LL37 (respectively Figure 4.20 and Figure 4.21), show a clear increase in density of the acyl chain region upon addition of the peptides. The magnitude of the increase in density and expansion of the trough of the chain region of the EH100 bilayer is greater for LL37 than LFb , indicating a possible insertion of the peptide LL37 into the bilayer. The SLD profiles in H_2O and SMW (Figure F.1 and F.3) indicate a similar effect of the peptides on the headgroup region of the EH100 bilayer. The modification induced by LL37 on the chain region density of the J5 bilayer in D_2O (Figure 4.21) are of smaller magnitude compared to the ones of the EH100 bilayer. Similar results occur for the H_2O and SMW contrasts (Appendix F) indicating a lesser activity of the peptide on the J5 bilayer. Such changes of density could not be completely detected by the model fitting applied, as a result of which the parameters reported above may be an underestimation of the real density changes; this limitation may be due to the restricted number of contrasts which reduced the sensitivity of the measurements to SLD changes.

4.5 Conclusion

The experiments presented in this chapter aimed to assess the interactive capacity of LL37 anf LFb antimicrobial peptides with models of the outer membrane of Gram negative bacteria composed of DPPC and different rough chemotypes of LPS. Some data have been difficult to interpret and further investigations are required to elucidate better the mechanism of interaction. Nevertheless some conclusions can be drawn. Both the amphiphilic, cationic peptides are interacting with the membrane models by electrostatic interaction with the negative charge of LPS. Models containing the Ra EH100 chemotype of LPS are more susceptible to the activity of CAPs than models containing the Rc J5 chemotype, hence a bigger core region of the LPS does not provide any shielding effect but actually favors the peptide interaction. The α-helical peptide LL37 possesses a greater rate of binding and penetration activity than the β-sheet peptide LFb ; due to its conformation, LL37 binds to the negative charges at the interface of the membrane and penetrates the chain region via its hydrophobic side, disrupting the bilayer (Section 1.3.2). As speculated in Section 1.3.1, the activity of LFb is concentrated at the interface of the models and it exerts a limited penetration of the hydrophobic region, hence its microbicidal activity may not be the result of membrane disruption [130]. The results presented in this study show benefits of the application of the Gram negative bacteria OM model which includes the presence of lipopolysaccharide; such a realistic model may expand the knowledge of the mechanism of action of CAP. These investigations can lead to fruitful evidence thanks to the application of powerful techniques such a solid state NMR and neutron scattering. More studies using neutron techniques are desirable, implementing the model with a greater range of solvent and lipid component contrasts which would increase the sensitivity of the experiment.

Chapter 5

General discussion.

The study of lipopolysaccharide physicochemical characteristics began more than three decades ago with the discovery of its endotoxic principle, the lipid A molecule [211]. The interest in this bacterial membrane component resulted in the detailed determination of its molecular structure and its high degree of structural variability [29, 44, 283]. Since then many biophysical studies have revealed the close connection between the structure of the LPS and its toxicity, leading to the development of the "conformational concept of endotoxicity" [84]. According to this theory a conical molecular shape of LPS which favors aggregates of a non-lamellar form is highly toxic, whereas LPS in a cylindrical conformation forms lamellar aggregates which are less toxic [84, 91, 92]. The molecular conformation of LPS is determined by its structure, hence different chemotypes of LPS exhibiting different toxicities [199].

The toxic effect of LPS takes place after the release of monomers of LPS (in a conical shape) from aggregates released from the OM of the bacteria, and their subsequent recognition by specific lipopolysaccharide binding proteins (LBPs) which present the molecules to membrane receptors (mCD14 and TLR4) of the immune system cells such as macrophages and neutrophils [61]. This exceptionally sensitive immune response results in a cascade of inflammatory signals (prostaglandins, chemokines, cytokines, reactive oxygen species) aimed at eradicating the stimulating infection, however in the eventuality of an elevated quantity of LPS in the body, the over-stimulated immune system provokes the pathological condition called septic shock [62]. Amongst the various inflammatory mediators produced by immune cells, nitric oxide (NO) produced by cultured macrophages can be directly correlated to the inflammatory stimulation induced by LPS [201, 203]. This

relationship was used to evaluate the inflammatory activation of cultured murine J774.1 cells stimulated by nanograms/mL quantities of several chemotypes of LPS through the measurement of the level of NO produced by the cells. The preliminary study presented in this thesis has some statistical limitations, nevertheless it shows that the smooth 0111B4, the Ra EH100 and the Rc J5 rough chemotypes of LPS from *E. coli* are more potent immunostimulators than the Re LPS (the lipid A-2Kdo). Amongst the three most potent chemotypes the most toxic chemotype seems to be the Ra EH100, whereas no significant differences have been observed between the smooth 0111B4 and the Rc J5 chemotypes. In order to improve the accuracy of the toxicity test, it would be desirable to study the LPS-induced inflammatory stimulation of whole blood, which provides a more sensitive test and would compensate for the limitations of the NO assay such as the lack of LFb. Nevertheless as result of the toxicity test performed, the question arises as to whether the differences in the inflammatory stimulation are correlated with the diversity of the structures of aggregates formed by the different LPS chemotypes. Previous studies on the morphology of LPS aggregates have been conducted using X-ray radiation in non-physiological conditions with a high concentration of LPS [84, 85, 87]. The use of small-angle neutron scattering (SANS) and cryo-transmission electron microscopy (cryo-TEM) has allowed us to reduce the concentration of lipopolysaccharide considerably, thus resulting in a more biomimetic model system. In the experiments presented here the structures of smooth 0111B4, Ra D21 and Rc E7 LPSs were determined in solution at 6 mg/mL in the presence of $MgCl_2$. The smooth LPS forms elongated micellar particles, sometimes branched and interconnected, whereas rough Ra D21 and Rc E7 chemotypes formed complex lamellar structures. According to the "conformational concept of endotoxicity" introduced above, those structures should not have elicited an inflammatory activation of the macrophages, which actually happened in the biological assay performed in this study. Still the absence of LBP in the culture medium poses a limitation to the possible speculations on the different toxic activities of LPS, restrictions which need to be explored with further biological studies as suggested above.

Based on the knowledge built up so far on the mechanism of lipopolysaccharide toxicity, few studies have focused on the investigation of anti-endotoxic molecules which could reduce the activation of the immune system induced by the LPS. Some studies have, however, tried to develop small molecules able to bind and sequester LPS to reduce the activation of the immune system [284]. A different approach

based on the rationale of the "conformational concept of endotxicity" consists of the study of molecules which would modify the supramolecular structure of LPS aggregates from a more toxic (non-lamellar) to a less toxic (lamellar) form. These studies focus on the anti-endotoxic activity of natural and synthetic antimicrobial peptides [114–116]. Following the latter idea, the studies presented in this thesis have concentrated on the assessment of the putative anti-endotoxic role of the two amphphilic cationic antimicrobial peptides (CAPs) LL37 and LFb .

The NO assay performed on J774.1 macrophage cells described above, was carried out on the same smooth 0111B4, Ra EH100, Rc J5 and Re lipid A-2Kdo rough LPS chemotypes in the presence of different concentrations of either LL37 or LFb in the cell culture medium to assess any anti-endotoxic activity of the CAPs. Unfortunately the data were not conclusive due to the high degree of error of the measurements and a definite conclusion can not be formed. It is clear though that LL37 and LFb have different effects on the LPS-induced inflammatory stimulation of macrophages cells.

The structural modifications induced by the peptides LL37 and LFb on aggregates of smooth and rough LPS were investigated by SANS and cryo-TEM. Neither peptide was able to modify the morphology of aggregates consisting of smooth 0111B4 LPS probably due to the shielding effect of the very large O-antigen moiety which would hinder the interaction of the amphiphilic peptides. The removal of the O-antigen, as for the case of the rough chemotypes, resulted in a stronger electrostatic interaction of the peptides with the aggregates due to the exposure of the negative charges of the LPS core oligosaccharide and lipid A regions. LB experiments on monolayers at the air/liquid interface and static fluorescence experiments on model membranes containing mixtures of hDPPC and rough LPS chemotypes revealed the essential role of the electrostatic interaction for the CAPs' binding activity.

The lamellar structures formed by the Ra D21 LPS were challenged by the LL37 peptide which induces the formation of elongated micelles closing up into irregular toroids and a significant modification of the innermost hydrophobic region of the LPS aggregates. The peptide LFb , on the other hand, induces lesser changes in the structure of the lamellar aggregates of D21 LPS resulting in the formation of tightly packed, regular toroidal structures which resemble pores spanning a bilayer. The SANS data revealed that LFb acts more at the interface of the aggregates, where the core oligosaccharide of LPS is located, rather than deeply

into the hydrophobic region, inducing a curling effect on the bilayer [130]. The different mechanism of action of the LL37 and LFb peptides is corroborated by solid state NMR experiments and neutron reflectivity (NR) experiments on monolayers of mixed DPPC/Ra EH100 LPS and on supported asymmetric bilayers composed of an outer leaflet of pure EH100 LPS; the experiments show that LL37 is more likely to interact with the hydrophobic region of the LPS whereas LFb has an interfacial activity on the core oligosaccharide region.The complex lamellar aggregates formed by the Rc E7 LPS, which lacks part of the core oligosaccharide region and its negative charges, are modified upon the addition of the peptides, either LL37 or LFb . Both peptides induce the formation of a mixed population of aggregate morphologies which comprise complex lamellae, toroids and worm-like micelles, generating SANS data which is difficult to interpret. The effect of the peptides on the E7 LPS aggregates is not as evident as for the Rc D21 LPS case. This apparent inhomogeneity of the population of aggregate morphologies may be due to the higher number of E7 LPS molecules compared to the experiments carried out with the smooth and the Ra chemotypes, resulting in the sequestration of the peptides in area of high lipoplysaccharide concentration. The absence of negative charges in the core region may allow the peptides to interact directly with the negative charges of the lipid A region of the E7 LPS inducing strong modification of the aggregates. Whereas static tryptophan fluorescence and NR experiments on membrane models composed of Rc J5 LPS chemotype, which retains the negative charges in the core region, suggest a reduced interaction of the peptides with these models. The negative charges of this chemotype may help to stabilize the monolayers and bilayers containing J5 LPS reducing the activity of the peptides due to a stronger cross-linking between adjacent molecules with a Mg^{2+} ion which is not so readily displaced because of the lower lateral pressure created by the smaller headgroup of J5 compared to the EH100 LPS.

The action of the peptides on rough chemotypes of LPS aggregates suggests that both LL37 and LFb act in opposition to the conformational concept of endotoxicity, leading to a theoretically more toxic form of LPS. It has to be taken into consideration that the conditions in which these investigations are performed differ substantially from the experimental conditions used during the development of the theory. The structural information which sustain the theory have been obtained from experiments where condition are unlike those encountered in biology. The neutron scattering technique is undoubtedly a potential tool which can be used to study this system at very low LPS concentrations, closer to a biological

conditions. This technique provides a better insight into the mechanism of action of CAPs focusing at the molecular level on the localization of the peptide interacting with membrane models. The evidence presented in this thesis point out the necessity to verify and further investigate the basis of the conformational concept of endotoxicity and the mechanism of interaction of CAPs with membrane models by the use of experiments which mimic more closely the biological conditions. Our experiments indicate that there may be a more complex relationship between aggregate structure, peptide interaction and toxicity of LPS.

5.1 Future works

The data presented in this thesis showed a greater bio-activity of the peptide LL37 compared to LFB, in both the biological and the biophysical experiments. Therefore, future experiments will focus mainly on the LPS/LL37 interactions. In order to obtain more realistic and conclusive biological data regarding the anti-endotoxic role of antimicrobial peptides, whole-blood experiments could be carried out using antibodies specific for different inflammatory markers (TNF-α and IFN-γ), which would help to reduce the error of the measurement. Using a high-throughput screening methodology such as the fluorescence-activated cell sorting (FACS) technique, will allow sensitive and accurate assessment of the inflammatory response of the blood's immune cells (neutrophils and macrophages), increasing the number of experimental repetitions and reducing measurement error.

The growth of Gram negative bacteria in specialized media allows the production and purification of deuterated LPS, which would be very useful in all the neutron scattering techniques used in this thesis. In order to obtain such a compound, it would be necessary to collaborate with institutions such as ISIS or ILL, which possess the facilities required for the production of deuterated biomolecules. The use of isotopically labelled LPS would increase the number of contrasts which could be applied in both SANS and NR experiments, allowing for a better understanding at the molecular level of the peptide/LPS interaction.

Depending on the results obtained from the biological studies in whole-blood, it may be interesting to carry out further SANS and cryo-TEM experiments to clearly determine if the anti-endotoxic role of CAPs is due to LPS sequestration or modification of the LPS aggregate morphologies. The use of asymmetric bilayers composed of smooth LPS would be initially tested because they represent a very

realistic model for the interaction studies with CAPs. In addition, the use of solid state NMR and infrared spectroscopy should enable a deeper understanding of the chain order of LPS in aggregates and bilayers, aiding the elucidation of the effect of CAPs on the molecular packing of the endotoxin within the model.

Appendix A

Protein identification in LPS extracts by SDS gel electrophoresis.

Figure A.1 reports a SDS gel electophoresis of several of extracted and purchased LPS chemotypes. The LPS chemotypes smooth 055B5, Rd F583 and Ra EH100 were purchased from Sigma-Aldrich Ltd. (Dorset, UK) and analysed without further purification. The LPS chemotypes Ra D21, Rb e19, Rc e7, Rd f1, and Re f2 from *E. coli* K12 were cultured as described in Section 3.2.2 and purified according to the original PCP method of Galanos *et al.* [230]. The Figure A.1 shows the bands relative to each LPS chemotype and, in the upper part of the gel, the stripes produced by the contaminants in the preparation. A Biorad Mini Protean 3 electrophoresis casting chamber (Biorad, Hercules, USA) was used to run a 1.0 mm thick SDS gel according to methods described elsewhere [231, 285, 286]. Briefly, the gel was composed of a 4% acrylamide in 1 M Tris HCl, pH 6.8, stacking layer and a 15% acrylamide in 1 M Tris HCl pH 8.8 running layer, both obtained from a Biorad 30% Acrylamide/Bis stock solution (Biorad, Hercules, USA). The LPS samples were prepared by dissolving the LPSs in water and mixing with loading buffer at a sample/buffer ratio of 1:1, in order to obtain approximately 12 μg weight of LPS in each well. The gel was run through a Tris-tricine-SDS running buffer (Sigma-Aldrich Ltd., Dorset, UK) in order to achieve a better resolution [287] than the standard glycine buffer. The gel was run for one hour at constant voltage of 200 mV. The gel was fixed and developed using the silver staining technique of Tsai and Frasch [288] by the use of a Proteosilver kit (Sigma-Aldrich

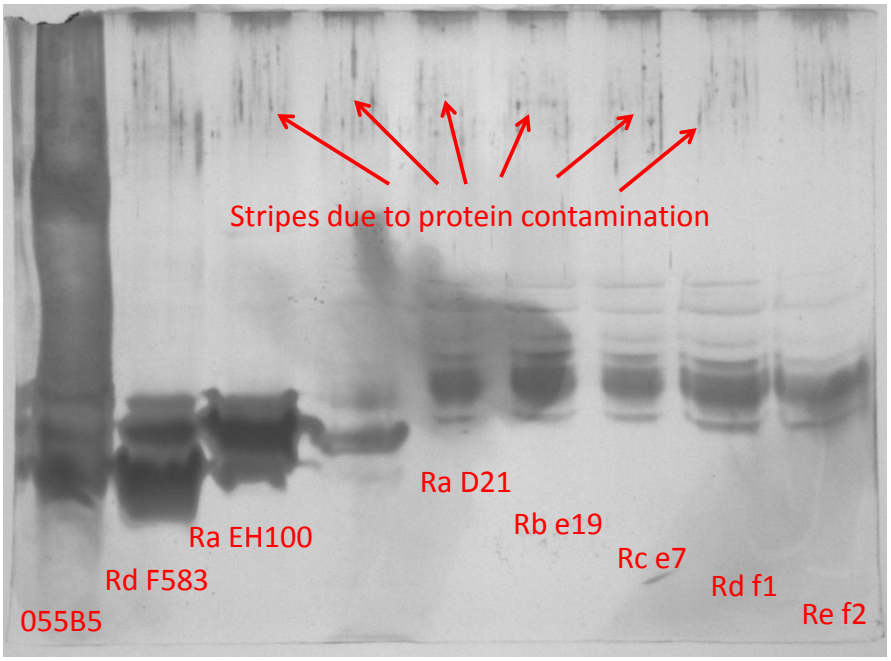

FIGURE A.1: Picture of a 4%/15% SDS gel electrophoresis run in tris-glycine running buffer. From the left the bands correspond to the separation of purschased LPS chemotypes 055B5, Rd F583, Ra Eh100 and the extracted LPS chemotypes Ra D21, Rb e19, Rc e7, Rd f1, and Re f2 from *E. coli* K12.

Ltd., Dorset, UK) and picture of the gel was taken using an Alpha imager EP system (Aplha Innothec, San Leandro, USA).

Appendix B

Details of the peptides LL37 and LFb.

The peptide here referred to as LL37 used in this thesis is a modification of the wild-type peptide cathelicidin LL37 (see Table B.1) . The modified LL37 presents a substitution of the original 17^{th} residue phenylalanine (F) with a tryptophan residue (W). The modified LL37 was purchased from GenScript USA Inc. (Piscataway, USA) with a purity higher than 94%. The cyclic bovine lactoferricin peptide LFb used in this thesis is the fragment of the bovine lactoferrin protein from residue 17 to residue 41 and was purchased from Alpha Diagnostic International Inc. (Sant Antonio, USA).The peptide presents one disulfide bridge formed by the two cysteins residues in position 3 and 21 of the peptide's sequence. The peptides were analysed by RP-HPLC and ESI-MS (see spectra below). The protein data bank (PDB) code for the wild type LL37 and the LFb peptides are respectively "2k6o" and "1lfc" and details of the structures are reported elsewhere [119, 138, 139]. The peptides LL37 and LFb were assessed by electrospray ionization mass spectrometry (ESI-ms) at King's College centre for mass spectrometry and examples of the the spectra are reported. The entire ESI-ms spectra for the peptides LL37 and LFb are shown in Figure B.1 and Figure B.4 respectively. The details of the ESI-MS spectra of the different fragment ions are reported in Figures B.2 and B.3 for LL37 and in Figure B.5 for LFb .

The SLD values of the hydrogenated peptides in different solvents are reported in

TABLE B.1: Primary structure and molecular weight of the LL37 and LFb peptides used in the thesis. Details of the wild type LL37 are reported.

Peptide acronym	Number of amino acid s	Peptide Sequence	Molecular weight (g/mol)
LL37	37	LLGDFFRKSKEKIGKE-W KRIVQRIKDFLRNLVPRTES	4532.4
w.t.[i] LL37	37	LLGDFFRKSKEKIGKEF KRIVQRIKDFLRNLVPRTES	4493.3
LFb [ii]	25	FKCRR-W-Q-W-R MKKLGAPSITCVRRAF	3123.9

[i] wild type [ii] cyclic peptide

Table B.2

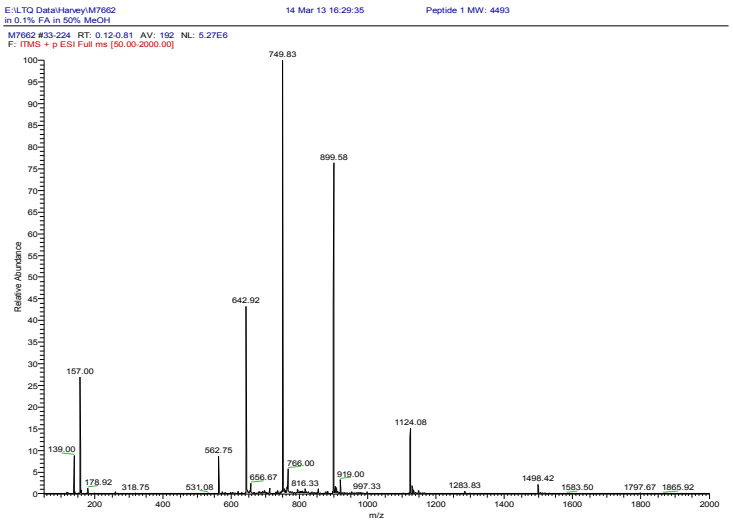

FIGURE B.1: ESI-ms of the peptide LL37 in methanol/water 1:1 with 0.1% trifluoroacetic acid.

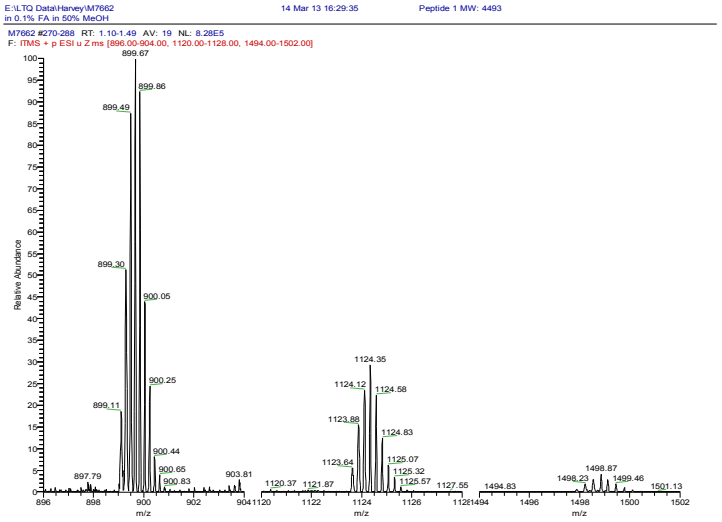

FIGURE B.2: ESI-ms of the peptide LL37 in methanol/water 1:1 with 0.1% trifluoroacetic acid. From the left the details show the peaks for the 5^{th}, 4^{th} and 3^{th} charged ions.

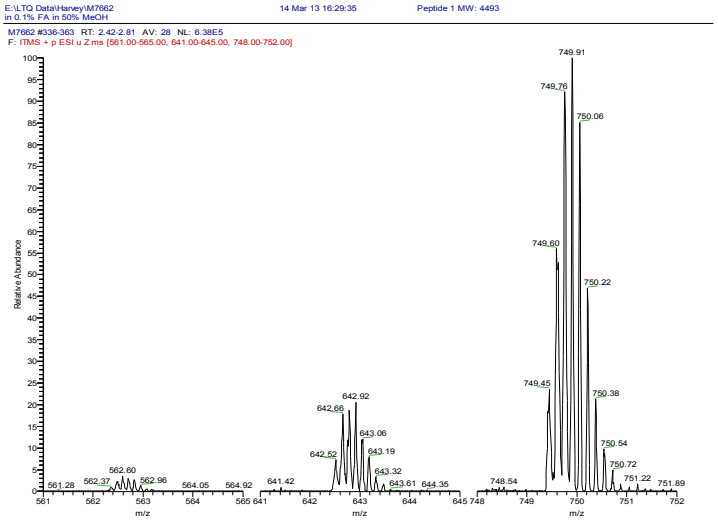

FIGURE B.3: ESI-ms of the peptide LL37 in methanol/water 1:1 with 0.1% trifluoroacetic acid. From the left the details show the peaks for the 8^{th}, 7^{th} and 6^{th} charged ions.

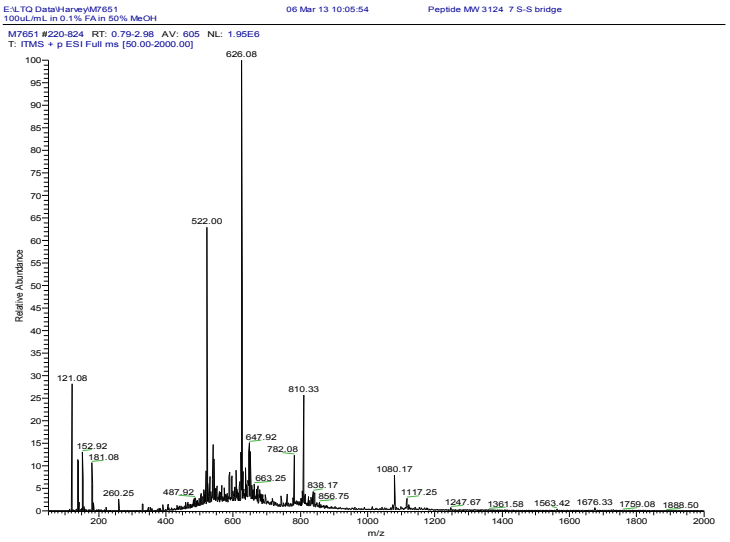

FIGURE B.4: ESI-ms of the peptide LFb in methanol/water 1:1 with 0.1% trifluoroacetic acid.

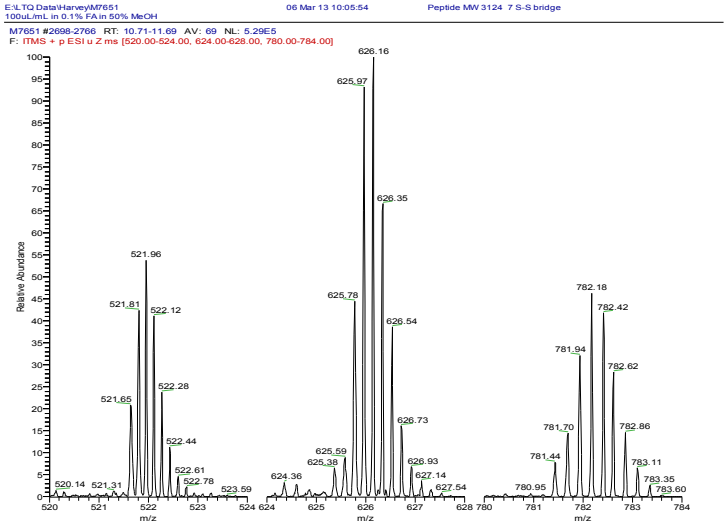

FIGURE B.5: ESI-ms of the peptide LFb in methanol/water 1:1 with 0.1% trifluoroacetic acid. From the left the details show the peaks for the 6^{th}, 5^{th} and 4^{th} charged ions.

TABLE B.2: SLD of the hydrogenated peptides calculated from the online tool [289]. All the SLD values are expressed as $\times 10^{-6}$ Å^{-2} .

	in D_2O	in H_2O	in SMW	in ACMW
	6.38	-0.55	2.08	0.00
LL37	3.27	1.68	2.29	1.81
LFb	3.50	1.73	2.40	1.87

Appendix C

^{2}H NMR supplementary data.

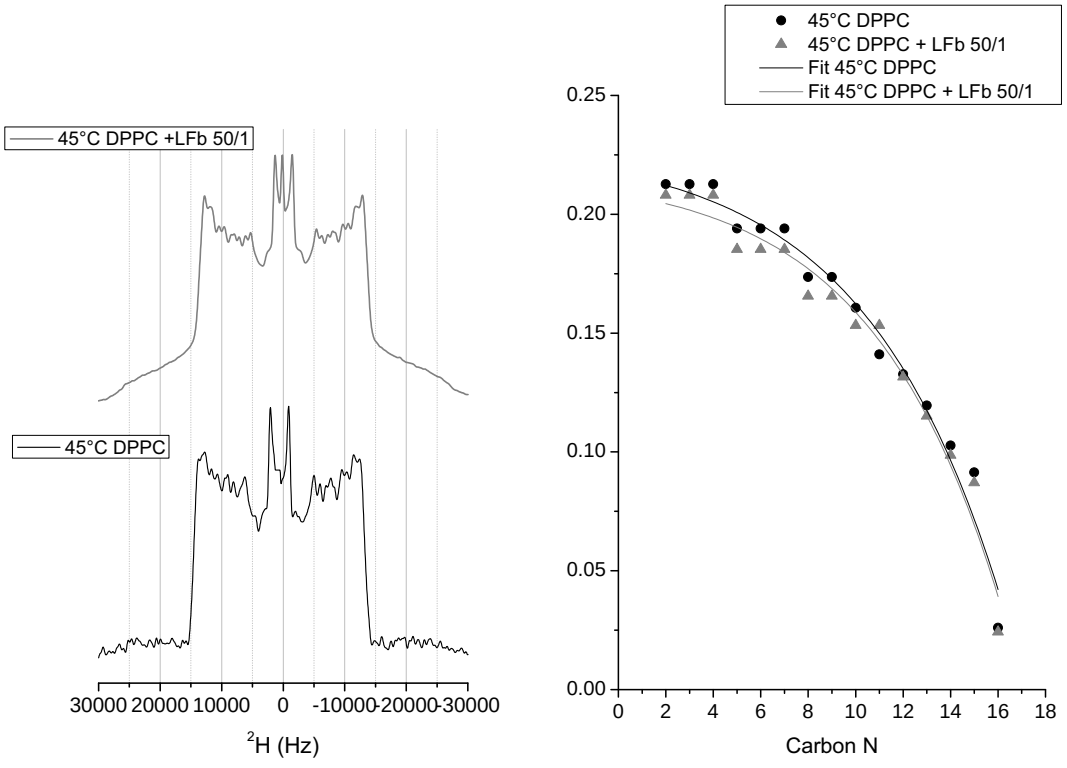

FIGURE C.1: ^{2}H NMR analysis at 45°C of DPPC vesicle in the presence or absence of the peptide LFb at a lipid/peptide molar ratio of 50/1. (A) De-paked powder spectra of D_{62}DPPC signal. (B) Smoothed order parameter (S_{CD}) plot versus the carbon position of the D_{62}DPPC NMR spectra.

Appendix D

Neutron scattering calculations.

The SLD values of the lipids and LPS chemotypes used in this thesis are reported in Table D.1 below. The SLDs were calculated with the use of the SLD calculator provided by the Sansview software in consideration of the chemical formula of the different parts of each molecule. The SLD of hDPPC and D_{62}DPPC were obtained from previously published data [161]. The structures of the LPSs are reported in Figures 1.5 and 1.6.

Table D.1: SLD values of molecules and solvents used in this thesis.

Molecule	Description	formula	SLD x10^{-6} (Å^{-2})
Water		H_2O	-0.56
Deuterium oxide		D_2O	6.36
ACMW solution	8% D_2O in water		0.00
SMW solution	38% D_2O in water		2.07
Silicon		Si	2.07
Silicon oxide		SiO_2	3.41
hDPPC	Tails	C32H62O2	-0.39
	headgroup	C8H18NO6P	1.98
D_{62}DPPC	Tails	C32H2D62O2	7.45
	headgroup	C8H18NO6P	1.98
lipid A-2Kdo			
tails	Tails	C78H160O6	-0.39
inner core	2GlcN-2P-2Kdo	C32H48N2O33P2(-2)	1.60
LPS Rc J5			
inner core	2GlcN-2Kdo-1PEtn	C32H48N2O33P2(2-)	1.56
outer core	3Hep-2Glc-1P-1PPEtn	C33H58NO30P2(-2)	1.26
LPS Rc^- E7			
inner core	2GlcN-2P-2Kdo	C32H48N2O33P2(-2)	1.60
outer core	2Hep-1Glc	C20H36O17	1.17
LPS Ra D21			
inner core	2GlcN-2Kdo-1Rha	C38H56N2O37P2(-2)	1.55
outer core	3Hep-3Glc-1Gal-1P-1PEtn	C56H99N2O47P2(-1)	1.25
LPS Ra Eh100			
inner core	2GlcN-2Kdo-1Gal-1PEtn	C40H64N3O41P3(-2)	1.53
outer core	3Hep-3Glc-1Gal-1GlcNac-1P-1PEtn	C55H97N2O50P2(-1)	1.29

Appendix E

Neutron reflectivity of mixed LPS/DPPC monolayers at the air/liquid interface and interaction with antimicrobial peptides.

Comparison of the reflectivity and SLD profiles of the mixed monolayers containing hDPPC (Eh-20 and J5-20 monolayers) or D_{62}DPPC (d-Eh-20 and d-J5-20 monolayers) in D_2O subphase in the presence or absence in the subphase of the peptides, either LL37 or LFb .

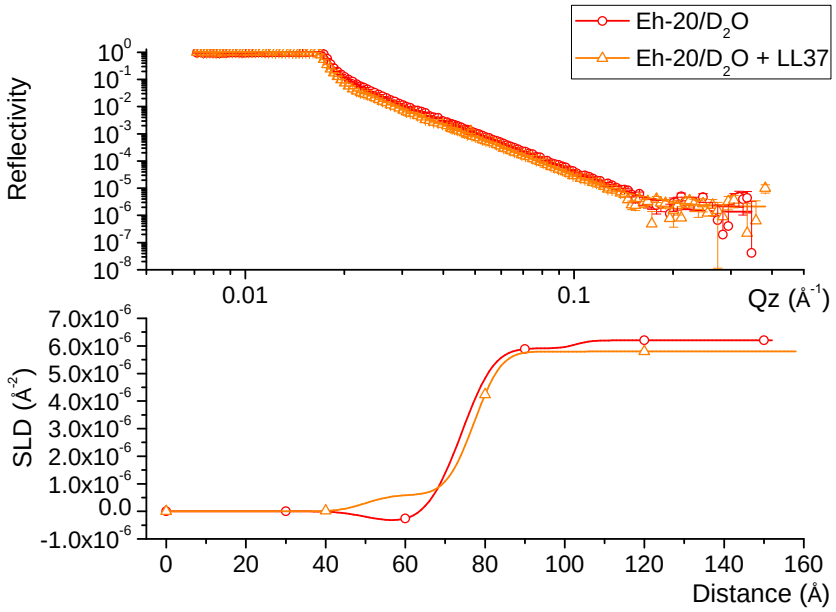

FIGURE E.1: NR fitted data of Eh-20 monolayer on D_2O subphase containing 1 mM $MgCl_2$ solution at 22°C before and after the subphase injection of the peptides LL37 and LFb. Upper plot: reflectivity profile. Lower plot: SLD profile

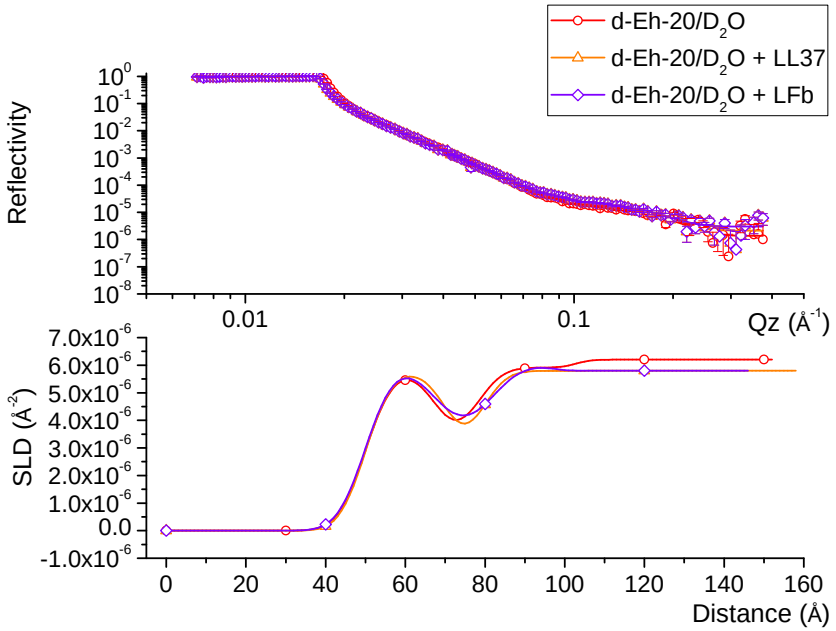

FIGURE E.2: NR fitted data of d-Eh-20 monolayer on D_2O subphase containing 1 mM $MgCl_2$ solution at 22°C before and after the subphase injection of the peptides LL37 and LFb Upper plot: reflectivity profile. Lower plot: SLD profile

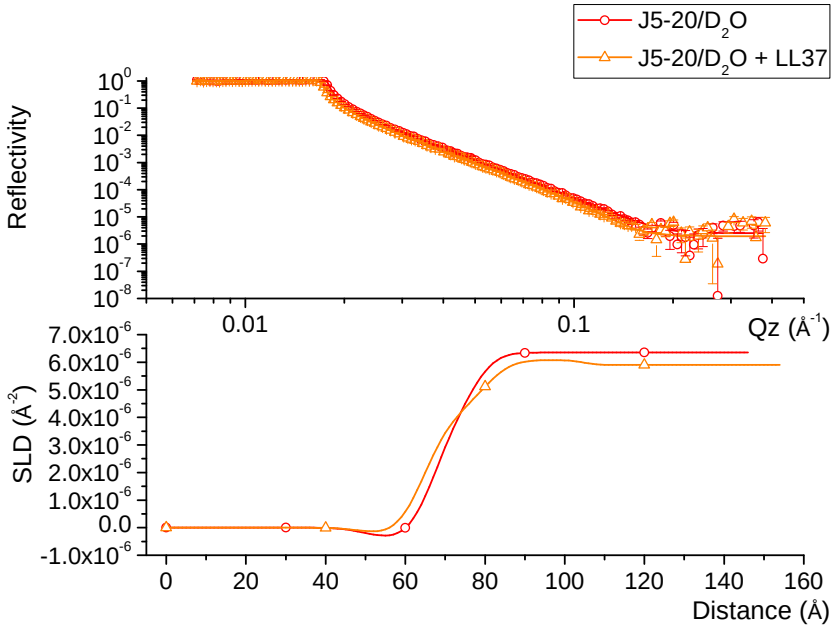

FIGURE E.3: NR fitted data of J5-20 monolayer on D_2O subphase containing 1 mM $MgCl_2$ solution at 22°C before and after the subphase injection of the peptides LL37 and LFb Upper plot: reflectivity profile. Lower plot: SLD profile

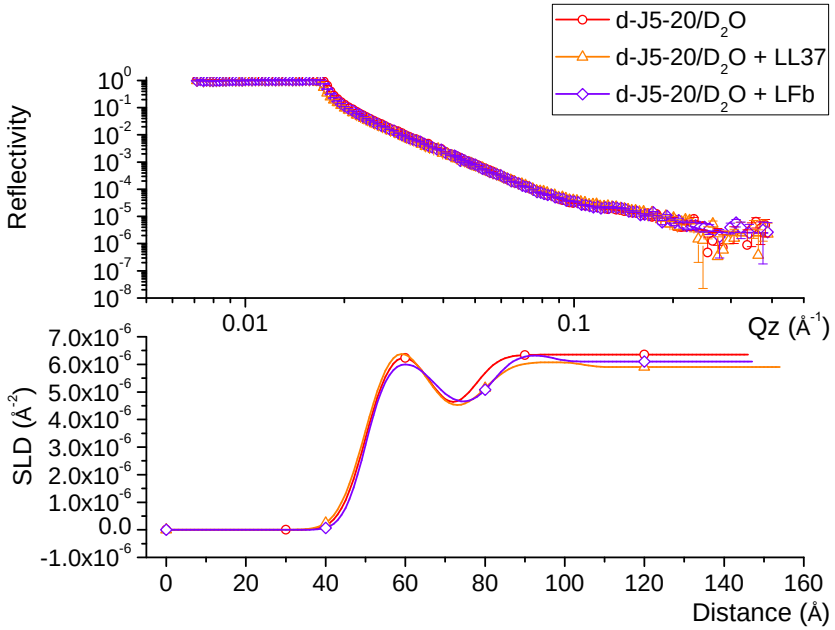

FIGURE E.4: NR fitted data of d-J5-20 monolayer on D_2O subphase containing 1 mM $MgCl_2$ solution at 22°C before and after the subphase injection of the peptides LL37 and LFb Upper plot: reflectivity profile. Lower plot: SLD profile

Appendix F

Neutron reflectivity data of asymmetric bilayers of DPPC and LPS and interaction with antimicrobial peptides.

Figures F.1 and F.3 show the comparison of the neutron reflectivity profiles of the bilayer Eh100 in H_2O and SMW contrasts, in the absence and in the presence of the peptides, either LL37 or LFb . Figures F.2 and F.2 show the comparison of the neutron reflectivity profiles of the bilayer J5 in H_2O and SMW contrasts, in the absence and in the presence of the peptide LL37 . The discussion of the plots is reported in Section 4.3.5.

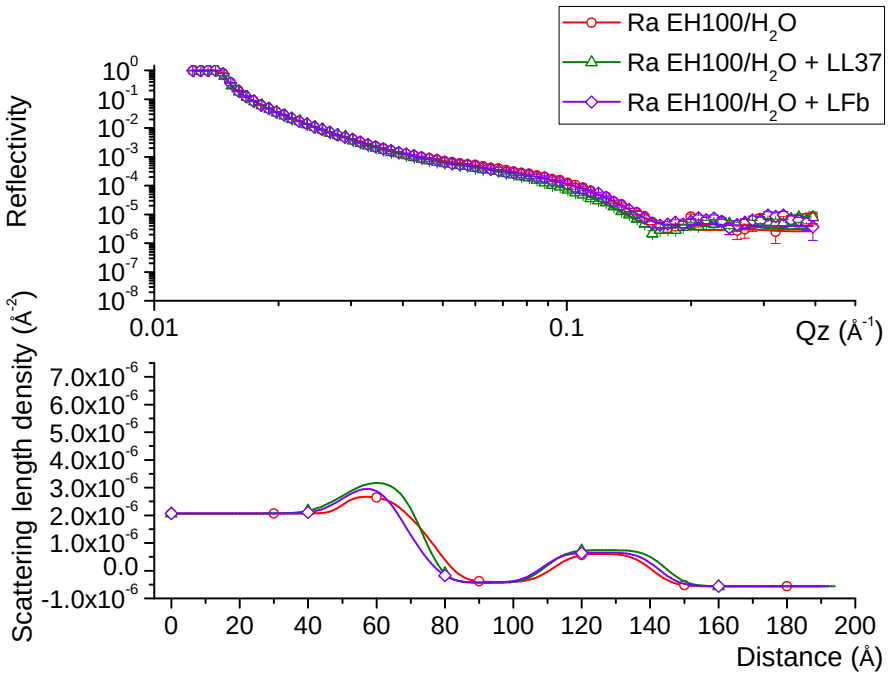

FIGURE F.1: Reflectivity (upper plot) and SLD (lower plot) profiles of the EH100 bilayer in H_2O solution containing 1 mM $MgCl_2$ at 37°C in the absence or presence of the peptides, either LL37 or LFb.

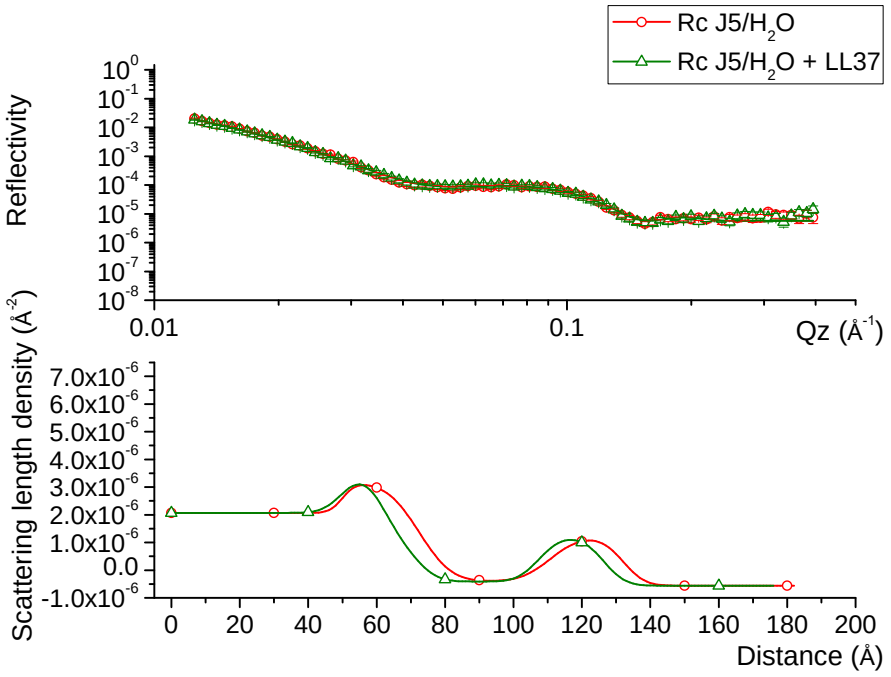

FIGURE F.2: Reflectivity (upper plot) and SLD (lower plot) profiles of the J5 bilayer in H_2O solution containing 1 mM $MgCl_2$ at 37°C in the absence or presence of the peptide LL37.

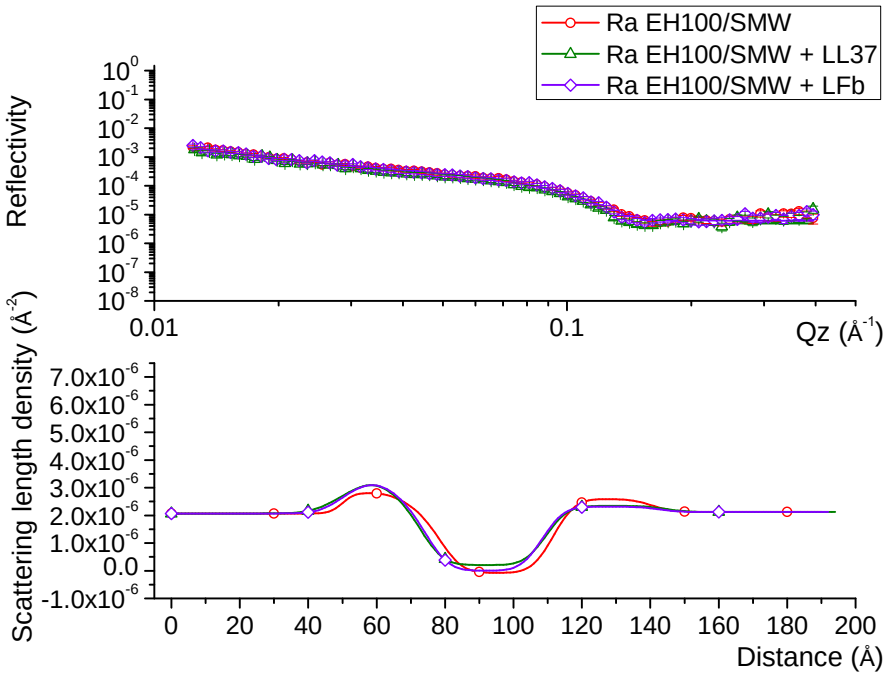

FIGURE F.3: Reflectivity (upper plot) and SLD (lower plot) profiles of the EH100 bilayer in SMW solution containing 1 mM $MgCl_2$ at 37°C in the absence or presence of the peptides, either LL37 or LFb.

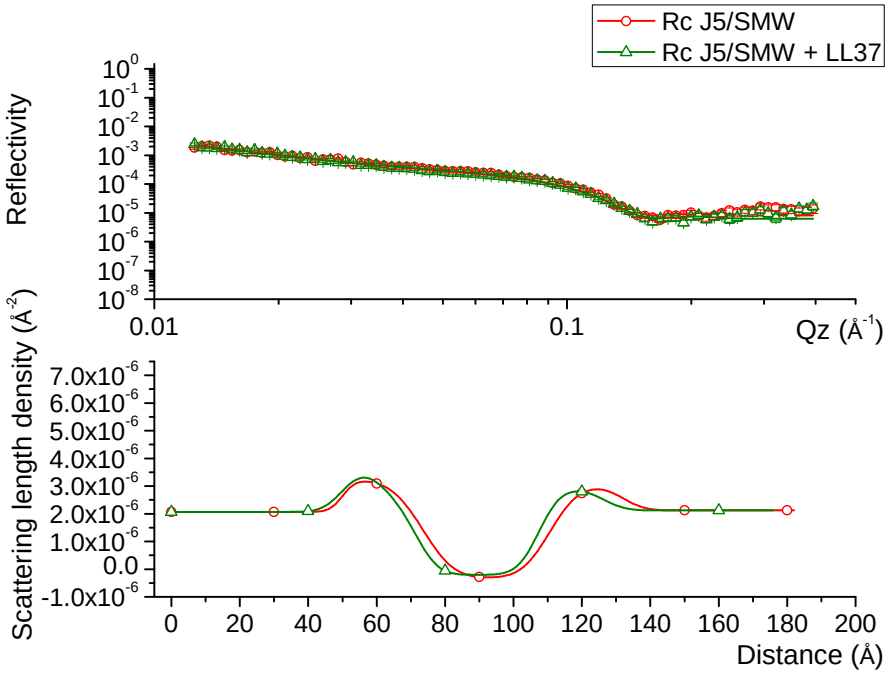

FIGURE F.4: Reflectivity (upper plot) and SLD (lower plot) profiles of the J5 bilayer in SMW solution containing 1 mM $MgCl_2$ at 37°C in the absence or presence of the peptide LL37.

Bibliography

[1] Agency for Healthcare Research and Quality (US), "HCUP Facts and Figures: Statistics on Hospital-Based Care in the United States (2009)," 2011. Online: http://www.ncbi.nlm.nih.gov/books/NBK91984/

[2] A. I.Hidron, J. R.Edwards *et al.*, "NHSN annual update: antimicrobial-resistant pathogens associated with healthcare-associated infections: annual summary of data reported to the National Healthcare Safety Network at the Centers for Disease Control and Prevention, 2006-2007." *Infection Control and Hospital Epidemiology*, vol. 29, no. 11, pp. 996–1011, 2008.

[3] Public Health England, "HCAI and Antimicrobial Point Prevalence Survey England," 2011. Online: http://www.hpa.org.uk/Topics/InfectiousDiseases/InfectionsAZ/AntimicrobialResistance/HCAIPointPrevalenceSurvey/

[4] S.Elgohari, E. S.S. Thelwall, T. Lamagni, and A.Charlett, "Surveillance of Surgical Site Infections in NHS hospitals in England," p. 29, 2011. Online: http://www.hpa.org.uk/Publications/InfectiousDiseases/SurgicalSiteInfectionReports/1311SSIreport2012to2013data/

[5] D. M.Livermore, R.Hope *et al.*, "Non-susceptibility trends among Enterobacteriaceae from bacteraemias in the UK and Ireland, 2001-06." *The Journal of Antimicrobial Chemotherapy*, vol. 62, no. 2, pp. 41–54, 2008.

[6] R. A.Weinstein, "Epidemiology and control of nosocomial infections in adult intensive care units," *American Journal of Medicine*, vol. 91, no. 3, Supplement 2, pp. 179–184, 1991.

[7] R. A.Weinstein, R.Gaynes, and J. R.Edwards, "Overview of nosocomial infections caused by Gram-negative bacilli," *Clinical Infectious Diseases*, vol. 41, no. 6, pp. 848–854, 2005.

[8] G. M.Rossolini and E.Mantengoli, "Antimicrobial resistance in Europe and its potential impact on empirical therapy." *Clinical Microbiology and infection*, vol. 14, pp. 2–8, 2008.

[9] European centre for disease prevention and control (ECDC), "Publications: Annual Epidemiological Report 2012," 2012. Online: http://ecdc.europa.eu/en/publications/Publications/Forms/ECDC_DispForm.aspx?ID=1069

[10] European Center for Disease Prevention and Control (ECDC), "European Antimicrobial Resistance Surveillance Network (EARS-Net)," 2012. Online: http://ecdc.europa.eu/en/activities/surveillance/EARS-Net/database/Pages/database.aspx

[11] Centre for Disease Control and Prevention (CDC), "CDC Online Newsroom Press Release : Action needed now to halt spread of deadly bacteria," 2013. Online: http://www.cdc.gov/media/releases/2013/p0305_deadly_bacteria.html

[12] D.Cressey, "Drug-resistant bacteria and lack of new antibiotics pose catastrophic threat : Nature News Blog," 2013. Online: http://blogs.nature.com/news/2013/03/drug-resistant-bacteria-and-lack-of-new-antibiotics-pose-catastrophic-threat.html

[13] B.Spellberg, J. H.Powers *et al.*, "Trends in antimicrobial drug development: implications for the future." *Clinical Infectious Diseases*, vol. 38, no. 9, pp. 1279–86, 2004.

[14] C. J.Thomson, E.Power *et al.*, "Antibacterial research and development in the 21(st) Century an industry perspective of the challenges." *Current Opinion in Microbiology*, vol. 7, no. 5, pp. 445–50, 2004.

[15] S. R.Norrby, C. E.Nord, and R.Finch, "Lack of development of new antimicrobial drugs: a potential serious threat to public health." *The Lancet Infectious Diseases*, vol. 5, no. 2, pp. 115–9, 2005.

[16] R. E. W.Hancock and H. G.Sahl, "Antimicrobial and host-defense peptides as new anti-infective therapeutic strategies." *Nature Biotechnology*, vol. 24, no. 12, pp. 1551–7, 2006.

[17] A.Peschel and H.-G.Sahl, "The co-evolution of host cationic antimicrobial peptides and microbial resistance." *Nature Reviews Microbiology*, vol. 4, no. 7, pp. 529–36, 2006.

[18] H.Nikaido, "Prevention of drug access to bacterial targets: permeability barriers and active efflux." *Science*, vol. 264, no. 5157, pp. 382–8, 1994.

[19] H.Nikaido, "Molecular Basis of Bacterial Outer Membrane Permeability Revisited," *Microbiology and Molecular Biology Reviews*, vol. 67, no. 4, pp. 593–656, 2003.

[20] F. C.Neidhardt and R.Curtiss, *Escherichia coli and Salmonella : cellular and molecular biology*, ser. Progress in Molecular Biology and Translational Science, F.Neidhardt, R.Curtiss 3rd *et al.*, Eds. ASM Press, 1996, vol. 2, no. 155.

[21] A. P.Le Brun, L. A.Clifton *et al.*, "Structural characterization of a model gram-negative bacterial surface using lipopolysaccharides from rough strains of Escherichia coli." *Biomacromolecules*, vol. 14, no. 6, pp. 2014–22, 2013.

[22] E. T.Rietschel, T.Kirikae *et al.*, "Bacterial endotoxin: molecular relationships of structure to activity and function," *FASEB Journal*, vol. 8, no. 2, pp. 217–225, 1994.

[23] B. L.Reynolds and H.Pruul, "Protective role of smooth lipopolysaccharide in the serum bactericidal reaction." *Infection and Immunity*, vol. 4, no. 6, pp. 764–71, 1971.

[24] M.Vaara, "Antibiotic-supersusceptible mutants of Escherichia coli and Salmonella typhimurium," *Antimicrobial Agents and Chemotherapy*, vol. 37, no. 11, pp. 2255–2260, 1993.

[25] S.Snyder, D.Kim, and T. J.McIntosh, "Lipopolysaccharide bilayer structure: effect of chemotype, core mutations, divalent cations, and temperature," *Biochemistry*, vol. 38, no. 33, pp. 10 758–10 767, 1999.

[26] D. S.Snyder and T. J.McIntosh, "The lipopolysaccharide barrier: Correlation of antibiotic susceptibility with antibiotic permeability and fluorescent probe binding kinetics," *Biochemistry*, vol. 39, no. 38, pp. 11 777–11 787, 2000.

[27] M.Boll, J.Radziejewska-Lebrecht *et al.*, "4-Amino-4-Deoxy-L-Arabinose in LPS of Enterobacterial R-Mutants and Its Possible Role for Their Polymyxin Reactivity," *FEMS Immunology and Medical Microbiology*, vol. 8, no. 4, pp. 329–341, 1994.

[28] S.Das, M.Ramm *et al.*, "Structural Studies of the Side-Chain of Outer-Membrane Lipopolysaccharide from Pseudomonas-Syringae Pv Coriandricola W-43," *Journal of Bacteriology*, vol. 176, no. 21, pp. 6550–6557, 1994.

[29] S. G.Wilkinson, "Bacterial lipopolysaccharides - Themes and variations," *Progress in Lipid Research*, vol. 35, no. 3, pp. 283–343, 1996.

[30] R. S.Conrad, M.Boll *et al.*, "The occurrence of 4-amino-4-deoxy-arabinose in LPS of supersusceptible strain Pseudomonas aeruginosa Z61: noncorrelation with polymyxin resistance," *Current Microbiology*, vol. 38, no. 4, pp. 228–232, 1999.

[31] G.Stevenson, B.Neal *et al.*, "Structure of the O-Antigen of Escherichia-Coli-K-12 and the Sequence of Its Rfb Gene-Cluster," *Journal of Bacteriology*, vol. 176, no. 13, pp. 4144–4156, 1994.

[32] O.Holst, S.Mullerloennies *et al.*, "Chemical-Structure of the Lipid-a of Escherichia-Coli J-5," *European Journal of Biochemistry*, vol. 214, no. 3, pp. 695–701, 1993.

[33] S.Müller-Loennies, B.Lindner, and H.Brade, "Structural analysis of deacylated lipopolysaccharide of Escherichia coli strains 2513 (R4 core-type) and F653 (R3 core-type)," *European Journal of Biochemistry*, vol. 269, no. 23, pp. 5982–5991, 2002.

[34] N. A.Fuller, M. C.Wu *et al.*, "Biosynthesis of cell-wall lipopolysaccharide in Escherichia coli .7. characterization of heterogeneous core oligosaccharide structures," *Journal of Biological Chemistry*, vol. 248, no. 22, pp. 7938–7950, 1973.

[35] O.Holst, "The structures of core regions from enterobacterial lipopolysaccharides - an update," *FEMS Microbiology Letters*, vol. 271, no. 1, pp. 3–11, 2007.

[36] H. G.Boman and D. A.Monner, "Characterization of Lipopolysaccharides from Escherichia-Coli K-12 Mutants," *Journal of Bacteriology*, vol. 121, no. 2, pp. 455–464, 1975.

[37] G.Hammerling, O.Luderitz *et al.*, "Structural Investigations on the Core Polysaccharide of Escherichia coli 0100," *European Journal of Biochemistry*, vol. 22, no. 3, pp. 331–344, 1971.

[38] P. E.Jansson, A. A.Lindberg *et al.*, "Structural studies on the hexose region of the core in lipopolysaccharides from enterobacteriaceae," *European Journal of Biochemistry*, vol. 115, no. 3, pp. 571–577, 1981.

[39] S.Müller-Loennies, O.Holst, and H.Brade, "Chemical structure of the core region of Escherichia coli J-5 lipopolysaccharide." *European Journal of Biochemistry*, vol. 224, no. 2, pp. 751–60, 1994.

[40] S.Müller-Loennies, O.Holst *et al.*, "Isolation and structural analysis of phosphorylated oligosaccharides obtained from Escherichia coli J-5 lipopolysaccharide." *European Journal of Biochemistry*, vol. 260, no. 1, pp. 235–249, 1999.

[41] M.Inagaki, T.Kawaura *et al.*, "Different contributions of the outer and inner R-core residues of lipopolysaccharide to the recognition by spike H and G proteins of bacteriophage phiX174." *FEMS Microbiology Letters*, vol. 226, no. 2, pp. 221–7, 2003.

[42] S.Müller-Loennies, B.Lindner, and H.Brade, "Structural analysis of oligosaccharides from lipopolysaccharide (LPS) of Escherichia coli K12 strain W3100 reveals a link between inner and outer core LPS biosynthesis," *Journal of Biological Chemistry*, vol. 278, no. 36, pp. 34 090–34 101, 2003.

[43] D.Karibian, C.Deprun, and M.Caroff, "Comparison of lipids A of several Salmonella and Escherichia strains by 252Cf plasma desorption mass spectrometry." *Journal of Bacteriology*, vol. 175, no. 10, pp. 2988–93, 1993.

[44] C. R. H.Raetz, "Bacterial Lipopolysaccharides: a remarkable family of bioactive macroamphiphiles," Washington, 1996.

[45] H. G.Boman, S.Jonsson *et al.*, "Cell surface alterations in Escherichia coli K-12 with chromosomal mutations changing ampicillin resistance," *Annals of the New York Academy of Sciences*, vol. 182, pp. 342–352, 1971.

[46] J. H.Banoub, A.El Aneed *et al.*, "Structural investigation of bacterial lipopolysaccharides by mass spectrometry and tandem mass spectrometry," *Mass Spectrometry Reviews*, vol. 29, no. 4, pp. 606–650, 2010.

[47] K. R.Eriksson-Grennberg, K.Nordstrom, and P.Englund, "Resistance of Escherichia coli to penicillins. IX. Genetics and physiology of class II ampicillin-resistant mutants that are galactose negative or sensitive to bacteriophage C21, or both," *Journal of Bacteriology*, vol. 108, no. 3, pp. 1210–1223, 1971.

[48] J.Gmeiner and S.Schlecht, "Molecular composition of the outer membrane of Escherichia coli and the importance of protein-lipopolysaccharide interactions," *Archives of Microbiology*, vol. 127, no. 2, pp. 81–86, 1980.

[49] P.Prehm, S.Stirm *et al.*, "Cell-wall lipopolysaccharides of ampicillin-resistant mutants of Escherichia coli K-12," *European Journal of Biochemistry*, vol. 66, no. 2, pp. 369–377, 1976.

[50] H.Mayer, A. M.Rapin *et al.*, "Immunochemical studies on lipopolysaccharides from wild-type and mutants of Escherichia coli K-12," *European Journal of Biochemistry*, vol. 66, no. 2, pp. 357–368, 1976.

[51] J. A.Yethon, D. E.Heinrichs *et al.*, "Involvement of waaY, waaQ, and waaP in the modification of Escherichia coli lipopolysaccharide and their role in the formation of a stable outer membrane," *Journal of Biological Chemistry*, vol. 273, no. 41, pp. 26 310–26 316, 1998.

[52] C. A.Schnaitman and J. D.Klena, "Genetics of lipopolysaccharide biosynthesis in enteric bacteria," *Microbiological Reviews*, vol. 57, no. 3, pp. 655–682, 1993.

[53] K.Brandenburg and U.Seydel, "Investigation into the fluidity of lipopolysaccharide and free lipid A membrane systems by Fourier-transform infrared spectroscopy and differential scanning calorimetry," *European Journal of Biochemistry*, vol. 191, no. 1, pp. 229–236, 1990.

[54] H.Labischinski, G.Barnickel *et al.*, "High state of order of isolated bacterial lipopolysaccharide and its possible contribution to the permeation barrier property of the outer membrane," *Journal of Bacteriology*, vol. 162, no. 1, pp. 9–20, 1985.

[55] P.Plésiat and H.Nikaido, "Outer membranes of Gram negative bacteria are permeable to steroid probes." *Molecular Microbiology*, vol. 6, no. 10, pp. 1323–33, 1992.

[56] U.Seydel, M. H.Koch, and K.Brandenburg, "Structural polymorphisms of rough mutant lipopolysaccharides Rd to Ra from Salmonella minnesota," *Journal of Structural Biology*, vol. 110, no. 3, pp. 232–243, 1993.

[57] R. T.Coughlin, A.Haug, and E. J.Mcgroarty, "Physical properties of defined lipopolysaccharide salts," *Biochemistry*, vol. 22, no. 8, pp. 2007–2013, 1983.

[58] K.Brandenburg and U.Seydel, "Physical aspects of structure and function of membranes made from lipopolysaccharides and free lipid A," *Biochimica et Biophysica Acta - Biomembranes*, vol. 775, no. 2, pp. 225–238, 1984.

[59] U.Seydel, K.Brandenburg *et al.*, "Supramolecular structure of lipopolysaccharide and free lipid A under physiological conditions as determined by synchrotron small-angle X-ray diffraction," *European Journal of Biochemistry*, vol. 186, no. 1-2, pp. 325–332, 1989.

[60] C.Galanos and O.Lüderitz, "Electrodialysis of lipopolysaccharides and their conversion to uniform salt forms." *European Journal of Biochemistry*, vol. 54, no. 2, pp. 603–10, 1975.

[61] C.Alexander and E. T.Rietschel, "Bacterial lipopolysaccharides and innate immunity," *Journal of Endotoxin Research*, vol. 7, no. 3, pp. 167–202, 2001.

[62] J.Cohen, "The immunopathogenesis of sepsis," *Nature*, vol. 420, no. 6917, pp. 885–891, 2002.

[63] R.Jerala, "Structural biology of the LPS recognition," *International Journal of Medical Microbiology*, vol. 297, no. 5, pp. 353–363, 2007.

[64] B.Yu and S. D.Wright, "Catalytic properties of lipopolysaccharide (LPS) binding protein - Transfer of LPS to soluble CD14," *Journal of Biological Chemistry*, vol. 271, no. 8, pp. 4100–4105, 1996.

[65] M.Mueller, B.Lindner *et al.*, "Aggregates are the biologically active units of endotoxin," *Journal of Biological Chemistry*, vol. 279, no. 25, pp. 26 307–26 313, 2004.

[66] J. K.Eckert, Y. J.Kim *et al.*, "The crystal structure of lipopolysaccharide binding protein reveals the location of a frequent mutation that impairs innate immunity." *Immunity*, vol. 39, no. 4, pp. 647–60, 2013.

[67] N.Lamping, A.Hoess *et al.*, "Effects of site-directed mutagenesis of basic residues (Arg 94, Lys 95, Lys 99) of lipopolysaccharide (LPS)-binding protein on binding and transfer of LPS and subsequent immune cell activation," *Journal of Immunology*, vol. 157, no. 10, pp. 4648–4656, 1996.

[68] S.Roes, F.Mumm *et al.*, "Localization of the lipopolysaccharide-binding protein in phospholipid membranes by atomic force microscopy." *Journal of Biological Chemistry*, vol. 281, no. 5, pp. 2757–63, 2006.

[69] T.Gutsmann, M.Müller *et al.*, "Dual role of lipopolysaccharide (LPS)-binding protein in neutralization of LPS and enhancement of LPS-induced activation of mononuclear cells." *Infection and Immunity*, vol. 69, no. 11, pp. 6942–50, 2001.

[70] M.Müeller, B.Lindner *et al.*, "Endotoxin: physical requirements for cell activation," *Journal of Endotoxin Research*, vol. 11, no. 5, pp. 299–303, 2005.

[71] N.Iovine, J.Eastvold *et al.*, "The carboxyl-terminal domain of closely related endotoxin-binding proteins determines the target of protein-lipopolysaccharide complexes." *Journal of Biological Chemistry*, vol. 277, no. 10, pp. 7970–8, 2002.

[72] J. A.Gegner, R. J.Ulevitch, and P. S.Tobias, "Lipopolysaccharide (LPS) signal transduction and clearance. Dual roles for LPS binding protein and membrane CD14." *Journal of Biological Chemistry*, vol. 270, no. 10, pp. 5320–5, 1995.

[73] R. I.Tapping and P. S.Tobias, "Cellular binding of soluble CD14 requires lipopolysaccharide (LPS) and LPS-binding protein," *Journal of Biological Chemistry*, vol. 272, no. 37, pp. 23 157–23 164, 1997.

[74] R.Dziarski, "Recognition of bacterial peptidoglycan by the innate immune system." *Cellular and Molecular Life Sciences*, vol. 60, no. 9, pp. 1793–804, 2003.

[75] T. L.Gioannini, A.Teghanemt *et al.*, "Monomeric endotoxin:protein complexes are essential for TLR4-dependent cell activation." *Journal of Endotoxin Research*, vol. 11, no. 2, pp. 117–23, 2005.

[76] S.Viriyakosol, P. S.Tobias *et al.*, "MD-2 binds to bacterial lipopolysaccharide." *Journal of Biological Chemistry*, vol. 276, no. 41, pp. 38 044–51, 2001.

[77] M.Manček, P.Pristovšek, and R.Jerala, "Identification of LPS-binding peptide fragment of MD-2, a Toll-receptor accessory protein," *Biochemical and Biophysical Research Communications*, vol. 292, no. 4, pp. 880–885, 2002.

[78] A.Visintin, E.Latz *et al.*, "Lysines 128 and 132 enable lipopolysaccharide binding to MD-2, leading to Toll-like receptor-4 aggregation and signal transduction." *Journal of Biological Chemistry*, vol. 278, no. 48, pp. 48 313–20, 2003.

[79] Y.-C.Lu, W.-C.Yeh, and P. S.Ohashi, "LPS/TLR4 signal transduction pathway," *Cytokine*, vol. 42, no. 2, pp. 145–151, 2008.

[80] C. A.Dinarello, "Proinflammatory and Anti-inflammatory Cytokines as Mediators in the Pathogenesis of Septic Shock," *CHEST Journal*, vol. 112, p. 321S, 1997.

[81] C. A.Aurell, M. E.Hawley, and A. O.Wiström, "Direct visualization of Gram-negative bacterial lipopolysaccharide self-assembly," *Molecular Cell Biology Research Communications*, vol. 2, no. 1, pp. 42–46, 1999.

[82] J. N.Israelachvili, "The science and applications of emulsions an overview," *Colloids and Surfaces A: Physicochemical and Engineering Aspects*, vol. 91, pp. 1–8, 1994.

[83] J. N.Israelachvili, *Intermolecular and Surface Forces*, J. N.Israelachvili, Ed. Academic Press, 1992, vol. 450, no. 2.

[84] K.Brandenburg, J.Andrä *et al.*, "Physicochemical properties of bacterial glycopolymers in relation to bioactivity," *Carbohydrate Research*, vol. 338, no. 23, pp. 2477–2489, 2003.

[85] K.Brandenburg, L.Hawkins *et al.*, "Structural polymorphism and endotoxic activity of synthetic phospholipid-like amphiphiles." *Biochemistry*, vol. 43, no. 13, pp. 4039–46, 2004.

[86] K.Brandenburg, S.Kusumoto, and U.Seydel, "Conformational studies of synthetic lipid A analogues and partial structures by infrared spectroscopy," *Biochimica et Biophysica Acta-Biomembranes*, vol. 1329, no. 1, pp. 183–201, 1997.

[87] K.Brandenburg, M. H.Koch, and U.Seydel, "Phase diagram of deep rough mutant lipopolysaccharide from Salmonella minnesota R595," *Journal of Structural Biology*, vol. 108, no. 2, pp. 93–106, 1992.

[88] K.Brandenburg and U.Seydel, "Infrared spectroscopy of glycolipids," *Chemistry and Physics of Lipids*, vol. 96, no. 1, pp. 23–40, 1998.

[89] K.Brandenburg, S.Funari *et al.*, "Investigation into the Acyl Chain Packing of Endotoxins and Phospholipids under Near Physiological Conditions by WAXS and FTIR Spectroscopy," *Journal of Structural Biology*, vol. 128, no. 2, pp. 175–186, 1999.

[90] P.Garidel, M.Rappolt *et al.*, "Divalent cations affect chain mobility and aggregate structure of lipopolysaccharide from Salmonella minnesota reflected in a decrease of its biological activity," *Biochimica et Biophysica Acta-Biomembranes*, vol. 1715, no. 2, pp. 122–131, 2005.

[91] A. B.Schromm, K.Brandenburg *et al.*, "The charge of endotoxin molecules influences their conformation and IL-6-inducing capacity." *Journal of Immunology*, vol. 161, no. 10, pp. 5464–71, 1998.

[92] E. T.Rietschel, T.Gutsmann *et al.*, "The physicochemistry of endotoxins in relation to bioactivity," *International Journal of Medical Microbiology*, vol. 297, no. 5, pp. 341–352, 2007.

[93] K.Nomura, T.Inaba *et al.*, "Interaction of lipopolysaccharide and phospholipid in mixed membranes: solid-state 31P-NMR spectroscopic and microscopic investigations," *Biophysical Journal*, vol. 95, no. 3, pp. 1226–1238, 2008.

[94] H. G.Boman, "Peptide antibiotics and their role in innate immunity." *Annual Review of immunology*, vol. 13, pp. 61–92, 1995.

[95] R. E. W.Hancock, "Peptide antibiotics," *Lancet*, vol. 349, no. 9049, pp. 418–422, 1997.

[96] M.Zasloff, "Antimicrobial peptides of multicellular organisms." *Nature*, vol. 415, no. 6870, pp. 389–95, 2002.

[97] H. G.Boman, "Antibacterial peptides: basic facts and emerging concepts," *Journal of Internal Medicine*, vol. 254, no. 3, pp. 197–215, 2003.

[98] G.Wang, X.Li, and Z.Wang, "APD2: the updated antimicrobial peptide database and its application in peptide design." *Nucleic Acids Research*, vol. 37, pp. 933–937, 2009.

[99] G.Wang, Z. and Wang, "Welcome to the Antimicrobial Peptide Database and Analysis System," 2013. Online: http://aps.unmc.edu/AP/main.php

[100] P. M.Hwang and H. J.Vogel, "Structure-function relationships of antimicrobial peptides." *Biochemistry and Cell Biology*, vol. 76, pp. 235–46, 1998.

[101] M. R.Yeaman and N. Y.Yount, "Mechanisms of antimicrobial peptide action and resistance." *Pharmacological Reviews*, vol. 55, no. 1, pp. 27–55, 2003.

[102] P.Bulet, R.Stöcklin, and L.Menin, "Anti-microbial peptides: from invertebrates to vertebrates." *Immunological Reviews*, vol. 198, pp. 169–84, 2004.

[103] L. J.Zhang, A.Rozek, and R. E. W.Hancock, "Interaction of cationic antimicrobial peptides with model membranes," *Journal of Biological Chemistry*, vol. 276, no. 38, pp. 35 714–35 722, 2001.

[104] R. E.Hancock, "Host Defence (Cationic) Peptides," *Drugs*, vol. 57, no. 4, pp. 469–473, 1999.

[105] M. R.Yeaman and N. Y.Yount, "Mechanisms of antimicrobial peptide action and resistance," *Pharmacological Reviews*, vol. 55, no. 1, pp. 27–55, 2003.

[106] H. W.Huang, "Action of antimicrobial peptides: two-state model," *Biochemistry*, vol. 39, no. 29, pp. 8347–8352, 2000.

[107] Y.Shai and Z.Oren, "From carpet mechanism to de-novo designed diastereomeric cell-selective antimicrobial peptides," *Peptides*, vol. 22, no. 10, pp. 1629–1641, 2001.

[108] C. B.Park, H. S.Kim, and S. C.Kim, "Mechanism of action of the antimicrobial peptide buforin II: buforin II kills microorganisms by penetrating the cell membrane and inhibiting cellular functions," *Biochemical and Biophysical Research Communications*, vol. 244, no. 1, pp. 253–257, 1998.

[109] H.Haukland, H.Ulvatne *et al.*, "The antimicrobial peptides lactoferricin B and magainin 2 cross over the bacterial cytoplasmic membrane and reside in the cytoplasm," *FEBS Letters*, vol. 508, no. 3, pp. 389–393, 2001.

[110] P.Nicolas, "Multifunctional host defense peptides: intracellular-targeting antimicrobial peptides." *FEBS Journal*, vol. 276, no. 22, pp. 6483–96, 2009.

[111] M. G.Scott, D. J.Davidson *et al.*, "The human antimicrobial peptide LL-37 is a multifunctional modulator of innate immune responses," *Journal of Immunology*, vol. 169, no. 7, pp. 3883–3891, 2002.

[112] A.Izadpanah and R. L.Gallo, "Antimicrobial peptides," *Journal of the American Academy of Dermatology*, vol. 52, no. 3, pp. 381–392, 2005.

[113] C.Auvynet and Y.Rosenstein, "Multifunctional host defense peptides: Antimicrobial peptides, the small yet big players in innate and adaptive immunity," *FEBS Journal*, vol. 276, no. 22, pp. 6497–6508, 2009.

[114] T.Gutsmann, I.Razquin-Olazarán *et al.*, "New antiseptic peptides to protect against endotoxin-mediated shock." *Antimicrobial Agents and Chemotherapy*, vol. 54, no. 9, pp. 3817–24, 2010.

[115] Y.Rosenfeld and Y.Shai, "Lipopolysaccharide (Endotoxin)-host defense antibacterial peptides interactions: role in bacterial resistance and prevention of sepsis," *Biochimica et Biophysica Acta*, vol. 1758, no. 9, pp. 1513–1522, 2006.

[116] J. S.Kim, M. B.Ellman *et al.*, "Lactoferricin mediates anti-inflammatory and anti-catabolic effects via inhibition of IL-1 and LPS activity in the intervertebral disc." *Journal of Cellular Physiology*, vol. 228, no. 9, pp. 1884–96, 2013.

[117] W.Bellamy, M.Takase *et al.*, "Identification of the bactericidal domain of lactoferrin," *Biochimica et biophysica acta*, vol. 1121, no. 1-2, pp. 130–136, 1992.

[118] Y.Liu, F.Han *et al.*, "Comparative antimicrobial activity and mechanism of action of bovine lactoferricin-derived synthetic peptides." *Biometals*, vol. 24, no. 6, pp. 1069–78, 2011.

[119] P. M.Hwang, N.Zhou *et al.*, "Three-dimensional solution structure of lactoferricin B, an antimicrobial peptide derived from bovine lactoferrin," *Biochemistry*, vol. 37, no. 12, pp. 4288–4298, 1998.

[120] D. J.Schibli, P. M.Hwang, and H. J.Vogel, "The structure of the antimicrobial active center of lactoferricin B bound to sodium dodecyl sulfate micelles," *FEBS Letters*, vol. 446, no. 2, pp. 213–217, 1999.

[121] L. T.Nguyen, D. J.Schibli, and H. J.Vogel, "Structural studies and model membrane interactions of two peptides derived from bovine lactoferricin." *Journal of Peptide Science*, vol. 11, no. 7, pp. 379–89, 2005.

[122] H. N.Hunter, A. R.Demcoe *et al.*, "Human lactoferricin is partially folded in aqueous solution and is better stabilized in a membrane mimetic solvent." *Antimicrobial Agents and Chemotherapy*, vol. 49, no. 8, pp. 3387–95, 2005.

[123] T. J. G.Lars H. Vorland, Hilde Ulvatne, Jill Andersen, Hanne H. Haukland, Øystein Rekdal, John S. Svendsen, "Lactoferricin of Bovine Origin is More Active than Lactoferricins of Human, Murine and Caprine Origin," *Scandinavian Journal of Infectious Diseases*, vol. 30, no. 5, pp. 513–517, 1998.

[124] K.Shin, K.Yamauchi *et al.*, "Antibacterial activity of bovine lactoferrin and its peptides against enterohaemorrhagic Escherichia coli O157:H7." *Letters in Applied Microbiology*, vol. 26, no. 6, pp. 407–11, 1998.

[125] M. I.van derKraan, J.vanMarle *et al.*, "Ultrastructural effects of antimicrobial peptides from bovine lactoferrin on the membranes of Candida albicans and Escherichia coli," *Peptides*, vol. 26, no. 9, pp. 1537–1542, 2005.

[126] Y. H.Tu, Y. H.Ho *et al.*, "Identification of lactoferricin B intracellular targets using an Escherichia coli proteome chip." *PloS One*, vol. 6, no. 12, p. 28197, 2011.

[127] M.Arseneault, S.Bédard *et al.*, "Study of the interaction of lactoferricin B with phospholipid monolayers and bilayers." *Langmuir*, vol. 26, no. 5, pp. 3468–78, 2010.

[128] M.Umeyama, A.Kira *et al.*, "Interactions of bovine lactoferricin with acidic phospholipid bilayers and its antimicrobial activity as studied by solid-state NMR," *Biochimica et Biophysica Acta-Biomembranes*, vol. 1758, no. 9, pp. 1523–1528, 2006.

[129] S.Farnaud, C.Spiller *et al.*, "Interactions of lactoferricin-derived peptides with LPS and antimicrobial activity," *FEMS Microbiology Letters*, vol. 233, no. 2, pp. 193–199, 2004.

[130] H.Ulvatne, H.Haukland *et al.*, "Lactoferricin B causes depolarization of the cytoplasmic membrane of Escherichia coli ATCC 25922 and fusion of negatively charged liposomes," *FEBS Letters*, vol. 492, no. 1, pp. 62–65, 2001.

[131] A.Prlic, S.Bliven *et al.*, "Pre-calculated protein structure alignments at the RCSB PDB website." *Bioinformatics*, vol. 26, no. 23, pp. 2983–5, 2010.

[132] P.Pristovsek, S.Simcic *et al.*, "Structure of a synthetic fragment of the lipopolysaccharide (LPS) binding protein when bound to LPS and design of a peptidic LPS inhibitor." *Journal of Medicinal Chemistry*, vol. 48, no. 24, pp. 7911–4, 2005.

[133] M. G.Scott, A. C. E.Vreugdenhil *et al.*, "Cationic antimicrobial peptides block the binding of lipopolysaccharide (LPS) to LPS binding protein," *Journal of Immunology*, vol. 164, no. 2, pp. 549–553, 2000.

[134] E.Elass-Rochard, A.Roseanu *et al.*, "Lactoferrin-lipopolysaccharide interaction: involvement of the 28-34 loop region of human lactoferrin in the high-affinity binding to Escherichia coli 055B5 lipopolysaccharide." *Biochemical Journal*, vol. 312, pp. 839–45, 1995.

[135] Y.Hirakura, S.Kobayashi, and K.Matsuzaki, "Specific interactions of the antimicrobial peptide cyclic beta-sheet tachyplesin I with lipopolysaccharides," *Biochimica et Biophysica Acta*, vol. 1562, no. 1-2, pp. 32–36, 2002.

[136] M. E.Drago-Serrano, M.de laGarza-Amaya *et al.*, "Lactoferrin-lipopolysaccharide (LPS) binding as key to antibacterial and antiendotoxic effects," *International Immunopharmacology*, vol. 12, no. 1, pp. 1–9, 2012.

[137] B.Ramanathan, E. G.Davis *et al.*, "Cathelicidins: microbicidal activity, mechanisms of action, and roles in innate immunity," *Microbes and Infection*, vol. 4, no. 3, pp. 361–372, 2002.

[138] M. F.Burton and P. G.Steel, "The chemistry and biology of LL-37," *Natural Product Reports*, vol. 26, no. 12, pp. 1572–1584, 2009.

[139] G.Wang, "Structures of human host defense cathelicidin LL-37 and its smallest antimicrobial peptide KR-12 in lipid micelles," *Journal of Biological Chemistry*, vol. 283, no. 47, pp. 32 637–32 643, 2008.

[140] Z.Oren, J. C.Lerman *et al.*, "Structure and organization of the human antimicrobial peptide LL-37 in phospholipid membranes: relevance to the molecular basis for its non-cell-selective activity." *Biochemical Journal*, vol. 341, pp. 501–13, 1999.

[141] D.Xhindoli, S.Pacor *et al.*, "Native oligomerization determines the mode of action and biological activities of human cathelicidin LL-37." *Biochemical Journal*, vol. 15, pp. 263–275, 2014.

[142] S.Sandgren, A.Wittrup *et al.*, "The human antimicrobial peptide LL-37 transfers extracellular DNA plasmid to the nuclear compartment of mammalian cells via lipid rafts and proteoglycan-dependent endocytosis." *Journal of Biological Chemistry*, vol. 279, no. 17, pp. 17 951–6, 2004.

[143] W. K. K.Wu, G.Wang *et al.*, "Emerging roles of the host defense peptide LL-37 in human cancer and its potential therapeutic applications." *International Journal of Cancer*, vol. 127, no. 8, pp. 1741–7, 2010.

[144] K. A.Sochacki, K. J.Barns *et al.*, "Real-time attack on single Escherichia coli cells by the human antimicrobial peptide LL-37." *Proceedings of the National Academy of Sciences of the United States of America*, vol. 108, no. 16, pp. E77–81, 2011.

[145] D.Vandamme, B.Landuyt *et al.*, "A comprehensive summary of LL-37, the factotum human cathelicidin peptide," *Cellular Immunology*, vol. 280, no. 1, pp. 22–35, 2012.

[146] J.Noore, A.Noore, and B.Li, "Cationic antimicrobial peptide LL-37 is effective against both extra- and intracellular Staphylococcus aureus." *Antimicrobial Agents and Chemotherapy*, vol. 57, no. 3, pp. 1283–90, 2013.

[147] J.Säll, M.Carlsson *et al.*, "The antimicrobial peptide LL-37 alters human osteoblast Ca(2+) handling and induces Ca(2+)-independent apoptosis." *Journal of Innate Immunity*, vol. 5, no. 3, pp. 290–300, 2013.

[148] J. W.Larrick, M.Hirata *et al.*, "Human Cap18 - a novel antimicrobial lipopolysaccharide-binding protein," *Infection and Immunity*, vol. 63, no. 4, pp. 1291–1297, 1995.

[149] K. L.Brown, G. F. T.Poon *et al.*, "Host defense peptide LL-37 selectively reduces proinflammatory macrophage responses," *Journal of Immunology*, vol. 186, no. 9, pp. 5497–5505, 2011.

[150] S.Thennarasu, A.Tan *et al.*, "Antimicrobial and membrane disrupting activities of a peptide derived from the human cathelicidin antimicrobial peptide LL37." *Biophysical Journal*, vol. 98, no. 2, pp. 248–57, 2010.

[151] B.Ding, L.Soblosky *et al.*, "Physiologically-relevant modes of membrane interactions by the human antimicrobial peptide, LL-37, revealed by SFG experiments." *Scientific Reports*, vol. 3, p. 1854, 2013.

[152] I.Nagaoka, S.Hirota *et al.*, "Augmentation of the lipopolysaccharide-neutralizing activities of human cathelicidin CAP18/LL-37-derived antimicrobial peptides by replacement with hydrophobic and cationic amino acid residues," *Clinical and Diagnostic Laboratory Immunology*, vol. 9, no. 5, pp. 972–982, 2002.

[153] D. S.Sivia, *Elementary scattering theory: for X-ray and neutron users.* Oxford, 2011.

[154] G. L.Squires, *Introduction to the Theory of Thermal Neutron Scattering.* Cambridge University Press, 2012.

[155] B. T. M.Willis and C. J.Carlile, *Experimental Neutron Scattering.* Oxford University Press, 2009.

[156] J. S.Higgins and H. C.Benoit, *Polymers and Neutron Scattering.* Oxford University Press, 1997.

[157] R. J.Roe, *Methods of X-ray and Neutron Scattering in Polymer Science.* Oxford University Press, 2000.

[158] B.Jacrot, "The study of biological structures by neutron scattering from solution," *Reports on Progress in Physics*, vol. 39, no. 10, pp. 911–953, 1976.

[159] R.Borsali and R.Pecora, *Soft Matter Characterization.* Springer, 2008.

[160] J. H.Lakey, "Neutrons for biologists: a beginner's guide, or why you should consider using neutrons." *Journal of the Royal Society Interface*, vol. 6, pp. 567–73, 2009.

[161] L. A.Clifton, C.Neylon, and J. H.Lakey, "Examining protein-lipid complexes using neutron scattering." *Methods in Molecular Biology*, vol. 974, pp. 119–50, 2013.

[162] J.Lu, T.Su, and R.Thomas, "Structural conformation of bovine serum albumin layers at the airwater interface studied by neutron reflection," *Journal of Colloid and Interface Science*, vol. 213, no. 2, pp. 426–437, 1999.

[163] G. L.Gaines, *Insoluble Monolayers at Liquid-gas Interfaces.* Bell & Howell Company, 1994.

[164] P.Dynarowicz-Latka, A.Dhanabalan, and O. N.Oliveira, "Modern physicochemical research on Langmuir monolayers," *Advances in Colloid and Interface Science*, vol. 91, no. 2, pp. 221–293, 2001.

[165] D.Marsh, "Lateral pressure in membranes." *Biochimica et Biophysica Acta*, vol. 1286, no. 3, pp. 183–223, 1996.

[166] U.Klenz, M.Saleem *et al.*, "Influence of lipid saturation grade and headgroup charge: a refined lung surfactant adsorption model." *Biophysical Journal*, vol. 95, no. 2, pp. 699–709, 2008.

[167] C.Luna, K. M.Stroka *et al.*, "Thermodynamics of monolayers formed by mixtures of phosphatidylcholine/phosphatidylserine," *Colloids and Surfaces. B: Biointerfaces*, vol. 85, no. 2, pp. 293–300, 2011.

[168] A. D.Petelska, M.Naumowicz, and Z. A.Figaszewski, "The influence of pH on phosphatidylethanolamine monolayer at the air/aqueous solution interface." *Cell Biochemistry and Biophysics*, vol. 65, no. 2, pp. 229–35, 2013.

[169] J. F.Nagle, "Theory of lipid monolayer and bilayer phase transitions: effect of headgroup interactions," *Journal of Membrane Biology*, vol. 27, no. 1, pp. 233–250, 1976.

[170] R. C.MacDonald and S. A.Simon, "Lipid monolayer states and their relationships to bilayers." *Proceedings of the National Academy of Sciences of the United States of America*, vol. 84, no. 12, pp. 4089–93, 1987.

[171] V.Kaganer, H.Möhwald, and P.Dutta, "Structure and phase transitions in Langmuir monolayers," *Reviews of Modern Physics*, vol. 71, no. 3, pp. 779–819, 1999.

[172] R.Maget-Dana, "The monolayer technique: a potent tool for studying the interfacial properties of antimicrobial and membrane-lytic peptides and their interactions with lipid membranes," *Biochimica Et Biophysica Acta-Biomembranes - Biomembranes*, vol. 1462, no. 1, pp. 109–140, 1999.

[173] R. E.Hancock and A.Rozek, "Role of membranes in the activities of antimicrobial cationic peptides," *FEMS Microbiology Letters*, vol. 206, no. 2, pp. 143–149, 2002.

[174] T.Abraham, S. R.Schooling *et al.*, "Monolayer film behavior of lipopolysaccharide from pseudomonas aeruginosa at the air-water interface," *Biomacromolecules*, vol. 9, no. 10, pp. 2799–2804, 2008.

[175] O.Canadas, K. M. W.Keough, and C.Casals, "Bacterial lipopolysaccharide promotes destabilization of lung surfactant-like films," *Biophysical Journal*, vol. 100, no. 1, pp. 108–116, 2011.

[176] I.Garcia-Verdugo, O.Canadas *et al.*, "Surfactant protein A forms extensive lattice-like structures on 1,2-Dipalmitoylphosphatidylcholine/Rough-Lipopolysaccharide- mixed monolayers," *Biophysical Journal*, vol. 93, no. 10, pp. 3529–3540, 2007.

[177] E.Schneck, T.Schubert *et al.*, "Quantitative determination of ion distributions in bacterial lipopolysaccharide membranes by grazing-incidence X-ray

fluorescence," *Proceedings of the National Academy of Sciences of the United States of America*, vol. 107, no. 20, pp. 9147–9151, 2010.

[178] J. R.Lakowicz and B. R.Masters, *Principles of fluorescence spectroscopy*, 3rd ed. Springer, 2008, vol. 13, no. 2.

[179] A. S.Ladokhin, S.Jayasinghe, and S. H.White, "How to measure and analyze tryptophan fluorescence in membranes properly, and why bother?" *Analytical Biochemistry*, vol. 285, no. 2, pp. 235–45, 2000.

[180] K.Matsuzaki, O.Murase *et al.*, "Orientational and Aggregational States of Magainin 2 in Phospholipid Bilayers," *Biochemistry*, vol. 33, no. 11, pp. 3342–3349, 1994.

[181] D. J.Schibli, R. F.Epand *et al.*, "Tryptophan-rich antimicrobial peptides: comparative properties and membrane interactions." *Biochemistry and Cell Biology*, vol. 80, no. 5, pp. 667–77, 2002.

[182] J. E.Gable, D. E.Schlamadinger *et al.*, "Fluorescence and UV resonance Raman study of peptide-vesicle interactions of human cathelicidin LL-37 and its F6W and F17W mutants." *Biochemistry*, vol. 48, no. 47, pp. 11 264–72, 2009.

[183] F.Neville, M.Cahuzac *et al.*, "Lipid headgroup discrimination by antimicrobial peptide LL-37: insight into mechanism of action." *Biophysical Journal*, vol. 90, no. 4, pp. 1275–87, 2006.

[184] F.Porcelli, R.Verardi *et al.*, "NMR structure of the cathelicidin-derived human antimicrobial peptide LL-37 in dodecylphosphocholine micelles." *Biochemistry*, vol. 47, no. 20, pp. 5565–72, 2008.

[185] K.Gawrisch and B. W.Koenig, "Lipid-peptide interaction investigated by NMR," *Current Topics in Membranes*, vol. 52, pp. 163–190, 2002.

[186] M. F.Brown and A. A.Nevzorov, "2H-NMR in liquid crystals and membranes," *Colloids and Surfaces A: Physicochemical and Engineering Aspects*, vol. 158, no. 1, pp. 281–298, 1999.

[187] H.Schäfer, B.Mädler, and E.Sternin, "Determination of orientational order parameters from 2H NMR spectra of magnetically partially oriented lipid bilayers." *Biophysical Journal*, vol. 74, no. 2, pp. 1007–14, 1998.

[188] M. L.Kilfoil and M. R.Morrow, "Slow motions in bilayers containing anionic phospholipid," *Physica A: Statistical Mechanics and its Applications*, vol. 261, no. 1-2, pp. 82–94, 1998.

[189] M F Brown, S Lope-Piedrafita,H I Petrache, G V Martinez, "Solid-State Deuterium NMR spectroscopy of membranes," in *Modern Magnetic Resonance*, G. A.Webb, Ed. Springer, 2006.

[190] B. W.Koenig, H. H.Strey, and K.Gawrisch, "Membrane lateral compressibility determined by NMR and x-ray diffraction: effect of acyl chain polyunsaturation." *Biophysical Journal*, vol. 73, no. 4, pp. 1954–66, 1997.

[191] A. J.Mason, J. J.Lopez *et al.*, "A spectroscopic study of the membrane interaction of tuberoinfundibular peptide of 39 residues (TIP39)." *Biochimica et Biophysica Acta*, vol. 1714, no. 1, pp. 1–10, 2005.

[192] B. W.Koenig, J. A.Ferretti, and K.Gawrisch, "Site-specific deuterium order parameters and membrane-bound behavior of a peptide fragment from the intracellular domain of HIV-1 gp41." *Biochemistry*, vol. 38, no. 19, pp. 6327–34, 1999.

[193] T.Doherty, A. J.Waring, and M.Hong, "Peptide-lipid interactions of the beta-hairpin antimicrobial peptide tachyplesin and its linear derivatives from solid-state NMR." *Biochimica et Biophysica Acta*, vol. 1758, no. 9, pp. 1285–91, 2006.

[194] A. J.Mason, W.Moussaoui *et al.*, "Structural determinants of antimicrobial and antiplasmodial activity and selectivity in histidine-rich amphipathic cationic peptides." *Journal of Biological Chemistry*, vol. 284, no. 1, pp. 119–33, 2009.

[195] B.Kwon, A. J.Waring, and M.Hong, "A 2H solid-state NMR study of lipid clustering by cationic antimicrobial and cell-penetrating peptides in model bacterial membranes," *Biophysical Journal*, vol. 105, no. 10, pp. 2333–2342, 2013.

[196] N. E.Gomes, M. K. C.Brunialti *et al.*, "Lipopolysaccharide-induced expression of cell surface receptors and cell activation of neutrophils and monocytes in whole human blood." *Brazilian Journal of Medical and Biological Research*, vol. 43, no. 9, pp. 853–858, 2010.

[197] M. K. C.Brunialti, P. S.Martins *et al.*, "TLR2, TLR4, CD14, CD11B, and CD11C expressions on monocytes surface and cytokine production in patients with sepsis, severe sepsis and septic shock." *Shock*, vol. 25, no. 4, pp. 351–357, 2006.

[198] H.Loppnow, H.Brade *et al.*, "IL-1 induction-capacity of defined lipopolysaccharide partial structures." *Journal of Immunology*, vol. 142, no. 9, pp. 3229–38, 1989.

[199] A. B.Schromm, K.Brandenburg *et al.*, "Biological activities of lipopolysaccharides are determined by the shape of their lipid A portion," *European Journal of Biochemistry*, vol. 267, no. 7, pp. 2008–2013, 2000.

[200] K.Brandenburg, U.Seydel *et al.*, "Conformation of lipid A, the endotoxic center of bacterial lipopolysaccharide," *Journal of Endotoxin Research*, vol. 3, no. 3, pp. 173–178, 1996.

[201] C. F.Nathan and J. B.Hibbs, "Role of nitric oxide synthesis in macrophage antimicrobial activity," *Current Opinion in Immunology*, vol. 3, no. 1, pp. 65–70, 1991.

[202] C. F.Nathan, "Mechanisms of macrophage antimicrobial activity," *Transactions of the Royal Society of Tropical Medicine and Hygiene*, vol. 77, no. 5, pp. 620–630, 1983.

[203] J. D.Laskin, D. E.Heck, and D. L.Laskin, "Multifunctional role of nitric oxide in inflammation," *Trends in Endocrinology & Metabolism*, vol. 5, no. 9, pp. 377–382, 1994.

[204] I. J.Schytte Blix and K.Helgeland, "LPS from Actinobacillus actinomycetemcomitans and production of nitric oxide in murine macrophages J774," *European Journal of Oral Sciences*, vol. 106, no. 1, pp. 576–581, 1998.

[205] S. E.Applequist, "Variable expression of Toll-like receptor in murine innate and adaptive immune cell lines," *International Immunology*, vol. 14, no. 9, pp. 1065–1074, 2002.

[206] C.-C.Tseng, Y.Hattori *et al.*, "Decreased production of nitric oxide by lps-treated J774 macrophages in high-glucose medium," *Life Sciences*, vol. 60, no. 7, pp. 99–106, 1997.

[207] J.Andrä, K.Lohner *et al.*, "Enhancement of endotoxin neutralization by coupling of a C12-alkyl chain to a lactoferricin-derived peptide." *Biochemical Journal*, vol. 385, no. 1, pp. 135–143, 2005.

[208] W.Strober, "Trypan blue exclusion test of cell viability." in *Current Protocols in Immunology*, 2001, vol. Appendix 3, p. Appendix 3B. Online: http://www.ncbi.nlm.nih.gov/pubmed/18432654

[209] R.Tamai, S.Sugawara *et al.*, "Synergistic effects of lipopolysaccharide and interferon-gamma in inducing interleukin-8 production in human monocytic THP-1 cells is accompanied by up-regulation of CD14, Toll-like receptor 4, MD-2 and MyD88 expression." *Journal of Endotoxin Research*, vol. 9, no. 3, pp. 145–53, 2003.

[210] T.Mosmann, "Rapid colorimetric assay for cellular growth and survival: Application to proliferation and cytotoxicity assays," *Journal of Immunological Methods*, vol. 65, no. 1, pp. 55–63, 1983.

[211] I.Nagaoka, S.Hirota *et al.*, "Cathelicidin family of antibacterial peptides CAP18 and CAP11 inhibit the expression of TNF-alpha by blocking the binding of LPS to CD14(+) cells," *Journal of Immunology*, vol. 167, no. 6, pp. 3329–3338, 2001.

[212] E. T.Rietschel, C.Galanos *et al.*, "Biological activities of chemically modified endotoxins," *European Journal of Biochemistry*, vol. 22, no. 2, pp. 218–224, 1971.

[213] E. T.Rietschel, T.Kirikae *et al.*, "The chemical structure of bacterial endotoxin in relation to bioactivity," *Immunobiology*, vol. 187, no. 3, pp. 169–190, 1993.

[214] E. T.Rietschel, T.Kirikae *et al.*, "Bacterial endotoxin: molecular relationships of structure to activity and function." *FASEB Journal*, vol. 8, no. 2, pp. 217–25, 1994.

[215] M. U.Hammer, A.Brauser *et al.*, "Lipopolysaccharide interaction is decisive for the activity of the antimicrobial peptide NK-2 against Escherichia coli and Proteus mirabilis," *Biochemical Journal*, vol. 427, no. 3, pp. 477–488, 2010.

[216] K.Brandenburg, P.Garidel *et al.*, "Molecular basis for endotoxin neutralization by amphipathic peptides derived from the alpha-helical cationic core-region of NK-lysin." *Biophysical Chemistry*, vol. 150, no. 1, pp. 80–87, 2010.

[217] Y.Kaconis, I.Kowalski *et al.*, "Biophysical mechanisms of endotoxin neutralization by cationic amphiphilic peptides." *Biophysical Journal*, vol. 100, no. 11, pp. 2652–61, 2011.

[218] S.Pochet, S.Tandel *et al.*, "Modulation by LL-37 of the responses of salivary glands to purinergic agonists." *Molecular Pharmacology*, vol. 69, no. 6, pp. 2037–46, 2006.

[219] T.Hirsch, M.Metzig *et al.*, "Role of host defense peptides of the innate immune response in sepsis," *Shock*, vol. 30, no. 2, pp. 117–126, 2008.

[220] A.Scott, S.Weldon *et al.*, "Evaluation of the ability of LL-37 to neutralise LPS in vitro and ex vivo," *PLoS One*, vol. 6, no. 10, p. 26525, 2011.

[221] Y.Rosenfeld, H. G.Sahl, and Y.Shai, "Parameters involved in antimicrobial and endotoxin detoxification activities of antimicrobial peptides," *Biochemistry*, vol. 47, no. 24, pp. 6468–6478, 2008.

[222] G.-H.Zhang, D. M.Mann, and C.-M.Tsai, "Neutralization of endotoxin in vitro and in vivo by a human lactoferrin-derived peptide," *Infection and Immunity*, vol. 67, no. 3, pp. 1353–1358, 1999.

[223] D. S.Chapple, R.Hussain *et al.*, "Structure and association of human lactoferrin peptides with Escherichia coli lipopolysaccharide." *Antimicrobial Agents and Chemotherapy*, vol. 48, no. 6, pp. 2190–8, 2004.

[224] J. B.Hayter, M.Rivera, and E. J.Mcgroarty, "Neutron scattering analysis of bacterial Lipopolysaccharide phase structure - changes at high Ph," *Journal of Biological Chemistry*, vol. 262, no. 11, pp. 5100–5105, 1987.

[225] H.Labischinski, E.Vorgel *et al.*, "Architecture of bacterial lipid-A in solution - a neutron small-angle scattering study," *European Journal of Biochemistry*, vol. 190, no. 2, pp. 359–363, 1990.

[226] R. I.Roth, J. S.Wong, and R. L.Hamilton, "Ultrastructural changes in bacterial lipopolysaccharide induced by human hemoglobin," *Innate Immunity*, vol. 3, no. 4, pp. 361–366, 1996.

[227] A.Bergstrand, C.Svanberg *et al.*, "Aggregation behavior and size of lipopolysaccharide from Escherichia coli O55:B5," *Colloids and Surfaces B: Biointerfaces*, vol. 53, no. 1, pp. 9–14, 2006.

[228] W.Richter, V.Vogel *et al.*, "Morphology, size distribution, and aggregate structure of lipopolysaccharide and lipid A dispersions from enterobacterial origin," *Innate Immunity*, vol. 17, no. 5, pp. 427–438, 2011.

[229] X.Chen, J.Howe *et al.*, "Biophysical analysis of the interaction of granulysin-derived peptides with enterobacterial endotoxins," *Biochimica et Biophysica Acta*, vol. 1768, no. 10, pp. 2421–2431, 2007.

[230] S.Singh, P.Papareddy *et al.*, "Importance of lipopolysaccharide aggregate disruption for the anti-endotoxic effects of heparin cofactor II peptides." *Biochimica et Biophysica Acta*, vol. null, no. null, 2013.

[231] C.Galanos, O.Luderitz, and O.Westphal, "A new method for the extraction of R lipopolysaccharides," *European Journal of Biochemistry*, vol. 9, no. 2, pp. 245–249, 1969.

[232] M. A.Apicella, "Isolation and characterization of lipopolysaccharides," *Methods in Molecular Biology*, vol. 431, pp. 3–13, 2008.

[233] R. P.Darveau and R. E. W.Hancock, "Procedure for isolation of bacterial lipopolysaccharides from both smooth and rough Pseudomonas aeruginosa and Salmonella typhimurium strains," *Journal of Bacteriology*, vol. 155, no. 2, pp. 831–838, 1983.

[234] M.Almgren, K.Edwards, and G.Karlsson, "Cryo transmission electron microscopy of liposomes and related structures," *Colloids and Surfaces A: Physicochemical and Engineering Aspects*, vol. 174, no. 1-2, pp. 3–21, 2000.

[235] ISIS, "LoQ instrument technical information," 2012. Online: http://www.isis.stfc.ac.uk/instruments/loq/technical/loq-technical-information7485.html

[236] R. K.Heenan, J.Penfold, and S. M.King, "SANS at pulsed neutron sources: Present and future prospects," *Journal of Applied Crystallography*, vol. 30, pp. 1140–1147, 1997.

[237] S. M.King, *Small-angle neutron scattering.* J. Wiley, 1999, ch. 7, pp. 171–231.

[238] J. S.Pedersen and P.Schurtenberger, "Scattering functions of semiflexible polymers with and without excluded volume effects," *Macromolecules*, vol. 29, no. 23, pp. 7602–7612, 1996.

[239] P.Thiyagarajan, T.Burkoth *et al.*, "pH dependent self assembly of β-amyloid(10-35) and β-amyloid(10-35)-PEG3000," *Journal of Applied Crystallography*, vol. 33, no. 3, pp. 535–539, 2000.

[240] A. L.Kholodenko, "Analytical calculation of the scattering function for polymers of arbitrary flexibility using the Dirac propagator," *Macromolecules*, vol. 26, no. 16, pp. 4179–4183, 1993.

[241] M.Kotlarchyk, E.Sheu, and M.Capel, "Structural and dynamical transformations between neighboring dense microemulsion phases," *Physical Review A*, vol. 46, no. 2, pp. 928–939, 1992.

[242] R. J.Ulevitch and A. R.Johnston, "The modification of biophysical and endotoxic properties of bacterial lipopolysaccharides by serum." *Journal of Clinical Investigation*, vol. 62, no. 6, pp. 1313–24, 1978.

[243] C. A.Aurell and A. O.Wistrom, "Critical aggregation concentrations of Gram negative bacterial lipopolysaccharides (LPS)," *Biochemical and Biophysical Research Communications*, vol. 253, no. 1, pp. 119–123, 1998.

[244] C.Risco, J. L.Carrascosa, and M. A.Bosch, "Visualization of lipopolysaccharide aggregates by freeze-fracture and negative staining." *Journal of Electron Microscopy*, vol. 42, no. 3, pp. 202–204, 1993.

[245] Y.Miyazaki, M.Aoki *et al.*, "Interaction of antimicrobial peptide magainin 2 with gangliosides as a target for human cell binding." *Biochemistry*, vol. 51, no. 51, pp. 10 229–35, 2012.

[246] M.Price, R.Cornelius, and J.Brash, "Protein adsorption to polyethylene glycol modified liposomes from fibrinogen solution and from plasma," *Biochimica et Biophysica Acta - Biomembranes*, vol. 1512, no. 2, pp. 191–205, 2001.

[247] O.Aguilera, H.Ostolaza *et al.*, "Permeabilizing action of an antimicrobial lactoferricin-derived peptide on bacterial and artificial membranes," *FEBS Letters*, vol. 462, no. 3, pp. 273–277, 1999.

[248] N. Y.Yount, A. S.Bayer *et al.*, "Advances in antimicrobial peptide immunobiology." *Biopolymers*, vol. 84, no. 5, pp. 435–58, 2006.

[249] K.Matsuzaki, K.Sugishita *et al.*, "Relationship of membrane curvature to the formation of pores by magainin 2." *Biochemistry*, vol. 37, no. 34, pp. 11 856–63, 1998.

[250] J.Andrä, T.Gutsmann *et al.*, "Mechanisms of endotoxin neutralization by synthetic cationic compounds," *Journal of Endotoxin Research*, vol. 12, no. 5, pp. 261–277, 2006.

[251] P. G.Barlow, Y.Li *et al.*, "The human cationic host defense peptide LL-37 mediates contrasting effects on apoptotic pathways in different primary cells of the innate immune system." *Journal of Leukocyte Biology*, vol. 80, no. 3, pp. 509–20, 2006.

[252] R.Saravanan, H.Mohanram *et al.*, "Structure, activity and interactions of the cysteine deleted analog of tachyplesin-1 with lipopolysaccharide micelle: mechanistic insights into outer-membrane permeabilization and endotoxin neutralization," *Biochimica et Biophysica Acta*, vol. 1818, no. 7, pp. 1613–24, 2012.

[253] H. G.Boman, "Antibacterial peptides: basic facts and emerging concepts." *Journal of Internal Medicine*, vol. 254, no. 3, pp. 197–215, 2003.

[254] Z. V.Leonenko, E.Finot *et al.*, "Investigation of temperature-induced phase transitions in DOPC and DPPC phospholipid bilayers using temperature-controlled scanning force microscopy." *Biophysical Journal*, vol. 86, no. 6, pp. 3783–93, 2004.

[255] M. D.Lad, F.Birembaut *et al.*, "Antimicrobial peptide-lipid binding interactions and binding selectivity." *Biophysical Journal*, vol. 92, no. 10, pp. 3575–86, 2007.

[256] H.Brockman, "Lipid monolayers: why use half a membrane to characterize protein-membrane interactions?" *Current Opinion in Structural Biology*, vol. 9, no. 4, pp. 438–443, 1999.

[257] Avanti polar lipid Inc., "Preparation of liposomes," 1997. Online: http://avantilipids.com/index.php?option=com_content&view=article&id=1384&Itemid=372

[258] F.Menges, "Spekwin32 - Spectroscopy Software." Online: http://www.effemm2.de/spekwin/index_en.html

[259] J. M.Rodríguez Patino, C. C.Sánchez, and M. R.Rodríguez Niño, "Morphological and structural characteristics of monoglyceride monolayers at the airwater interface observed by Brewster angle microscopy," *Langmuir*, vol. 15, no. 7, pp. 2484–2492, 1999.

[260] T.Kaercher, D.Hönig, and D.Möbius, "Brewster angle microscopy. A new method of visualizing the spreading of Meibomian lipids." *International Ophthalmology*, vol. 17, no. 6, pp. 341–8, 1993.

[261] J.Miñones, J.Rodrguez Patino *et al.*, "The effect of polar groups on structural characteristics of phospholipid monolayers spread at the airwater interface," *Colloids and Surfaces A: Physicochemical and Engineering Aspects*, vol. 203, no. 1, pp. 273–286, 2002.

[262] X.Chen, Z.Huang *et al.*, "Reorganization and caging of DPPC, DPPE, DPPG, and DPPS monolayers caused by dimethylsulfoxide observed using Brewster angle microscopy." *Langmuir*, vol. 26, no. 24, pp. 18 902–8, 2010.

[263] M. M.Lipp, K. Y.Lee *et al.*, "Fluorescence, polarized fluorescence, and Brewster angle microscopy of palmitic acid and lung surfactant protein B monolayers." *Biophysical Journal*, vol. 72, no. 6, pp. 2783–804, 1997.

[264] P.Krüger, M.Schalke *et al.*, "Effect of hydrophobic surfactant peptides SP-B and SP-C on binary phospholipid monolayers. I. Fluorescence and dark-field microscopy." *Biophysical Journal*, vol. 77, no. 2, pp. 903–14, 1999.

[265] L. A.Clifton, M. W. A.Skoda *et al.*, "Asymmetric phospholipid: lipopolysaccharide bilayers; a Gram-negative bacterial outer membrane mimic." *Journal of the Royal Society Interface*, vol. 10, no. 89, p. 20130810, 2013.

[266] H. H.Haukland, "Post-antibiotic effect of the antimicrobial peptide lactoferricin on Escherichia coli and Staphylococcus aureus," *Journal of Antimicrobial Chemotherapy*, vol. 48, no. 4, pp. 569–571, 2001.

[267] J. H.Davis, "The description of membrane lipid conformation, order and dynamics by 2H-NMR," *Biochimica et Biophysica Acta - Biomembranes*, vol. 737, no. 1, pp. 117–171, 1983.

[268] A.Ramamoorthy, S.Thennarasu *et al.*, "Solid-State NMR investigation of the membrane-disrupting mechanism of antimicrobial peptides MSI-78 and MSI-594 derived from magainin 2 and melittin," *Biophysical Journal*, vol. 91, no. 1, pp. 206–216, 2006.

[269] Y.-L.Lee, J.-Y.Lin, and C.-H.Chang, "Thermodynamic characteristics and Langmuir-Blodgett deposition behavior of mixed (DPPA/DPPC) monolayers at air/liquid interfaces," *Journal of Colloid and Interface Science*, vol. 296, no. 2, pp. 647–654, 2006.

[270] W.Ou-Yang, M.Weis *et al.*, "Effect of external electrostatic charge on condensed phase domains at the air-water interface: Experiment and shape equation analysis." *The Journal of Chemical Physics*, vol. 130, no. 10, p. 104706, 2009.

[271] W.Ou-Yang, M.Weis *et al.*, "Study of relaxation process of dipalmitoyl phosphatidylcholine monolayers at air-water interface: effect of electrostatic energy." *The Journal of Chemical Physics*, vol. 134, no. 15, p. 154709, 2011.

[272] F.Behroozi, "Theory of elasticity in two dimensions and its application to Langmuir-Blodgett films," *Langmuir*, vol. 12, no. 9, pp. 2289–2291, 1996.

[273] P.Dynarowicz-Latka and K.Hac-Wydro, "Interactions between phosphatidylcholines and cholesterol in monolayers at the air/water interface." *Colloids and surfaces B: Biointerfaces*, vol. 37, no. 1-2, pp. 21–5, 2004.

[274] D.Risović, S.Frka, and Z.Kozarac, "Application of Brewster angle microscopy and fractal analysis in investigations of compressibility of Langmuir monolayers." *Journal of Chemical Physics*, vol. 134, no. 2, p. 024701, 2011.

[275] A. L.Mackay, C. P.Nichol *et al.*, "A proton and deuterium nuclear magnetic reasonance study of orientational order in aqueous dispersions of lipopolysaccharide and lipopolysaccharide/dipalmitoylphosphatidylcholine mixtures," *Biochimica et Biophysica Acta -Biomembranes*, vol. 774, no. 2, pp. 181–187, 1984.

[276] S.-s.Feng, "Interpretation of mechanochemical properties of lipid bilayer vesicles from the equation of state or pressurearea measurement of the monolayer at the airwater or oilwater interface," *Langmuir*, vol. 15, no. 4, pp. 998–1010, 1999.

[277] D.Vaknin, K.Kjaer *et al.*, "Structural properties of phosphatidylcholine in a monolayer at the air/water interface: Neutron reflection study and re-examination of x-ray reflection measurements." *Biophysical Journal*, vol. 59, no. 6, pp. 1325–32, 1991.

[278] V.Rondelli, G.Fragneto *et al.*, "Reflectivity from floating bilayers: can we keep the structural asymmetry?" *Journal of Physics: Conference Series*, vol. 340, no. 1, p. 012083, 2012.

[279] K. A.Henzler-Wildman, G. V.Martinez *et al.*, "Perturbation of the hydrophobic core of lipid bilayers by the human antimicrobial peptide LL-37." *Biochemistry*, vol. 43, no. 26, pp. 8459–69, 2004.

[280] K. T.Nguyen, S. V.Le Clair *et al.*, "Molecular interactions between magainin 2 and model membranes in situ." *Journal of Physical Chemistry B*, vol. 113, no. 36, pp. 12 358–63, 2009.

[281] E. L.Wu, O.Engström *et al.*, "Molecular dynamics and NMR spectroscopy studies of E. coli lipopolysaccharide structure and dynamics," *Biophysical Journal*, vol. 105, no. 6, pp. 1444–1455, 2013.

[282] F.Ciesielski, D. C.Griffin *et al.*, "Interactions of lipopolysaccharide with lipid membranes, raft models - A solid state NMR study." *Biochimica et Biophysica Acta*, vol. 1828, no. 8, pp. 1731–1742, 2013.

[283] C. R. H.Raetz and C.Whitfield, "Lipopolysaccharide endotoxins," *Annual Review of Biochemistry*, vol. 71, pp. 635–700, 2002.

[284] S. A.David and D.Sil, "Development of small-molecule endotoxin sequestering agents." *Subcellular Biochemistry*, vol. 53, pp. 255–83, 2010.

[285] U. K.Laemmli, "Cleavage of structural proteins during the assembly of the head of bacteriophage T4," *Nature*, vol. 227, no. 5259, pp. 680–685, 1970.

[286] L. G. M.Duchesne, J. S.Lam *et al.*, "Effect of Ph and acrylamide concentration on the separation of lipopolysaccharides in polyacrylamide gels," *Current Microbiology*, vol. 16, no. 4, pp. 191–194, 1988.

[287] A. J.Lesse, A. A.Campagnari *et al.*, "Increased resolution of lipopolysaccharides and lipooligosaccharides utilizing tricine-sodium dodecyl sulfate-polyacrylamide gel electrophoresis," *Journal of Immunological Methods*, vol. 126, no. 1, pp. 109–117, 1990.

[288] C. M.Tsai and C. E.Frasch, "A sensitive silver stain for detecting lipopolysaccharides in polyacrylamide gels," *Analytical Biochemistry*, vol. 119, no. 1, pp. 115–119, 1982.

[289] D.Myatt and L.Clifton, "Biomolecular Scattering Length Density Calculator." Online: http://psldc.isis.rl.ac.uk/index.html